Probing Barrier-Type Anodic Alumina Films on Nano-Patterned Substrates

A thesis submitted to the University of Manchester for the degree of

Doctor of Philosophy

in the Faculty of Engineering and Physical Sciences

2010

Nicolas Trigoulet

School of Materials

Corrosion and Protection Centre

Contents

Contents 2

List of Tables 6

List of Figures 8

Abstract 29

Declaration 30

Copyright Statement 31

Acknowledgements 32

Introduction 33

Literature Survey 37

1 Introduction 38

2 Aluminium and Aluminium Alloys - Generalities 39

2.1 General Properties 39

2.2 Designation System: Nomenclature 40

3 Growth Mechanisms of Anodic Oxide Films 44

3.1 Passivation 45

3.1.1 Description 45

3.1.2 Corrosion behaviour of active-passive metals 46

3.2 Anodizing 47

3.2.1 Barrier-type anodic alumina films 47
3.2.2 Porous-type anodic alumina films 49
3.3 Growth of Barrier-Type Anodic Oxide on Patterned Surfaces . 50
3.3.1 High field ionic conduction 50
3.3.2 Plasticity 52
3.3.3 Stress-driven transport 53
3.3.4 Markers and tracers 54

4 Sputtering-Induced Depth Profiling Analyses 63
4.1 Sputtering 63
4.1.1 Sputtering process 63
4.1.2 Sputtering yield 66
4.2 Sputtering-Induced Surface Modifications 67
4.2.1 Topographical modifications 67
4.2.2 Compositional modifications 69
4.3 Elemental Depth Profiling Analysis Techniques 70
4.3.1 Selection of elemental depth profiling analysis techniques . . . 70
4.3.2 Time-of-flight secondary ion spectrometry 70
4.3.3 Glow discharge spectrometry 71
4.4 Depth Resolution 74
4.4.1 Definition 74
4.4.2 Degradation of the depth resolution 76
4.4.3 Profile reconstruction 77

5 Introduction to the Present Work 92

EXPERIMENTAL PROCEDURE **94**

1 Specimens of Controlled Roughnesses 95
1.1 Material and Surface Cleaning 95
1.2 Surface Treatments 96
1.2.1 Electropolishing 96
1.2.2 Growth of ordered cell array anodic alumina films 96
1.2.3 Stripping of the porous anodic alumina films 97
1.2.4 Growth of barrier-type anodic alumina films 98

2 Characterisation 99
2.1 Topography and Morphology . . . 99
2.1.1 Atomic force microscopy . . . 99
2.1.2 Scanning electron microscopy . . . 101
2.1.3 Transmission electron microscopy . . . 104
2.2 Elemental Depth Profiles . . . 106
2.2.1 X-ray photoelectron spectroscopy . . . 106
2.2.2 Rutherford backscattering spectrometry . . . 108
2.2.3 Medium energy ion scattering . . . 114
2.2.4 Time-of-flight secondary ion mass spectrometry . . . 115
2.2.5 Glow discharge optical emission spectroscopy . . . 116
2.2.6 Glow discharge time-of-flight mass spectrometry . . . 117

Results and Discussion 123

1 Aluminium Substrates of Controlled Patterns 124
1.1 Characterisation of the Substrate Topographies . . . 124
1.1.1 Cross-section examination . . . 124
1.1.2 3D surface analysis . . . 126
1.2 Incorporation of Electrolyte-Derived Species . . . 128
1.2.1 Compositional analysis . . . 128
1.2.2 Quantification . . . 132
1.3 Elemental Depth Profiling . . . 135
1.4 Conclusions . . . 142

2 Anodizing of Patterned Substrates 170
2.1 Anodizing Process . . . 170
2.1.1 Voltage-time responses . . . 170
2.1.2 Thickness measurements . . . 171
2.1.3 Development of surface topography . . . 172
2.2 Mobilities of Incorporated Species . . . 175
2.2.1 Cross-sectional analysis . . . 175
2.2.2 Elemental depth profiling analysis . . . 179
2.3 Conclusions . . . 184

3 Depth Profiling Analyses of Patterned Specimens **224**
3.1 Sputtering Sources 224
3.2 Surface Roughnesses 227
3.3 Elemental Depth Profiles 229
3.3.1 Glow discharge analyses 230
3.3.2 Secondary ion mass analysis 231
3.4 Sputtering-Induced Surface Modifications 233
3.4.1 Glow-discharge induced surface modifications 233
3.4.2 Ion-beam induced surface modifications 236
3.5 Conclusions 237

4 Growth Mechanism of Barrier-Type Anodic Alumina **260**
4.1 Potential and Stress Distributions 260
4.1.1 Potential distribution 260
4.1.2 Stress distribution 261
4.2 Distributions of the Incorporated Species 264
4.2.1 Boron marker 264
4.2.2 Phosphorus tracer 265
4.2.3 Chromium tracer 267
4.3 Oxide Surface and Metal / Oxide Interface Smoothing 268
4.4 Conclusions 270

General Summary and Conclusions **290**

Suggestions for Future Work **297**

Bibliography **299**

Final Word Count: 39,413

List of Tables

Literature Survey

2.1 Aluminium and aluminium alloy designation system. 42

2.2 Unalloyed aluminium designation. 43

Experimental Procedure

2.1 Standardized 3D Surface Texture Parameters, ISO 25178. 119

2.2 Comparative summary of the analytic performances of the main techniques for thin film analysis. 120

Results and Discussion

1.1 Surface pattern characterisation (TEM). 143

1.2 Surface roughness characterisation (AFM). 144

1.3 Motif analysis of the surface patterns 145

1.5 Parameters for the conversion of the energy scale into a depth scale. . . 147

1.6 MEIS - Quantification 148

2.1 Thicknesses of anodic oxide layers formed by anodizing differently patterned aluminium substrates in 0.1 M ammonium pentaborate. . . . 186

2.2 Depths of the chromium and phosphorus tracers as well as the boron marker relative to the total anodic oxide film thicknesses. 187

2.3 Migration rates of the chromium and phosphorus tracers 188

2.4 Comparison of the amplitude (thickness) of the pattern (layer) of the distributions of chromium species measured by sputtering-induced, depth profiling techniques and by scanning transmission electron microscopy. . 189

2.5 Comparison of the amplitude of the distribution of the phosphorus-enriched layers measured by sputtering-induced depth profiling techniques scanning transmission electron microscopy and transmission electron microscopy. 190

List of Figures

Literature Survey

3.1 Pourbaix diagram for aluminium with an $Al_2O_3.3H_2O$ (hydrargillite) film at 25 °C. Potential values are for the standard hydrogen electrode (SHE) scale (Pourbaix, 1966). 57
3.2 Schematic anodic polarisation curve for a metal that shows an active-passive behaviour. 58
3.3 a. Schematic diagram of a porous-type film on aluminium, b. Sketch of a section of the porous morphology of an oxide layer (Safrany, 2007). . . 59
3.4 a. Schematic diagram of the current-time behaviour showing the kinetics of porous oxide growth on aluminium in potentiostatic regime and b. Schematic diagram of the different stages of development of an anodic oxide layer showing a porous morphology (Safrany, 2007). 60
3.5 Two consequences arising from the exponential dependence of current upon field during anodizing: a. The variation of current density within an oxide film on a rough metal surface and b. the smoothing effect of anodic oxidation on a rough metal surface; the rate of metal consumption is proportional to the current density at its surface, as indicated by the arrow heads in the upper diagram. In both diagrams, two dimensional roughness is assumed (Pringle, 1980). 61

3.6 a. Schematic diagrams of the aluminium substrate: (1) after electropolishing and immersion in 20 g l^{-1} CrO_3 / 35 ml l^{-1} H_3PO_4 solution at 90°C for 5 min, (2) after anodizing of (a.1) to 300 V at constant current density of 5 mA cm^{-2} in 0.1 ammonium pentaborate solution at 20 °C. b. GD-OES depth profile of the anodic film formed under the conditions of (a.2) showing that the chromium ions, generated by high field-assisted dissociation of the incorporated units of Cr_2O_3, migrate outward at a constant rate of 0.74 relative to that of aluminium ions, while the incorporated phosphorus species ions migrate inward at a constant rate of 0.50 relative to that of oxygen ions (Shimizu et al., 1999a). 62

4.1 Schematic of collisional cascade events (Hofmann, 1998). 82

4.2 Cross-sectional views of one-half of the static Cu (100) target for sputter depths z = 2, 3, 5 and 8.5 ML. The projectile species (3 keV Ar) are incident from the left side of the target. Black spheres visible in the plane of bisection of the target represent embedded projectiles (Karolewski, 2009). 83

4.3 Perspective view of the crater formed in a Au (111) crystal, 40 ps after bombardment with a 64 keV Au_4 cluster. Colours denote height above the surface (Urbassek, 2007). 84

4.4 Cross-sectional view of the temporal evolution of a typical collision event leading to ejection of atoms due to 15 keV Ga and C_{60} ion bombardment of a Ag (111) surface at normal incidence (Postawa et al., 2004). 85

4.5 Example of diversity of pattern formation on Si (a, b, d-g, i, m) and Ge (c, h, k, l) surfaces by low-energy ion-beam erosion. Beginning with top left, the following surface topographies measured by AFM are shown: (a) ultra-smooth surface, (b, c) meshworks of randomly arranged troughs, (d) domains of hexagonally ordered dots, (e) highly ordered ripple pattern, (f) coexistence of dots and ripples, (g) long range square ordered dots on Si, (h) long range hexagonally ordered dots, (i, k, l, m) curved ripples. The individual patterns are formed under various erosion conditions (ion energy between 500 eV and 2000 eV; ion species used Ar^+, Kr^+, Xe^+; ion incidence angle between 0° and 75° with respect to the surface normal, partly with simultaneous sample rotation). All experiments were performed keeping the samples at room temperature (Frost et al., 2008). 86
4.6 a. Voltage distribution and discharge characteristics of a dc glow discharge with (A-C) the Towsend regime, (C) the break-down voltage, (D-E) the normal glow, (E-F) abnormal glow and after the glow-to-arc transition (F-G) non-thermal regime, and b. Luminous regions in a dc glow discharge (Laude and Chapon, 2005). 87
4.7 Schematic diagram of the profile distortion of a. a step-like interface and b. a delta layer. 88
4.8 GD-OES depth quantified profile of a 20 multi-layer coating on silicon. The multi-layers comprise alternating layer of chromium (55 nm) and titanium (70 nm). The dashed lines follow the variation of the metal peak intensities with depth (Escobar-Galindo et al., 2005b). 89
4.9 Crater shape obtained after GD-OES depth profiling of a superpure aluminium specimen, showing the relatively flat bottom of the crater as well as the crater edge and wall inherent to the technique. 90
4.10 White-light interferometry images of craters resulting from a. TOF-SIMS (Starke, 2003) and b. GD-OES (Laude and Chapon, 2005) depth profiling analyses. 91

Experimental Procedure

2.1 Schematic of the relevant energy levels for binding energy measurements by X-ray photoelectron spectroscopy. The conducting specimen and spectrometer housing are in electrical contact and thereby have common Fermi levels. The incident X-ray photons, of energy $h\nu$, create electrons by photoelectric effect. The kinetic and binding energy of the photoelectrons on the kth level, E_{kin} and $E_B^F(k)$, are relative to the Vacuum and Fermi levels of the specimen respectively. The kinetic energy of the photoelectrons is measured by a spectrometer with a work function ϕ_{spec} so that $E'_{kin} = E_{kin} - (\phi_{spec} - \phi_s)$. 121

2.2 Schematic of the trajectories for the elastic collision between two masses m_1 and m_2. The incident particle has an initial energy E_0, and an energy E after scattering. 122

2.3 Schematic of the backscattering of incident particles of energy, E_0, which are backscattered at the surface of the specimen with an energy KE_0 and at a depth x with an energy E_f. 122

Results and Discussion

1.1 Transmission electron micrographs of ultramicrotomed sections of a. the as-rolled superpure aluminium material and b. a superpure aluminium specimen after electropolishing for 3 min. 149

1.2 Transmission electron micrographs of ultramicrotomed sections of superpure aluminium specimens after anodizing for 5 min in a. sulphuric acid, b. oxalic acid and c. phosphoric acid. 150

1.3 Transmission electron micrographs of ultramicrotomed sections of superpure aluminium specimens after stripping, in a chromic / phosphoric acids solution, of the porous anodic oxide films formed by anodizing for 5 min, in a. sulphuric acid, b. oxalic acid and c. phosphoric acid. 151

1.4 Atomic force microscopy images of superpure aluminium specimens after electropolishing for 3 min a. raw image and b. image corrected using a Gaussian filter (0.25 µm) and after stripping of a porous film formed in sulphuric acid c. raw image and d. image corrected using a Gaussian filter (0.80 µm). 152

1.5 Atomic force microscopy images of superpure aluminium substrates after stripping of a porous film formed in oxalic acid a. raw image and b. image corrected using a Gaussian filter (0.25 µm), and in phosphoric acid c. raw image and d. image corrected using a Gaussian filter (0.80 µm). 153

1.6 Atomic force microscopy images of a superpure aluminium specimen after a. electropolishing for 3 min and stripping of the air-formed film, showing a regular furrow pattern and a regular hexagonal pattern in particular grain orientations, and anodizing in b. sulphuric acid, c. oxalic acid, d. phosphoric acid for 5 min and stripping of the porous anodic oxide, disclosing an hexagonal cell-array pattern. 154

1.7 Motif analysis of the controlled textures of superpure aluminium substrates patterned by growth of porous anodic oxide films in different acids and revealed by stripping of the porous films in a chromic / phosphoric acids solution, patterning in a. sulphuric acid, b. oxalic acid and c. phosphoric acid. 155

1.8 Measured (dots) and simulated (solid line) XPS spectra of superpure aluminium specimens electropolished and successively electropolished and stripped, showing a comparison of the core levels a., b. O 1s; c.,d. Al 2p; e.,f. Cl 2p and g. P 2p, h. Cr 2p, All spectra are presented uncorrected for charging, except Cr 2p and P 2p which are charge-corrected to C 1s at 285 eV. 156

1.9 Measured (dots) and simulated (solid line) XPS spectra showing a comparison of the core levels Cr 2p for a. the CrO_3 powder used for the preparation of the stripping solution and b. a superpure aluminium specimen successively electropolished and immersed in a chromic / phosphoric solution. Both spectra are charge-corrected to C 1s at 285 eV. 157

1.10 Measured (dots) and simulated (solid line) MEIS spectra of a superpure aluminium specimen after electropolishing, a. general energy spectra, and magnification of the energy spectra of the impurities present b. chlorine, c. copper and after successive electropolishing and stripping in a chromic / phosphoric acid solution, d. general spectra, and magnification of the the energy spectra of the impurities present e. phosphorus / chlorine, f. chromium / copper. 158

1.11 Elemental depth profile calculated from the MEIS spectra of a superpure aluminium specimen electropolished and immersed in a chromic / phosphoric acid solution. The dashed line indicates the metal / oxide interface. 159
1.12 Superimposition of elemental spectra (solid line), simulated for P, Cl, Cr and Cl species, on MEIS spectra of a superpure aluminium specimen patterned by a. electropolishing, b. sulphuric acid, c. oxalic acid and d. phosphoric acid. 160
1.13 Comparison of GD-OES elemental depth profiles, measured in the pulsed mode, of air-formed films formed on superpure aluminium substrate a. electropolished in a perchloric acid / ethanol solution and b. successively electropolished and stripped in a chromium / phosphoric acid solution. General profiles are presented as well as magnifications of chlorine, phosphorus and chromium depth profiles. 161
1.14 Comparison of elemental depth profiles of air-formed films formed on a superpure aluminium substrates successively electropolished and stripped in a chromium / phosphoric acid solution, using a. GD-OES, b. TOF-SIMS and c. GD-TOF-MS. 162
1.15 Elemental depth profile analysis of anodic alumina films, formed by anodizing electropolished superpure aluminium substrates in ammonium pentaborate to 30 and 360 nm, using a. GD-OES, b. TOF-SIMS and c. GD-TOF-MS. 163
1.16 GD-OES elemental depth profile analysis of native oxide films present on superpure aluminium substrates patterned by a. electropolishing, b. sulphuric acid, c. oxalic acid and d. phosphoric acid. 164
1.17 GD-TOF-MS elemental depth profile analysis of native oxide films present on superpure aluminium substrates patterned by a. electropolishing, b. sulphuric acid, c. oxalic acid and d. phosphoric acid. 165
1.18 TOF-SIMS elemental depth profile analysis of native oxide films present on superpure aluminium substrates patterned by a. electropolishing, b. sulphuric acid, c. oxalic acid and d. phosphoric acid. 166

1.19 Atomic force microscopy images of native oxide films, formed on superpure aluminium specimens patterned by anodizing in phosphoric acid and subsequently stripped, a. original oxide film surface; and b., c. surface after sputtering, using GD-OES, of the oxide for b. 0.15 s and c. 1.15 s. The scanning area of the top view image is 5 μm^2, whereas the 3 D view area is reduced to 2 μm^2 and the z-scales represent about 200 nm for a. and 40 nm for b. and c. 167

1.20 Scanning electron micrographs of native oxide films, formed on superpure aluminium specimens patterned by anodizing in phosphoric acid and subsequent stripping of the porous film, a. original oxide film surface; and b., c. surface after sputtering, using GD-OES, of the oxide for b. 0.15 s and c. 1.15 s. 168

1.21 Comparison of GD-OES elemental depth profiles measured in the continuous mode of a. an air-formed film formed on a superpure aluminium substrate successively electropolished and stripped in a chromium / phosphoric acid solution and of anodic oxide films formed by anodizing of similarly prepared substrates in ammonium pentaborate at 50 mA cm^{-2} to b. 5 V, c. 10 V and d. 25 V. 169

2.1 Voltage-time responses of superpure aluminium specimens anodized at 5 mA cm^{-2} in 0.1 M ammonium pentaborate electrolyte at 293 K; a. comparison of the voltage-time responses during anodizing of electropolished substrates from 10 to 300 V, b. and c. influence of the substrate roughnesses during anodizing of differently patterned substrates to 25 V and 200 V respectively. 192

2.2 Measured (dots) and simulated (solid line) RBS spectra of superpure aluminium specimens successively electropolished, immersed in a chromic / phosphoric acid stripping solution and anodized in 0.1 M ammonium pentaborate solution to a. 25, b. 50, c. 200 and d. 300 V. 193

2.3 Measured (dots) and simulated (solid line) RBS spectra of superpure aluminium specimens successively patterned in phosphoric acid, immersed in a chromic / phosphoric acid stripping solution and anodized in 0.1 M ammonium pentaborate solution to a. 25, b. 50, c. 200 and d. 300 V. . 194

2.4 Measured and fitted (solid line) thicknesses of anodic oxide films formed on differently patterned superpure aluminium specimens, by anodizing in 0.1 M ammonium pentaborate solution up to 300 V. 195
2.5 Atomic force microscopy images of superpure aluminium specimens patterned in phosphoric acid, and subsequently stripped of the porous film, a. air-formed film, then, anodized in 0.1 M ammonium pentaborate solution to b. 10 V, c. 25 V, d. 50 V, e. 100 V and f. 200 V. 196
2.6 Transmission electron micrographs of ultramicrotomed sections of superpure aluminium specimens patterned by electropolishing a. air-formed film, and anodized in a 0.1 M ammonium pentaborate solution to b. 50 V, c. 100 V, d. 300 V. 197
2.7 Transmission electron micrographs of ultramicrotomed sections of superpure aluminium specimens patterned by anodizing in sulphuric acid and subsequent stripping of the porous film, and anodized in 0.1 M ammonium pentaborate solution to a. 10 V, b. 25 V, c. 50 V and d. 100 V. 198
2.8 Transmission electron micrographs of ultramicrotomed sections of superpure aluminium specimens patterned by anodizing in oxalic acid and subsequent stripping of the porous film, and anodized in a 0.1 M ammonium pentaborate solution to a. 10 V, b. 25 V, c. 50 V and d. 100 V. 199
2.9 Transmission electron micrographs of ultramicrotomed sections of superpure aluminium specimens patterned in phosphoric acid and subsequent stripping of the porous film, and anodized in 0.1 M ammonium pentaborate solution to a. 10 V, b. 25 V, c. 50 V, d. 100 V and e. 200 V. 200
2.10 Evolution of the substrate ridge heights as a function of increasing anodizing voltage, showing the flattening of the superpure aluminium substrates, initially textured by anodizing in sulphuric acid, oxalic acid, phosphoric acid and subsequent stripping of the porous films, during anodizing in 0.1 M ammonium pentaborate solution to various voltages. The height of the aluminium substrate ridges were measured from the transmission electron micrographs of ultramicrotomed sections of specimens anodized to 10, 25, 50, 100, 200 and 300 V. 201

2.11 Comparison of a. a scanning transmission electron micrograph and b. a transmission electron micrograph of ultramicrotomed sections of electropolished superpure aluminium specimens immersed in a chromic / phosphoric acid stripping solution and anodized in 0.1 M ammonium pentaborate solution to 100 V. 202

2.12 Scanning transmission electron micrograph of an ultramicrotomed section of an electropolished superpure aluminium specimen, immersed in a chromic / phosphoric acid stripping solution and anodized in 0.1 M ammonium pentaborate solution to 200 V. 203

2.13 Scanning transmission electron micrograph of an ultramicrotomed section of a superpure aluminium specimen patterned by anodizing in sulphuric acid and subsequent stripping of the porous film, and anodized in 0.1 M ammonium pentaborate solution to 200 V. 204

2.14 Scanning transmission electron micrograph of an ultramicrotomed section of a superpure aluminium specimen patterned by anodizing in oxalic acid and subsequent stripping of the porous film, and anodized in 0.1 M ammonium pentaborate solution to 200 V. 205

2.15 Scanning transmission electron micrographs of ultramicrotomed section of superpure aluminium specimens patterned by anodizing in phosphoric acid and subsequent stripping of the porous film, and anodized in 0.1 M ammonium pentaborate solution to a. 100 V and b. 200 V. 206

2.16 Scanning transmission electron micrograph of an ultramicrotomed section of an electropolished superpure aluminium specimen, immersed in a chromic / phosphoric acid solution and anodized in 0.1 M ammonium pentaborate solution to 100 V. A transmission electron micrograph of an ultramicrotomed section of the initial superpure aluminium substrate, i.e. before anodizing in 0.1 M ammonium pentaborate solution, is superimposed on the STEM image. The amplitude of the distribution of the phosphorus species within the anodic oxide film is 12 nm, while the amplitude of the pattern of the electropolished superpure aluminium substrate immersed in a chromic / phosphoric acid solution, is measured at 10 nm. 207

2.17 Scanning transmission electron micrograph of an ultramicrotomed section of a superpure aluminium specimen patterned by anodizing in oxalic acid and subsequent stripping of the porous film, and anodized in 0.1 M ammonium pentaborate solution to 200 V. A transmission electron micrograph of an ultramicrotomed section of the patterned superpure aluminium substrate, i.e. before anodizing in 0.1 M ammonium pentaborate solution, is superimposed to the STEM image. The amplitude of the distribution of the phosphorus species within the anodic oxide film is 36 nm, while the amplitude of the initial pattern of the superpure aluminium substrate is measured at 35 nm. 208

2.18 Scanning transmission electron micrograph of an ultramicrotomed section of a superpure aluminium specimen patterned by anodizing in phosphoric acid and subsequent stripping of the porous film, and anodized in 0.1 M ammonium pentaborate solution to 200 V. A transmission electron micrograph of an ultramicrotomed section of the initial superpure aluminium substrate, i.e. before anodizing in 0.1 M ammonium pentaborate solution, is superimposed to the STEM image. The amplitude of the distribution of the phosphorus species within the anodic oxide film is 59 nm, while the amplitude of the initial pattern of the superpure aluminium substrate is measured at 65 nm. 209

2.19 Scanning transmission electron micrograph of an ultramicrotomed section of a superpure aluminium specimen patterned in phosphoric acid and anodized in 0.1 M ammonium pentaborate solution to a. 100 V and b. 200 V. The comparison of the amplitude of the distributions of the chromium-enriched layers from the micrographs presented in a. and b. shows significant flattening of the chromium-enriched layers during anodic alumina growth. 210

2.20 Scanning transmission electron micrograph of an ultramicrotomed section of a superpure aluminium specimen patterned by anodizing in phosphoric acid and subsequent stripping of the porous film, and anodized in 0.1 M ammonium pentaborate solution to 300 V. 211

2.21 Elemental depth profile analysis of anodic alumina films, formed by anodizing electropolished superpure aluminium substrates in ammonium pentaborate to 360 nm, using a. GD-OES, b. TOF-SIMS and c. GD-TOF-MS. 212

2.22 Positions of the chromium and phosphorus tracers as well as the boron marker as a function of the anodic oxide film thickness, measured from elemental depth profiles, acquired using a. GD-OES, b. TOF-SIMS and c. GD-TOF-MS, of anodic oxide layers formed by anodizing electropolished superpure aluminium substrates in 0.1 M ammonium pentaborate to 10, 25, 50, 100, 200, 225, 250, 275 and 300 V. 213

2.23 Positions of the chromium and phosphorus tracers as well as the boron marker as a function of the anodic oxide film thickness, measured from elemental depth profiles, acquired using a. GD-OES, b. TOF-SIMS and c. GD-TOF-MS, of anodic oxide layers formed by anodizing superpure aluminium substrates, patterned by anodizing in sulphuric acid and subsequent stripping of the porous film, in 0.1 M ammonium pentaborate to 50, 100, 200, 225, 250, 275 and 300 V. 214

2.24 Positions of the chromium and phosphorus tracers as well as the boron marker as a function of the anodic oxide film thickness, measured from elemental depth profiles, acquired using a. GD-OES, b. TOF-SIMS and c. GD-TOF-MS, of anodic oxide layers formed by anodizing superpure aluminium substrates, patterned by anodizing in oxalic acid and subsequent stripping of the porous film, in 0.1 M ammonium pentaborate to 100, 200, 225, 250, 275 and 300 V. 215

2.25 Positions of the chromium and phosphorus tracers as well as the boron marker as a function of the anodic oxide film thickness, measured from elemental depth profiles, acquired using a. GD-OES, b. TOF-SIMS and c. GD-TOF-MS, of anodic oxide layers formed by anodizing superpure aluminium substrates, patterned by anodizing in phosphoric acid and subsequent stripping of the porous film, in 0.1 M ammonium pentaborate to 200, 225, 250, 275 and 300 V. 216

2.26 GD-OES elemental depth profile analysis of anodic alumina films, formed by anodizing in ammonium pentaborate to 360 nm of superpure aluminium substrates patterned by a. electropolishing and by anodizing in b. sulphuric acid, c. oxalic acid, d. phosphoric acid, and subsequent stripping of the porous films. 217
2.27 GD-TOF-MS elemental depth profile analysis of anodic alumina films, formed by anodizing in ammonium pentaborate to 360 nm of superpure aluminium substrates patterned by a. electropolishing and by anodizing in b. sulphuric acid, c. oxalic acid, d. phosphoric acid, and subsequent stripping of the porous films. 218
2.28 TOF-SIMS elemental depth profile analysis of anodic alumina films, formed by anodizing in ammonium pentaborate to 360 nm of superpure aluminium substrates patterned by a. electropolishing and by anodizing in b. sulphuric acid, c. oxalic acid, d. phosphoric acid, and subsequent stripping of the porous films. 219
2.29 Depth profiling using TOF-SIMS, GD-OES and GD-TOF-MS of anodic oxide films formed on substrates patterned by electropolishing; depth resolution as a function of depth measured for a. the chromium tracer and b. the phosphorus tracer. 220
2.30 GD-OES elemental depth profile analysis of anodic alumina films, formed by anodizing in ammonium pentaborate to 360 nm of superpure aluminium substrates patterned by anodizing in a. sulphuric acid, b. oxalic acid, c. phosphoric acid and subsequent stripping of the porous films. 221
2.31 GD-TOF-MS elemental depth profile analysis of anodic alumina films, formed by anodizing in ammonium pentaborate to 360 nm of superpure aluminium substrates patterned by anodizing in a. sulphuric acid, b. oxalic acid, c. phosphoric acid and subsequent stripping of the porous films. 222
2.32 TOF-SIMS elemental depth profile analysis of anodic alumina films, formed by anodizing in ammonium pentaborate to 360 nm of superpure aluminium substrates patterned by anodizing in a. sulphuric acid, b. oxalic acid, c. phosphoric acid and subsequent stripping of the porous films. 223

3.1 Comparison of the elemental depth profiles performed by GD-OES on anodic oxide layers, formed by anodizing in ammonium pentaborate of superpure aluminium substrates differently patterned to 30 nm. 239
3.2 Comparison of the elemental depth profiles performed by GD-TOF-MS on anodic oxide layers, formed by anodizing in ammonium pentaborate of superpure aluminium substrates differently patterned to 30 nm. . . . 240
3.3 Comparison of the elemental depth profiles performed by TOF-SIMS on anodic oxide layers, formed by anodizing in ammonium pentaborate of superpure aluminium substrates differently patterned to 30 nm. 241
3.4 GD-OES elemental depth profile analysis of anodic alumina films, formed by anodizing in ammonium pentaborate to 30, 60, 240 and 360 nm of aluminium substrates patterned by electropolishing (a - d) and of aluminium substrates successively electropolished, patterned in phosphoric acid and stripped in a chromic / phosphoric acid solution (e - h). 242
3.5 GD-TOF-MS elemental depth profile analysis of anodic alumina films, formed by anodizing in ammonium pentaborate to 30, 60, 240 and 360 nm of aluminium substrates patterned by electropolishing (a - d) and of aluminium substrates successively electropolished, patterned in phosphoric acid and stripped in a chromic / phosphoric acid solution (e - h). The sputtering times have been normalized as a function of the sputtering rate of the 360-nm thick specimen. 243
3.6 TOF-SIMS elemental depth profile analysis of anodic alumina films, formed by anodizing in ammonium pentaborate to 30, 60, 240 and 360 nm of aluminium substrates patterned by electropolishing (a - d) and of aluminium substrates successively electropolished, patterned in phosphoric acid and stripped in a chromic / phosphoric acid solution (e - h). The sputtering times have been normalized as a function of the sputtering rate of the 360-nm thick specimen. 244
3.7 Comparison of the elemental depth profiles performed by GD-OES on anodic oxide layers, formed by anodizing in ammonium pentaborate of superpure aluminium substrates differently patterned to 360 nm. 245

3.8 Comparison of the elemental depth profiles performed by GD-TOF-MS on anodic oxide layers, formed, by anodizing in ammonium pentaborate of superpure aluminium substrates differently patterned to 360 nm. . . . 246
3.9 Comparison of the elemental depth profiles performed by TOF-SIMS on anodic oxide layers, formed, by anodizing in ammonium pentaborate of superpure aluminium substrates differently patterned to 360 nm. 247
3.10 Atomic force microscopy images of 30 nm thick oxide films, formed on substrates patterned by anodizing in phosphoric acid and subsequent stripping of the porous film: a. original oxide film surface; after GD-OES elemental depth profiling for b. 0.5 s, c. 1 s, d. 2 s. 248
3.11 Atomic force microscopy images of 120 nm thick oxide films, formed on substrates patterned by anodizing in phosphoric acid and subsequent stripping of the porous film: a. original oxide film surface; after GD-OES elemental depth profiling for b. 2 s, c. 5 s, d. 7 s. 249
3.12 Atomic force microscopy images of 30 nm thick oxide films, formed on substrates patterned by anodizing in phosphoric acid and subsequent stripping of the porous film: a. original oxide film surface; after GD-TOF-MS elemental depth profiling for b. 1 s, c. 4 s, d. 6 s. 250
3.13 Atomic force microscopy images of 120 nm thick oxide films, formed on substrates patterned by anodizing in phosphoric acid and subsequent stripping of the porous film: a. original oxide film surface; after GD-TOF-MS elemental depth profiling for b. 5 s, c. 15 s, d. 18 s. 251
3.14 Transmission electron micrographs of ultramicrotomed sections of superpure aluminium specimens patterned in phosphoric acid and stripping of the porous film, and anodized in ammonium pentaborate to 100 V, a. initially patterned oxide film; after GD-OES depth profile analysis for b. 1 s. 252
3.15 Transmission electron micrographs of ultramicrotomed sections of superpure aluminium specimens patterned in phosphoric acid and stripping of the porous film, and anodized in ammonium pentaborate to 100 V, a. initially patterned oxide film; after GD-OES depth profile analysis for b. 2 s, c. 3 s, d. 4 s and e. 5 s. 253

3.16 Scanning electron micrographs of 30-nm oxide films, formed on superpure aluminium specimens patterned by anodizing in phosphoric acid and subsequent stripping of the porous film, a. and b. micrographs in the InLens mode and in the SE2 mode of the original anodic oxide surface. . 254
3.17 Scanning electron micrographs of 30-nm oxide films, formed on superpure aluminium specimens patterned by anodizing in phosphoric acid and subsequent stripping of the porous film, after sputtering for 0.15 s, a. and b. micrographs in the InLens mode and in the SE2 mode, c. and d. micrographs in the InLens mode and in the EsB mode. 255
3.18 Scanning electron micrographs of 30-nm oxide films, formed on superpure aluminium specimens patterned by anodizing in phosphoric acid and subsequent stripping of the porous film, after sputtering for 2.15 s, a. and b. micrographs in the InLens mode and in the SE2 mode, c. and d. micrographs in the InLens mode and in the EsB mode. 256
3.19 Scanning electron micrographs of 30-nm oxide films, formed on superpure aluminium specimens patterned by anodizing in phosphoric acid and subsequent stripping of the porous film, after sputtering for 3.15 s, a. and b. micrographs in the InLens mode and in the SE2 mode, c. and d. micrographs in the InLens mode and in the EsB mode. 257
3.20 Atomic force microscopy images of material removal during TOF-SIMS depth profiling of 30 nm thick oxide films, formed on substrates patterned by anodizing in phosphoric acid and stripping of the porous film, and sputtered to different times a. original oxide film surface; b. 150 s, c. 300 s, d. 500 s. 258
3.21 Atomic force microscopy images of material removal during TOF-SIMS depth profiling of 30 nm thick oxide films, formed on substrates patterned by anodizing in phosphoric acid and stripping of the porous film, and sputtered to different times a. original oxide film surface; b. 150 s, c. 300 s, d. 950 s. 259

4.1 Simulation of the potential distribution on a. a flat surface and b. a rough surface, showing the pattern dimension of a specimen patterned by anodizing in phosphoric acid and stripping of the porous film. The potential gradient is given by the equilines. Arrows indicate the direction of the electric field. The colour scale represents the field strength a. 7.98 x 10^6 - 8.02 x 10^6 V m^{-1} and b. 0.38 x 10^7 - 1.85 x 10^7 V m^{-1}. 273

4.2 Scanning transmission electron micrograph of an ultramicrotomed section of an electropolished superpure aluminium specimen, after immersion in a chromic / phosphoric acid stripping solution and anodizing at a current density of 5 mA cm^{-2} in 0.1 M ammonium pentaborate solution to 200 V. 274

4.3 Scanning transmission electron micrograph of an ultramicrotomed section of a superpure aluminium specimen patterned by anodizing in sulphuric acid and subsequent stripping of the porous film, with final anodizing at a current density of 5 mA cm^{-2} in 0.1 M ammonium pentaborate solution to 200 V. 275

4.4 Scanning transmission electron micrograph of an ultramicrotomed section of a superpure aluminium specimen patterned by anodizing in oxalic acid and subsequent stripping of the porous film, with final anodizing at a current density of 5 mA cm^{-2} in 0.1 M ammonium pentaborate solution to 200 V. 276

4.5 Scanning transmission electron micrograph of an ultramicrotomed section of a superpure aluminium specimen patterned by anodizing in phosphoric acid and subsequent stripping of the porous film, with final anodizing at a current density of 5 mA cm^{-2} in 0.1 M ammonium pentaborate solution to 200 V. 276

4.6 Scanning transmission electron micrograph of an ultramicrotomed section of a superpure aluminium specimen patterned by anodizing in phosphoric acid and subsequent stripping of the porous film, with final anodizing at a current density of 5 mA cm^{-2} in 0.1 M ammonium pentaborate solution to 200 V. 277

4.7 Schematic diagrams of a concavity in a patterned specimen surface, showing the aluminium oxide (white) and the boron-containing oxide (grey) supported by the aluminium substrate (black). a. The schematic diagram describes the augmentation and reduction in the transport number (TN) of aluminium and oxygen respectively as a result of the curvature of the substrate and the associated decrease and increase in surface area respectively, the boron-rich / boron-free oxide interface is used as a reference for the determination of the transport number of aluminium and oxygen species. The dashed lines represent the location of the oxide surface and metal / oxide interface for aluminium and oxygen transport numbers of 0.4 and 0.6 (flat surface). b. The schematic diagram illustrates the flattening of the oxide surface in a valley as a result of growth of anodic oxide associated with aluminium egress in directions converging toward the centre of the curvature defined by the metal / oxide interface. 278

4.8 Schematic diagrams of a convexity in a patterned specimen surface, showing the aluminium oxide (white) and the boron-containing oxide (grey) supported by the aluminium substrate (black). a. The schematic diagram describes the reduction and augmentation of the transport number (TN) in aluminium and oxygen respectively as a result of the curvature of the substrate and the associated decrease and increase in surface area respectively, the boron-rich / boron-free oxide interface is used as a reference for the determination of the transport number of aluminium and oxygen species. The dashed lines represent the location of the oxide surface and metal / oxide interface for aluminium and oxygen transport numbers of 0.4 and 0.6 (flat surface). b. The schematic diagram illustrates the flattening of the metal / oxide interface in a valley as a result of growth of anodic oxide associated with ingress of oxygen species in directions converging toward the centre of the curvature defined by the metal / oxide interface. 279

4.9 Scanning transmission electron micrograph of an ultramicrotomed section of a superpure aluminium specimen patterned by anodizing in phosphoric acid and subsequent stripping of the porous film, and anodized in 0.1 M ammonium pentaborate solution to 200 V. A transmission electron micrograph of an ultramicrotomed section of the initial superpure aluminium substrate, i.e. before anodizing in 0.1 M ammonium pentaborate solution, is superimposed to the STEM image. The amplitude of the distribution of the phosphorus species within the anodic oxide film is 59 nm, while the amplitude of the initial pattern of the superpure aluminium substrate is measured at 65 nm. 280

4.10 Schematic diagram of the evolution of the substrate pattern during anodizing in 0.1 M ammonium pentaborate, the aluminium oxide surface is not represented; showing a. an homothetic transformation of the substrate pattern, the substrate presents patterns of similar shapes, but with reduction of the tip dimensions, and b. changes in the shape of the patterns, with preferential oxidation of the tips in the substrate. 281

4.11 Schematic diagram of the evolution of the direction of the electric field as a function of the aluminium substrate topography, showing a. a constant direction of the electric field associated with an homothetic transformation of the substrate pattern during anodizing and b. a variation of the direction of the electric field induced by the preferential oxidation of the tips in the substrate pattern. 282

4.12 Schematic diagram of a concavity in a patterned specimen surface, showing the aluminium oxide (white) and the boron-containing oxide (grey) supported by the aluminium substrate (black). The schematic diagram illustrates the apparent increase of migration rate (MR) in the phosphorus species (red) relative to that of the oxygen species. The increase in the migration rate of the phosphorus species is associated with the reduction in the transport number (TN) of the oxygen species as a result of the curvature of the substrate and the associated increase of surface area. The phosphorus species migrate under the high electric field at a rate of 0.50 relative to that of the oxygen species, as if the oxygen species were presenting a transport number of 0.60. The boron-rich / boron-free oxide interface is used as a reference for the determination of the transport number of aluminium and oxygen species. The dashed lines represent the location of the oxide surface and metal / oxide interface for aluminium and oxygen transport numbers of 0.4 and 0.6 (flat surface). 283

4.13 Schematic diagram of a convexity in a patterned specimen surface, showing the aluminium oxide (white) and the boron-containing oxide (grey) supported by the aluminium substrate (black). The schematic diagram describes the decrease in the migration rate (MR) of the phosphorus species (red) relative to that of the oxygen species. The reduction in the migration rate of the phosphorus species is associated with the increase in the transport number (TN) of the oxygen species as a result of the curvature of the substrate and the associated decrease of surface area. The phosphorus species migrate under the high electric field at a rate of 0.50 relative to that of the oxygen species, as if the oxygen species were presenting a transport number of 0.60. The boron-rich / boron-free oxide interface is used as a reference for the determination of the transport number of aluminium and oxygen species. The dashed lines represent the location of the oxide surface and metal / oxide interface for aluminium and oxygen transport numbers of 0.4 and 0.6 (flat surface). 284

4.14 Schematic diagram of a concavity in a patterned specimen surface, showing the aluminium oxide (white) and the boron-containing oxide (grey) supported by the aluminium substrate (black). The schematic diagram illustrates the flattening of the chromium-enriched layer in a valley simultaneously to the flattening of the oxide surface as a result of growth of anodic oxide associated with aluminium egress in directions converging toward the centre of the curvature defined by the metal / oxide interface. 285

4.15 Schematic diagram of a convexity in a patterned specimen surface, showing the aluminium oxide (white) and the boron-containing oxide (grey) supported by the aluminium substrate (black). The schematic diagram describes the increase in the migration rate (MR) of the chromium species associated with the reduction in the transport number (TN) of the aluminium species as a result of the curvature of the substrate and the associated increase of surface area. The boron-rich / boron-free oxide interface is used as a reference for the determination of the transport number of aluminium and oxygen species. The dashed lines represent the location of the oxide surface and metal / oxide interface for aluminium and oxygen transport numbers of 0.4 and 0.6 (flat surface). 286

4.16 Schematic diagram of a peak in the surface topography showing a local enhancement of the electric field at the tip (long arrows) in comparison with the valley (short arrow), which results in a faster thickening of the oxide layer over the tip than at the valley in the surface. 287

4.17 Schematic diagram of a peak in the surface topography showing a local enhancement of the electric field at the tip (long arrows) in comparison with the valley (short arrow), resulting in oxide flow from the tip to the valley in order to equalise the oxide thickness over the surface topography. Consequently, the chromium and phosphorus tracers are absent from the tip of the peak as a result of the oxide flow. 288

4.18 Schematic diagram of a peak in the surface topography showing a redistribution of the electric field from the tip to the valley (long arrow) resulting in a faster thickening of oxide film over the valley, thereby equalising the thickness of the oxide layer over the surface topography. In this case, the chromium and phosphorus tracers are present uniformly along the oxide layer. 289

Abstract

The University of Manchester

Nicolas Trigoulet

Doctor of Philosophy in the Faculty of Engineering and Physical Sciences

Probing Barrier-Type Anodic Alumina Films on Nano-Patterned Substrates

2010

The growth of barrier-type anodic alumina films formed by anodizing relatively rough substrates has been shown to proceed by high field ionic conduction. As a result of the ionic transport and the induced plasticity, smoothing of the oxide surfaces and the metal / oxide interfaces arises. However, such a smoothing model was deduced from topographical observations and, therefore little insight was gained about the transport mechanism leading to the flattening of the anodized specimens. Recently, the development of porous anodic alumina has been demonstrated to proceed by coupled ionic migration and material flow resulting from the field-induced mechanical stress. For rough metal surfaces, the electric field distribution is non-uniform across the specimen surface. Considering the square-dependence of the electrostrictive stress on the electric field and the distribution of the electric field across surface, a significant gradient of mechanical stress may arise across the anodic oxide layer during anodizing. As a result, stress-driven transport may participate, in addition to high field ionic conduction, to the smoothing of the specimen surface. Transport mechanisms were investigated during anodizing of patterned superpure aluminium specimens, by examination of the distributions of incorporated species, used as markers and tracers. The nature of the migration processes have been determined in correlation with the changes in the concentration of the tracer profiles as well as the variations in the anodic oxide film compositions.

Declaration

No portion of the work referred to in the thesis has been submitted in support of an application for another degree or qualification of this or any other university or other institute of learning.

Copyright Statement

i. The author of this thesis (including any appendices and/or schedules to this thesis) owns any copyright in it (the "Copyright") and s/he has given The University of Manchester the right to use such Copyright for any administrative, promotional, educational and/or teaching purposes.

ii. Copies of this thesis, either in full or in extracts, may be made only in accordance with the regulations of the John Rylands University Library of Manchester. Details of these regulations may be obtained from the Librarian. This page must form part of any such copies made.

iii. The ownership of any patents, designs, trade marks and any and all other Intellectual property rights except for the Copyright (the "Intellectual Property Rights") and any reproductions of copyright works, for example graphs and tables ("Reproductions"), which may be described in this thesis, may not be owned by the author and may be owned by third parties. Such Intellectual Property Rights and Reproductions cannot and must not be made available for use without the prior written permission of the owner(s) of the relevant Intellectual Property Rights and/or Reproductions.

iv. Further information on the conditions under which disclosure, publication and exploitation of this thesis, the Copyright and any Intellectual Property Rights and/or Reproductions described in it may take place is available from the Head of School of Materials (or the Vice-President) and the Dean of the Faculty of Life Sciences, for Faculty of Life Sciences' candidates.

Acknowledgements

I am heartily grateful to Prof. George Thompson and Prof. Peter Skeldon for their guidance and support during the thesis.

I would like to acknowledge Dr Agnès Tempez and Mr Patrick Chapon for their sound advices during the EMDPA project.

I thank Prof. Antonino Licciardello, Dr Nunzio Tuccitto and Dr Ivan Delfanti from the Università di Catania as well as Prof. Nerea Bordel, Dr Lara Lobo Revilla and Dr Jorge Pisonero from the Universidad de Oviedo for warmly welcoming me to their laboratories and for their help with the TOF-SIMS and GD-TOF-MS measurements respectively.

I thank the European Commission for the funding of the research, as a part of the EMDPA project through the 6th Framework Programme under the STREP contract number 032202.

I am grateful to my mates from the CPC and the MPC, Abdullah, Aleksandra, Anna, Chen, Endzhe, Fabien, Francisco, Fred, Kayoko, Mirnali, Michele, Michael, Raul (Big Gun), Suraj, Teruo and Yang Wen, for providing a stimulating and entertaining work environment.

I am indebted to my mother for her understanding, endless patience and encouragement when it was most required.

Lastly, and most importantly, I wish to thank my wife, Jinthira, for her permanent support.

Introduction

Technological breakthroughs rely on the development and production of materials with enhanced and controlled properties. In materials science, most problems are approached using coating technologies in order to customize the material surface properties. Thus, enhancements of the material surface properties are achieved using various surface processes, namely heat treatments, thermochemical treatments, plasma coatings, electrochemical platings, conversion coatings. Such engineering processes tailor the material surface to specific properties by generation of particular layers, which may vary in composition, structure and thickness.

Among the various surface treatments, anodizing consists in an electrochemical passivation of selected metals (mainly aluminium, titanium, tantalum and niobium) and leads to the thickening of the native oxide layer present at their surfaces. The formation of anodic aluminium oxides by anodizing of aluminium is widely utilized in materials engineering in order to tailor aluminium surfaces for specific applications. Thus, anodizing enhances corrosion resistance, wear resistance and is used for the preparation of surfaces for subsequent treatments. In addition, barrier-type anodic aluminium oxide films have been key materials for the fabrication of nanodevices, such as electronic, optoelectronic and magnetic devices. Indeed, depending on the anodizing conditions, such films may contain electrolyte-derived species, which influence the chemical, physical and electrical properties of the films.

Additionally, surface properties are dramatically influenced by the material surface roughness, which is generally associated with the forming process. Thus, surface interactions are conditioned by the material roughnesses, which determine the ranges of application and performance of the materials.

For anodizing of relatively rough aluminium substrates, the formation of barrier-type oxide films has been shown to proceed by high field ionic conduction. As a result of the ionic transport and the induced plasticity, smoothing of the oxide surfaces and the metal / oxide interfaces arises. However, such a smoothing model was deduced from topographical observations and, consequently, little insight was gained about the mechanism leading to the flattening of the anodized specimens. Recently, the development of porous anodic alumina has been demonstrated to proceed by coupled ionic migration and material flow due to the field-induced mechanical stress. For

rough metal surfaces, the electric field distribution is non-uniform across the specimen surface, with an increased value at the peaks in comparison with the valleys in the surface. Considering the square-dependence of the mechanical stress on the electric field and the distribution of the electric field across the peaks and valleys in the metal surface, a significant gradient of stress may arise across the anodic oxide layer during anodizing. As a result, stress-driven transport may contribute, in addition to high field ionic conduction, to the smoothing of the specimen surface. Hence, studying the distributions of incorporated species, used as markers and tracers, may reveal variations of the anodic oxide film compositions associated with surface topography modifications during anodizing of relatively rough aluminium substrates; and consequently, to the understanding of the nature of the processes taking place during the growth of barrier-type anodic aluminium oxide layers.

Surface sensitive instruments such as Auger electron spectroscopy (AES), Rutherford backscattering spectrometry (RBS), secondary ion mass spectrometry (SIMS), glow discharge optical emission spectroscopy (GD-OES) have been of particular importance for the evaluation of the in-depth distributions of trace elements in thin films. Ion-bombardment induced depth profiling techniques are effective and reliable methods for thin film analysis. However, for such techniques, the depth resolution has been demonstrated to be limited by the distortion of the original elemental depth distribution as a result of the interaction of the energetic ions with the specimen surface. The different phenomena involved result in compositional and topographical modifications of the surface, therefore limiting the depth resolution achieved. Of the different contributions to the degradation of the depth resolution, the initial roughness and the sputtering-induced roughness of the specimen surface are the most important.

The present work investigates the growth mechanism of barrier-type anodic oxide films formed anodically on patterned superpure aluminium substrates. In order to understand the processes taking place during formation of barrier-type anodic oxide films, both surface topography modification, and the incorporation and migration of marker and tracers within the anodic oxide films, have been examined. The in-depth compositions of the anodic oxide films were determined using sputtering-induced elemental depth profiling techniques, namely SIMS, GD-OES and GD-TOF-MS (glow discharge time-of-flight mass spectrometry). In addition, the locations of the marker

and tracers were probed using scanning transmission electron microscopy, thereby allowing direct comparison with the elemental depth profiling techniques. Finally, the sputtering mechanisms arising during depth profiling analysis were studied in order to certify the results.

This Ph.D thesis was performed in the framework of the EMDPA European Project (Elemental and Molecular Depth Profiling Analysis of advanced materials by modulated radio frequency glow discharge time-of-flight mass spectrometry). The overall aim of the EMDPA project was to develop a new instrument, coupling a glow discharge sputtering lamp and time-of-flight mass detection technology. Anodic oxide layers of tailored patterns were used to investigate the depth resolution and the sputtering associated with the design of the different instrument prototypes.

Literature Survey

1 Introduction

In order to elucidate the growth mechanism taking place during the formation of barrier-type anodic alumina on patterned specimens, understanding of the anodizing of aluminium and its alloys is required. Thus, generalities about aluminium and aluminium alloys properties are described in the second Section of the Literature Survey. Then, the third Section is dedicated to the growth mechanisms involved during the development of barrier- and porous-type anodic oxide films. The formation of barrier-type anodic alumina layers by anodizing of differently patterned superpure aluminium substrates was examined by following the distributions of different species incorporated within the oxide film, namely boron, chromium and phosphorus. Sputtering-induced elemental depth profiling analysis is treated in the fourth Section, with particular attention given to the interpretation of the elemental depth profiles in correlation with the sputtering processes associated with the different techniques employed. Finally, a brief introduction to the present work is given.

2 Aluminium and Aluminium Alloys - Generalities

The unique combination of properties provided by aluminium and its alloys make aluminium one of the most versatile, attractive and economical metallic materials for a wide range of engineering applications. Indeed, due to the numerous alloy compositions, the functional properties of aluminium and its alloys can be tailored for specific applications.

2.1 General Properties

Aluminium has a density of 2.70 g cm^{-3}, approximately one-third that of steel (7.83 g cm^{-3}), copper (8.93 g cm^{-3}), or brass (8.53 g cm^{-3}). Such light weight, coupled with the high-strength of selected aluminium alloys (pure aluminium and certain aluminium alloys are noted for their extremely low strength and hardness) permits design and construction of strong, lightweight structures that are particularly advantageous for all types of vehicles, such as automobiles or aircraft (Rooy, 2002). The main properties that aluminium can display are (Rooy, 2002):

- Excellent corrosion resistance in most environments, including atmosphere, water (including salt water), petrochemicals and chemical systems.
- Excellent thermal and electrical conductivity, the latter being nearly twice that of copper on an equivalent weight basis.
- Non-ferromagnetism, property of importance in the electronics industries.
- Non-toxicity, aluminium is routinely used in containers for foods and beverages.
- High reflectivity, the reflectance of polished aluminium, over a broad range of wavelengths, leads to its selection for a variety of decorative and functional uses.

2.2 Designation System: Nomenclature

Aluminium and its alloys may be cast or formed by variable processes. Manufactured forms of aluminium and aluminium alloys can be broken down into two groups (Cayless, 2002):

- Standardized products including sheet, plate, foil, rod, bar, wire, tube, pipe, and structural forms.
- Engineered products designed for specific applications and including extruded shapes, forgings, impacts, castings, stampings, powder metallurgy (P/M) parts, machined parts, and metal-matrix composites.

Thus, the major categories used to distinguish aluminium and aluminium alloys are the wrought and the cast compositions. Therefore, nomenclatures for these two categories have been developed. A further differentiation for each category is based on the primary mechanical or thermal treatments, or both, applied during the process to produce the various tempers.

The composition designation system regarding the wrought aluminium and aluminium alloys is presented in the following section; the distinctions in the designation nomenclature are not treated.

A four-digit numerical designation system has been developed by The Aluminium Association and has been used to identify wrought aluminium and aluminium alloys (Cayless, 2002). As recorded in Table 2.1, the first digit of the four-digit designation indicates the group. The last two digits indicate the minimum aluminium percentage, these digits correspond to the two decimal digits in the minimum aluminium percentage when expressed to the nearest 0.01 %. The second digit is used to indicate modifications of the original alloy; zero indicating the original alloy.

Compositions of controlled unalloyed aluminium are designated by the group 1xxx. In this group, the series 10xx is used to designate unalloyed compositions that have natural impurity limits, Table 2.2. The major impurities of smelted aluminium are iron, silicon and copper, but zinc, gallium, titanium, and vanadium are typically present as minor contaminants. The copper and part of the silicon are in solid solution. The second-phase particles present contain either iron or iron and silicon (Hatch, 1984). The specific

phases present or the relative amounts when more than one phase are present depend on the ratio of iron to silicon and on the thermal history of the specimen.

Aluminium alloys are designated by the 2xxx through 8xxx alloy groups. The alloy group is determined by the alloying element present in the greatest mean percentage. The second digit in the designation indicates alloy modification. The last two digits in the 2xxx through 8xxx groups have no specific significations, but serve to identify the different aluminium alloys in the groups.

Tables

Table 2.1 – Aluminium and aluminium alloy designation system (Cayless, 2002).

Aluminium $\geq$ 99.00 %	1xxx
Aluminium alloys grouped by major alloying element(s):	
Copper	2xxx
Manganese	3xxx
Silicon	4xxx
Magnesium	5xxx
Magnesium and silicon	6xxx
Zinc	7xxx
Other elements	8xxx
Unused series	9xxx

Table 2.2 – Unalloyed aluminium designation (Hunsicker, 2002).

Aluminium (%)	Designation
99.50 - 99.79	Commercial purity
99.80 - 99.949	High purity
99.950 - 99.9959	Super purity
99.9960 - 99.9990	Extreme purity
99.9990	Ultra purity

3 Growth Mechanisms of Anodic Oxide Films

The anodizing process consists in an electrochemical passivation of selected metals, leading to the thickening of the native oxide layers present at their surfaces. Thus, films of controlled morphologies and functional properties may be formed by careful selection of the electrolytes (concentration, composition, presence of additives, temperature) and film-forming conditions (constant voltage, constant current density).

For aluminium, anodizing results in the conversion of the specimen surface into barrier or porous aluminium oxide films, depending on the selected conditions. Anodic aluminium oxide films are widely used in order to enhance performance for:

- Corrosion resistance: sealed anodic coatings of aluminium oxide are corrosion resistant and highly resistant to atmospheric and salt-water attack. The anodic coating protects the underlying metal by serving as a barrier to corrosive agents.
- Abrasion resistance: hard anodizing processes produce coatings from 25 µm to more than 100 µm thick. Such coatings, with the inherent hardness of aluminium oxide, are sufficiently thick for use in applications where abrasion resistance is required.
- Paint adhesion: anodic coatings offer a chemically active surface for most paint systems.
- Decorative appearance enhancement: electrolytic colouring is a two-step process involving conventional anodizing followed by electro-deposition of metallic pigments in the pores of the coating.

In addition, barrier anodic aluminium oxide films have been key material for the fabrication of nano-devices, such as electronic, optoelectronic, and magnetic devices (Masuda and Fukuda, 1995). Indeed, these films grown on high-purity aluminium

are effective insulators and used as electrolytic capacitors, thin film transistor in liquid crystal display (TFT-LCD) devices, metal-insulator-metal (MIM) cathodes for electron beam lithography systems, vacuum micro-transistors.

The different growth mechanisms associated with the formation of barrier- and porous-type anodic alumina are described in this section.

3.1 Passivation

3.1.1 Description

Aluminium is a thermodynamically reactive metal, as indicated by its position in the electrochemical series; among structural metals, only beryllium and magnesium are more reactive (Hollingsworth and Hunsicker, 2002). Passivation is defined as a condition of corrosion resistance due to the formation of thin oxide films, under oxidizing conditions, resulting from high anodic polarisation (Jones, 1995). Thus, the corrosion rate of aluminium is substantially reduced when the passive film begins to grow, forming a barrier-type oxide layer between the surface of the active metal and its environment.

Under atmospheric conditions, native oxide films have been shown to grow up to 20 nm thick (Godard et al., 1967). Aluminium oxide films are composed of two layers, while the inner oxide next to the metal is a compact amorphous barrier layer, the outer layer above the barrier layer is a thicker, more permeable hydrated oxide (Hunter and Fowle, 1956). Additionally, the thickness of the inner layer is determined solely by the temperature of the environment; at any given temperature, the limiting barrier thickness is the same in oxygen, dry air, or moist air.

The conditions for thermodynamic stability of the oxide film are expressed by the Pourbaix diagram, Fig. 3.1. The Pourbaix diagram shows that aluminium presents a passive behaviour in the pH range of about 4 to 8.5. However, the limits of this range may vary with temperature and with the presence of substances that can form soluble complexes or insoluble salts with aluminium. Beyond the limits of the passive range, aluminium may corrode in aqueous solutions due to the solubility of its oxides in certain acids and bases. However, corrosion of aluminium may not take place outside

the passive range, as a result of either the non-solubility of the oxide film or of the film being maintained by the oxidizing nature of the solution (Hatch, 1984).

3.1.2 Corrosion behaviour of active-passive metals

Aluminium and aluminium alloys present barrier-type oxide films at their surface, thereby reducing corrosion under oxidizing conditions. In contrast, some metals and alloys, while subjected to corrosion at active potentials, present properties of corrosion resistance due to formation of thin surface films under oxidizing conditions with high anodic polarisation, such metals and alloys are referred to as active-passive materials (Jones, 1995).

Generally, the passivation behaviour of selected metals is typically studied following a potentiostatic procedure; many metals, unlike aluminium, display a distinctive active-passive behaviour as anodic polarisation increases. A schematic potentiostatic polarisation curve of a metal that shows an active-passive behaviour is illustrated in Figure 3.2.

For a metal in the active state, a raise of potential results in an increase of the driving force for corrosion by anodic reaction. Thus, the dissolution rate increases as measured by the anodic current density. Then, once the passivation potential, E_{pp}, is exceeded, the formation of a passive film becomes stable, due to the reaction of the metal surface with the electrolyte, such as:

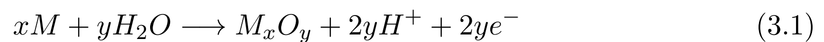

$$xM + yH_2O \longrightarrow M_xO_y + 2yH^+ + 2ye^- \quad (3.1)$$

Thus, the anodic dissolution reaction is limited as the migration of metal ions through the passive film takes place slowly. Consequently, a dramatic reduction of the current density occurs in the passive state while the oxide spreads gradually over the metal surface, and the dissolution rate remains low with further potential increase.

Finally, once the passive film has completely covered the metal surface, the film thickness increases and the current of metal ions passing through the film becomes independent of the potential. The most negative potential at which this state is attained is called the Flade potential, E_F, which represents the most negative limit of stability of

the passive state and is generally close to the critical passivation potential. At increased potential, the passive film breaks down and the anodic dissolution rate increases in the transpassive state.

The initial passivation potential depends on the pH value of the solution and slightly on its composition, particularly to the presence of anions which may favour or hinder passivation. The critical passivation current density, i_{cc}, which is the current density required to reach the passivation potential, is an important parameter of the passivation process. Indeed, i_{cc} gives a measure of the easiness of the process, i.e. the smaller the current density, the easier the passivation.

3.2 Anodizing

As seen in the previous section, polarisation in the passive state of specific metals, which fulfil the description of active-passive metals, results in the formation of passive oxide films. Increasing the potential in the passive state, while increasing the driving force towards oxidation, serves to thicken the passive oxide films, thereby enhancing the resistance to further oxidation. The phenomenon is used in high-voltage anodizing of some metals, where highly resistive oxide films can be grown to thicknesses of several hundred nanometres. Depending on the anodizing conditions, anodic oxide films with two different morphologies can be formed, namely barrier-type and porous-type.

3.2.1 Barrier-type anodic alumina films

For aluminium, growth of barrier-type films of controlled morphology may be developed by appropriate selection of electrolyte and film-forming conditions. Thus, films grown in near-neutral electrolytes at ambient temperatures are highly uniform in thickness and relatively compact (Thompson, 1997).

The anodic oxide films, formed in near-neutral electrolyte at a constant current density of 5 mA cm^{-2}, develop at constant electric field strength of the order 10^6 - 10^7 V cm^{-1}. Considering the range of field strength, the ionic charge transport and thereby the anodic oxide film growth are assumed to take place under high field ionic conduction (the electric field strength is assumed to be sufficiently high to prevent movement of

cations against the field direction). Thus, the driving force for anodic oxide film growth can be expressed as (Diggle et al., 1969):

$$i = A\,exp\,(BE) \tag{3.2}$$

where:

- i is the anodic current density.
- E is the electric field strength.
- A and B are temperature-dependent constants.

The growth of thin films both by anodic and atmospheric oxidation has been discussed by Cabrera and Mott. Thus, they described an oxidation model based on the following assumptions:

- The transfer of ion across the metal / oxide interface is the step determining the rate of oxide growth.
- The transfer of an ion through the oxide bulk is fast due to the lowering of diffusion barriers by the applied electric field.
- The field is sufficiently high to ensure that negligible amounts of ions are moving against the electric field direction.

The implication of the assumptions is that the number of charges carried through the film is small and, consequently, the accumulation of charge (space charge) is negligible. As a result, the electric field strength becomes a function of the oxide thickness in order to maintain a constant ionic current density (Cabrera and Mott, 1948).

Thus, as the film thickens, the voltage increases in order to maintain the constant current density. Additionally, the electric field strength being necessarily constant across the film thickness, induces oxide growth of highly uniform thickness.

In near-neutral electrolyte, the growth of barrier-type anodic alumina layers proceeds by both Al^{3+} and OH^{-} and / or O^{2-} migration, outward and inward respectively, through the pre-existing air-formed film present over aluminium substrates (Davies et al., 1965). Hence, barrier-type anodic alumina layers develop simultaneously at the film / electrolyte and metal / oxide interfaces. The transport numbers for aluminium

and oxygen species are 0.4 and 0.6 respectively (Skeldon et al., 1985).

For anodic oxide films developing in part, at the film / electrolyte interface, the incorporation of anion species from the electrolyte arises. Depending on the nature of the incorporated species, electrolyte-derived species can show contrasting behaviour under the high electric field. Thus, incorporated anion species can migrate inward, e.g. phosphate species, or may transform within the film into positively charged species and consequently migrate outward, e.g. tungsten; in addition, species can be incorporated as neutral species and are immobile, e.g. boron from aqueous solution, (Skeldon et al., 1985). Depending on their range of mobility, such species can be utilized as markers or tracers if the species are immobile or mobile respectively.

The formation of anodic aluminium oxide may involve the accumulation of alloying elements or of impurities, at the metal / oxide interface. The high enrichments of alloying elements, dopants or impurities may result in the development of a layer of about 1 to 5 nm thickness presents underneath the growing anodic oxide film. Thus, due to preferential oxidation of aluminium in comparison with more noble alloying elements or impurities, a virtually pure anodic alumina is formed and the alloying elements or impurities are concentrated adjacent to the metal / oxide interface. With further film growth, the developed enriched layer reaches a critical concentration; and consequently, the oxidation of both aluminium and the alloying elements or impurities takes place. As a result, contaminant-containing anodic oxide films form (Habazaki et al., 1997).

3.2.2 Porous-type anodic alumina films

Conversely, anodizing conducted in selected acid or alkaline electrolytes, which are reactive to the oxide, leads to the growth of porous-type anodic films. Porous anodic aluminium oxide films are described as a close-packed array of hexagonal columnar cells, containing a central pore, Fig. 3.3. The diameter of the pore and the interpore distance can be controlled by varying the anodizing conditions (O'Sullivan and Wood, 1970). Porous anodic oxide growth includes several stages that are easily detectable by monitoring the dependence of voltage (or current) as a function of time (Parkhutik and Shershulsky, 1992). The stages are schematically presented in Figure 3.4.

The anodic oxide film morphology presents a thin barrier-type layer of anodic alumina

next to the metal surface, which develops during stage I. Relatively fine-featured pathways are then revealed in the outer regions of the barrier oxide prior to any true pore formation, stage II. Further anodizing results in propagation of individual paths through the barrier oxide with their heads becoming enlarged, stage III. Finally, regular or steady pore morphology is formed by closely packed cylindrical cells, each containing a pore at the centre and separated from the aluminium metal by a layer of scalloped hemispherical barrier-type oxide, stage IV (Parkhutik and Shershulsky, 1992). Geometrical parameters of the pores are related to the anodizing variables (electrolyte concentration, applied voltage, regime of anodizing).

3.3 Growth of Barrier-Type Anodic Oxide on Patterned Surfaces

3.3.1 High field ionic conduction

Pringle presented some observations on the influence of the specimen surface roughness during anodizing of niobium and tantalum (Pringle, 1972, 1980).

Anodizing of both metals proceeds, with an efficiency close to 100 %, by metal cation egress and oxygen anion ingress. For niobium and tantalum, the transport numbers are almost identical. The transport number for the metal and the oxygen species are 0.25 and 0.75 respectively.

The kinetics for galvanostatic anodizing of niobium and tantalum can be described approximately by Equation 3.2. As a result of the exponential dependence followed by the current and the field, anodic oxide films must be of uniform thickness in the direction of the electric field, i.e. perpendicular to the local metal surface, and this requirement has to be fulfilled throughout the anodizing process.

For rough metal surfaces, the electric field distribution is non-uniform across the specimen surface, with the field being stronger on the convexities in the surface.

Thereby, the amount of metal consumed in forming oxide is greater at a convexity in the metal surface than at a concavity, and the rate of consumption is proportional to

the local convexity of the curvature. The formation of an anodic oxide therefore leads to the smoothing of the metal surface, Fig. 3.5.b, with the sharpest asperities being smoothed first.

Finally, the oxide film has to be sufficiently plastic to follow the changing contours of the metal surface, and particularly the reduction in surface area. The necessary plasticity arises directly from the amorphous structure of the oxide and by the nature of the anodizing process which results from ionic migration (Pringle, 1980).

The formation of barrier-type anodic oxide film on relatively rough aluminium surfaces was investigated by Shimizu et al. and later by Takashima et al. from morphological observations using transmission electron microscopy as well as atomic force microscopy for the second author.

Identical to the model of surface smoothing presented by Pringle for niobium and tantalum, Shimizu et al. demonstrated the flattening of the aluminium surfaces as a result of three factors (Shimizu et al., 1991), namely:

- The anodic oxide films are amorphous, so that they can follow the continuously changing and reducing aluminium surfaces.
- The oxide films should be of uniform thickness in the direction perpendicular to the local metal surfaces as required by the oxide growth kinetics.
- Part of the oxide growth occurs at the oxide / electrolyte interface by the outward migration of aluminium ions.

In contrast, Takashima et al. did not consider a growth mechanism but presented a theoretical simulation of the flattening process based on the transmission electron microscopy and atomic force microscopy observations of the decrease in the aluminium substrate ridge height with the anodizing potential (Takashima et al., 2000).

Thus, similarly to niobium and tantalum, the growth of barrier-type anodic aluminium oxide takes place by simultaneous migration in opposite directions of metal and oxygen species. With the driving force for the anodic oxide growth being high field ionic conduction, the current-electric field dependence requires uniformity of the oxide thickness following the direction of the field. Metal consumption, and therefore metal

/ oxide recession, results in the smoothing of the specimen surface. Importantly, given the plasticity of the anodic aluminium oxide structure, the anodic film can adapt to the gradually changing contours of the metal surface.

3.3.2 Plasticity

For anodic aluminium oxide films, plasticity has been widely studied (Diggle et al., 1969). The presence of stress in anodic oxide films has been reported both at open circuit (Wuthrich, 1981) and during anodizing (Bradhurst and Leach, 1966), and has been shown to be a complex phenomenon that depends on various factors, namely:

- The nature of the ionic species and of the transport process. If the oxide growth proceeds by anion transport, then since the oxide metal volume ratio is greater than unity, compressive stress arises within the oxide (Vermilyea, 1963). Conversely, when both anions and cations participate to the oxide formation, compressive stress was found to be significantly lower than when anion transport only was involved (Davies et al., 1965).
- The presence of an electric field across the oxide film results in electrostrictive stress (Wuthrich, 1980); the magnitude of the compressive stress produced is proportional to the square of the electric field (Hebert and Houser, 2009; Sato, 1971; Vanhumbeeck and Proost, 2008). For barrier-type films on aluminium, transition from tensile stress to compressive stress when an electric is applied, and tensile stress increases when the electric field is suppressed, were reported. Thus, the authors expressed the growth stress as the sum of the open circuit stress and electrostrictive stress (Bradhurst and Leach, 1966).
- The presence of hydrated oxide within the oxide film (Vermilyea, 1963).
- Finally, other factors may partly or wholly determine the nature and magnitude of the stress which develops in a growing oxide film, namely the purity of the anodized metal involved in the film formation, epitaxy, surface roughness and residual stresses in the metal (Bradhurst and Leach, 1966).

Thus, growing anodic oxide films undergo an important stress, electrostriction, due to the applied electric field. The resulting electrostrictive stress is comprised of two components (Vanhumbeeck and Proost, 2008). The first stress contribution, usually referred to as the Maxwell stress, results from the Coulomb attraction between charges of opposite sign located on both sides of the dielectric. The second contribution arises from the alignment of dipoles along the direction of the applied electric field

and leads to the modification of the dielectric constant of the material, and it is called dielectrostriction. The dielectrostriction can be taken into account using two electrostriction parameters, α_1 and α_2, function of the dielectric constant of the specimen.

The electrostrictive stress, σ_{ES}, resulting from the electric field, E, along the thickness of a dielectric film attached to a substrate can be expressed as:

$$\sigma_{ES} = -\frac{\nu}{1-\nu}\,\frac{\varepsilon_0}{2}\left[\varepsilon - (\alpha_1 + \alpha_2)\right] E^2 \tag{3.3}$$

where:

- ν and ε are the Poisson coefficient and the relative dielectric constant of the oxide film respectively.
- ε_0 is the vacuum permittivity.
- α_1 and α_2 are two electrostriction parameters.

3.3.3 Stress-driven transport

While anodic aluminium oxide is likely to be under tensile stress, the presence of an electric field induces a compressive stress in the oxide film as a result of electrostriction. Additionally, aluminium oxide has been shown to accommodate the electrostrictive stress by deformation or flow (Sato, 1971; Skeldon et al., 2006).

Of relevance for the present study, a flow model was established for the growth of porous anodic film on aluminium (Garcia-Vergara et al., 2006; Houser and Hebert, 2008, 2009; Skeldon et al., 2006). The growth mechanism of porous anodic alumina is briefly presented in this section.

The formation of porous anodic alumina was shown to proceed initially by the formation of a barrier-type anodic oxide layer, which is then converted into a porous film. The thickness of the barrier-type anodic alumina, adjacent to the metal oxide interface and beneath the porous structure, remains constant during the formation of the porous film.

Generally, the conversion of the barrier layer into a porous layer has been attributed to field-assisted dissolution of the barrier layer. In contrast to the dissolution model, the generation of the porous anodic alumina has been demonstrated to result from the flow of material from the barrier layer at the bottom of the pores to the cell walls. The material flow is ascribed to electrostrictive stress and field-assisted plasticity. Thus, formation of the porous alumina film arises from a combination of high field ionic conduction and stress-driven transport (Garcia-Vergara et al., 2006; Skeldon et al., 2006).

3.3.4 Markers and tracers

The development of porous anodic alumina proceeds by coupled ionic migration and material flow due to electrostriction. The induced compressive stress is proportional to the square of the electric field (Hebert and Houser, 2009; Sato, 1971).

For rough metal surfaces, the electric field distribution is non-uniform across the specimen surface, with an increased value at the peaks in comparison with the valleys in the surface. Considering the square-dependence of the mechanical stress on the electric field and the distribution of the electric field across the peaks and valleys in the metal surface, a significant gradient of stress may arise across the anodic oxide layer during anodizing. As a result, stress-driven transport may participate, in addition to high field ionic conduction, to the smoothing of the specimen surface.

Hence, studying the distributions of incorporated species, which may be immobile (marker) or mobile (tracer) during the anodizing process, may reveal variations of the anodic oxide film compositions associated with surface topography modifications during anodizing of relatively rough aluminium substrates; and consequently, to the understanding of the processes taking place during growth mechanism of barrier-type anodic aluminium oxide layers.

Ion transport mechanisms occurring during anodic film formation were widely studied using marker and tracer experiments (Pringle, 1973a,b). Thus, marker experiments allow determination of the transport numbers of the metal and oxygen species during anodizing. Tracer experiments are required to elucidate the transport mechanism, with the nature of the migration process being identified by correlation with the changes in

the concentration profile of the tracer (Pringle, 1980).

The stripping of oxide coatings from the substrates consists in the dissolution of the oxide films. Generally, the stripping of porous anodic alumina layer is performed using a chromic / phosphoric acid solution. The stripping solution dissolves preferentially aluminium oxide in comparison with aluminium; and thereby, reveals the pattern of aluminium surface through development of the hexagonal alumina cells that penetrate the substrate in a hemispherical manner.

Additionally, the stripping solution, by reaction with aluminium, develops a thin oxide layer over the surface which contains chromium and phosphorus species (Lewis and Plumb, 1956).

Chromium- and phosphorus-enriched layers have been used as tracers, for the determination of migration mechanism of aluminium and oxygen species respectively, during anodizing of aluminium substrates in 0.1 M ammonium pentaborate electrolyte.

The chromium ions, generated by high field-assisted dissociation of the incorporated units of Cr_2O_3, migrate outward at a constant rate of 0.74 relative to that of aluminium ions, while the incorporated phosphorus species ions migrate inward at a constant rate of 0.50 relative to that of oxygen ions, Fig. 3.6 (Shimizu et al., 1999a).

In addition, during film growth, boron species are incorporated into the film at the film / electrolyte interface, with a pure aluminium oxide layer developing at the metal / oxide interface. Thus, boron species allow the determination of the location of the original metal surface.

Thus, initially, the boron marker and the chromium and phosphorus tracer distributions are replicas of the surface topography; and therefore, they appear highly appropriate for the determination of the influence of the substrate roughness on the migration processes associated with the anodic aluminium oxide growth.

Hence, the investigations of the formation of barrier-type anodic aluminium oxide were carried out on superpure aluminium substrates patterned by electropolishing

as well as anodizing in sulphuric acid, oxalic acid, phosphoric acid and subsequent stripping in a chromic / phosphoric acid solution of either the electropolished or porous films respectively. The distributions of the incorporated species were examined by transmission electron microscopy and sputtering-induced depth profiling analyses.

Figures

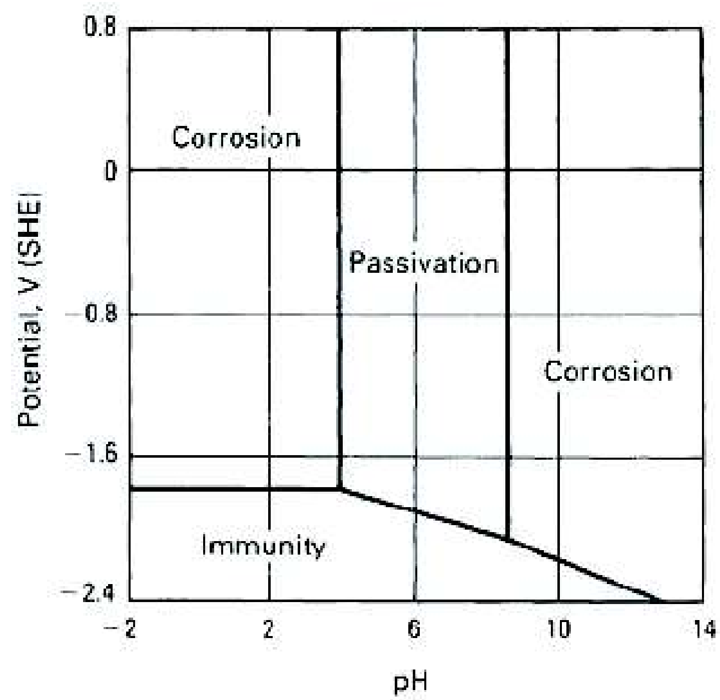

Figure 3.1 – Pourbaix diagram for aluminium with an $Al_2O_3.3H_2O$ (hydrargillite) film at 25 °C. Potential values are for the standard hydrogen electrode (SHE) scale (Pourbaix, 1966).

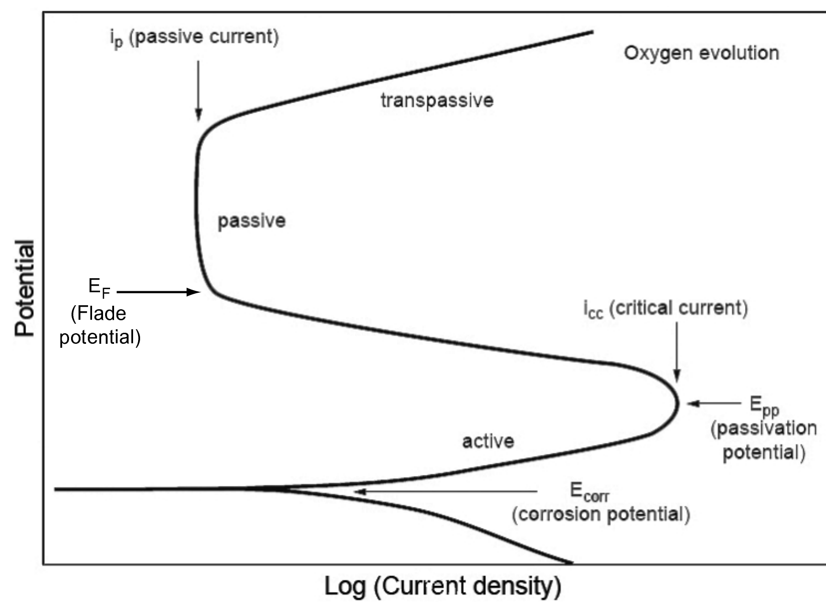

Figure 3.2 – Schematic anodic polarisation curve for a metal that shows an active-passive behaviour.

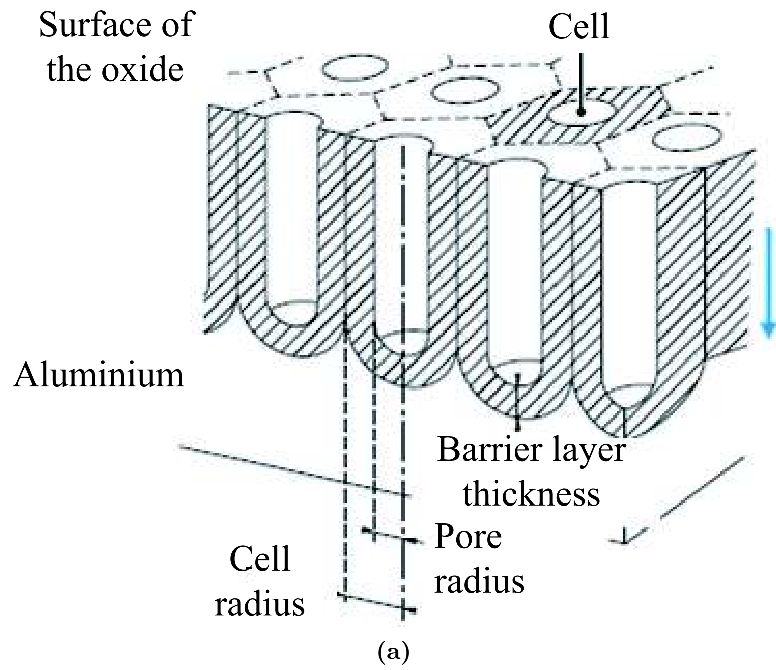

(a)

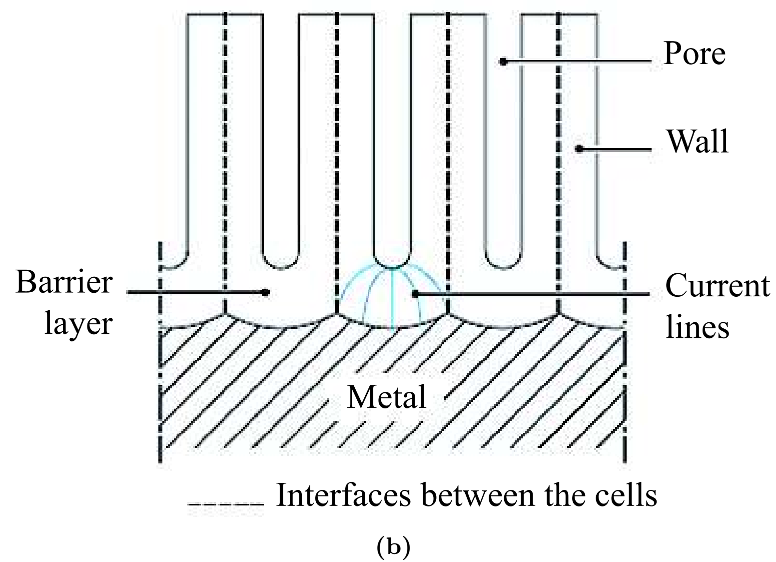

(b)

Figure 3.3 – a. Schematic diagram of a porous-type film on aluminium, b. Sketch of a section of the porous morphology of an oxide layer (Safrany, 2007).

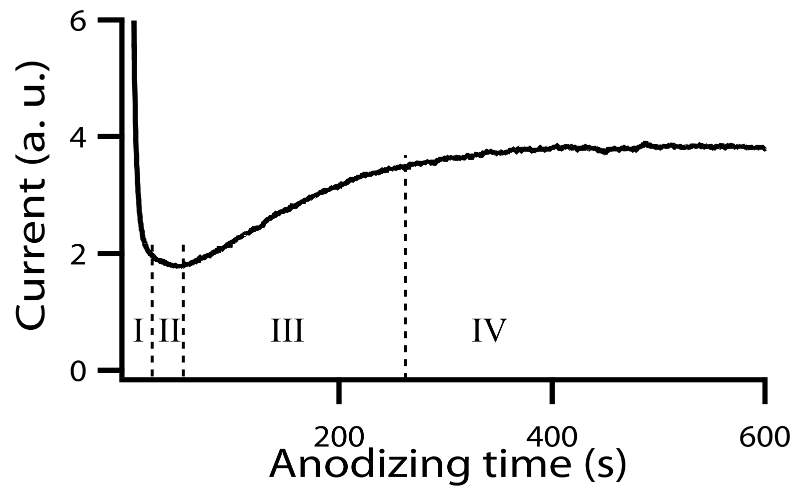

(a)

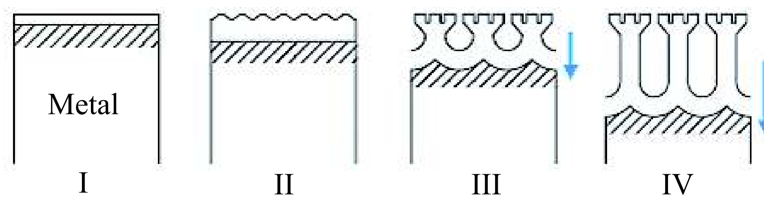

(b)

Figure 3.4 – a. Schematic diagram of the current-time behaviour showing the kinetics of porous oxide growth on aluminium in potentiostatic regime and b. Schematic diagram of the different stages of development of an anodic oxide layer showing a porous morphology (Safrany, 2007).

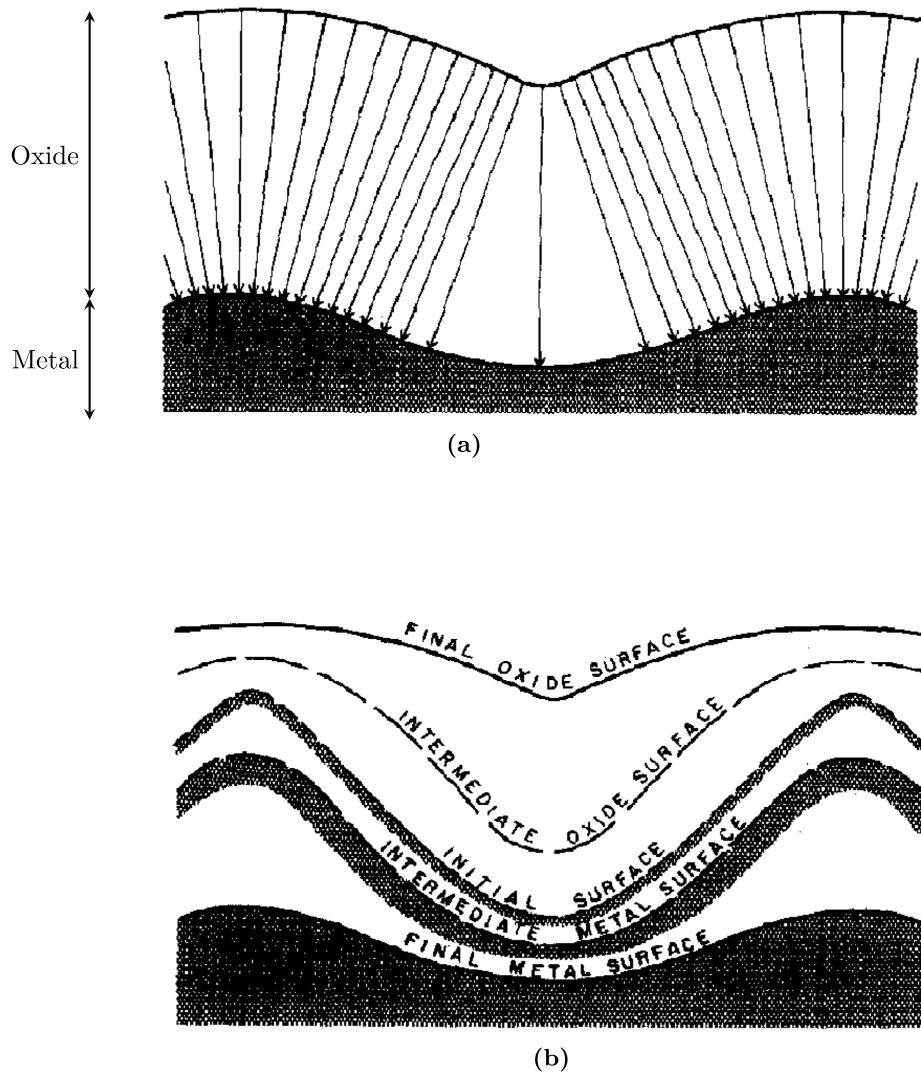

Figure 3.5 – Two consequences arising from the exponential dependence of current upon field during anodizing: a. The variation of current density within an oxide film on a rough metal surface and b. the smoothing effect of anodic oxidation on a rough metal surface; the rate of metal consumption is proportional to the current density at its surface, as indicated by the arrow heads in the upper diagram. In both diagrams, two dimensional roughness is assumed (Pringle, 1980).

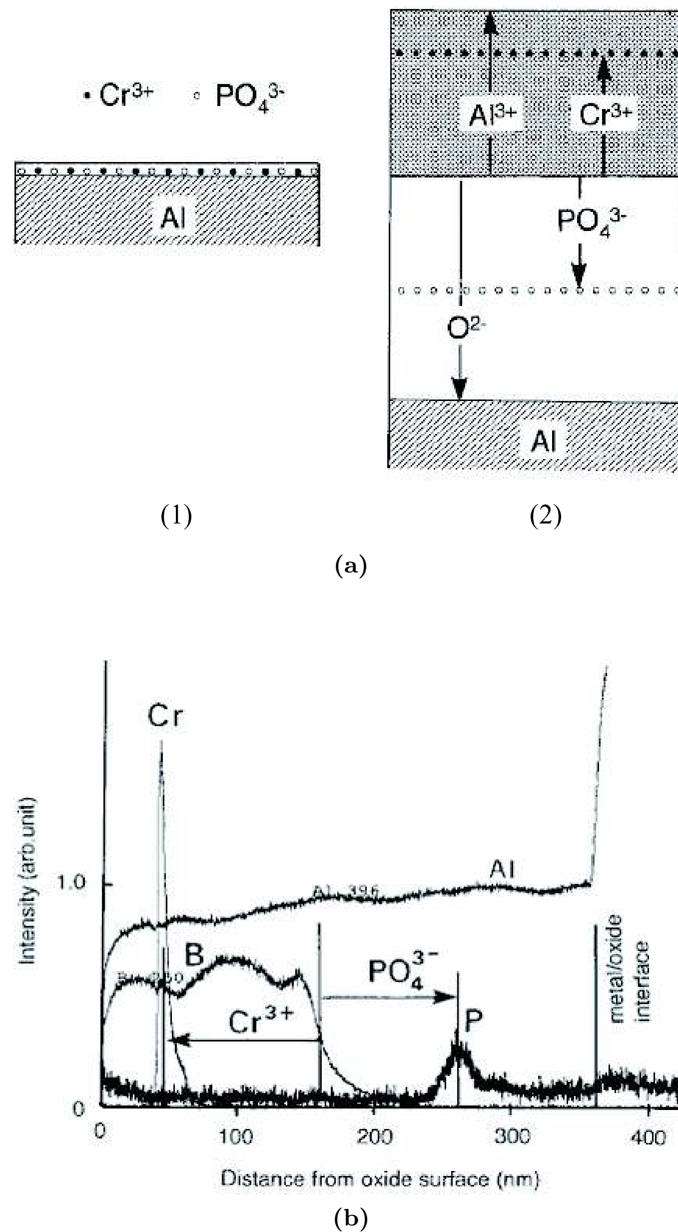

Figure 3.6 – a. Schematic diagrams of the aluminium substrate: (1) after electropolishing and immersion in 20 g l^{-1} CrO_3 / 35 ml l^{-1} H_3PO_4 solution at 90°C for 5 min, (2) after anodizing of (a.1) to 300 V at constant current density of 5 mA cm^{-2} in 0.1 ammonium pentaborate solution at 20 °C. b. GD-OES depth profile of the anodic film formed under the conditions of (a.2) showing that the chromium ions, generated by high field-assisted dissociation of the incorporated units of Cr_2O_3, migrate outward at a constant rate of 0.74 relative to that of aluminium ions, while the incorporated phosphorus species ions migrate inward at a constant rate of 0.50 relative to that of oxygen ions (Shimizu et al., 1999a).

4 Sputtering-Induced Depth Profiling Analyses

The distributions of the different marker and tracers have been investigated using sputtering-induced elemental depth profiling analyses, namely GD-OES, GD-TOF-MS and TOF-SIMS. The accuracy of sputtering-induced depth profiling techniques is related to the erosion process, which may involve atomic mixing, re-deposition of sputtered material and sputtering-induced surface topography development. The sputtering processes associated with ion-beam and glow discharge techniques are presented in this section as well as the sputtering-induced surface modifications. Understanding of the erosion processes involved during sputtering-induced elemental depth profiling analysis is essential for the interpretation of the in-depth composition of the specimens studied.

4.1 Sputtering

4.1.1 Sputtering process

Sputtering consists in emission of (neutral or charged) atoms due to the bombardment of the surface of a material by energetic particles. The incident projectiles are usually ions, but atoms, clusters or other species, namely neutrons, energetic electrons and photons may be employed. The incident particles penetrate into the surface and set-up a series of collisions until the lost of their energy (Bogaerts and Gijbels, 1998). In these primary collisions, energy is either transferred to the target nuclei via elastic collisions (nuclear energy loss) or to the electrons as either ionisation or excitation (electronic energy loss) (King, 1997). In addition to sputtering, the particle impact result in various processes, as follows:

- A fraction of the incident particles is backscattered in collisions with target atoms.

- Some primary particles are implanted in the solid, transferring their energy to electrons and lattice atoms.
- The particle bombardment leads to the emission of electrons and photons
- Sputtering-induced modifications arise in the surface layers of the solid, such as the composition and morphology of the specimen are altered.

Thus, for energies in the range of 10 eV to a few keV, the energetic particles penetrate the specimen and transfer energy to target atoms by nuclear collisions, thereby, initiating a collision cascade between the lattice atoms in the solid. In this three-dimensional collision cascade, atoms lying at the surface can gain sufficient energy to overcome the surface binding energy and to escape from the surface. The surface binding energy describes the binding strength of surface atoms to the specimen, and is generally approximated by the heat of sublimation of the material (Seah et al., 1981).

Material sputtering, resulting from cascades of atomic collisions, has been successfully treated by Sigmund (Sigmund, 1969, 1987) in terms of series of binary collisions occurring between the incident ion and the target atoms, consequently causing the scattering of multiple target atoms and subsequent ejection of the neighbouring atoms, Fig. 4.1.

For physical sputtering, several collision regimes have been identified, depending on the energy of the incident particles and the collision cross-section between the incident particles and the atoms of the solid, namely:

- The single knock-on regime; the recoil atoms from the incident particle / target collisions receive sufficiently high energy to be sputtered, but not enough to generate a recoil cascade.
- The low-density cascade (linear regime); the recoil atoms from incident particle / target collisions receive sufficient energy to generate recoil cascades. However, the density of recoil atoms is low, such as knock-on collisions dominate and collisions between moving atoms are unlikely.
- The high-density cascades (spike regime); the density of recoil atoms is so high that the majority of atoms within a certain volume, the spike volume, are in motion.

For particle bombardment of energies in the range of a few keV, the approximation of the linear cascade is appropriate to describe the particle-target collisions, except

for heavy projectiles on heavy substrates where the spike regime can be expected. However, in Sigmund's theory, sputtering due to electronic excitation is disregarded. Such approximation may not be adequate to describe interactions between incident particles of very low energy, hundreds of eV, and target atoms, for which the electronic excitation may not be negligible.

While Sigmund's theory gave an important fundamental model for basic issues, a computer simulation approach is required in order to understand the particle interactions during the sputtering process (Urbassek, 2007; Vickerman, 2009). In this regard, molecular dynamics (MD) simulations, despite of the limitations on the short period of time of calculation, typically < 1 ns and on small spatial scales, have been of immense value in understanding irradiation-induced processes at an atomistic scale.

Figures 4.2 - 4.4 display examples of applications for which information gained by MD simulation are significant. Figure 4.2 illustrates the topographic development of the target at various stages in the simulation. The target surface develops a slope downwards in the direction of projectile incidence. This is a further manifestation of edge effects. Early in the simulations, a lip emerges above the leftmost edge of the target surface, due to recrystallisation after melting induced by hard projectile collisions near the edge. The section of the target surface that is shadowed by this edge is subsequently eroded more slowly than other parts of the surface. As the simulations proceed, this less-eroded region also begins to shadow the surface region adjacent to it. In due course a slope extending across most of the target surface is produced (Karolewski, 2009).

Figure 4.3 shows a view of a crater formed by the sputtering process. Urbassek discussed crater formation by Cu_n clusters (n = 13, 43) impinging with total energies between 5 and 20 keV on a Cu (100) surface. They found craters were formed above the threshold bombarding energy of around 5 keV; subsequently, linear increase of the crater volume with the energy of the incident particles was determined (Urbassek, 2007).

Finally, Figure 4.4 presents cross-sectional views of the temporal evolution of typical collision events leading to ejection of atoms due to 15 keV Ga and C_{60} bombardment. The nature of the energy deposition process is very different for these two projectiles. The high-energy Ga projectile penetrates deeper into the crystal, creating a damaged

area that is cylindrical in shape. Conversely, the C_{60} bombardment event creates a meso-scale crater with a concomitant pressure wave into the solid. The impact leads to nearly simultaneous motion and high disorder in a relatively shallow volume of the crystal below the surface in a very short time. This dense, liquid-like region closes off open channels so that individual carbon atoms have difficulty penetrating deeply into the sample. Consequently, a significant amount of the energy of the projectile energy is deposited close to the surface, leading to the emission of many particles. The motions due to the meso-scale impact of the entire C_{60} particle and the collisions induced by the individual C atoms have inherently different character and different time scales. These two components influence the yields and kinetic energy distributions (Postawa et al., 2004).

4.1.2 Sputtering yield

The theory developed by Sigmund describes sputtering as a result of linear collision cascades. This theory led to the definition of the sputtering yield, Y, which represents the mean number of atoms removed from the surface of a solid per incident particle. Thus, in the linear cascade approach, Sigmund established the following expression for the sputtering yield:

$$Y = \frac{3}{4\pi^2}\alpha\left(\frac{m_t}{m_i}\right)\frac{S_n(E)}{U_s} \tag{4.1}$$

where:

- $\alpha\left(\frac{m_t}{m_i}\right)$ is a function depending only on the masses of the incident and target atoms.
- $S_n(E)$ is the nuclear stopping cross-section, i.e. the mean energy of the projectile transferred by nuclear collisions on the path length travelled by the incident particle.
- E is the energy of the incident particles.
- U_s is the binding energy of an atom of the target.

The sputtering yield depends on the material of the target, on the species of bombarding particles and their energy and angle of incidence. Thus, for a given energy of the bombarding projectiles, the sputtering yield increases with increasing mass of the incident particles as a result of a rise of the nuclear stopping cross-section. Additionally,

the angular dependence of the sputtering yield has been empirically determined to be well approximated by $1/(cos\theta)^{-f}$, with f between 1 and 2 (Yamamura and Shindo, 1984); thus the sputtering yield increases considerably beyond 70° and reaches a maximum between 80° and 85°.

4.2 Sputtering-Induced Surface Modifications

As a result of the large energy consumption by formation of lattice defects and heat generation in the collisional cascade, only a small fraction of the primary-ion energy is available for the sputtering of the atoms of the target. Thus, the formation of lattice defects leads to an atomic mixing in the cascade region, inducing pronounced alterations of the surface topography and composition.

4.2.1 Topographical modifications

During material sputtering, transfer of kinetic energy from the impinging particles to the surface atoms leads to the ejection of the latter. Due to the nature of the sputtering process under low energy ion particle bombardment, material removal is not performed by sequential monolayer. As a result, sputtering-induced modifications of surface topography and subsequent roughening of the material surface may appear (Carter et al., 1982b).

Various effects, namely the target material, its crystallinity and temperature as well as the nature of the incident particles as well as their energy and angle of incidence and finally the total fluence, contribute to the modifications of the surface topography during sputtering-induced depth profiling analysis, with subsequent alteration of the depth resolution (Hofmann, 1998). The development of surface topography during sputtering depends on the following (Carter and Nobes, 1994; Carter et al., 1982b):

- The statistics of the sputter erosion process: on the atomic scale, each impinging particle leads to the ejection of individual atoms or atomic clusters resulting in atomic scale changes in the surface morphology.
- The lattice orientation dependence of the sputtering and the presence of lattice defects: the ejection probability depends on local atomic configuration, namely crystal surface orientation, presence of jogs and ledges and of point and extended defects, which leads to an atomic and larger scale differential changes of roughness.

- The surface-site dependence of the sputtering yield: the surface curvature dependence of the sputtering tends to effectively erode peaks more quickly than valleys (Carter et al., 1982a), with shadowing of the valleys by the peaks of the surface. Indeed, each atom of the surface present a sputtering probability inversely proportional to its instantaneous bonding with the matrix (Seah et al., 1981). The sputtering is site dependent, with the most exposed atoms having the highest sputtering probability; thus, atoms in the edge sites on the surface have lower surface binding energies and so will be more easily ejected than atoms in a valley position (Seah et al., 1981).

- Surface diffusion and second-phase formation by primary-ion implantation: transfer of kinetic energy from incident particles to atoms of the surface can lead to through diffusion.

Additionally, if the original surface is rough, by shadowing of the impinging particles, the differently inclined microplanes cause variations of the sputtering rate across the surface, complicating the previously mentioned effects (Hofmann and Zalar, 1987).

Thus, the sputtering process inevitably causes some random surface roughening (Benninghoven, 1971) that was described by the so-called sequential layer sputtering (SLS) model (Hofmann, 1980; Hofmann and Zalar, 1979), and confirmed by modelling.

However, surface roughening may be balanced by some forms of atomic transport, which ensure a competitive smoothing. Smoothing of surfaces initially roughened can be obtained by such processes. Depending on the various random roughening and transport smoothing processes implied, their competition may lead to further roughening, smoothing or to no averages change in surface roughness. The result is a function of the incident particle parameters, namely ion flux, energy and mass and substrate temperature (Carter, 1996).

Thus, depending on the processes involved different surface topography developments may arise. Prominent examples are the formation of well-ordered ripples or dot patterns and surface smoothing of originally rough surfaces, when surface relaxation dominates. Thus, pattern formation in ion-beam erosion is not restricted to a specific material class, and can be found for amorphous, crystalline surfaces, dielectrics, semiconductors and metals. In contrast, low-energy ion-beam erosion has also been established for polishing of high-quality optical surfaces, e.g. for smoothing of surfaces or interfaces

of thin films. Frost investigated the evolution of the surface topography of Si and Ge surfaces during low-energy ion-beam erosion (Frost et al., 2008), with considerations of critical parameters for the incident particle / target interactions, namely:

- The angle of ion incidence, varied between 0° and 85°.
- The erosion time, i.e. a total fluence up to 4 x 10^{19} cm^{-2} was applied.
- The ion-beam energy, varied between 300 and 2000 eV.
- The divergence of the ion beam / angular distribution within the ion beam.
- The ion species used as projectile, namely Ne^{+}, Ar^{+}, Kr^{+}, Xe^{+}.
- The temperature.
- The specimen rotation during the sputtering process.

Figure 4.5 presents the diversity of structures and patterns that can result from the ion-beam erosion of Si and Ge surfaces; and therefore, the different possibilities of the surface topography modifications (Frost et al., 2008).

4.2.2 Compositional modifications

In addition to the surface topography modifications, energetic particles sputtering induces alteration of the surface composition, (Hofmann, 1998), namely:

- Atomic mixing in the the collisional cascade, primary-ion and recoil implantations,
- Preferential sputtering,
- Radiation-enhanced diffusion,
- Interfacial segregation,
- Redeposition of sputtered material

4.3 Elemental Depth Profiling Analysis Techniques

The objective of sputtering-induced depth profiling analyses is to probe the elemental composition of a specimen as a function of depth. Generally, the elemental depth profiles are measured as a function of the sputtering time. Thereby, the determination of the in-depth composition of the specimen requires the conversion of sputtering time into a depth scale as well as the conversion of the intensity of the measured signals into concentrations. Sputtering-induced depth profiling techniques have been developed to perform elemental depth profile analyses with low detection limits and a high accuracy. The accuracy of a depth profile is limited by the depth resolution achieved, Δz, defined as the deviation between the original elemental depth distribution and the measured profile.

4.3.1 Selection of elemental depth profiling analysis techniques

The selection of the techniques for depth profiling analyses followed different requirements. In order to ascertain the distributions of the different species present within the anodic oxide films, depth profiling techniques relying on different methods for material removal were selected, namely time-of-flight secondary ion mass spectrometry (TOF-SIMS) and glow discharge optical emission spectroscopy (GD-OES), for which sputtering is ensured by primary ion beams and glow discharge plasma respectively.

Additionally, elemental depth profile analysis using GD-OES of anodic oxide films containing chromium and phosphorus markers have been reported in the Literature (Shimizu et al., 1999a,b,c,d,e), and thereby, present an important background for the study of the growth mechanism of anodic oxide films.

4.3.2 Time-of-flight secondary ion spectrometry

TOF-SIMS instruments have been designed for molecular analysis and shallow depth profiling capabilities, based on a dual beam approach which allows independent optimization of the analysis and the sputtering. Thus, compositional information of the topmost atomic layers of the surface is achieved by the application of a very low primary ion dose densities (10^{12} ions cm^{-2}, static limit), in order to prevent surface modifications and to investigate the original, non-modified surface composition. In contrast, erosion of the specimen is performed using etching at relatively higher ion

dose densities compared with the analysis. Thus, material removal is carried out in a controlled manner to obtain information on the in-depth distribution of elements. Excellent depth resolution is achieved as the analysis is performed on a restricted area at the bottom of the crater formed using the etching beam (Vickerman, 2009). Thus, TOF-SIMS is highly regarded as it is a versatile technique that offers in-depth information associated with low detection limits (high sensitivity), an excellent depth resolution and a high lateral resolution.

4.3.3 Glow discharge spectrometry

The analytical spectroscopic sources for elemental analysis used in glow discharge spectrometry (GDS) applications are based on the phenomenon of sputtering involved in glow discharge plasmas. Thus, in addition to secondary electron emission from the cathode (specimen), the ion bombardment causes the sputtering of the material of the cathode. The sputtered species consists predominantly of free atoms that make the glow discharge appropriate for elemental analysis (Bogaerts et al., 1995).

The surface analytical capabilities of glow discharge spectrometry rely on the intrinsic properties of the sputtering process occurring during depth profile measurements. Specimen atomization is performed by cathodic sputtering, which is the basis for depth-resolved analysis. In comparison with high vacuum sputtering used in SIMS, in GDS specimens are sputtered by particles of very low energies, >1 keV and <100 eV respectively, under a high current flux, 1 μA cm^{-2} and $\simeq$ 100 mA cm^{-2} respectively (Broekaert, 2003). As a result, the glow discharge plasma ensures high sputtering rates, >1 μm min^{-1}, due to the high flux of energetic species. Additionally, the species contributing to sputtering are of low energy, resulting in a low penetration depth and limiting the surface damage to a very shallow layer of about 2 nm thick (Laude and Chapon, 2005).

The depth resolution and the sputtering process taking place during GDS depth profile analysis depend on the glow discharge plasma characteristics, which are described in the following sections.

For GDS analyses, the radiation source is a plasma produced by an electrical discharge applied between electrodes. When a dc or rf power is applied between two electrodes

placed in a gas-filled discharge tube, initially a very small current flows through the discharge due to the limited number of charges present. As the applied cathode voltage increases, the number of charges rises as a result of the secondary electrons that are emitted from the specimen under primary ion bombardment (secondary electron emission) and of ionization during collisions. Consequently, the current rises and a Townsend discharge is created, Fig. 4.6.a. This is the beginning of an avalanche process which leads to a steady state where the number of electrons and ions produced are equal; as a result the plasma becomes self-sustaining, that corresponds to the normal glow state. The glow becomes increasingly visible, accompanied by a sharp rise in the current and a drop in a voltage (Shah, 1995), this is the abnormal glow state. The abnormal regime is used for sputtering during GDS analysis (Broekaert, 2003).

Thus, once the plasma is ignited, free electrons and ions are generated. Both species move under the influence of the electric field within the plasma chamber and influence this field through the creation of local charge distributions. Finally, as a result of various mechanisms, different areas are established, characterizing the glow discharge plasma. The glow discharge can be subdivided in several zones between the anode and the cathode but, in the case of an analytical glow discharge, only two zones are usually considered, namely the cathode dark space and the negative glow. The cathode dark space is characterised by a high electric field attracting the positive ions toward the cathode, thereby generating material sputtering. Conversely, the negative glow is free of electrical field but shows a high charge density for both ions and electrons, resulting in excitation and ionization collisions. The negative glow is a quasi-equipotential region and occupies nearly the entire inter-electrode space. The cathode dark space is the most important region of the glow discharge. A glow discharge can be maintained without negative glow and the other zones, but not without the cathode dark space (Bogaerts and Gijbels, 1998).

Figure 4.6.b presents a sketch of the glow discharge region. In the vicinity of the cathode (specimen) the cathode dark space is present, inside which most of the applied potential is dropped. The thickness of the cathode dark space depends on the sputtering pressure and, typically, is equal to the mean free path of the secondary electrons emitted from the specimen surface. Strong fields are therefore formed. The ions are accelerated across these fields to impact the cathode and cause sputtering of the specimen material. In

addition to sputtering, secondary electrons are produced due to particle impacts. Then, secondary electrons are accelerated across the cathode dark space into the negative glow region where they lose their energy through collisions, participating in excitation and ionization processes and thus sustaining the glow discharge (Shah, 1995). Thus, sputtering and ionization is a two-step process. The sputtering rate depends strongly on the specimen material and its surface properties, but once the atoms are sputtered, they move as single atoms into the negative glow where they can be ionized (Nelis and Pallosi, 2006).

Analytical rf and dc glow discharges are very similar in many aspects such as their structures and their overall analytical performances. The extreme similarities can be extended to the basic plasma physics, at least to a first approximation. Owing to the extent of similarities, the rf discharge has been described as a dc discharge with a superimposed high-frequency field. Even though dc and rf glow discharge devices and plasmas are extremely similar in many ways, there are also some important differences related to the physics of high-frequency fields (Winchester and Payling, 2004).

The most important difference from an analytical point of view is that the rf glow discharge device can be used to sputter both electrically conductive and insulating solid specimens, while the dc glow discharge device can be applied only to conductive materials. However, there are other more subtle differences such as the densities and energy distributions of charged particles, which can lead to differences in the efficiencies of important physical processes, such as excitation and ionization (Winchester and Payling, 2004).

4.4 Depth Resolution

Ion-bombardment induced depth profiling techniques are effective and reliable methods for thin film analysis. However, for such techniques, the depth resolution has been demonstrated to be limited by the distortion of the original elemental depth distribution as a result of the interaction of the energetic ions with the specimen surface (Carter, 1996; Hofmann, 1998; Zalm, 1995). The different phenomena involved result in compositional and topographical modifications of the surface, therefore limiting the depth resolution achieved. Of the different contributions to the degradation of the depth resolution, the initial roughness and the sputtering-induced roughness of the specimen surface and the atomic mixing are the most important (Hofmann and Zalar, 1987).

4.4.1 Definition

TOF-SIMS and GDS rely on different techniques for material removal, with the former using a primary ion-beam and the latter employing a glow discharge plasma. However, despite the different sputtering techniques, both SIMS and GDS perform elemental depth profiling analysis with high depth resolution (Payling, 1997; Shimizu et al., 1999a).

The depth resolution is defined as the capability of the surface analytical technique to distinguish between two consecutive layers in a multi-layer material (Nelis et al., 2006).

The depth resolution can be described by means of a Gaussian-like error function (Dapor and Marchetti, 1989; Hofmann, 1980, 1986; Hofmann and Mader, 1990). Indeed, sputter profiles, obtained on sharp ideal step-like interfaces using SIMS, indicate that the measured profiles can be approximated by the integrated error function, Eq. 4.2.

$$erf(z) = \frac{2}{\sqrt{\pi}} \int_0^z e^{-\eta^2} d\eta \tag{4.2}$$

The variation of the intensity of an element at the interfacial transition is expressed by:

$$I(z) = \frac{I_0}{2} \left[1 \pm erf\left(\frac{z-\mu}{s\sqrt{2}} \right) \right] \tag{4.3}$$

where μ is the position of the interface on the depth scale, z.

The interface width, expressed in terms of sputtering time or sputtered depth, respectively Δt and Δz, is defined by convention for SIMS as the interval where the intensity of the measured profile, $I(z)$, drops from 84 to 16 %, of the maximal signal, I_0. The depth resolution, Δz, is thus defined as twice the standard deviation, 2σ, of the error function, Fig. 4.7.a. For depth profiling of delta-layer, Fig. 4.7.b, a well-recognised approach is to define the depth resolution of the profile by the measure of the full width half maximum of the profile (FWHM). A delta-layer consists in a very narrow layer located at a precise depth within the specimen, and thus used for depth scale calibration.

In order to check the increase of depth resolution with increasing sputtered depth, either monolayers of different thickness or multi-layer structures with constant single-layer thickness, t_d, can be used. If the condition $t_d \gg \Delta z$ is not valid, the multi-layer structure can not be resolved completely and the observed line intensity extends into neighbouring layers, Fig. 4.8.

In the generalised case of a system of N multi-layers of finite thickness, the contributions from adjacent layers can be calculated by superimposing the different profiles, using the Equation 4.4.

$$I(z) = \frac{I_0}{2} \sum_{i=1}^{N} \left[erf\left(\frac{z - \mu_i}{s(\mu_i)\sqrt{2}} \right) - erf\left(\frac{z - \mu_i^*}{s(\mu_i^*)\sqrt{2}} \right) \right] \tag{4.4}$$

where μ_i and μ_i^* represent the interface positions of each element and $s(\mu_i)$ and $s(\mu_i^*)$ the corresponding interface widths, respectively. The depth resolution, Δz, can then be derived by a regressive iteration procedure.

However, a major difficulty is that the signal-time functions can hardly be approximated by the integrated error function, Eq. 4.2, since the signals never decline or increase at a sufficiently high rate towards a minimum or a maximum respectively (Carter et al., 1982a).

Additionally, the validity of the use of the previous equations relies on the prerequisite that the measured profiles can be approximated by the integrated error function, which

is not respected for an optimised depth profile in glow discharge spectrometry (Angeli et al., 2003; Quentmeier, 1994). Indeed, while the central area of the crater bottom presents a flat profile, the edges are either convex or concave, Fig. 4.9. Thus, for the convex case, a signal from the lower layer appears before the sharp transition, whereas for the concave case, the upper layer produces a signal after the sharp transition (Payling, 1997).

4.4.2 Degradation of the depth resolution

During sputtering-induced depth profile analysis, using techniques relying on ion-beam technology for material removal, the degradation of the depth resolution is governed by several phenomena inherent to the action of the primary ions on the substrate. Indeed, as presented previously, the different interactions between the energetic particles and the target atoms, in the collision cascade, result in various compositional and topographical modifications of the specimen surface. Consequently, atomic mixing arises, which contributes to the degradation of the depth resolution. Atomic mixing can be reduced by lowering the energy of the incident particles or by using clusters instead of mono-atomic particle. In addition, the initial surface roughness of the specimen, as well as the development of surface topography under energetic particle bombardment, influences significantly the depth resolution achieved (Hofmann, 1998).

Conversely, for the glow-discharge based depth profiling techniques, since the particles contributing to the sputtering process are of very low energy, < 100 eV, the atomic mixing is limited. Additionally, the initial specimen roughness and the development of the surface morphology, which is mainly due to the structure of the specimen, affect dramatically the sputtering process and consequently the depth resolution during depth profiling analysis. Finally, for GDS techniques, the most significant factor limiting the depth resolution is the formation of a curved crater bottom.

Figure 4.10 compares the craters obtained by TOF-SIMS and GD-OES, showing the significant difference in shape associated with each technique. Thus, the areas of the craters associated with the TOF-SIMS and GD-OES techniques are about 300 x 300 μm^2 and 12 mm^2 respectively, making the glow discharge crater about 130 times larger than the crater obtained by TOF-SIMS. Additionally, while for GDS the analysis is

performed on the entire crater area, for TOF-SIMS the analysis is performed over an area concentric to the sputter crater of about 15 x 15 to 50 x 50 µm^2. Thus, in contrast to the TOF-SIMS technique, for GDS techniques the depth resolution is dramatically influenced by the shape of the crater.

Thus, even though the roughening of the analysed specimens plays a dominant role in depth profile analysis, the main parameter contributing to the degradation of the depth resolution during GDS depth profiling is often not the intrinsic nature of sputtering but the overall shape of the bottom of the crater. In addition to the continuous change in shape of the crater after each interface that induces a high mixing of the surface layers, further mixing results from the sputtering of re-deposited material located at the crater wall surrounding the crater (Escobar-Galindo et al., 2005a).

Depending on the operating conditions, the crater shape can evolve from flat to convex or concave. Thus, the gas pressure, the secondary emission yield and the anode-to-cathode distance influence mainly the crater shape (Jones, 1997; Nelis and Pallosi, 2006). A concave crater shape is obtained by operating the glow discharge source under low impedance conditions, i.e. high pressure and high secondary electron emission yield. Under these conditions, the glow discharge does not cover the entire cathode with the same density. Conversely, convex crater shape is obtained by operating at high impedance conditions, i.e. low pressure and low secondary emission yield (Nelis et al., 2006). The edge effect results from an increase of the sputtering rate caused by the perturbation of the electric field by the grounded anode tube.

Finally, optimisation of the flatness of the crater bottom allows a quasi-uniform sputtering, limiting simultaneous sputtering of the specimen at different depths and subsequent distortion of the elemental depth profile. However, optimum crater shape is rarely achieved during depth profiling due to the variations of the source parameters, namely gas flow and working distance.

4.4.3 Profile reconstruction

The depth resolution achieved during elemental depth profiling analysis, is mainly governed by the sputtering-induced compositional and topographical modifications of the specimen surface. Therefore, sputtering-induced depth profiles have to be

interpreted based on a model describing the sputtering-induced changes in the surface composition and morphology in order to reconstruct the original depth distribution from the measured profile.

Various procedures have been reported in the Literature for the interpretations of sputtering-induced elemental depth profiles. Atomistic computer simulations are increasingly used for interpretation of depth profiles. Thus, MD simulations have contributed to depth profile analysis and theory, by predicting collisional mixing behaviour and surface composition changes in ion-bombarded targets and to simulate the fluence-dependent sputtered particle yields during multilayer analyses (Karolewski, 2009). Thus, molecular dynamics involve reconstruction / simulation of elemental depth profiles using models derived from the physics associated with projectile / surface interactions; however, due the computational cost, simulations are limited to a few atomic mono-layers.

For SIMS, the development of altered surface layers due to preferential sputtering has been modelled by different approaches, for example, King reported an algorithm relying on the diffusion theory of atomic mixing using a depth dependent diffusion coefficient (King and Tsong, 1984) whereas Allen proposed a maximum entropy (MaxEnt) reconstruction method (Allen and Dowsett, 1994). Alternatively, Hofmann introduced the mixing-roughness-information (MRI) model, a fitting procedure of the so-called convolution integral (convolution of the original distribution and depth resolution functions) including the effects of atomic mixing, surface roughening, and the information depth associated with the analytical technique.

Provided that the basic conversions of intensity (I) to concentrations (X) and of sputtering time to sputtered depth (z) have already been done, a simple mathematical description of the action of sputter depth profiling on the original in depth distribution of composition, is possible by the so-called convolution integral (Hofmann, 1998):

$$I(z)/I(0) = \int_{-\infty}^{+\infty} X(z').g(z-z')dz' \tag{4.5}$$

Thus, the convolution integral represents the measured and normalized intensity at the sputtered depth z, I(z)/I(0), as a function of the original in depth distribution of

composition, $X(z')$ by action of the depth resolution function (DRF), $g(z-z')$.

Deconvolution of the measured profile involves the resolution of Equation 4.5 for $X(z')$, for example by inverse Fourier transformation schemes if $g(z-z')$ and $I(z)/I(0)$ are known. However, since inverse Fourier transform resolution may lead to different solutions, forward calculations of the convolution integral have been applied, i.e. assuming a suitable $X(z')$ and comparing the calculated profile with the measured profile $I(z)/I(0)$. By changing the input $X(z')$ until an optimum fit is obtained, the original in-depth elemental distribution is finally reconstructed.

The MRI model provides a mathematical description of the DRF $g(z-z')$ that is the convolution of three partial DRF based on the three fundamental contributions, namely atomic mixing g_ω, surface roughness g_σ and information depth g_λ. These contributions are given by physically well-defined parameters. The information depth parameter is given by the secondary ion escape depth in SIMS and is about 1 - 2 monolayers. The atomic mixing parameter is based on a simple mixing model which assumes that mixing is instantaneous and extends to a depth w. The roughness parameter consists of three contributions:

- The original interface roughness.
- The sputtering induced surface roughness.
- The straggling of the mixing length.

The dependencies with depth of the atomic mixing and the information depth are described by exponential functions with characteristic mixing zone length, ω, and length, λ respectively:

$$g_\omega = \frac{1}{\omega}\, exp\left[\frac{-z(z-z'+\omega)}{\omega}\right] \tag{4.6}$$

$$g_\sigma = \frac{1}{\sqrt{2\pi\sigma}}\, exp\left[\frac{-(z-z')^2}{2\sigma^2}\right] \tag{4.7}$$

The roughness is best represented by a Gaussian function of standard deviation σ, which corresponds to the roughness of the surface, S_q.

$$g_\lambda = \frac{1}{\lambda}\, exp\left[\frac{-z(z-z')}{\lambda}\right] \tag{4.8}$$

The mixing length can be estimated by the TRIM code (Ziegler, 2010) and can be measured using angle resolved XPS. The surface roughness after profiling can be measured by atomic force microscopy and original interface roughness by grazing incidence X-ray reflectivity.

Based on these three physical parameters, that can be measured, the MRI model allows a mathematical extraction of the DRF that can in turn be applied to fit a measured profile by solving the convolution integral.

The MRI model has been applied for the reconstruction of SIMS and AES elemental depth profiles of AlAs-delta doped GaAs, B-delta doped Si and As doped Si; however, simulations of GD-OES have been shown to be limited mainly due to the characteristic of the DRF which does not present a Gaussian distribution as a result of the development of a very particular crater shape (Quentmeier, 1994).

Finally, reconstruction of elemental depth profiles measured by sputtering-induced depth profile technique, despite being essential is not straightforward, especially for glow discharge spectrometry for which there are no simulation codes available that take into account the influence of the crater geometry. Thus, the use of complementary techniques, e.g. transmission electron microscopy, is a reasonable alternative to ascertain the in-depth composition of the specimens of interest.

The growth of barrier-type anodic oxide films formed anodically on patterned superpure aluminium substrates have been investigated following the development of the distributions of a boron marker and chromium and phosphorus tracers. Superpure aluminium substrates have been patterned either by electropolishing or by anodizing in sulphuric acid, oxalic acid, phosphoric acid and stripping of the porous films in a chromic / phosphoric acid solution. Characterisation of the resulting topography of the differently patterned superpure aluminium substrates as well as the incorporation of the chromium and phosphorus species have been undertaken. Then, The in-depth compositions of the anodic oxide films were determined using sputtering-induced elemental depth profiling techniques, namely SIMS, GD-OES and GD-TOF-MS. In addition, the locations of the marker and tracers were probed using scanning transmission electron microscopy, thereby allowing direct comparison with the elemental depth profiling techniques.

Finally, the sputtering mechanisms arising during depth profiling analysis were studied in order to certify the results.

Figures

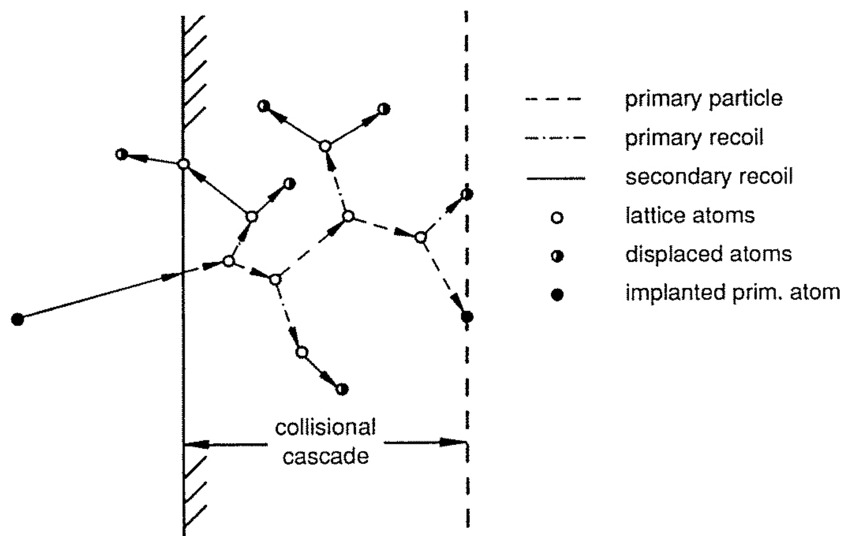

Figure 4.1 – Schematic of collisional cascade events (Hofmann, 1998).

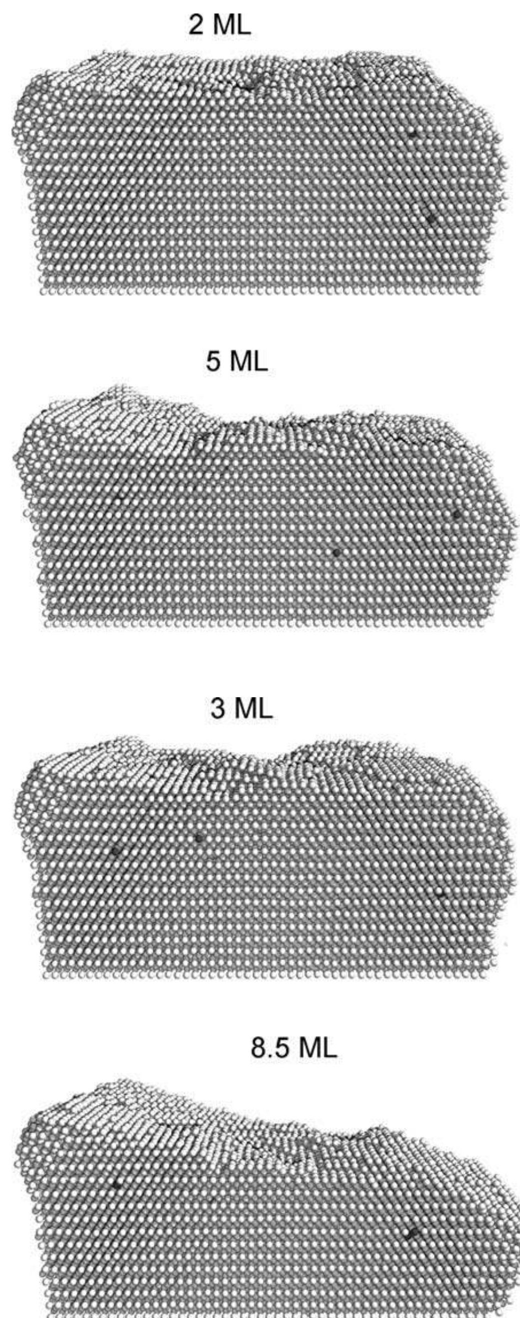

Figure 4.2 – Cross-sectional views of one-half of the static Cu (100) target for sputter depths z = 2, 3, 5 and 8.5 ML. The projectile species (3 keV Ar) are incident from the left side of the target. Black spheres visible in the plane of bisection of the target represent embedded projectiles (Karolewski, 2009).

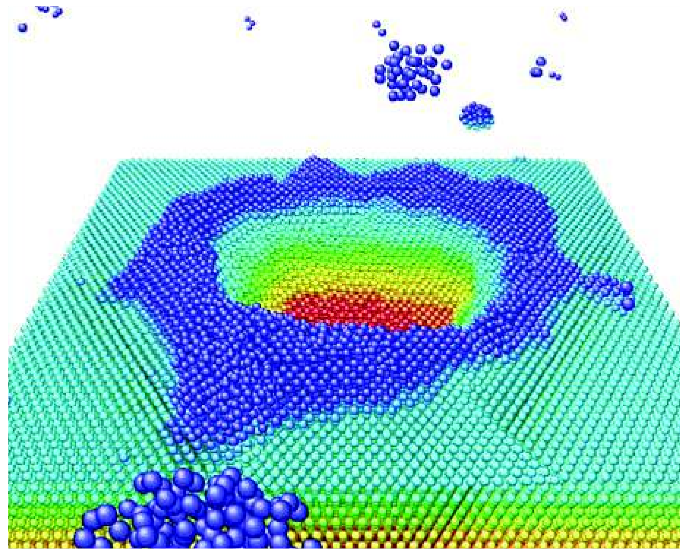

Figure 4.3 – Perspective view of the crater formed in a Au (111) crystal, 40 ps after bombardment with a 64 keV Au_4 cluster. Colours denote height above the surface (Urbassek, 2007).

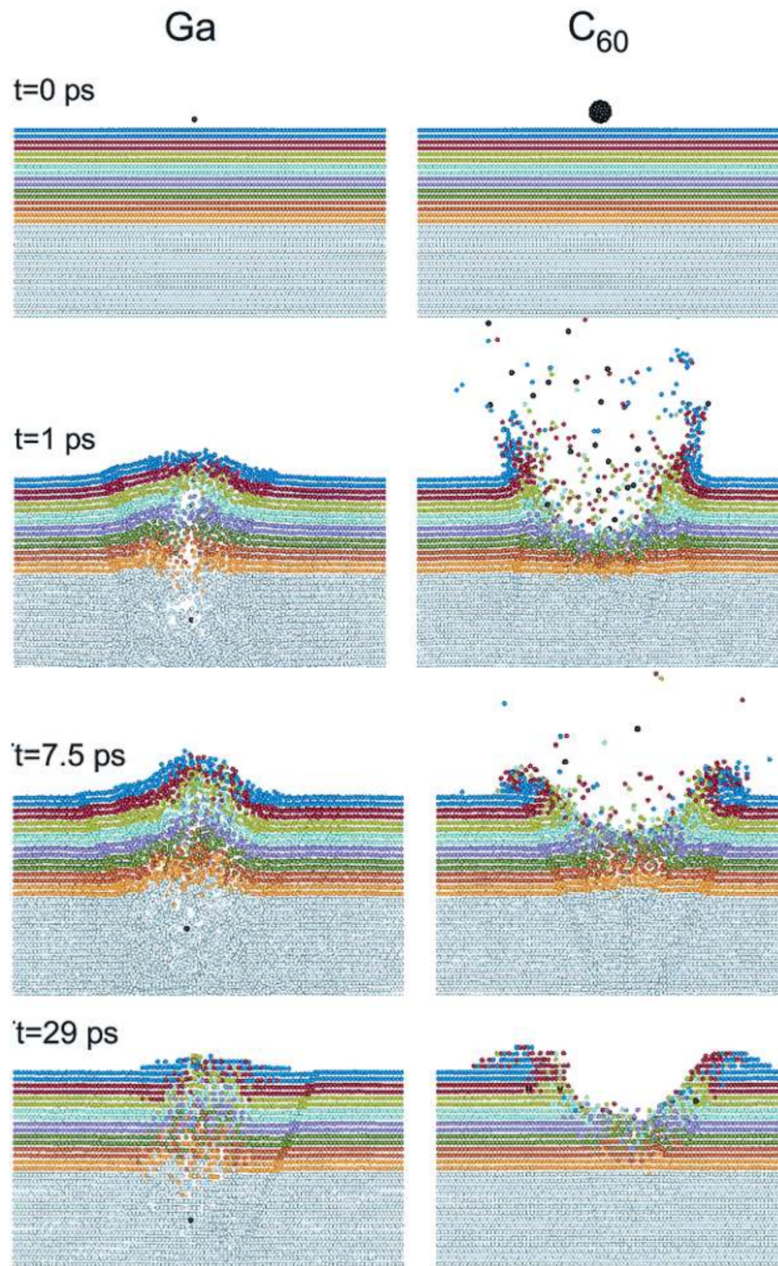

Figure 4.4 – Cross-sectional view of the temporal evolution of a typical collision event leading to ejection of atoms due to 15 keV Ga and C_{60} ion bombardment of a Ag (111) surface at normal incidence (Postawa et al., 2004).

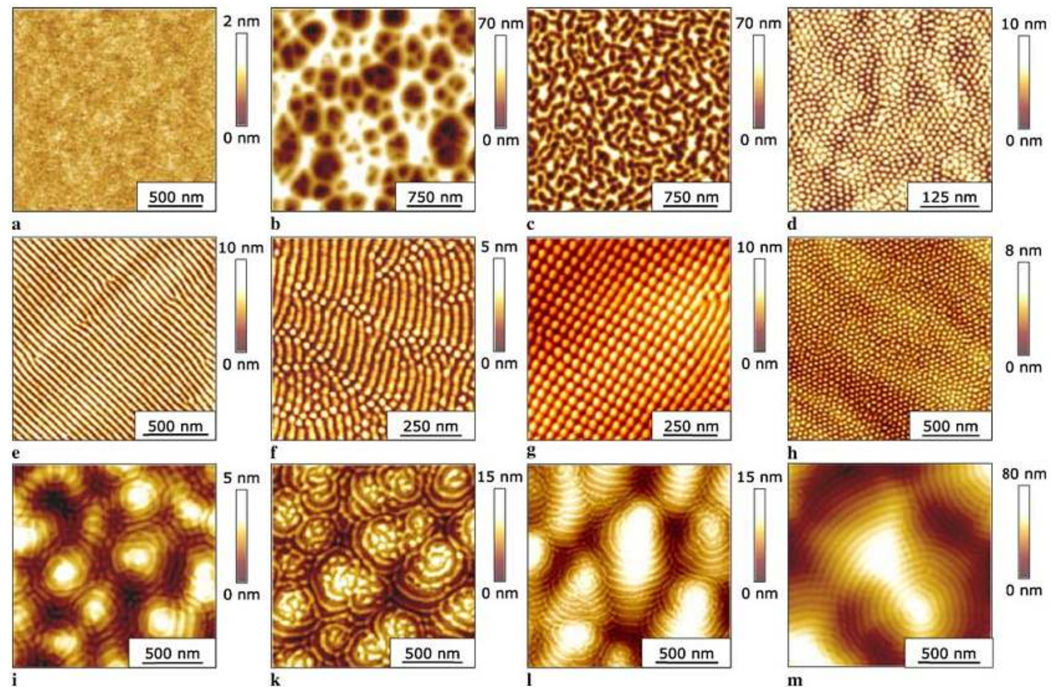

Figure 4.5 – Example of diversity of pattern formation on Si (a, b, d-g, i, m) and Ge (c, h, k, l) surfaces by low-energy ion-beam erosion. Beginning with top left, the following surface topographies measured by AFM are shown: (a) ultra-smooth surface, (b, c) meshworks of randomly arranged troughs, (d) domains of hexagonally ordered dots, (e) highly ordered ripple pattern, (f) coexistence of dots and ripples, (g) long range square ordered dots on Si, (h) long range hexagonally ordered dots, (i, k, l, m) curved ripples. The individual patterns are formed under various erosion conditions (ion energy between 500 eV and 2000 eV; ion species used Ar^+, Kr^+, Xe^+; ion incidence angle between 0° and 75° with respect to the surface normal, partly with simultaneous sample rotation). All experiments were performed keeping the samples at room temperature (Frost et al., 2008).

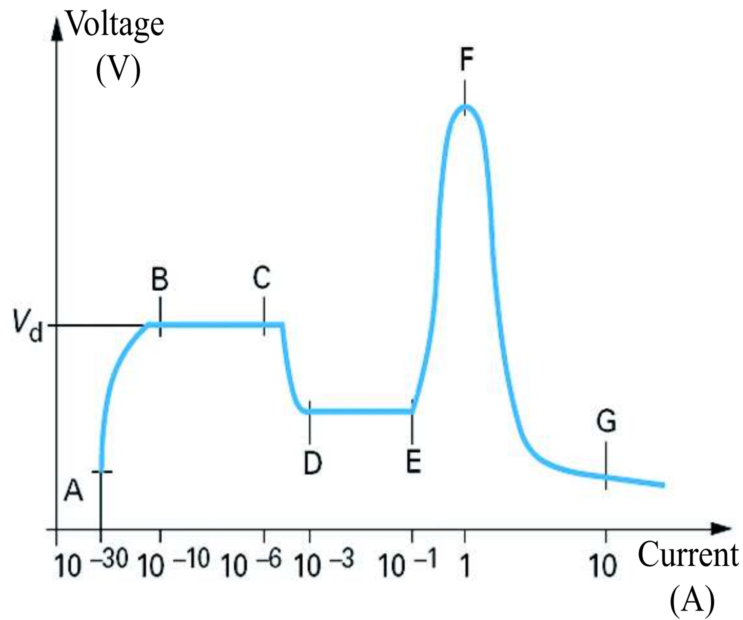

(a)

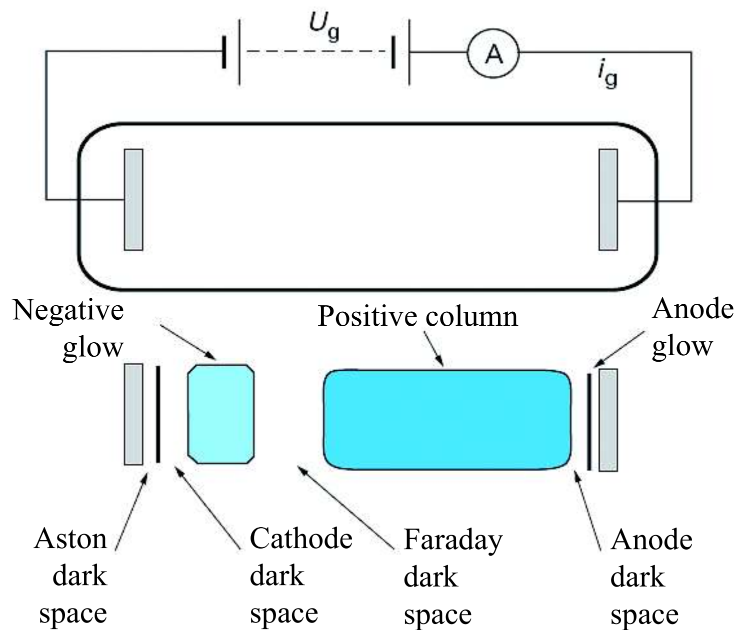

(b)

Figure 4.6 – a. Voltage distribution and discharge characteristics of a dc glow discharge with (A-C) the Towsend regime, (C) the break-down voltage, (D-E) the normal glow, (E-F) abnormal glow and after the glow-to-arc transition (F-G) non-thermal regime, and b. Luminous regions in a dc glow discharge (Laude and Chapon, 2005).

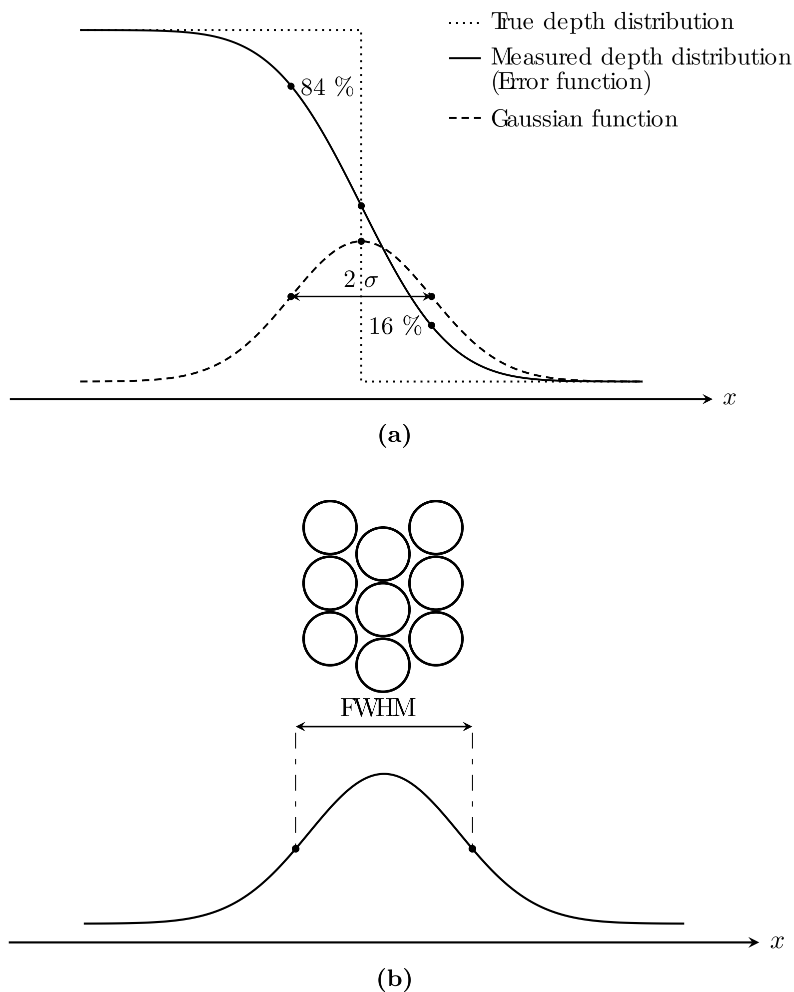

Figure 4.7 – Schematic diagram of the profile distortion of a. a step-like interface and b. a delta layer.

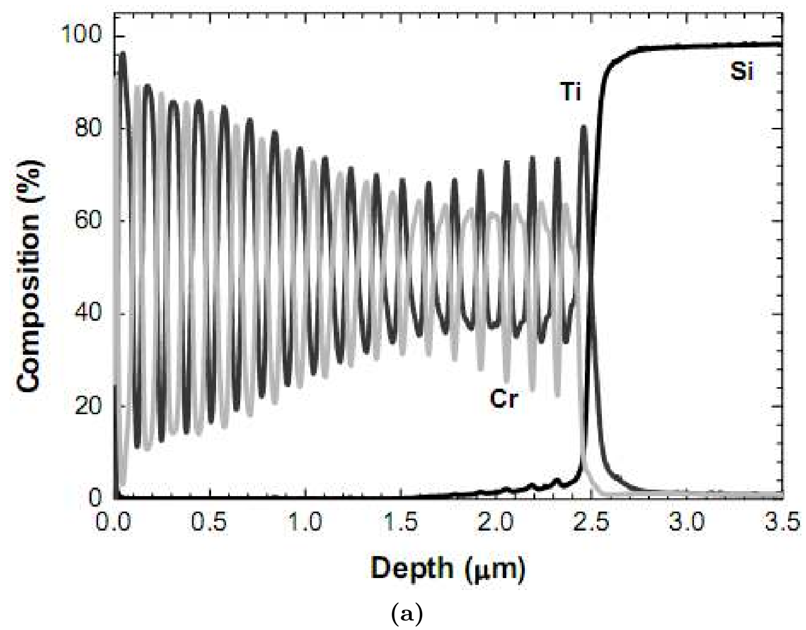

(a)

Figure 4.8 – GD-OES depth quantified profile of a 20 multi-layer coating on silicon. The multi-layers comprise alternating layer of chromium (55 nm) and titanium (70 nm). The dashed lines follow the variation of the metal peak intensities with depth (Escobar-Galindo et al., 2005b).

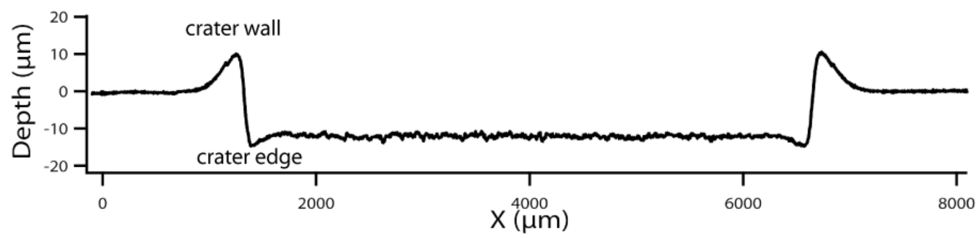

Figure 4.9 – Crater shape obtained after GD-OES depth profiling of a superpure aluminium specimen, showing the relatively flat bottom of the crater as well as the crater edge and wall inherent to the technique.

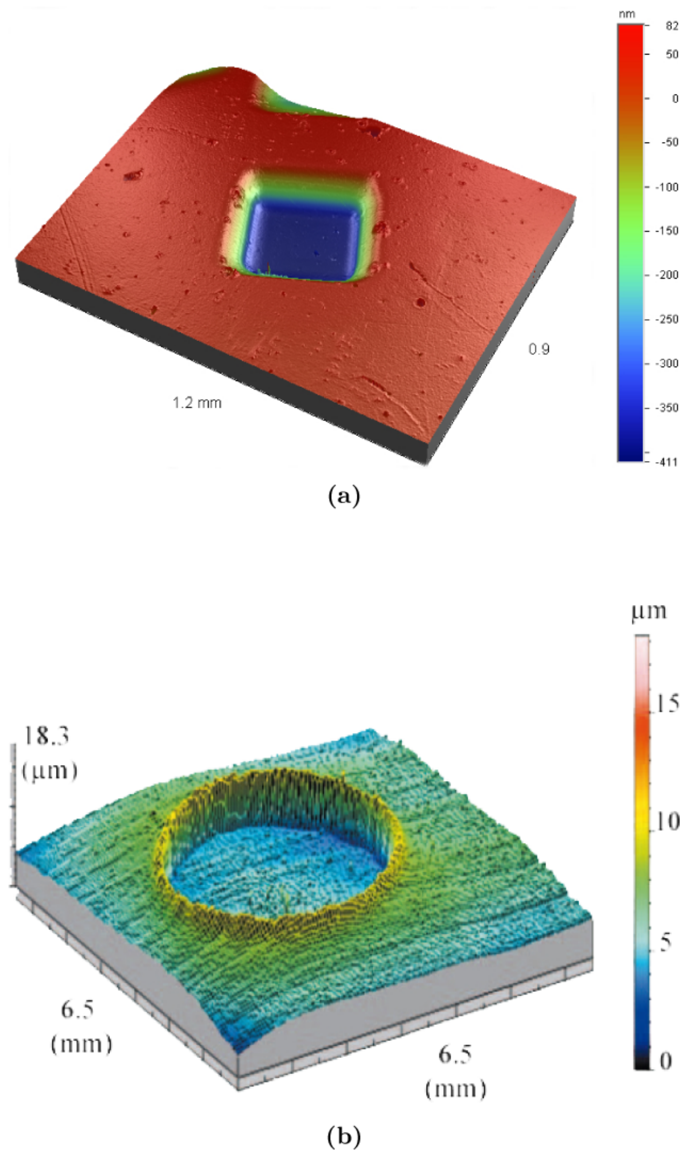

Figure 4.10 – White-light interferometry images of craters resulting from a. TOF-SIMS (Starke, 2003) and b. GD-OES (Laude and Chapon, 2005) depth profiling analyses.

5 Introduction to the Present Work

Examination of the growth mechanism proceeding during the development of barrier-type aluminium oxide films formed by anodizing of superpure aluminium substrates of controlled pattern has been undertaken by the study of the distributions of boron, chromium and phosphorus species incorporated with the alumina layers. To date, few investigations have been performed on the influence of the substrate roughness on the formation mechanism of barrier-type anodic alumina. In addition, those studies have relied exclusively on the topographic development of the oxide surface and metal / oxide interface during the anodizing process.

The preparation of superpure aluminium substrates of controlled patterns has been undertaken by electropolishing and anodizing in sulphuric acid, oxalic acid, phosphoric acid and by stripping of the porous films in a chromic / phosphoric acid solution. Each treatment results in the development of patterns of different dimensions. The topographies of the differently patterned superpure aluminium substrates have been characterised by atomic force microscopy and transmission electron microscopy. In addition to the characterisation of the substrate topographies, investigation on the incorporation of chromium and phosphorus species are treated in the first Section entitled “Aluminium Substrates of Controlled Patterns” of the Results and Discussion Chapter.

The second Section entitled “Anodizing of Patterned Substrates” deals with the growth of alumina layers formed by anodizing of differently patterned superpure aluminium substrates in 0.1 M ammonium pentaborate solution. Examination of the smoothing of the oxide surfaces and metal / oxide interfaces has been carried out by transmission electron microscopy. In addition, the incorporation of boron species from the electrolyte

and the migration of chromium and phosphorus species within the anodic alumina layers are investigated by scanning transmission electron microscopy and sputtering-induced elemental depth profiling techniques.

The third Section entitled "Depth Profiling Analyses of Patterned Specimens" is dedicated to the development of surface topographies associated with sputtering-induced elemental depth profiling analyses. The topographical modifications reveal the limitations of the different depth profiling techniques for the analysis of patterned specimens.

Finally, the growth mechanisms involved during barrier-type anodic aluminium oxide layers are discussed in the last Section. The study takes into consideration the different data obtained, concerning the smoothing of the specimens as well as the changes in the distributions of the incorporated species.

Experimental Procedure

1 Specimens of Controlled Roughnesses

The formation of barrier-type anodic alumina film on relatively rough surfaces was investigated. Aluminium substrates showing regular patterns were required for the characterisation of the anodic oxide growth mechanism. Thus, specimens of tailored roughnesses were prepared by formation of porous anodic aluminium oxide layers grown anodically with different cell dimensions. The growth of porous- and barrier-type anodic oxide films have been shown to be reproducible processes, with the properties of the anodic film being associated with the anodizing conditions. The generation of anodic aluminium oxide films formed on differently patterned superpure aluminium substrates required four successive treatments, which are described in this section.

1.1 Material and Surface Cleaning

Anodic oxide films of controlled roughnesses were prepared using superpure aluminium sheet (99.99 wt% Al, impurities Fe, 8 ppm; Si, 8 ppm; Cu, 50 ppm). Specimens were cut to dimensions of 19 x 90 mm prior to the sequence of treatments.

The superpure aluminium specimens were degreased with acetone using an ultrasonic bath and rinsed in ethanol prior to electropolishing. The main function of the cleaning stage is to provide a chemically clean aluminium surface (free of grease and oil, or corrosion products) so that subsequent treatments proceed uniformly over the macroscopic surface (Chalk, 2002). Traditionally, the first step employed is vapour degreasing using chlorofluorocarbons such as 1, 1, 1-trichloroethane; however, due to restrictions on ozone-depleting compounds, many of these degreasing solvents are no longer in wide use. Consequently, a combination of ultrasonic and immersion cleaning technologies have been used as alternatives to vapour degreasing, to remove contaminants with similar effectiveness (Chalk, 2002).

1.2 Surface Treatments

1.2.1 Electropolishing

Electropolishing allows dissolution of the metal surface by anodic electrochemical polarisation. Electropolishing treatment is mainly used to remove defects or to reduce surface roughnesses. During electropolishing of superpure (99.99 %) aluminium foil at various voltages in an acidic electrolyte, relatively ordered patterns may be obtained, namely hexagonal patterns, highly regular or randomly packed nano-scale furrows and mixed patterns depending on the grain orientation (Yuzhakov et al., 1997).

The superpure aluminium specimens were electropolished at a constant voltage of 20 V in a perchloric acid - ethanol (20 - 80 %vol.) bath at temperatures below 7°C for 3 min. The backface of the specimen was coated with a lacquer layer (Lacquer 45); the front face, of defined area, was then exposed to the electropolishing solution. The specimens were rinsed thoroughly with ethanol, then with deionised water and, finally, dried in a cold air stream.

1.2.2 Growth of ordered cell array anodic alumina films

The growth of a porous anodic alumina films leads to texturing of the aluminium surface through development of the hexagonal alumina cells that penetrate the substrate in a hemispherical manner (Thompson, 1997). The surface roughness of the metal is determined by the alumina cell array pattern generated by anodizing. Thus, control of the roughness requires production of porous aluminium oxide layers displaying arrangements of highly-ordered cells in order to obtain patterned metal surfaces with well defined topography.

Ordering of the cell arrangement has been shown to be dependent on the applied voltage in the electrolyte employed. Thus, the production of porous alumina of highly-ordered cell morphology can be achieved by anodizing of aluminium substrates under appropriate conditions (electrolyte nature and concentration, anodizing voltage, temperature...). Additionally, Masuda reported that a long period of anodizing and two-step anodizing improve the regularity of the cell arrangement, increasing the defect-free domains, and producing an almost ideally honeycomb morphology in sulphuric acid, oxalic acid and phosphorus acid solutions, (Hideki Masuda and Osaka, 1998; Masuda

and Fukuda, 1995; Masuda et al., 1997) respectively.

The most appropriate voltages for the ordering of the cell arrangements in 0.3 M sulphuric acid, 0.3 M oxalic acid and 1.2 M phosphoric acid, maintained at temperatures below 0°C, were reported by Masuda to be 25 - 27 V, 40 V and 195 V, (Hideki Masuda and Osaka, 1998; Masuda and Fukuda, 1995; Masuda et al., 1997). Jessensky and Li investigated cell arrangements during anodizing of aluminium in sulphuric acid and oxalic acid solutions (Jessensky et al., 1998), and sulphuric acid, oxalic acid and phosphoric acid solutions (Li et al., 1998) respectively. Optimal results were obtained with conditions corresponding to the oxidation parameters recommended by Masuda for sulphuric and oxalic acids; further, Li reported a highly-ordered cell arrangement in a 1.2 M phosphoric acid solution at an applied voltage of 160 V.

In order to grow porous anodic alumina layers of different controlled cell dimensions, individual specimens were anodized in one of three different acids (sulphuric, oxalic, phosphoric acids) as forming electrolyte. The voltages reported by Masuda were used for anodizing in sulphuric acid and oxalic acid, whereas anodizing in phosphoric acid was performed at 120 V, following the procedure presented elsewhere (Shimizu et al., 1999e). The main reasons for carrying out anodizing in phosphoric acid with a voltage lower than the setting recommended by Masuda were the difficulty for anodizing at 195 V at room temperature and the extensive anodizing time required to develop an ordered cell structure when anodizing was performed at temperatures kept below 0°C. Thus, the electropolished specimens were anodized for 5 min at room temperature at constant voltages of 25 V, 40 V and 120 V in 0.3 M sulphuric, oxalic and phosphoric acid solutions respectively.

1.2.3 Stripping of the porous anodic alumina films

Three main methods may be used to strip anodic aluminium oxide coatings from the substrates, with varying degrees of controllability (Pernick, 2002). Controllability determines the ability of the process to remove the anodic oxide without affecting the aluminium substrate. The three methods are listed as follows:

- Caustic etching by immersion in a warm NaOH solution. In addition to oxide removal, this process dissolves aluminium at a relatively high rate.

- Use of deoxidizers: immersion in a mixed H_2SO_4-CrO_3 solution. As for caustic etching, the sulphuric / chromic acids mixture dissolves aluminium metal.
- Stripping in a CrO_3-H_3PO_4 solution at a minimum temperature of 95°C. This is the most controllable method, with the oxide film dissolve preferentially while the aluminium substrate undergoes very limited damage.

The different specimens were immersed in a 20 g.l^{-1} CrO_3 - 35 m.l^{-1} H_3PO_4 solution at 95°C. The layer of lacquer present on the back-face of the specimens was removed before stripping and, after stripping, a new layer of lacquer was applied in order to define the exposed surface of the specimens to be anodized in ammonium pentaborate. Thus, a chromic / phosphoric acid solution was used in order to either strip the air-formed film developed over the electropolished aluminium surfaces or to dissolve the porous anodic alumina layers, thereby revealing the pattern of aluminium surface through development of the hexagonal alumina cells that penetrate the substrate in a hemispherical manner.

Additionally, the stripping solution, by reaction with aluminium, develops a thin oxide layer over the surface which contains chromium and phosphorus species (Lewis and Plumb, 1956). Both chromium- and phosphorus-enriched layers were used as tracers for the determination of migration mechanism of aluminium and oxygen species respectively during formation of barrier-type alumina on differently patterned superpure aluminium substrates.

1.2.4 Growth of barrier-type anodic alumina films

Finally, in order to form barrier-type anodic aluminium oxide films, the differently patterned substrates were anodized in an ammonium pentaborate solution at room temperature. Anodizing in 0.1 M ammonium pentaborate was performed at 5 mA cm^{-2} to 10, 25, 50, 100, 200, 225, 250, 275 and 300 V.

2 Characterisation

The basic principles of the various techniques utilized for the characterisation of the different specimens are presented in this section. The techniques have been separated into two categories, namely microscopy and elemental depth profiling techniques. The different microscopy techniques were used for the examination of the topography and morphology of the specimens at the different stages of their generation and for the characterisation of the glow-discharge sputtering-induced topographical modifications. In contrast, incorporation and migration of electrolyte-derived species have been investigated using elemental depth profiling analyses.

2.1 Topography and Morphology

2.1.1 Atomic force microscopy

Atomic force microscopy (AFM) is a very high-resolution derivative of scanning probe microscopy, that is able to examine the topography of insulating and conducting samples down to the atomic scale under ambient conditions, e.g. ambient air, liquids. In atomic force microscopy, a specimen surface is scanned using a silicon or silicon nitride tip mounted on a flexible cantilever; the specimen surface can then be reconstructed from the deflection of the cantilever due to forces arising between the tip and the specimen surface roughness (Godehardt et al., 2004).

The atomic force microscope can be operated in various modes depending, on the applications. Three different modes are available for imaging, namely the contact mode, the tapping mode and the non-contact mode. The advantages of the tapping mode in comparison with the contact mode are the elimination of a large part of the permanent shearing forces and decrease of damage to the specimen surface. The tapping mode

has been used to examine specimens and, consequently, is described here.

Atomic force microscopy, operated in the tapping mode (TM-AFM), has emerged as an important analytical tool for characterization of the topography and the properties of materials. In the TM-AFM, a cantilever equipped with the probing tip, is driven to oscillate near its resonance frequency ω_0, at a given amplitude a_0, i.e. free oscillation. The cantilever is then brought close to the specimen and made to probe the surface with a given reduced set-point amplitude a_{sp}. An electronic-feedback loop ensures that the oscillation amplitude remains constant in order to maintain a constant probe / specimen distance during scanning. The vertical displacements of the piezoelectric cantilever, required to keep the amplitude constant, are displayed as a height image. The probe-specimen interaction also involves a shift in the frequency and phase in the cantilever oscillations, with respect to that of the free oscillation; the variations of the phase are presented as a phase image.

The variations in the amplitude, frequency and phase in the cantilever oscillations are sensitive measures of the forces acting on the probe. Height images reflect the specimen topography, while phase images display variation of adhesive and mechanical properties associated with different components, thereby allowing compositional analysis. However, the contrast of height and phase images strongly depends on experimental conditions. Factors significantly affecting height and phase images in TM-AFM include the cantilever force constant, the tip shape, the amplitude a_0 of free vibration, and the set-point amplitude ratio, $rsp = a_0/a_{sp}$.

Specimens roughnesses were analysed by atomic force microscopy (AFM) in the tapping mode, using a Dimension 3100 microscope controlled by a NanoScope IIIa scanning probe microscope controller (Digital Instruments - Veeco Metrology). Data were analysed using MountainsMap software (Digital Surf). A Gaussian filter was used to separate the waviness and the roughness in the surface measurement, allowing thus more accurate determination of the roughness values, Sq. Additionally, symmetry of the surface texture and the presence of defects in the texture were expressed by the Ssk and Sku parameters. Ssk represents the degree of symmetry of the height about the mean value, and gives the preponderance of peaks ($Ssk > 0$) or valleys ($Ssk < 0$) in the surface texture. Sku indicates the presence ($Sku > 3$) or the lack ($Sku < 3$) of

excessively high peaks or deep valley in the texture. Textures can be compared with a surface with heights normally distributed (bell curve), which shows respective Ssk and Sku values equal to 0 and 3. The different parameters usually used to describe specimen roughness are presented in Table 2.1.

Finally, 3D surface motif analysis was performed on the specimens patterned by anodizing in sulphuric acid, oxalic acid, phosphoric acid and subsequent stripping of the porous films, using the segmentation method in order to differentiate and characterise cell array patterns of the surfaces.

2.1.2 Scanning electron microscopy

Scanning electron microscopy is an analytical technique for imaging of specimen surfaces. Images of specimens are obtained by scanning the specimen surfaces with a focused electron beam in a raster pattern. Different type of electrons and electromagnetic radiations are generated as a result of scattering events between the incident electrons and the specimen, namely, secondary electrons (SE), backscattered electrons (BSE), Auger electrons, phonons, and cathodoluminescence photons, characteristic X-rays, continuum X-rays, secondary fluorescence by characteristic and continuum X-rays, respectively (Egerton, 2005).

During scanning electron imaging, information associated with secondary electron and backscattered electron emissions are principally collected.

Secondary electrons are mostly used to resolve topographical information. The shallow escape depth for secondary electrons, generated from primary electrons, combined with the orientation dependence of the secondary-electron yield, result in local variations in the secondary electron intensity, associated with raised or recessed features of the specimen surface, thereby creating an image contrast that reveals the surface morphology.

During inelastic-scattering events arising between incident electrons and atomic electrons of the specimen, outer-shell (valence or conduction) electrons can gain energy from primary electrons. Such energy transfer may result in the emission of secondary electrons from the specimen surface. Escaping from the surface, secondary electrons

gradually lose their kinetic energy by inelastically scattering. Indeed, the probability of inelastic scattering increases with decreasing electron energy, thereby limiting the distance that secondary electrons can travel within solids to about 1 - 2 nm, known as the escape depth.

The average number of secondary electron produced per primary electron is called the secondary-electron yield and is typically in the range 0.1 to 10. For a given specimen material, the secondary-electron yield decreases with increasing energy of the incident electrons since the probability of inelastic scattering of a primary electron within the escape depth decreases. The secondary-electron yield also depends on the angle between the incident primary electron and the specimen surface, θ, varying as $1/cos\theta$. Consequently, the secondary-electron yield is at a minimum for normal incidence and increases with increasing angle between the primary beam and the normal to the surface.

The acceleration voltage determines the kinetic energy, E_0, of primary electrons and, therefore, their penetration depth and the information depth in the backscattered electron image. Since secondary electrons are generated within a narrow escape depth, the secondary electron image might be expected to be independent of the choice of E_0. However, the secondary electron signal is comprised of different components, namely SE1, SE2 and SE3. From the different secondary electron components, only SE1, comes from secondary electrons generated, near the surface, by primary electrons. The components SE2 and SE3 result from the generation of secondary electrons by backscattered electrons as they escape the specimen and when backscattered electrons strike the microscope chamber respectively. As a result of the SE2 component contribution, secondary electron images may show contrast from features present below the surface if the features result in a change in backscattering coefficient.

Backscattered electron images provide image contrast associated with elemental composition, crystal orientation and surface topography. Backscattered electrons are produced by deflection of primary electrons as a result of a single or several elastic collisions with atomic nuclei of the specimen.

Elastic scattering involves negligible energy loss and, as a result, most backscattered

electrons escape from the specimen with energies close to the primary electron energy. The backscattering coefficient, the fraction of primary electrons which escape as backscattered electrons, is proportional to the square of the specimen element atomic number, Z^2, which results in an image contrast associated with the specimen composition, i.e. higher atomic number elements appear brighter than low atomic number elements in backscattered electron images. Further, since backscattered electrons can escape from increased depths compared with secondary electrons, up to one-half the penetration depth, surface topography is not as accurately resolved as for secondary electron imaging.

Finally, the lateral resolution in a scanning electron microscope depends principally on three factors:

- The probe diameter at the specimen surface, i.e. the smaller the probe the better the resolution.
- The probe current; high probe currents coupled to a small probe diameter give a higher signal to noise ratio.
- The depth of penetration of the primary electron beam into the specimen surface; the deeper the penetration, the larger the interaction volume and the greater the tendency to degrade resolution, therefore requiring ultra-low acceleration voltage.

Specimen morphologies were examined by scanning electron microscopy using an ULTRA 55 FESEM (Zeiss), operated at an acceleration voltage of 1.5 kV and a working distance of 2 - 3 mm. Images of the specimens were acquired using the In-Lens SE detector, the lateral SE detector and the Energy and angle selective Backscattered (EsB) detector.

The detection and differentiation of the secondary electrons and backscattered electrons are performed by the different detectors as a function of the energy and take-off angle distributions of the electrons emitted from the surface (Jaksch, 1996).

Secondary electrons generated by primary electrons are attracted by the electrostatic lens and are focused on the annular In-lens SE detector. The In-lens SE detector provides high contrast images from secondary electrons of the narrowest escape depth and of the lowest energies, thereby allowing the use of ultra-low voltages, $\sim$ kV. Additionally, a lateral SE detector in the specimen chamber collects a mixture of

SE1, SE2, SE3 and backscattered electrons which provides depth and topographical information. Signals from both detectors may be mixed to combined surface and compositional information.

The EsB detector discriminates backscattered electrons according to their energy and take-off angle distributions, resulting in a detection efficiency of about 85 % of the high angle backscattered electrons. Additionally, potential secondary electrons are filtered from the backscattered electrons, in order to suppress undesirable surface information from the compositional signal.

2.1.3 Transmission electron microscopy

In a transmission electron microscope (TEM), accelerated electrons gaining sufficient energy, i.e. a sufficiently short wavelength, penetrate a thin specimen and are then imaged by appropriate lenses. Provided that the specimen is suitably thin, essentially all of the incoming electrons are transmitted through the specimen. The electrons, although not absorbed, are scattered by the atoms of the specimen. The formation of transmission electron images is related to the nature of the scattering processes.

Most transmission electron micrographs are viewed and recorded with an objective aperture (diameter D) inserted and centred about the optic axis of the microscope objective lens (focal length f). This aperture absorbs electrons that are scattered through an angle greater than $D \approx 0.5\ D\ /\ f$. In addition, any part of the field of view that does not contain material is formed from electrons that remain unscattered, so that part appears bright relative to the specimen. As a result, this central-aperture image is referred to as a bright-field image.

The main purpose of the objective-aperture is to provide scattering contrast in the transmission electron micrograph of a specimen whose composition or thickness varies between different regions. Thicker regions of the specimen scatter a larger fraction of the incident electrons, many of which are absorbed by the objective diaphragm, so that the corresponding regions in the image appear dark, giving rise to thickness contrast in the image. Regions of higher atomic number also appear dark relative to their surroundings, due mainly to an increase in the amount of elastic scattering, giving atomic-number contrast (Z-contrast). Further, for polycrystalline materials, the yield and angular

distributions of scattered electrons are associated with the orientation of the atomic rows and columns of the material relative to the incident electron beam, as a result a diffraction contrast rises from differences in diffracting conditions between different regions of the specimen. Thus, mass-thickness contrast and diffraction contrast provide the information content of bright-field TEM images (Williams and Carter, 2009).

Additionally, various analysis modes are provided by transmission electron microscopy, namely dark-field imaging (contribution of the diffracted beam of electrons to form the image), electron-diffraction, phase-contrast imaging, STEM.
Specimen morphologies were studied by transmission electron microscopy of ultramicrotomed sections of the differently patterned superpure aluminium substrates and of the alumina layers formed anodically in ammonium pentaborate to various voltages, using a JEM 2000 FX II (JEOL). The specimens were observed in the bright-field mode of the transmission electron microscope, which was operated at an acceleration voltage of 120 kV.

In addition, cross-sections of the specimens anodized in ammonium pentaborate were examined by scanning transmission electron microscopy (STEM) using the STEM detector in the Ultra 55 FESEM (Zeiss). The scanning transmission electron microscopy observations were carried out using an acceleration voltage of 20 kV.

The specimen cross-sections were prepared using an Ultracut UCT ultramicrotome (Leica) and a Microstar diamond knife; the nominal thickness was selected at 5 nm.

2.2 Elemental Depth Profiles

The basic principles and the main characteristics of the different elemental depth profiling techniques utilized for elemental depth profiling analyses of the various specimens are presented in this section, a summary of the figures of merit associated with the different techniques are displayed in Table 2.2.

2.2.1 X-ray photoelectron spectroscopy

X-ray photoelectron spectroscopy (XPS) is an analytical technique used to investigate the chemical composition of surfaces. X-ray photoelectron spectroscopy is based on the detection of electrons created by photoelectric process (Alford et al., 2007).

The photoelectric effect consists in the absorption of a quantum of energy $h\nu$ by a core electron and the ejection of an electron, the photoelectron, of kinetic energy related to the binding energy of the core electron in an atom of the target. Thus, in this process, incident photons transfer entirely their energy to the core electrons, and element identification is accomplished by the measurement of the characteristic energies of the photoelectrons that escape from the specimen, provided they have not undergone any energy loss. The probability for the electrons to emerge from the surface without energy loss is related to the inelastic mean-free-path, which is in turn a function of the kinetic energy of the ejected photoelectrons. The equation of energy conservation can be expressed as follows:

$$E_B^V(k) = h\nu - E_{kin} \tag{2.1}$$

where:

- $h\nu$ is the energy of the monoenergetic photons.
- E_{kin} is the kinetic energy of the photoelectron.
- $E_B^V(k)$ is the binding energy of an electron in the kth level referred to the vacuum level of the specimen.

For conductive specimens electrically connected to the spectrometer, a thermodynamic equilibrium is reached between the specimen and the spectrometer and their Fermi levels equalise. Passing from the specimen surface into the spectrometer, the photoelectron undergoes an acceleration or a deceleration due to the difference of potential between the spectrometer and the specimen. This potential equals the

difference between the work functions of the spectrometer and the specimen, ϕ_{spec} and ϕ_s respectively, which represent the difference in energy between their common Fermi level and their respective vacuum level, Fig. 2.1. The equation of energy conservation becomes:

$$E_B^F(k) = E_B^V(k) - \phi_s = h\nu - (E_{kin} + \phi_s) \tag{2.2}$$

with the binding energy of an electron in the k$^{\text{th}}$ level referred to the Fermi level of the specimen, $E_B^F(k)$.

The kinetic energy of a photoelectron, measured by the spectrometer, E'_{kin}, is then referenced to the vacuum level of the spectrometer, such as:

$$E'_{kin} = E_{kin} - (\phi_{spec} + \phi_s) \tag{2.3}$$

Finally, the binding energy of an electron in a metallic specimen may be determined relative to the common Fermi level of the spectrometer and the specimen, as follows:

$$E_B^F(k) = h\nu - E'_{kin} - \phi_{spec} \tag{2.4}$$

The calibration of the spectrometer in term of kinetic energy, requires the determination of the work function of the spectrometer, which is achieved by the measure of the Fermi level of reference specimens such as copper, silver and gold.

For the analysis of insulating materials, cautions should be considered regarding the referencing of binding energies. Indeed, if the electric contact between the specimen and spectrometer is not achieved perfectly, then, the Fermi levels of the spectrometer and the specimen do not equalise. In addition, the location of the Fermi level of non-conducting materials within the band gap is uncertain. Finally, non-conducting specimens require an external source of electrons in order to compensate the build-up of positive charge resulting from photoelectron emission and thereby avoid energy shifting. Thus, for insulating materials, referencing of binding energies is best achieved using a secondary standard, e.g. adventitious carbon.

The binding energies for core electrons depend on the chemical environment of elements constituting the specimen. Considering a core electron, the energy of the electron is determined by the Coulomb interaction with the other electrons and the attractive

potential of the nuclei. Thus, any change in the chemical state of the element involve a spatial redistribution of the valence electron charges of the atom and the creation of a different potential as seen by the core electrons, resulting in a modification of their binding energies. Therefore, shift in the binding energies of core electrons may be related to the chemical environment of a given element. However, binding energy shifts may be dramatically influenced by relaxation processes in the final state of the excited atom, which correspond to a rearrangement of electrons within the orbitals of the excited atom or to the movement of electrons from the surrounding atoms in the material. Thus, shift in the binding energies due to the chemical state of the atom may be balanced by final state relaxation. Other issues in interpreting peak shifting may arise due to different factors, namely overlapping peaks, charging, satellites.

The X-ray photoelectron analyses were carried out with a Kratos Axis Ultra spectrometer using a monochromatic Al Kα source (1486.69 eV, 10 mA, 15 kV). The instrument work function was calibrated to give a binding energy of 83.96 eV for the Au $4f_{7/2}$ line for metallic gold. The charge compensation system was used on all the specimens. Survey scan and high resolution analyses were carried out with identical analysis areas of 300 x 700 microns and a pass energy of 80 eV and 20 eV respectively. Spectra were charge corrected to the main line of the C 1s spectrum (adventitious carbon) set to 285.0 eV, except for the O 1s peak which is referenced to the Al 2p peak, as the Fermi level of the oxide varies with surface treatment (Cordier and Ollivier, 1995). Spectra were analysed using CasaXPS software.

2.2.2 Rutherford backscattering spectrometry

Rutherford backscattering spectrometry is dedicated to the discrimination and quantification of trace atoms located in the first 2 μm of any surface (Hsiung and Trocellier, 1987; Taglauer, 2009).

For energy ranges usually associated with analyses performed by ion beam, i.e. between a few hundred keV and a few MeV, charged particles moving through matter interact with the electron clouds of atoms in the material. Such Coulomb-like interactions result in energy loss of the travelling particles, which corresponds of the electronic stopping power of the material, S_e.

The Bethe relationship describes theoretically the energy loss per distance travelled of swift charged particles (protons, alpha particles, atomic ions) traversing matter:

$$\frac{-dE}{dx} = \frac{4\pi e^4 Z_1 N B}{m_e \nu^2} \tag{2.5}$$

with:

$$B = Z_2 \left[ln(\frac{2m_e\nu^2}{I}) - ln(1-\beta^2) - \beta^2 \right] \quad and \quad \beta = \frac{\nu}{c} \tag{2.6}$$

where:

- ν and E are the atomic velocity and the energy of the projectile respectively.
- Z_1 and Z_2 are the atomic number of the projectile and the target respectively.
- c is the velocity of the light.
- N is the atomic density of the solid.
- I is the mean energy of ionisation of the atoms of the target, ($I = 10\, Z_2$).
- e is the elementary charge.
- m_e is the rest mass of the electron.

The validity of the Bethe relationship is limited to protons and α particles of energies above 200 keV and 1 MeV respectively.

Once incident particles have lost most of their energy to the electrons, elastic interactions with nuclei of the target take place, which represents the nuclear stopping power of the material, S_n.

Thus, the path length of the incident particles into the target depends on both inelastic (with the electron clouds) and elastic (with the target nuclei) interactions, as a result the maximal depth of irradiation is determined by the sum of electronic and nuclear stopping power of the material, dE/dx.

The stopping power of the target is defined for incident particles of kinetic energy, E, and a defined target composition. For multi-elemental targets, the energy loss of incident particles equals the sum of the energy losses associated with the individual elements, with respect to their concentration in the target. Further, density of the

target, ρ, is taken into consideration.

When a flux of high energy ions strikes a material, in addition to the energy loss processes previously presented, very few of the incident particles undergo wide-angle elastic scattering as a result of Coulomb repulsion with target nuclei, Fig. 2.2. Such elastic collisions involve conservation of both kinetic energy and momentum, resulting in a transfer of energy from the incident particles to the target nuclei, and the recoil of incident particles with energies characteristic of the masses of the target nuclei.

The energy ratio transferred from the incident particle to a target nucleus can thereby be expressed by the kinematic factor of the interaction, K, such as:

$$K = \frac{E}{E_0} = \left[\frac{\left[m_2^2 - (m_1\, sin\theta)^2\right]^{1/2} + m_1\, cos\theta}{m_1 + m_2} \right]^2 \tag{2.7}$$

where:

- m_1 and m_2 are the masses of the incident ion and the target nucleus respectively.
- E_0 is the initial energy of the incident ion.
- E is the energy of the scattered ions.
- θ is the scattering angle.

The kinematic factor depends only on the mass ratio of the incident ion and the target nucleus, m_1 and m_2, and on the scattering angle, θ. When $m_1 < m_2$, the kinematic factor tends to 1.

The function of the kinematic factor, K, shows a unique dependence of the mass of the target, m_2, for given incident particle, of mass m_1, and scattering angle θ. Thereby, the measure of the backscattered particle energies allows theoretically the identification of the nuclei of the target. However, identification of the elements of the target is possible only if the difference of energies associated with the backscattering of energetic particles by two atoms of adjacent masses is sufficiently large. Thus, the mass resolution is given by the following expression:

$$\frac{dE}{dm_2} = E_0 \frac{dK}{dm_2} \tag{2.8}$$

Thus, the mass resolution is directly proportional to the energy of the incident particle, E_0. Enhancement of the mass resolution can be achieved by increasing E_0 or to set the detector close to 180°, as the most important variations of kinematic factor arise at such scattering angle. In practice, the observation angles used are chosen between 150° and 170°.

In addition, for angles close to 180°, the mass resolution shows a maximum when the mass ratio of the incident particle to the target nucleus equals 2. Thereby, the mass resolution can be optimized depending on the nature of the incident particles. However, the range of mass for the incident particles is limited, resulting in a better mass resolution for light elements than for heavy atomic mass targets.

Finally, Equation 2.7 correctly determines the energy of scattered particles for any particular scattering angle; but it does not describe the probability of observing such an event. The probability for a scattering event to happen by elastic interaction of an incident particle by a target nucleus is expressed by the differential cross-section $d\sigma/d\Omega$ for a given direction θ in a solid angle of detection $d\Omega$:

$$\frac{d\sigma}{d\Omega} = \frac{1}{N_0 N d_x} \frac{d_n}{d_\Omega} \tag{2.9}$$

where:

- N_0 is the number of primary particles incident to the target.
- N is the number of atoms per cm^3 of the target.
- dn is the number of backscattered particles in a solid angle $d\Omega$.
- dx is the thickness of the target.

For a range of energies between 1 keV to a few MeV, the particle interaction is considered purely Coulombian, thereby the differential scattering cross-section is given by the Darwin formula, as follows:

$$\frac{d\sigma}{d\Omega} = \left[\frac{Z_1 Z_2 e^2}{2E_0 sin^2\theta}\right]^2 \frac{\left[m_2^2 - (m_2 m_1 sin\theta)^2 + m_2 cos\theta\right]^2}{\left[m_2^2 - m_2 m_1 sin^2\theta\right]^{1/2}} \tag{2.10}$$

Finally, if m_1 is negligible in comparison with m_2 then Equation 2.10 can be simplified as follows:

$$\frac{d\sigma}{d\Omega} = \left[\frac{Z_1 Z_2 e^2}{4E_0}\right]^2 \frac{1}{sin^4\frac{\theta}{2}} \tag{2.11}$$

Equation 2.11 represents the differential cross-section for a backscattering event and is known as the Rutherford's formula.

Finally, with regard to Equation 2.11, the different parameters affecting the differential cross-section are evident:

- The yield of backscattered particles, for a given target, is proportional to Z_1^2: for a given energy the backscattering yield associated with He ions is 4 times larger than that obtained with α particles.
- The yield of backscattered particles is proportional to Z_2^2: the heavier the target atoms, the better the sensitivity.
- The backscattering yield is proportional to $1/E_0^2$: a good sensitivity is achieved for a incident particles of low energy.
- Finally, the yield shows a dependence on $1/sin^4\frac{\theta}{2}$ limiting dramatically the range of scattering angle.

Incident particles travelling inside the target matter undergo energy loss along the travel path as a result of interaction with the electron clouds and the nuclei of the target, before being backscattered by a nuclei of the target. Thus, a particle scattering from an element present at a certain depth in the specimen will have less energy than a particle which scattered from the identical element located at the surface of the specimen. The energy loss due to inelastic collisions can be converted in term of depth, thereby, allowing the determination of elemental depth distributions. The following set of equations establishes the formula for energy-depth conversion.

As stated by Equation 2.5, the total energy loss, dE, undergone by incident particles travelling into thin layers, is proportional to the distance travelled, dx, and the nature of the target. Thus, an incident particle of direction π, is backscattered in a direction $(\pi - \theta)$ at a depth x. A particle whose kinetic energy right before the collision is E_x, is detected with an energy E_d. The energy losses along the forward and recoil paths are

$\Delta E_f = E_0 - E_x$ and $\Delta E_r = KE_x - E_d$ respectively. The forward travel of the particles can be expressed as:

$$\frac{x}{|cos\,(\pi)|} = \int_{E_0}^{E_x} -\frac{dx}{dE}\,dE \tag{2.12}$$

Particles backscattered in a direction $(\pi - \theta)$ travel along:

$$\frac{x}{|cos\,(\pi - \theta)|} = \int_{KE_x}^{E_d} -\frac{dx}{dE}\,dE \tag{2.13}$$

As E_x is not accessible, therefore the stopping power of the material has to be assumed constant along the forward and recoil paths, the respective stopping powers are noted as follows:

$$\left(\frac{dE}{dx}\right)_f = S_f \quad and \quad \left(\frac{dE}{dx}\right)_r = S_r \tag{2.14}$$

Thereby, by integration of Equations 2.12 and 2.13:

$$E_x = E_0 - (S_f)\,x \quad and \quad E_d = KE_x - \frac{x}{|cos\,(\pi - \theta)|}S_r \tag{2.15}$$

The unknown variable E_x can be eliminated from the above equations considering particles scattered from the surface and from a depth x, which present an energy KE_0 and E_d respectively, Fig. 2.3.

$$\Delta E = KE_0 - E_d = (KS_f)\,x + \frac{x}{|cos\,(\pi - \theta)|}S_r \tag{2.16}$$

Finally, the energy scale can be converted into a depth scale due to inelastic losses, thereby allowing calculation of a depth profile of the different species in the specimen, such as:

$$x = \frac{\Delta E}{KS_f + \dfrac{S_r}{|cos(\pi - \theta)|}} \tag{2.17}$$

The compositional analysis of the specimens was performed by Rutherford backscattering spectrometry using 1.7 MeV $^4He^+$ ions provided by a 2.5 MeV Van de Graaff accelerator (University of Paris). The beam diameter was 1 mm. Scattered ions were detected at 165° to the direction of the incident beam. Simulation of the spectra was performed using the SIMNRA program.

2.2.3 Medium energy ion scattering

Medium energy ion scattering (MEIS) is an ion scattering technique, closely related to Rutherford backscattering spectrometry, that is used for compositional thin film analysis (Taglauer, 2009).

A MEIS experiment consists in exposing the specimen of interest to a primary ion beam, and consequently detecting the energy distribution of scattered ions as a function of scattering angles to produce a two dimensional spectrum. The primary ions, usually H^+, He^+ or Li^+, are initially accelerated to energies of about 100 keV. The resulting energies of scattered ions depend on energy transfer occurring by elastic scattering (nuclear stopping) and energy loss arising by inelastic collisions (electronic stopping). Consequently, for sufficiently high scattering angles, the variation of the kinematic factor involves the differentiation of element of different masses.

As demonstrated previously for Rutherford backscattering, the energy scale can be converted into a depth scale due to inelastic losses, thereby allowing calculation of a depth profile of the different species in the specimen. For MEIS the incident particles do not travel in a direction π, thereby Equation 2.17 is modified considering the incident and recoil angles, θ_1 and θ_2 respectively:

$$x = \frac{\Delta E}{\frac{KS_f}{|cos(\theta_1)|} + \frac{S_r}{|cos(\theta_2)|}} \tag{2.18}$$

The differently patterned superpure aluminium substrates were analysed using the MEIS facility at Daresbury Laboratory (Richards, 2010). A 100 keV He^+ ion beam of dimensions 1.0 x 0.5 mm^2 was incident on the specimen and scattered He^+ ions were detected by a toroidal electrostatic analyser equipped with a two-dimensional readout microchannel plate detector, providing simultaneous detection of energy and angle. For a single data set the energy resolution is 0.24 % of the pass energy and the angular resolution is $< 0.3°$. Scattered ions were detected at 90° to the direction of the incident beam. Simulation of the different spectra was performed using the SIMNRA program.

2.2.4 Time-of-flight secondary ion mass spectrometry

For secondary ion mass spectrometry analysis, the surface of the specimen is bombarded by primary ions of high energy (1 - 25 keV). The transfer of momentum from primary ions to target atoms via atomic collisions generates a collision cascade, which results in the ejection of neutral or charged species (atoms and molecular compounds) from the surface. Thus, sputtering allows a controlled removal of surface layers on a nearly atomic scale. Surface sensitivity of the technique results from the dimensions of the collision cascade which are limited to a few nanometre in diameter and depth. Hence, the emitted particles originate from the uppermost one or two monolayers of the specimen surface.

TOF-SIMS instruments have been designed for molecular analysis and shallow depth profiling capabilities, based on a dual beam approach which allows independent optimization of the analysis and the sputtering. Thus, compositional information of the topmost atomic layers of the surface is achieved by the application of a very low primary ion dose densities (10^{12} ions cm^{-2}, static limit), in order to prevent surface modifications and to investigate the original, non-modified surface composition. In contrast, erosion of the specimen is performed using a etching beam at relatively higher ion dose densities compared with the analysis. Thus, material removal is carried out in a controlled manner to obtain information on the in-depth distribution of elements. Excellent depth resolution is achieved as the analysis is performed on a restricted area at the bottom of the crater formed using the etching beam (Vickerman, 2009).

The use of a very low primary flux density results in a very low yield of secondary particles, thereby requiring high sensitivity on the detection equipment. Time-of-flight detector offers an appropriate approach, provided high transmission, parallel mass detection, unlimited mass range (up to 10,000 u) and high mass resolution (> 10,000).

Time-of-flight mass spectrometry is based on the fact that ions of same energy but with different masses travel with different velocities. Thus, ions accelerated by an electrostatic field to a common energy, travel over a drift path to the accelerator. The accelerated ions gain kinetic energy as a function of their mass-to-charge ratio, Eq.

2.19. As a result, different ions can be differentiated depending of their respective travelling times to the detector, located at a known distance, Eq. 2.21.

$$E_k = qU = \frac{1}{2}mv^2 = cst \tag{2.19}$$

$$qU = \frac{1}{2}m\left(\frac{d}{t}\right)^2 \tag{2.20}$$

$$t = \frac{d}{\sqrt{2U}}\sqrt{\frac{m}{q}} \tag{2.21}$$

where:

- m and q are the mass and charge of the travelling species respectively.
- U is the extraction voltage.
- v is the velocity of the charged species.
- d is the distance of flight.
- t is the time of flight.

TOF-SIMS analyses were carried out at the University of Catania. The specimens were depth profiled using a TOF-SIMS IV instrument (ION-TOF GmbH) in the dual beam mode by employing ion beams at an angle of incidence of 45° relative to the normal to the specimen surface. The sputter- and the primary-ion beams are separated by 90°. Etching of the specimen surface was undertaken by an argon ion beam (1 keV, 10 nA) over an area of 150 x 150 µm^2, while analysis was performed using a bismuth ion (Bi^+) beam (25 keV, 0.1 pA) over a concentric area of 15 x 15 µm^2. Charge compensation was achieved by applying low-energy electrons from a pulsed flood gun. Depth profiles were obtained in the non-interlaced mode, alternating 5 scans of analysis and 2 s of etching, with a pause of 500 µs between the etching and analysis phases. The profiles were measured in the positive ion mode, with detection of the following masses: ^{11}B, $^{13.5}Al$ (Al^{2+}), ^{31}P, ^{52}Cr, ^{63}Cu.

2.2.5 Glow discharge optical emission spectroscopy

During depth profile analysis performed by GD-OES, the erosion process is carried out by energetic particles (charged species and neutral atoms) present in the sheath

of the glow discharge plasma (Bogaerts, 2007). The glow discharge plasma ensures a high sputtering rate due to the high flux of energetic species induced by the high electric field present in the cathode dark space. Additionally, the species contributing to sputtering are of low energy ($<$ 50 eV), resulting in a low penetration depth and limiting the surface damage to a shallow layer of about 2 nm thick.

The sputtered species, mostly atoms, diffuse into the negative glow area, where they are excited and/or ionized (Nelis et al., 2006). Relaxation of the species is accompanied by photon emission of characteristic wavelength, enabling elements differentiation. Indeed, due to the specific energy level differences between atomic states (fundamental, excited) each element has a specific emission spectrum, thus wavelengths in the emission spectrum are directly associated with elements present in the specimen of interest (Broekaert, 2003). In addition, the intensity of an atomic emission line is related to the density of the radiating atoms in the plasma and thus to the concentration of the element in the specimen analysed. Finally, the radiation is spectrally resolved using a spectrometer and the intensities of the analytical lines are measured with suitable detectors.

GD-OES depth profiling analysis was undertaken using a GD-Profiler 2 instrument (Horiba Jobin Yvon). A sacrificial silicon wafer was sputtered in order to pre-condition the lamp. The specimens were then mounted on the lamp, and prior to measurement were cleaned in an argon plasma (800 Pa, 5 W, frequency 20 kHz, duty cycle 0.125).

Elemental depth profiling was performed in the continuous mode with an argon pressure and a power of 650 Pa and 40 W respectively; when the pulsed mode (800 Pa, 20 W) was used, a frequency of 20 kHz and a duty cycle of 0.5 were employed. The relevant wavelengths corresponding to the light emission of the species of interest were: Al, 396.15 nm; B, 249.68 nm; Cr, 425.43 nm; P, 178.29 nm and Cu, 324.75 nm.

2.2.6 Glow discharge time-of-flight mass spectrometry

Similar to GD-OES analysis, for GD-TOF-MS depth profiling a glow discharge plasma is used as source of atomisation and excitation for the determination of trace elements. However, detection and differentiation of elements are carried out in term of mass. The detection limits associated with mass spectrometry and optical spectroscopy are

about 1 μg/kg (ppb) and 1 mg/kg (ppm) respectively, i.e. mass spectrometers present a sensitivity of about 3 orders of magnitude higher than optical spectrometers.

Thus, parallel detection of the secondary ions is ensured by time-of-flight mass spectrometry. The coupling of a time-of-flight mass analyser to a fast erosion glow discharge ion source allows quasi-simultaneous extraction of ions and, consequently, rapid depth profiling of nanometre-thick layers can be achieved. Additionally, time-of-flight mass spectrometers provide information about the chemical environment of the species, collecting both atomic and molecular ions (Tempez et al., 2009).

GD-TOF-MS elemental depth profiling analysis was performed at the University of Oviedo. The profiles were measured in the pulsed mode with an argon pressure and a power of 650 Pa and 35 W respectively, duty cycles of 0.20 or 0.45 were employed depending on the thickness of the different specimens. The different profiles were measured in the positive ion mode, with detection of the following masses: ^{11}B, ^{27}Al, ^{31}P, ^{52}Cr, ^{63}Cu.

Tables

Table 2.1 – Standardized 3D Surface Texture Parameters, ISO 25178.

Parameters	Description	Definition
Sq	Surface Root-Mean-Square deviation	$Sq = \sqrt{\frac{1}{a}\int\int_a z^2(x,y)dxdy}$
Sa	Surface Arithmetical mean deviation	$Sa = \frac{1}{a}\int\int_a \lvert z(x,y)\rvert dxdy$
Sp	Maximum height of peaks	
Sv	Maximum depth of valleys	
Sz	Maximum height of the surface	
Ssk	Skewness of the height distribution	$Ssk = \frac{1}{aSq^3}\int\int_a z^3(x,y)dxdy$
Sku	Kurtosis of the height distribution	$Sku = \frac{1}{aSq^4}\int\int_a z^4(x,y)dxdy$

Table 2.2 – Comparative summary of the analytic performances of the main techniques for thin film analysis.

	XPS	MEIS	RBS	TOF-SIMS	GD-OES	GD-MS
Incident particles						
- nature	Photon	H^+,He^+	He^{2+}	Ions	Ions	Ions
- energy (keV)	1 - 10	10^2	2 x 10^3	1	< 0.1	< 0.1
Detected particles	Electron	Ions	Ions	Ions	Photons	Ions
Element range (Z)	⩾ 3	⩾ 5	† ⩾ 5‡	⩾ 1	⩾ 1	⩾ 1
Information						
- elemental	✓	✓	✓	✓	✓	✓
- chemical	✓	-	-	✓	-	✓
- molecular	-	-	-	✓	-	✓
Limit of detection (µg/g or ppm)	10^3	10	10^3	< 1	1	10^{-3}
Sputtering	Possible	-	-	Ion beam	Plasma	Plasma
Crater effect	(-)	-	-	(-)	(++)	(++)
Resolution (nm)						
- depth	< 3	< 1	< 10	< 1	< 5	< 5
- lateral	10^2	10^5	10^5	10	10^6	10^6
Vacuum (mbar)	10^{-9}	10^{-6}	10^{-6}	10^{-9}	10^{-2}	10^{-2}
Acquisition time	Slow	Slow	Fast	Slow	Fast (s)	Fast (s)

†Z < 90 and mass resolution of 1 atomic mass unit for Z < 40

‡low-Z elements, namely lithium, boron, carbon, nitrogen, oxygen and fluorine:
detection and quantification using Nuclear Reaction Analysis (NRA),
hydrogen: detection and quantification using Elastic Recoil Detection Analysis (ERDA)

Figures

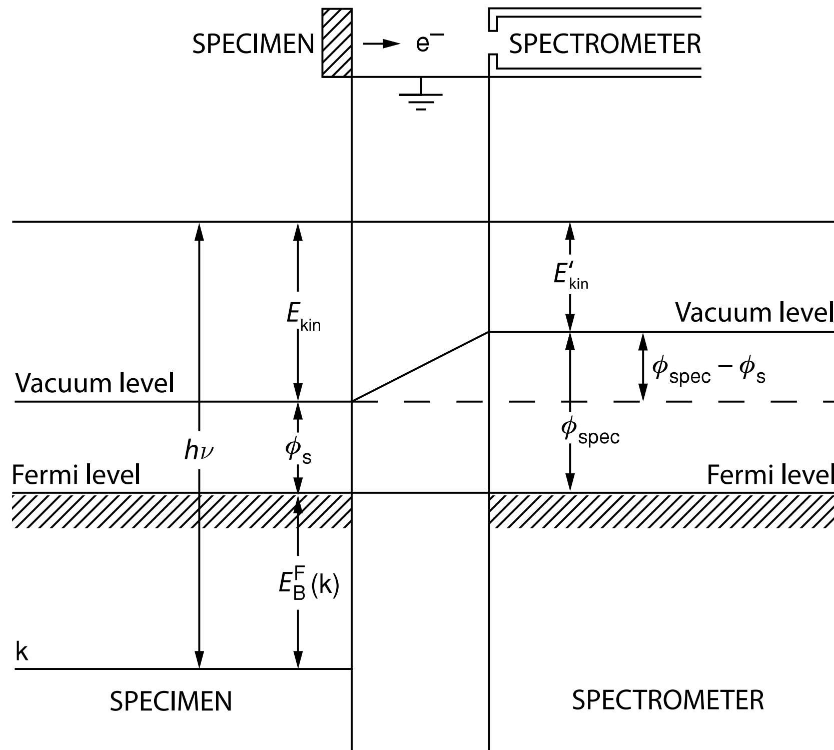

Figure 2.1 – Schematic of the relevant energy levels for binding energy measurements by X-ray photoelectron spectroscopy. The conducting specimen and spectrometer housing are in electrical contact and thereby have common Fermi levels. The incident X-ray photons, of energy $h\nu$, create electrons by photoelectric effect. The kinetic and binding energy of the photoelectrons on the k$^{\text{th}}$ level, E_{kin} and $E_B^F(k)$, are relative to the Vacuum and Fermi levels of the specimen respectively. The kinetic energy of the photoelectrons is measured by a spectrometer with a work function ϕ_{spec} so that $E'_{kin} = E_{kin} - (\phi_{spec} - \phi_s)$.

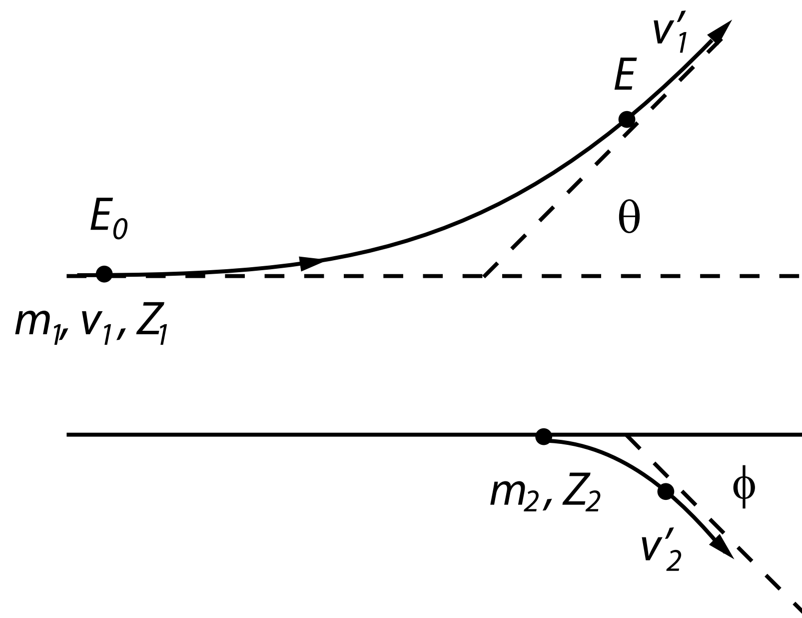

Figure 2.2 – Schematic of the trajectories for the elastic collision between two masses m_1 and m_2. The incident particle has an initial energy E_0, and an energy E after scattering.

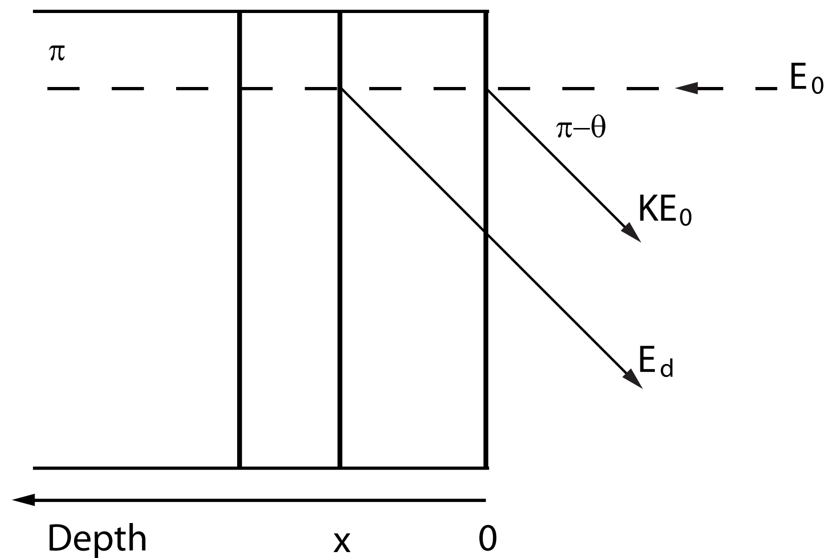

Figure 2.3 – Schematic of the backscattering of incident particles of energy, E_0, which are backscattered at the surface of the specimen with an energy KE_0 and at a depth x with an energy E_f.

Results and Discussion

1 Aluminium Substrates of Controlled Patterns

Superpure aluminium substrates of controlled roughnesses have been prepared by electropolishing or by anodizing in sulphuric acid, oxalic acid and phosphoric acid and subsequent stripping of the porous films in a chromic / phosphoric acid solution. The topography of the differently patterned superpure aluminium substrates have been characterized by atomic force microscopy and transmission electron microscopy. Additionally, the composition of oxide films formed, on the superpure aluminium substrates after electropolishing and stripping, have been investigated by XPS and MEIS. Finally, the distributions of the different species, namely chlorine, chromium and phosphorus, incorporated into the oxide films arising from the electropolishing and stripping treatments, have been examined by elemental depth profile analyses, using MEIS, GD-OES, GD-TOF-MS and TOF-SIMS.

1.1 Characterisation of the Substrate Topographies

1.1.1 Cross-section examination

Superpure aluminium substrates of controlled roughnesses were generated using successive treatments, namely electropolishing, followed by anodizing in sulphuric acid, oxalic acid or phosphoric acid in order to pattern the aluminium surface through growth of porous anodic aluminium oxide layers with different cell dimensions and finally, stripping of the porous oxide layers in a chromic / phosphoric acid solution. Examination of specimen cross-section has been undertaken by transmission electron microscopy after each treatment.

Transmission electron micrographs, Fig. 1.1, show ultramicrotomed sections of the as-rolled superpure aluminium material and of a superpure aluminium specimen after electropolishing for 3 min and subsequent stripping in a chromic / phosphoric acid solution. The texturing effect of the electropolishing treatment is evident; the specimen pattern presents a period and an amplitude of about 70 nm and 11 nm respectively. Additionally, the thickness of the oxide film, resulting from stripping, is 5 $\pm$ 1 nm.

In order to tailor the specimen surface by generating various patterns based on the organisation of approximately hexagonal cells, porous alumina films were grown in sulphuric acid, oxalic acid or phosphoric acid.

Figure 1.2 displays transmission electron micrographs of ultramicrotomed sections of the different porous anodic films, attached to the superpure aluminium substrates, formed by anodizing of the aluminium specimens in sulphuric acid, oxalic acid and phosphoric acid for 5 min.

The morphology of the anodic porous alumina is comprised of a close-packed array of columnar alumina cells, each containing a central pore. The cell diameters of the porous alumina films formed in sulphuric acid, oxalic acid and phosphoric acid have been measured from the transmission electron micrographs, giving values of about 50 $\pm$ 15 nm, 80 $\pm$ 20 nm and 200 $\pm$ 60 nm respectively. The standard deviation of the cell diameter distributions is relatively important, about 30 %, which indicates that the anodizing time was insufficient to reach uniformity of the pore dimensions in comparison with the regularity of the cell arrangements reported by Masuda (Hideki Masuda and Osaka, 1998).

A chromic / phosphoric acid solution was used in order to dissolve the porous anodic oxide layers, thereby revealing the pattern of aluminium surface through development of the hexagonal alumina cells that penetrate the substrate in a hemispherical manner, as presented in Figure 1.3.

The dimensions of the different surface patterns, amplitude and period, have been measured, from peak-to-valley and from peak-to-peak respectively, from the transmission electron micrographs, Fig. 1.3; a summary is presented in Table 1.1. A good

correlation exists between the cell diameters measured from the porous alumina layers and the period of the surface patterns after stripping. Thus, superpure aluminium specimens of tailored patterns have been generated with amplitudes and periods in the ranges of 6 - 65 nm and 54 - 200 nm respectively.

1.1.2 3D surface analysis

Electropolishing, anodizing and subsequent stripping have been used to produce patterned substrates of nano-scale roughnesses. A surface roughness study has been performed using atomic force microscopy. The parameters used to describe the surface roughness of the specimens are defined in the Characterisation section of the Experimental Procedure.

Atomic force microscopy images of the rolled aluminium material, used for the generation of substrates of controlled roughnesses, reveal a combination of large scale waviness as well as surface roughness. In order to determine precisely the roughness parameters associated with the differently patterned substrates, the waviness and the surface roughness have been separated using a Gaussian filter, thereby enhancing the accuracy of the surface parameters measured. The raw and filtered atomic force microscopy images are compared in Figs. 1.4 and 1.5, showing the important contribution of the waviness to the atomic force microscopy images before filtering.

Figure 1.6 presents atomic force microscopy images of a superpure aluminium specimen after electropolishing for 3 min and stripping of the oxide film resulting from the electropolishing process. The surface topography achieved by electropolishing consists of regular furrow and hexagonal patterns in particular grain orientations. Generally, electropolishing of grains of orientations near [110] and [100] leads to the formation of regular furrow and hexagonal patterns respectively (Caicedo-Martinez et al., 2002). The electropolished specimen shows a surface roughness, Sq, of about 1.4 ± 0.1 nm over an area of 5 μm^2. Additionally, the electropolished surface shows a symmetric height distribution, without a predominance of peaks or valleys (Ssk ≈ 0) and the absence of large defects (Sku $= 2.14$). Finally, the wavelength of the pattern has been determined by Fourier transform analysis to be about 69.2 nm.

Atomic force microscopy images, revealing the topography of the superpure aluminium

specimens after anodizing in sulphuric acid, oxalic acid and phosphoric acid for 5 min and subsequent stripping of the porous anodic oxide films, are shown in Figures 1.6.b, .c, .d respectively. The topography of the superpure aluminium substrates, patterned in the three acid electrolytes, consists of long-range ordering of hexagonal cell arrays. The surface roughnesses, Sq, of the specimens anodized in sulphuric acid, oxalic acid and phosphoric acid, are respectively about 7 ± 1 nm, 11 ± 1 nm and 31 ± 3 nm over an area of 5 μm^2.

The specimens patterned in the various acids show asymmetric height distributions with a preponderance of peaks (Ssk > 0). Excessively high or deep defects are absent in the substrates patterned in phosphoric acid (Sku < 3), but are present on the specimens anodized in sulphuric and oxalic acids (Sku > 3). Such defects may result from remnants of the porous alumina layers; thus, the stripping process appears to be more uniform for porous films of larger cell dimensions, as formed in phosphoric acid.

The prepared substrates present ordered hexagonal cell array patterns. However, the ordering of the cell arrays as well as the uniformity of the cell diameters are limited by the short period of time for which the specimens have been anodized. Indeed, an extended period of anodizing or a two-step anodizing improve the regularity of the cell arrangement, increasing the defect free domains, and producing an almost ideally honeycomb structure in sulphuric acid, oxalic acid and phosphorus acid solutions, (Hideki Masuda and Osaka, 1998; Masuda and Fukuda, 1995; Masuda et al., 1997) respectively . Consequently, a 3D surface motif analysis has been used to determine the period of the different surface patterns, instead of a Fourier transform analysis.

A 3D surface motif analysis has been performed using a segmentation method in order to describe the valleys of the surface pattern, Fig. 1.7. The surface pattern motif parameters (density, mean height, mean area and cell diameter) are presented in Table 1.3. The values calculated from the motif analysis for the mean height and the diameter of the cells, are lower than the values previously measured from the transmission electron micrographs. Nevertheless, both sets of measurement are consistent, the difference may be due to the sampling size associated with each technique.

Finally, generation of superpure aluminium specimens of controlled roughnesses has

been undertaken by electropolishing and anodizing in different acid electrolytes. Surfaces of tailored pattern have been produced with roughnesses in the range 1 - 32 nm. The standard deviation of the surface roughness values was calculated for the different patterned surfaces to be less than 10 %, indicating a good reproducibility for the different treatments.

1.2 Incorporation of Electrolyte-Derived Species

1.2.1 Compositional analysis

The elemental surface chemistry of oxide films on electropolished specimens as well as specimens successively electropolished and immersed in a chromic / phosphoric acid solution has been probed using X-ray photoelectron spectroscopy. Thus, the study deals with the analysis of the photoelectron peaks of O 1s, Al 2p, Cl 2p, P 2p and Cr 2p. A summary of the different binding energies, peak widths and component ratios is presented in Table. 1.4.

The shape of the different peaks, if not otherwise mentioned, was described by a Lorentzian-modified Gaussian function with a contribution of the Lorentzian function fixed at 0.3. The Shirley background was utilized to fit the baseline of the different photoelectron peaks analysed, except for the O 1s and the Cl 2p peaks for which, respectively, the Tougaard and linear background were more adequate, (Shirley, 1972) and (Tougaard, 1997) respectively.

Aluminium oxide / hydroxide systems are extremely difficult to differentiate by XPS due to overlapping of the different components. In addition, the characterization of the air-formed surface film of aluminium is complicated by the possibility of a range of distinct entities, i.e. than the than the cells Al_2O_3, $Al(OH)_3$ and AlOOH and intermediate entities such as hydroxyl ions in alumina.

Alexander (Alexander et al., 2000) assessed the degree of hydration of aluminium oxide hydroxide surface by curve fitting of the XPS peak of the O 1s core level; such a method has been applied here.

The O 1s photoelectron spectra of the electropolished specimens and the specimens successively electropolished and immersed in a chromic / phosphoric acid solution are presented in Figures 1.8.a and .b. The O 1s envelope was fitted with the components O 1s - 1, O 1s - 2 and O 1s - 3, which are associated with the contributions of Al_2O_3, AlOOH, carbon and water contamination respectively. The Lorentzian contribution of the Lorentzian-modified Gaussian function, used to represent the O 1s - 1 and O 1s - 2 peaks, was fixed at 0.5. The widths of the peaks associated with the 3 components were constrained to be equal. Thus, for both specimens, the separation of the binding energies of O 1s - 1 and O 1s - 2 components are 456.7 ± 0.1 eV and 457.7 ± 0.1 eV from the Al 2p oxide peak. The proportions of hydroxide-rich oxide and oxide present in the surface films have been assessed from the O 1s - 2 and O 1s - 1 components. Due to the presence of different impurities at the near surface of the oxide film, the fitting of the C 1s spectra was not straightforward, therefore, no corrections have been attempted for oxygen associated with carbonaceous contamination located at the surface of the specimens. The hydroxide-rich oxide to the total oxide ratio drops from 0.58 for the electropolished specimen to 0.33 for the specimen successively electropolished and immersed in a chromic / phosphoric acid solution.

Figures 1.8.c and 1.8.d display the Al 2p photoelectron spectra of the electropolished specimens and the specimens successively electropolished and immersed in a chromic / phosphoric acid solution. A clear separation of the metallic and oxidized components can be observed, with separations between the aluminium metal Al $2p_{3/2}$ and aluminium oxide peak of 3.2 and 2.9 eV for the electropolished and for the stripped specimen respectively. Additionally, a variation in the area ratio of the Al 2p oxide to Al 2p metal clearly appears. Thus, the Al 2p envelope has been fitted with aluminium metal and aluminium oxide components. The area ratio of the Al $2p_{1/2}$ and Al $2p_{3/2}$ components was fixed at 0.5 and the the widths constrained to be equal. Asymmetry has been introduced in the shape of Al $2p_{3/2}$ and $2p_{1/2}$ components with the Gaussian / Lorentzian function being modified by an exponential function of factor 1.4. No constraints have been introduced on the Al 2p oxide peak.

An estimation of the thickness of the surface films covering both the specimen electropolished and the specimen electropolished and immersed in a chromic / phosphoric acid solution have been made from the Al 2p oxide / metal peak ratio

using Strohmeier's equation (Strohmeier, 1990):

$$d = \lambda_o \, sin\theta \, ln \left(\frac{N_m \lambda_m I_o}{N_o \lambda_o I_m} + 1 \right) \tag{1.1}$$

where:

- θ is the take-off angle, 90°.
- λ_o and λ_m are the inelastic mean free paths of photoelectrons propagating through the oxide and the metal, they were assumed at 3.28 nm and 2.58 nm respectively, (Tanuma et al., 1994).
- N_m/N_o, the ratio of the volume densities of aluminium atoms in metal to oxide, equals 1.6, calculated from the densities for Al and anodic alumina 2.7 and 3.5 g cm^{-3} respectively.

There is a wide range of inelastic mean free paths (IMFP) or electron attenuation lengths (EAL) present in the Literature for Al (III) oxide / hydroxide / hydrate compounds. In addition, the inability of XPS to accurately differentiate the exact form of the Al (III) oxide present limits the accuracy of the oxide thickness measurement. Finally, considering the different enrichments as well as the presence of hydroxyl ions, the volume concentration of aluminium ions in the surface films may be altered, thereby Strohmeier's original assumptions seem reasonable given the data available. Thus, they are used here to calculate an estimation of the surface film thicknesses.

The thicknesses of the surface films have been calculated for the electropolished specimen and the specimen successively electropolished and immersed in a chromic / phosphoric acid solution to be about 4.1 and 3.1 nm respectively.

The Cl 2p photoelectron spectra of the electropolished specimens and successively electropolished and immersed in a chromic / phosphoric acid solution are presented in Figure 1.8.e, .f. The Cl 2p envelope was fitted with the contributions of the Cl 2p$_{3/2}$ and Cl 2p$_{1/2}$ levels. The Cl 2p$_{1/2}$ to Cl 2p$_{3/2}$ peak area ratio was constrained to one half; in addition, both peaks were constrained to equal widths. The binding energies of the Cl 2p$_{3/2}$ and Cl 2p$_{1/2}$ levels, without charge correction, were found at 195.9 and 197.6 eV respectively. There is no noticeable chemical shift indicative of changes in the chemical state of chlorine; therefore, both specimens are assumed to present chlorine ions as impurities. The amount of chlorine species was calculated to drop from

1.61 at.% for the electropolished specimens to 0.59 at.% for the specimens immersed in a chromic / phosphoric acid solution.

The P 2p photoelectron spectrum of the specimen successively electropolished and immersed in a chromic / phosphoric acid solution, Fig. 1.8.g, shows a peak at 134.0 eV, with a significant asymmetry towards the lower binding energies. From the analysis of the electropolished specimen, free of phosphorus, a peak associated with the plasmon losses of aluminium appears at 132.5 eV. The aluminium plasmon loss peak has been subtracted from the P 2p peak. The P $2p_{3/2}$ and P $2p_{1/2}$ levels were then fitted to the P 2p envelope. The P $2p_{1/2}$ to P $2p_{3/2}$ peak area ratio was constrained to one-half, while peak widths were constrained to be equal. From the fitting of the P 2p photoelectron spectrum, the phosphorus species appears to be in an oxidized state, with a chemical shift of 4.0 eV from the phosphorus metal binding energy, which is in agreement with the Literature (Takahashi and Nagayama, 1978).

The Cr 2p photoelectron spectrum of the specimen successively electropolished and immersed in a chromic / phosphoric acid solution, Fig. 1.8.h, presents the contributions of the Cr $2p_{3/2}$ level, the Cr $2p_{1/2}$ feature and its satellite.

Differentiation between Cr metal, Cr(III) oxide, Cr(III) hydroxide and Cr(VI) can been achieved by fitting of the chromium $2p_{3/2}$ core level spectra, as demonstrated by different groups (Biesinger et al., 2004; Unveren et al., 2004) with the characterisation of reference materials.

A classical Shirley background (Shirley, 1972) is not appropriate for Cr $2p_{3/2}$ spectra since crossing through the Cr $2p_{1/2}$ contribution. In order to take into consideration the Cr $2p_{1/2}$ contribution, the Shirley background was modified with an offset matching the high binding energy edge of the Cr $2p_{1/2}$ peak. The Cr $2p_{3/2}$ envelope was best fitted with a fine multiplet splitting structure. Each peak of the structure was constrained to a width of 1.0 eV. The separations of the peaks are 1.1, 0.8, 0.9 and 1.1 eV. Such discrete multiplet structure can be associated with the presence of chromium (III) in an oxide or hydroxide environment. The differentiation between chromium (III) oxide and hydroxide is not evident, here, from the fitting of the Cr $2p_{3/2}$ core level spectra.

In addition, Cr (VI) compounds are diamagnetic and, therefore, do not present a multiplet splitting structure. The CrO_3 powder used for the preparation of the stripping solution has been analysed by X-ray photoelectron spectroscopy. The Cr $2p_{3/2}$ component presents a main and narrow peak at 580 eV. A comparison of the Cr $2p_{3/2}$ spectra for the specimen immersed in a chromic / phosphoric acid solution and for the CrO_3 powder used for the preparation of the stripping solution is displayed in Figure 1.9; from the comparison of both spectra it is evident that the main oxidation state of the chromium species incorporated into the oxide film is not (+6). Chromium species being introduced by immersion in a chromium (VI) solution, presence of chromium (VI) residuals should not be disregarded. However, the identification of chromium (VI) compound is limited by two factors, namely the overlapping of the X-ray photoelectron spectra of the chromium (VI) compound with the multiplet splitting structure of the chromium (III) species and the potential shift in the binding energies due to final state relaxation.

Finally, X-ray photoelectron analysis revealed the incorporation of chlorine into the oxide film arising from electropolishing of the specimen in a perchloric acid / ethanol solution. Subsequently, changes in the chemistry of the oxide film arise with the incorporation of chromium and phosphorus species, resulting from the stripping solution, and the loss of about 37 % of the chlorine species incorporated during the electropolishing process. Additionally, the OH / O ratio of the species present in the oxide film drops from 0.6 after electropolishing to 0.3 after stripping; this decrease is possibly related to the presence of chromium (III) oxide.

1.2.2 Quantification

The electropolishing of aluminium in a perchloric acid / ethanol solution leads to the dissolution of the metal surface. In addition, the process results in the incorporation of chlorine species into the oxide film naturally formed over the aluminium surface. Subsequent to electropolishing, selected specimens were immersed in a chromic / phosphoric acid solution; the stripping solution, by reaction with the filmed aluminium, forms a thin layer over the surface which contains chromium and phosphorus species.

Compositions of the oxide films, present at the surface of the specimens, have been quantified by simulation of the scattered ion energy spectra obtained by medium energy

ion scattering.

For the electropolished specimens, the MEIS spectra disclose peaks for copper, chlorine and oxygen, with oxygen being superimposed on the aluminium yield, Figs. 1.10.a - 1.10.c. An aluminium oxide layer enriched in hydroxide through its uppermost part was found to best represent the surface film composition. The hydroxide-enriched layer represents 25 % of the surface film thickness; the atomic ratio of aluminium to oxygen rises from 0.52 in the hydroxide-rich oxide layer to 0.67 in the oxide layer. Additionally, the inner part of the oxide, adjacent to the metal / oxide interface, is doped with about 1.39 x 10^{15} at cm^{-2} of chlorine. Finally, a copper-enriched layer containing about 0.33 x 10^{15} at cm^{-2} is located underneath the metal / oxide interface. The enrichment of copper results from prior oxidation of aluminium and the associated initial formation of copper-free anodic alumina (Zhou et al., 1997).

For the specimens successively electropolished and immersed in a chromic / phosphoric acid solution, the MEIS spectra reveal two peaks at scattered ion energies between 77 to 82 keV and 86 to 89 keV respectively, Figs. 1.10.d - 1.10.f. The former peak results from the convolution of scattering of incident He ions associated with phosphorus and chlorine species, whereas the later peak is comprised of the incident He ions scattered by chromium and copper species.

For the specimen electropolished and immersed in the chromic / phosphoric acid solution, the elemental depth profiles of the different species have been calculated using for each species the energy profile obtained by simulation. Scattering energies from the various elements, if present at the specimen surface, have been calculated using the kinematic factor K, Eq. 2.7 of the Characterisation section. The conversion of the scattering energy scale into a depth scale has been performed using the Equation 2.18 of the Characterisation section, with both angles θ_1 and θ_2 equal to $\pi/4$. The forward and recoil stopping powers of the oxide layer, S_f and S_r, have been calculated using SRIM (Ziegler, 2010) considering a density of 3.1 g cm^{-3}. The scattering energies from the chromium, phosphorus, chlorine species have been measured at the centre of the peaks associated with the different distributions. The metal / oxide interface has been located by measuring a rise of 50 % in the aluminium profile before reaching the bulk, as established for a sigmoid profile (Hofmann and Mader, 1990). The different variables

calculated for the scale conversion are presented in Table 1.5.

The resulting elemental depth profiles for the specimen electropolished and immersed in the chromic / phosphoric acid solution is presented in Figure 1.11. The thickness of the oxide film is measured at about 3.6 nm. The distributions of the chromium and phosphorus species are located in the outermost part of the oxide, at a depth of 0.9 and 1.1 nm respectively; the FWHM of the chromium and phosphorus profiles are 1.1 nm. In contrast, the distributions of the chlorine and copper species are close to the metal / oxide interface, at depths of 3.5 and 3.6 nm respectively; the FWHM of the chlorine and copper profiles are 1.5 nm.

As in the previous case, the simulation of the energy spectra was best achieved by using an aluminium oxide layer enriched in hydroxide through its uppermost part and containing chlorine in the oxide closer to the metal / oxide interface. A Cr_2O_3 layer and a PO_4^{3-}-enriched layer separate the hydroxide-rich oxide from the oxide. As determined from the simulation of the energy spectra, the atomic ratio of aluminium to oxygen increases from 0.49 in the hydroxide-rich oxide layer to 0.69 in the oxide layer, the hydroxide-enriched oxide representing 15 % of the film thickness.

The contaminant amounts arising from the stripping solution were calculated for chromium and phosphorus to be approximately 0.88 and 0.45 x 10^{15} at cm^{-2} respectively. Chlorine and copper dopants were estimated at about 0.43 and 0.15 x 10^{15} at cm^{-2} respectively. Table 1.6 presents a summary of the contaminant amounts present in the oxide films arising from electropolishing and successive electropolishing and stripping respectively. Thus, significant losses of chlorine and copper arise during stripping of the electropolished specimens; indeed the stripped specimens present about one-third and one-half of the amounts of chlorine and copper incorporated into the oxide presents over the electropolished specimen. However, for the specimens immersed in the stripping solution, a larger uncertainty may affect the quantification of the different species due to the overlapping of the phosphorus and chromium peaks with the chlorine and copper peaks respectively. The losses of the copper and chlorine species may result from local dissolution of the superpure aluminium substrate. The stripping solution can dissolve both aluminium oxide and aluminium metal, with a faster rate for aluminium oxide in comparison with aluminium metal. Thus, local dissolution

of the filmed aluminium substrate, if any, may result in loss of copper and chlorine species which are located close to the metal / oxide interface. The presence of copper and chlorine after stripping, indicates that during the stripping process the oxide film resulting from electropolishing has not been entirely dissolved.

Medium energy ion scattering analysis has been performed on specimens patterned by anodizing in sulphuric acid, oxalic acid and phosphoric acid and subsequent stripping of the oxide film. However, global decrease of the ion yield and energy spreading arises as a result of substrate roughness induced straggling, Fig.1.12. Consequently, broadening of the phosphorus / chlorine and chromium / copper peaks occurs and a roughness-induced peak is revealed at an energy of about 82.5 keV.

Simulation of the energy spectra has been carried out, using the film composition obtained for the specimens successively electropolished and immersed in a chromic / phosphoric acid solution. Figures 1.12.b - 1.12.d present the superimposition of the experimental data and of the simulated peaks for the phosphorus, chlorine, chromium and copper species. The scattered energy values for the phosphorus and chromium peaks is comparable with the values obtained for the specimen immersed in a chromic / phosphoric acid solution; however, poor fitting of the peaks is achieved due to the asymmetric shape of the peaks, Figs. 1.12.f and 1.12.g. The signals of chlorine and copper species could not be distinguished in the spectra; the chlorine and copper signals may be overlapped by the phosphorus and chromium peaks as a result of energy losses.

1.3 Elemental Depth Profiling

In order to gain insight into the depth distribution of the species incorporated into the surface oxide films, elemental depth profiling analyses of the differently patterned specimens have been carried out using GD-OES, GD-TOF-MS and TOF-SIMS.

A comparison of the elemental depth profiling measured by GD-OES, in the pulsed mode, for an electropolished specimen and a specimen successively electropolished and immersed in a chromic / phosphoric acid solution is shown in Figure 1.13. General profiles are presented as well as magnifications of the elemental depth profiles associated with chlorine, phosphorus and chromium species. Additionally, the metal / oxide

interfaces are located by dotted lines, the interface positions have been determined by the position of the maximum slope in the aluminium depth profiles (Angeli et al., 2003).

For the conditions employed for the measurement (power: 20 W, pressure: 800 Pa and duty cycle: 0.20), the sputtering rate has been measured at about 5.3 nm s^{-1}, from depth profiling of anodic oxides of thicknesses up to 360 nm. The sputtering rate determined from anodic oxide films has been used to estimate the thicknesses of the oxide films formed on the superpure aluminium substrates after electropolishing and stripping. For the electropolished and the stripped specimens, the sputtering times required to reach the metal / oxide interfaces are about 0.34 and 0.60 s respectively, which correspond to oxide film thicknesses of about 2.0 and 3.2 nm, assuming a sputtering rate of 5.3 nm s^{-1}. However, these figures should be treated with caution since some material removal may occur during the time required for the plasma to reach an equilibrium state.

The elemental depth profile determined for the electropolished specimen discloses the presence of chlorine species all the way through the oxide film as well as a copper-enrichment at the metal / oxide interface. The chromium and phosphorus profiles are at the background level. The analysis performed on the specimen after stripping reveals the presence of chlorine, chromium and phosphorus species incorporated within the oxide layer. However, for both specimens, the location of the electrolyte-derived species may not be ascertained since the different elemental depth profiles present exponential decay features throughout the oxide; in addition, the peak centres are located in the first 0.05 s of sputtering. Finally, once magnified, the chromium profile obtained by GD-OES present a second peak, the position of the peak matches the intensity decrease of the copper signal, which is considered further later in the last section.

Investigation of the distribution of the species was carried on by TOF-SIMS and GD-TOF-MS analyses. Both techniques present the advantage of a faster detection speed in comparison with the GD-OES technique, due to the use of a time-of-flight detector. Additionally, the TOF-SIMS technique allows adjustment of the sputtering rate which is directly related to the selected etching surface area.

Comparison of the elemental depth profiles obtained by GD-OES, TOF-SIMS and

GD-TOF-MS for the superpure aluminium specimen electropolished and subsequently immersed in a chromic / phosphoric acid solution is presented Fig. 1.14; for clarity, the chlorine profiles were not plotted. In spite of depth profiling the surface film at very slow sputtering rates during the TOF-SIMS and the GD-TOF-MS analyses, 0.04 and 0.22 nm s^{-1} respectively, a better description of the oxide film is not achieved. Indeed, the elemental depth profiles associated with the chromium, phosphorus and chlorine species still present exponential decay characteristics throughout the oxide film thickness. In contrast, the elemental depth profiles measured by MEIS show narrow distributions for the chromium and phosphorus species in the outermost part of the oxide film, while the chlorine and copper species present discrete enrichments close to the metal / oxide interface.

Additionally, for each technique, the elemental depth profile of the 2 nm thick copper-enriched layer, which can be used as a marker for the metal / oxide interface, presents a significant width and tail. Broadening of the copper profile resulting from the development of the crater shape is not unusual during glow discharge analysis of thicker oxides, which present copper-enriched layers buried at greater depths, as displayed with the comparison of elemental depth profiles of 30 and 360 nm thicknesses measured with the 3 different sputtering-induced profiling techniques, Fig. 1.15. Examination of the different profiles indicates, however, that for TOF-SIMS, aluminium profiles show step-like interfaces and the profiles associated with the copper-enriched layers present a width about one-half narrower than the profiles measured for copper by the glow discharge techniques. Considering the thickness of the very thin layers to be analysed, the development of the crater shape, on a large scale, should have a very limited influence on the depth profile analysis performed by the 3 different techniques. However, non-uniform sputtering associated with the initial roughness of the specimen may result in the the development of surface topography and consequently in the broadening of the interfaces. Consequently, for non-uniform sputtering, the elemental depth profiles associated with specimens showing initial roughnesses can not be interpreted according to a model relating the elemental intensities to the sputtering time. The elemental depth profiles should be reconstructed considering a function that describes the sputtering process associated with the surface topographies.

Broadening of the profiles as a result of the initial pattern of the electropolished

superpure aluminium specimen has been investigated. The electropolishing treatment induces a well-defined wave-like pattern on specimens, as established by the topographical characterisation. The specimen pattern presents a period and an amplitude of about 70 nm and 11 nm respectively. Additionally, for the stripped specimen, the thickness of the oxide film covering the surface has been measured to 5 ± 1 nm. Thereby, the specimen presents a ratio of the film thickness to the amplitude of the substrate pattern of less than 1; as a result, the tips of the aluminium substrate are located above the valleys of the oxide layer. Sputtering-induced surface topography development associated with this type of layer configuration is discussed extensively in the Section 3: Depth Profiling Analysis of Patterned Specimens. A brief conclusion is presented here to illustrate the sputtering process for oxide films covering electropolished substrates.

Glow discharge bombardment, using GD-TOF-MS and GD-OES, of 30-nm thick anodic oxide layers, formed on superpure aluminium substrates anodized in phosphoric acid and subsequently immersed in a chromic / phosphoric acid solution, present similar morphologies. GD-TOF-MS and GD-OES elemental depth profiling of such oxide layers result in the development of a peak-like texture. The glow-discharge induced topography modifications of oxide surface arises from the combination of two effects, namely the locally enhanced sputtering of the surface ridges and the increased yield of sputtering for aluminium compared with alumina. Thus, the surface ridges are sputtered more rapidly than the valleys, consequently exposing the aluminium substrate. Finally, for prolonged sputtering, the difference in sputtering yields between the aluminium substrate and the remaining oxide contributes to the development of a peak-like texture. Thus, the sputtering yield appears to be surface curvature dependent and leads to preferential sputtering of the surface peaks. The surface-site dependence of the sputtering yield could possibly be correlated with the variation of the electric field induced by the surface roughness of the specimen. For TOF-SIMS, however, limited influence of the specimen topography on the sputtering process has been found.

Description of the development of a peak-like texture has been carried out with a 30 nm thick oxide layer on substrate showing a 60-nm amplitude. Characterisation of the morphological modifications of 4-nm thick oxide films over substrates patterned by electropolishing is significantly more ambitious. Therefore, oxide films covering substrates patterned by sulphuric, oxalic and phosphoric acid were utilized.

The effect of the substrate amplitudes on the elemental depth profiles performed by GD-OES, TOF-SIMS and GD-TOF-MS is evident in Figures 1.16 - 1.18. The main consequences of the surface roughnesses is the broadening of the aluminium interface and the shape modification of the elemental depth profile associated with the copper-enriched layer, from Gaussian-like into exponential-decay. Additionally, for the profiles obtained by glow discharge techniques, the chromium profiles present a few alterations with, occasionally, an increase of intensity concomitant with the rise of intensity in the aluminium depth profile when approaching the metal / oxide interface, Figs. 1.16.b, 1.16.c and Fig. 1.17.b.

In order to understand how the surface roughness influences depth profile measurements, atomic force microscopy and scanning electron microscopy examinations have been undertaken on partially depth profiled specimens. The specimens studied were native oxide films formed on aluminium substrates patterned by anodizing in phosphoric acid and subsequently immersed in a chromic / phosphoric acid solution.

Atomic force microscopy and scanning electron microscopy images reveal sputtering-induced topographical modifications, Figs. 1.19 and 1.20. The surface topography modifications indicate that the sputtering process is more efficient at the initial ridges of the surface in comparison with the valleys, which develop into peaks as a result of increased times of sputtering. For short times of sputtering, the bottom of the cells present pronounced features; the scanning electron micrograph acquired in the Inlens mode, comprised uniquely of secondary electrons, shows that secondary electron emission yield is lower at the bottoms of the cells than at the peaks of the surface. For longer time, identical contrast for the secondary electron emission yield are displayed. However, the scanning electron micrograph, acquired in the SE2 mode, shows that regions of low secondary electron emission yield correspond to protuberances on the surface. The atomic force microscopy images confirm the presence of features protruding from the surface, with the top part of these elements being concave.

Ion-induced secondary electrons are of primary importance for the self-sustaining or the enhancement of glow discharge plasmas. The topographical modifications of surfaces, under glow discharge bombardment, is believed to depend on the local differences of the

sputtering yield associated with the variations the electric-field and of the secondary electron emission yield induced by the surface roughness of the specimen.

Finally, ion-bombardment induced depth profiling analysis of native oxide film formed on electropolished substrates may be affected, in a similar manner, by the surface roughness of the specimen. Indeed, electropolished specimens display surface topography, despite being of smaller amplitude, similar to the specimens patterned by anodizing in sulphuric, oxalic and phosphoric acids. Therefore, the non-uniform sputtering modelled for specimens of larger roughnesses appears relevant in explaining the process of material removal for native oxide films formed on electropolished substrates and, consequently, the broadening of the profiles during their analysis by glow discharge techniques.

The bimodal distribution of the chromium profiles measured by GD-OES, previously presented, is discussed here. The GD-OES elemental depth profile associated with the chromium enrichment of the native oxide film formed on stripped specimen reveals an exponential-decay feature throughout the oxide film and the superimposition of a Gaussian-like peak, at a location that may be related with the intensity decrease in the copper profile. Highly localized deposition of Cr_2O_3 at residual flaws, has been assumed previously in order to interpret the bi-modal distribution of chromium species (Shimizu et al., 1999d).

However, a similar distribution could not be seen on the TOF-SIMS or GD-TOF-MS depth profiles; in addition, MEIS analysis displays the presence of a chromium-enrichment only in the outermost part of the oxide film.

In order to elucidate the presence of a chromium-enrichment close to the metal / oxide interface, elemental depth profiling of the native oxide and of 7, 12 and 30 nm thick anodic oxide films was undertaken by the different depth profiling techniques. The evolution of the GD-OES profiles, measured in the continuous mode, is presented Figure. 1.21; the TOF-SIMS and the GD-TOF-MS profiles for the respective anodic oxide films disclose a unique distribution of the chromium species.

Thus, the GD-OES profiles associated with the 7 and 12 nm thick anodic oxide films

reveal a peak in the chromium profile beneath the metal / oxide interface. However, the intensity of this peak decrease with the thickness of the film; indeed, the intensity for the 12 nm thick film is significantly less than for the native oxide or the 7 nm thick anodic oxide film and finally reaches the background level for the 30 nm thick oxide. During anodizing chromium species have been reported to migrate outward, with a migration rate of about 0.70 relative to aluminium ions. Therefore, the migration of chromium ions combined with the regressing metal / oxide interface as a result of oxygen migration, may result in the incorporation of the chromium species initially present underneath the metal / oxide interface, if any, into the anodic film. However, as displayed on the elemental depth profiles of the different anodic layers, the chromium depth profiles do not present any variations, within the oxide film at proximity of the metal interface, which could be associated with such a chromium incorporation.

Finally, the location of the chromium peak, close to the interface, is concomitant with the decrease of intensity in the copper profile, which corresponds approximately to the transition between the copper-enriched layer and the aluminium substrate. The change in the composition may significantly influence the local sputtering yield and result in the rise of the intensity of the chromium signal.

1.4 Conclusions

Superpure aluminium substrates of tailored pattern have been generated by electropolishing and anodizing in different acids, in a reproducible way, with surface roughnesses in the range 1 - 32 nm.

As a result of electropolishing and the oxide film stripping processes, incorporation of electrolyte-derived species into the oxide layer formed over the patterned substrates has been established. Estimation of the oxide film thickness has been undertaken from characterisation using TEM, XPS, MEIS and GD-OES; an average thickness of about 4 $\pm$ 1 nm has been calculated. The surface film composition has been described using XPS and MEIS techniques. The surface film formed on specimen successively electropolished and immersed in a chromic / phosphoric acid solution consists of an aluminium oxide layer variously doped with chromium, phosphorus and chlorine impurities at about 0.88 x 10^{15}, 0.45 x 10^{15} and 0.15 x 10^{15} at cm^{-2}. The chromium and phosphorus species are incorporated as oxides as determined by the XPS analysis. Additionally, the outermost part of the film is comprised of hydroxide-enriched oxide which represents between 15 % or 30 % of the total oxide thickness as calculated by MEIS and XPS respectively. The difference in the values is explained in part for XPS, since no corrections have been performed on the hydroxyl compounds for the oxygen associated with the carbonaceous contamination.

Insight into the growth of the anodic oxide film is considered further in the next Section, using the migration of the chromium and phosphorus species during anodizing of aluminium.

Tables

Table 1.1 – Surface pattern characterisation (TEM).

Pattern parameters (nm)	Substrate patterned by: electropolishing	sulphuric acid	oxalic acid	phosphoric acid
Amplitude	11	16	32	65
Period	70	54	80	200
Cell diameter	-	50 ± 15	80 ± 20	200 ± 60

Table 1.2 – Surface roughness characterisation (AFM).

Pattern parameters	Substrate patterned by: electropolishing	sulphuric acid	oxalic acid	phosphoric acid
Sq (nm)	1.42	7.07	11.4	31.4
Sa (nm)	1.21	5.23	9.00	25.7
Sp (nm)	4.71	76.2	73.6	165
Sv (nm)	5.72	19.3	28.4	67.7
Sz (nm)	10.4	95.5	102.0	233
Ssk	-0.00267	0.775	0.425	0.343
Sku	2.14	5.52	3.73	2.79

Table 1.3 – Motif analysis of the controlled patterns of superpure aluminium substrates patterned by the growth of porous anodic oxide films in different acids and revealed by stripping of the porous films in a chromic / phosphoric acids solution.

Motif parameters	Substrate patterned by: sulphuric acid	oxalic acid	phosphoric acid
density (μm^{-2})	958	447	62
mean height (nm)	13	27	48
mean area (μm^2)	0.00503	0.01120	0.08120
cell diameter† (nm)	40	60	161

† the cell diameters are calculated from the mean area values and assuming circular shape

Table 1.4 – Peak parameters from XPS fitted spectra measured on superpure aluminium specimens electropolished for 3 min as well as specimens successively electropolished for 3 min then stripped in a chromic / phosphoric acid solution; all binding energies (BE) are corrected to C 1s at 285.0 eV except for Al and O, O 1s BE being referenced to Al 2p - ox.

	after stripping			after electropolishing		
Peaks	BE (eV)	FWHM (eV)	Proportion (%)	BE (eV)	FWHM (eV)	Proportion (%)
Al $2p_{3/2}$	68.9	0.41	29.8	68.9	0.41	22.3
Al $2p_{1/2}$	69.4	0.41	14.9	69.3	0.41	11.2
Al 2p - ox	71.8	1.61	55.1	72.0	1.55	66.5
O 1s - 1	456.7	1.57	61.2	456.6	1.66	39.9
O 1s - 2	457.7	1.57	30.8	457.8	1.66	57.6
O 1s - 3	458.9	1.57	7.9	459.0	1.66	2.48
Cl 2p - 1	198.9	1.60	66.7	198.5	1.69	66.7
Cl 2p - 2	200.7	1.60	33.7	200.2	1.69	33.3
P $2p_{3/2}$	133.9	1.87	35.1	-	-	-
P $2p_{1/2}$	134.0	1.87	17.5	-	-	-
Cr 2p - 1	576.1	1.00	4.1	-	-	-
Cr 2p - 2	577.2	1.00	30.7	-	-	-
Cr 2p - 3	578.0	1.00	28.1	-	-	-
Cr 2p - 4	578.9	1.00	24.4	-	-	-
Cr 2p - 5	580.0	1.00	12.7	-	-	-

Table 1.5 – Parameters for the conversion of the energy scale into a depth scale.

Element	Atomic mass	Kinematic factor (K)	$^{\dagger}E_s$ (keV)	$^{\ddagger}E_d$ (keV)	ΔE (keV)	S_r (eV nm^{-1})	Δx (nm)
Al	27.0	0.74	75.60	73.40	2.20	232	3.6
P	31.0	0.77	76.62	77.90	0.71	238	1.1
Cl	35.5	0.80	77.06	79.00	2.26	240	3.5
Cr	52.0	0.86	84.89	86.75	0.59	250	0.9
Cu	63.5	0.88	85.42	87.35	2.47	250	3.6

† scattering energies from the different elements if they were present at the surface

‡ scattering energies detected from the different elements

Table 1.6 – Quantification from MEIS spectra of the electrolyte-derived species incorporated into the oxide films present on superpure aluminium specimens electropolished for 3 min and specimens successively electropolished for 3 min then stripped in a chromic / phosphoric acid solution.

Element	Amount (10^{15} at cm^{-2})	
	after stripping	after electropolishing
Cl	0.43	1.39
Cu	0.15	0.33
Cr	0.88	-
P	0.45	-

Figures

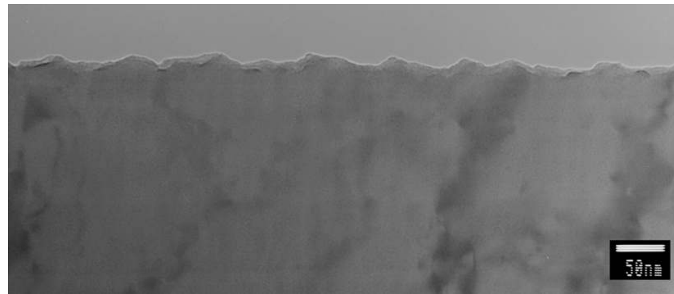

(a) – As-rolled superpure aluminium material

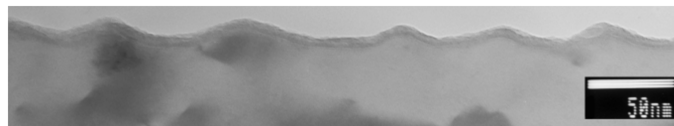

(b) – Superpure aluminium specimen after electropolishing for 3 min

Figure 1.1 – Transmission electron micrographs of ultramicrotomed sections of a. the as-rolled superpure aluminium material and b. a superpure aluminium specimen after electropolishing for 3 min.

(a) – Anodizing in 0.3 M sulphuric acid solution for 5 min

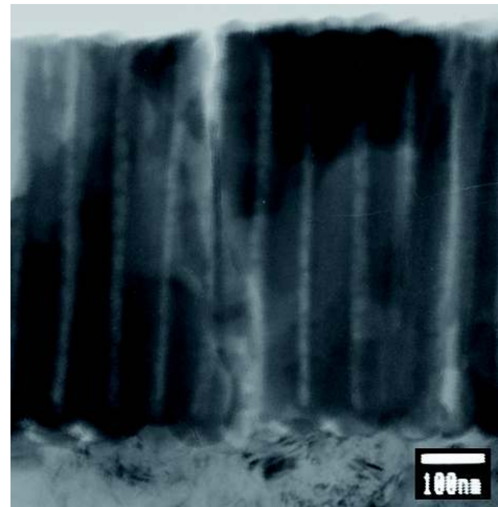

(b) – Anodizing in 0.3 M oxalic acid solution for 5 min

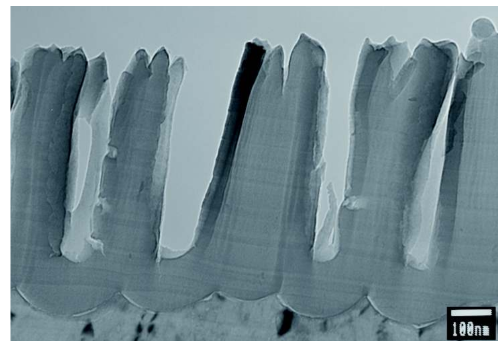

(c) – Anodizing in 0.3 M phosphoric acid solution for 5 min

Figure 1.2 – Transmission electron micrographs of ultramicrotomed sections of superpure aluminium specimens after anodizing for 5 min in a. sulphuric acid, b. oxalic acid and c. phosphoric acid.

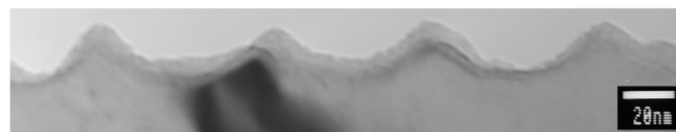

(a) – Patterning in sulphuric acid

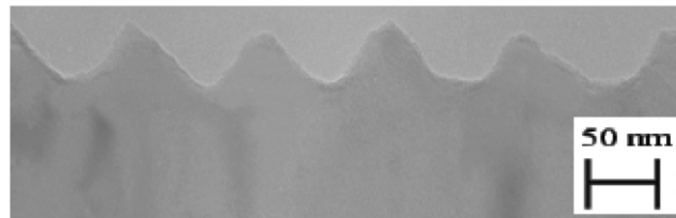

(b) – Patterning in oxalic acid

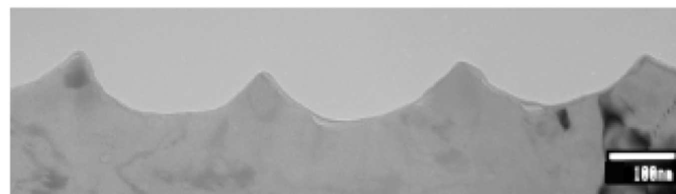

(c) – Patterning in phosphoric acid

Figure 1.3 – Transmission electron micrographs of ultramicrotomed sections of superpure aluminium specimens after stripping, in a chromic / phosphoric acids solution, of the porous anodic oxide films formed by anodizing for 5 min, in a. sulphuric acid, b. oxalic acid and c. phosphoric acid.

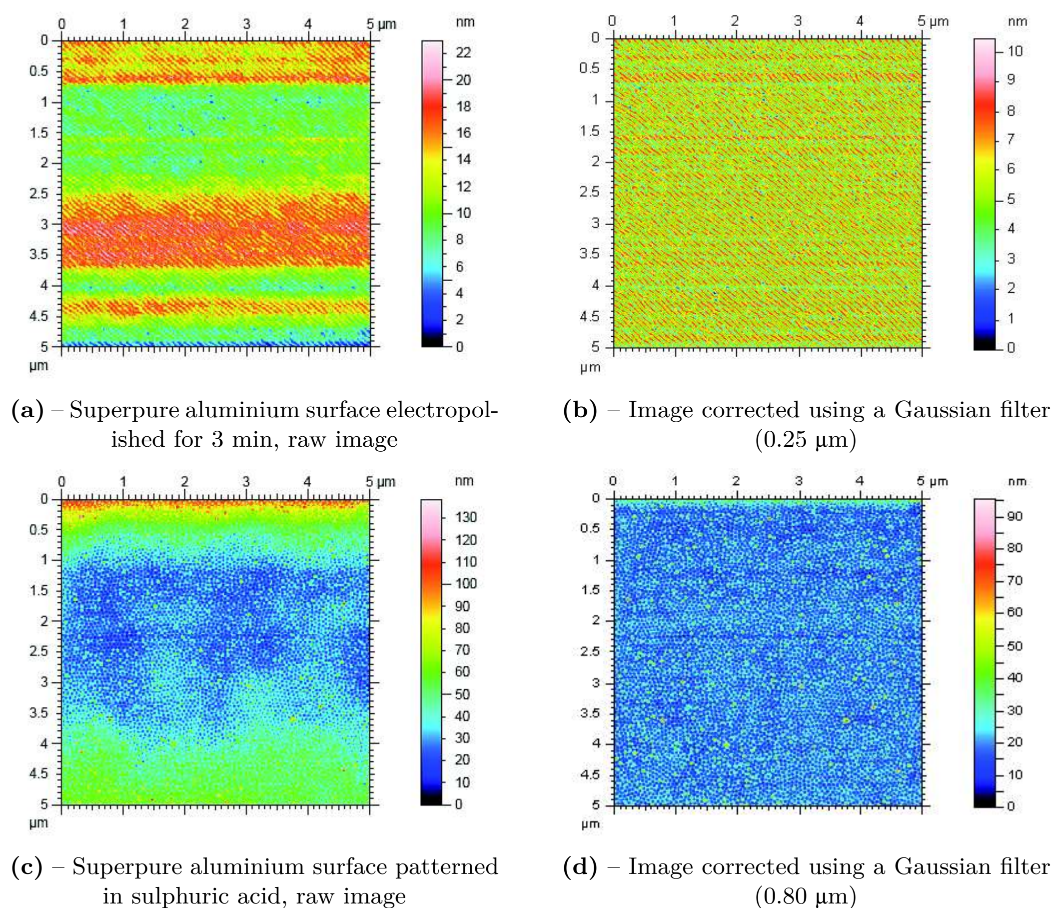

(a) – Superpure aluminium surface electropolished for 3 min, raw image

(b) – Image corrected using a Gaussian filter (0.25 µm)

(c) – Superpure aluminium surface patterned in sulphuric acid, raw image

(d) – Image corrected using a Gaussian filter (0.80 µm)

Figure 1.4 – Atomic force microscopy images of superpure aluminium specimens after electropolishing for 3 min a. raw image and b. image corrected using a Gaussian filter (0.25 µm) and after stripping of a porous film formed in sulphuric acid c. raw image and d. image corrected using a Gaussian filter (0.80 µm).

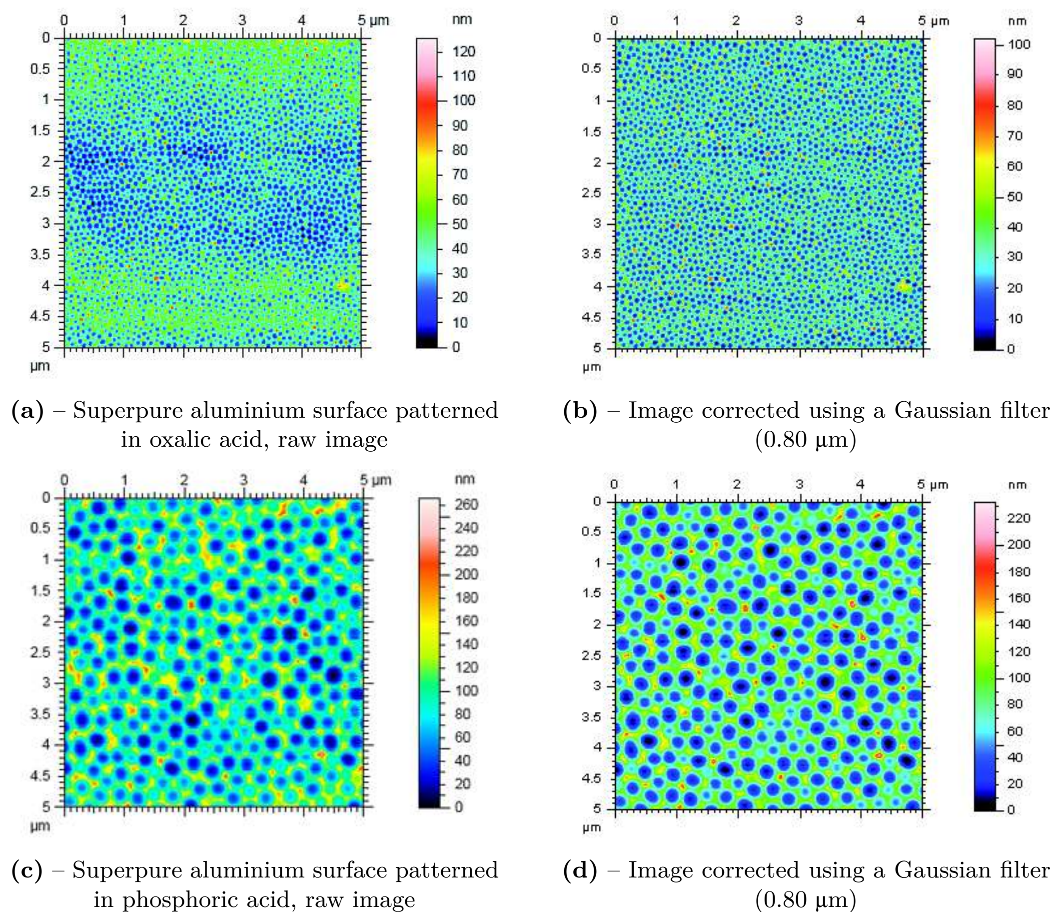

(a) – Superpure aluminium surface patterned in oxalic acid, raw image

(b) – Image corrected using a Gaussian filter (0.80 µm)

(c) – Superpure aluminium surface patterned in phosphoric acid, raw image

(d) – Image corrected using a Gaussian filter (0.80 µm)

Figure 1.5 – Atomic force microscopy images of superpure aluminium substrates after stripping of a porous film formed in oxalic acid a. raw image and b. image corrected using a Gaussian filter (0.25 µm), and in phosphoric acid c. raw image and d. image corrected using a Gaussian filter (0.80 µm).

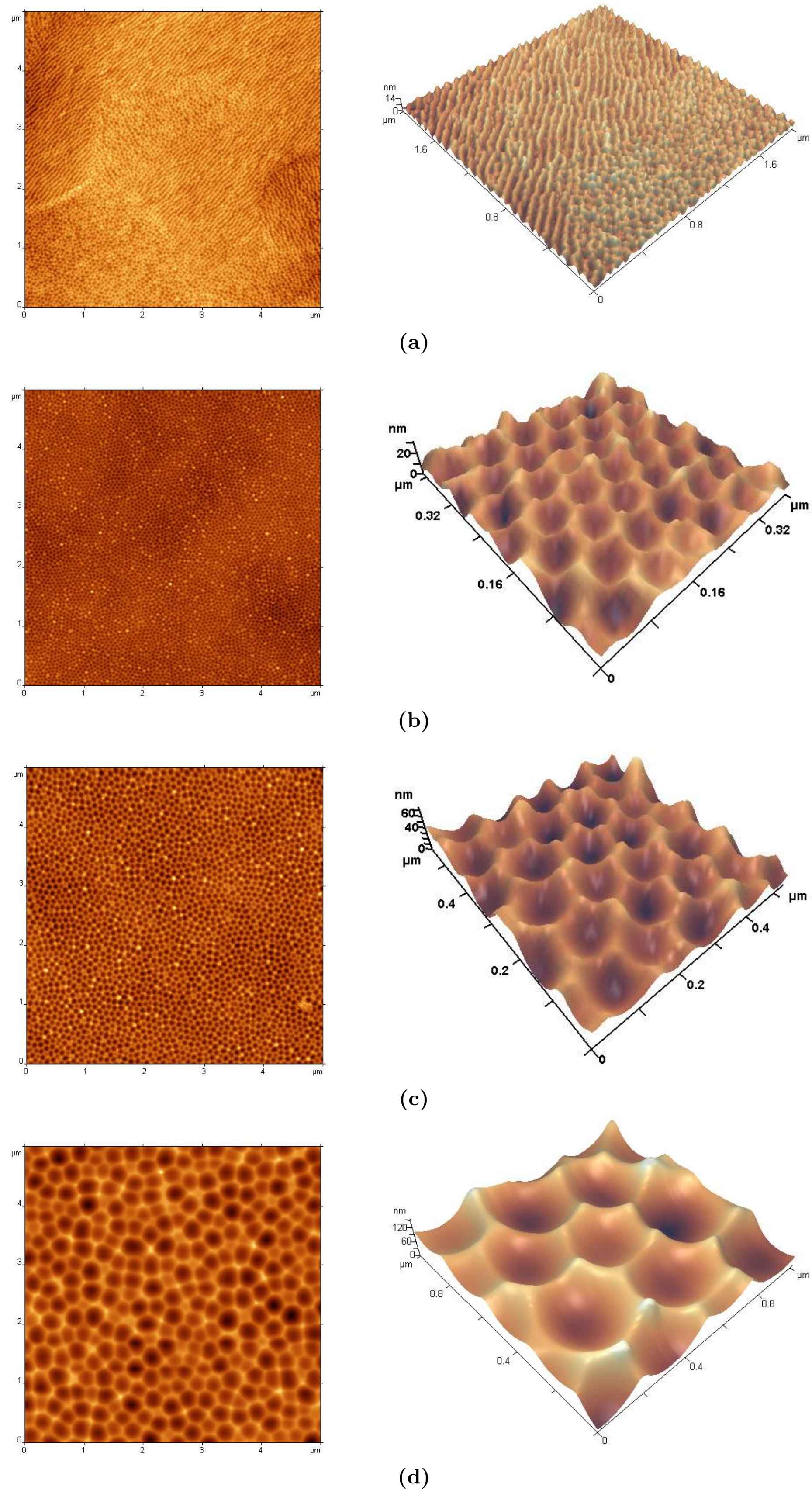

Figure 1.6 – Atomic force microscopy images of a superpure aluminium specimen after a. electropolishing for 3 min and stripping of the air-formed film, showing a regular furrow pattern and a regular hexagonal pattern in particular grain orientations, and anodizing in b. sulphuric acid, c. oxalic acid, d. phosphoric acid for 5 min and stripping of the porous anodic oxide, disclosing an hexagonal cell-array pattern.

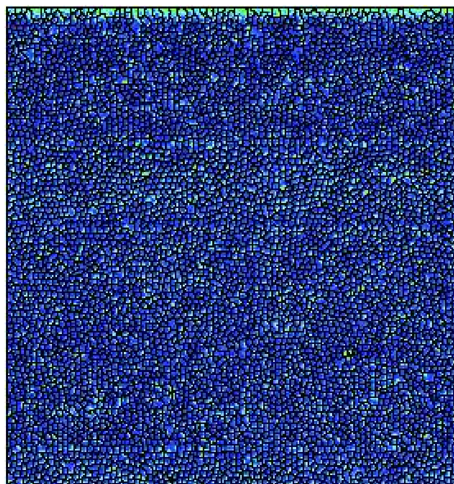

(a) – Patterning in sulphuric acid

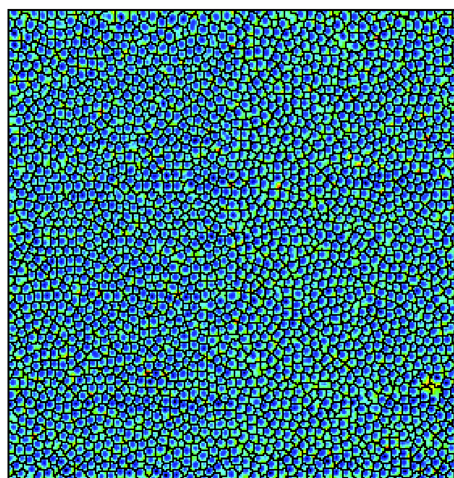

(b) – Patterning in oxalic acid

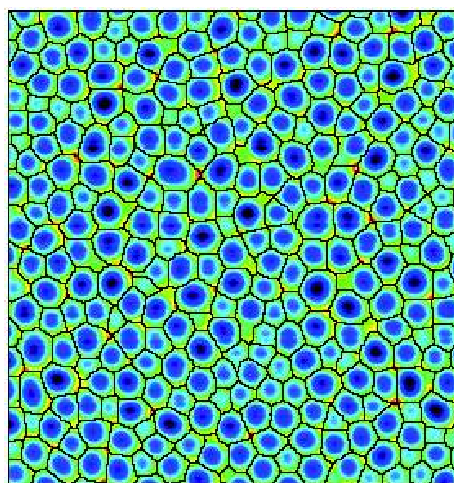

(c) – Patterning in phosphoric acid

Figure 1.7 – Motif analysis of the controlled textures of superpure aluminium substrates patterned by growth of porous anodic oxide films in different acids and revealed by stripping of the porous films in a chromic / phosphoric acids solution, patterning in a. sulphuric acid, b. oxalic acid and c. phosphoric acid.

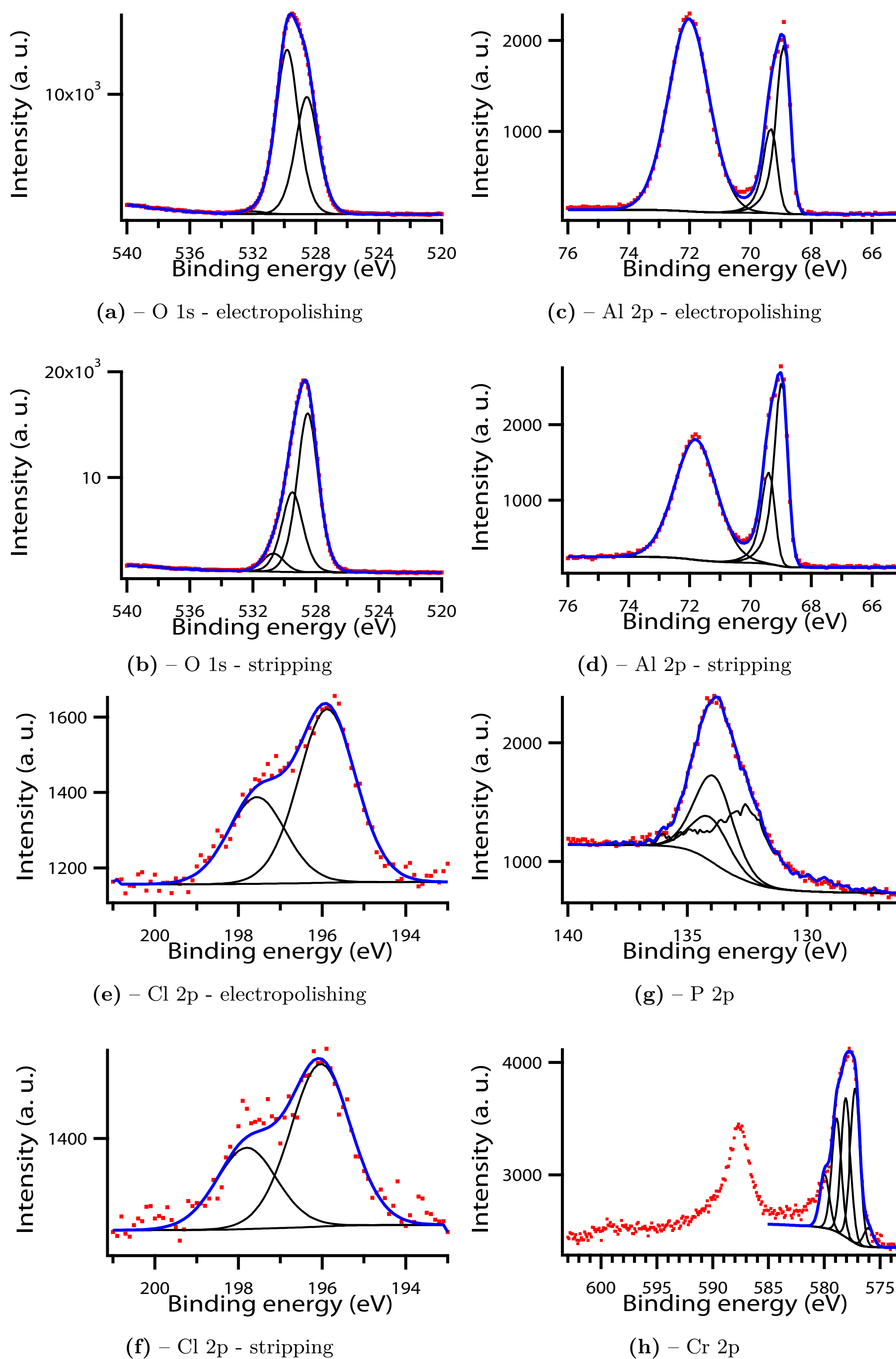

(a) – O 1s - electropolishing

(c) – Al 2p - electropolishing

(b) – O 1s - stripping

(d) – Al 2p - stripping

(e) – Cl 2p - electropolishing

(g) – P 2p

(f) – Cl 2p - stripping

(h) – Cr 2p

Figure 1.8 – Measured (dots) and simulated (solid line) XPS spectra of superpure aluminium specimens electropolished and successively electropolished and stripped, showing a comparison of the core levels a., b. O 1s; c.,d. Al 2p; e.,f. Cl 2p and g. P 2p, h. Cr 2p, All spectra are presented uncorrected for charging, except Cr 2p and P 2p which are charge-corrected to C 1s at 285 eV.

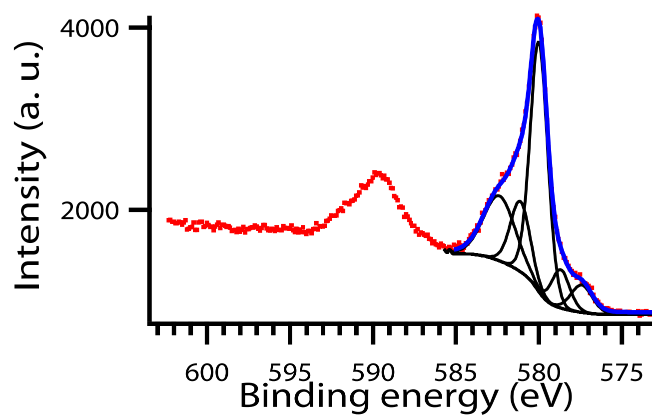

(a) – Cr (VI)

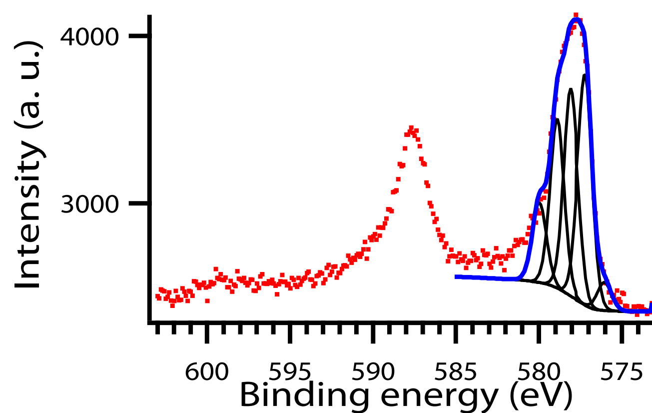

(b) – Cr (III)

Figure 1.9 – Measured (dots) and simulated (solid line) XPS spectra showing a comparison of the core levels Cr 2p for a. the CrO_3 powder used for the preparation of the stripping solution and b. a superpure aluminium specimen successively electropolished and immersed in a chromic / phosphoric solution. Both spectra are charge-corrected to C 1s at 285 eV.

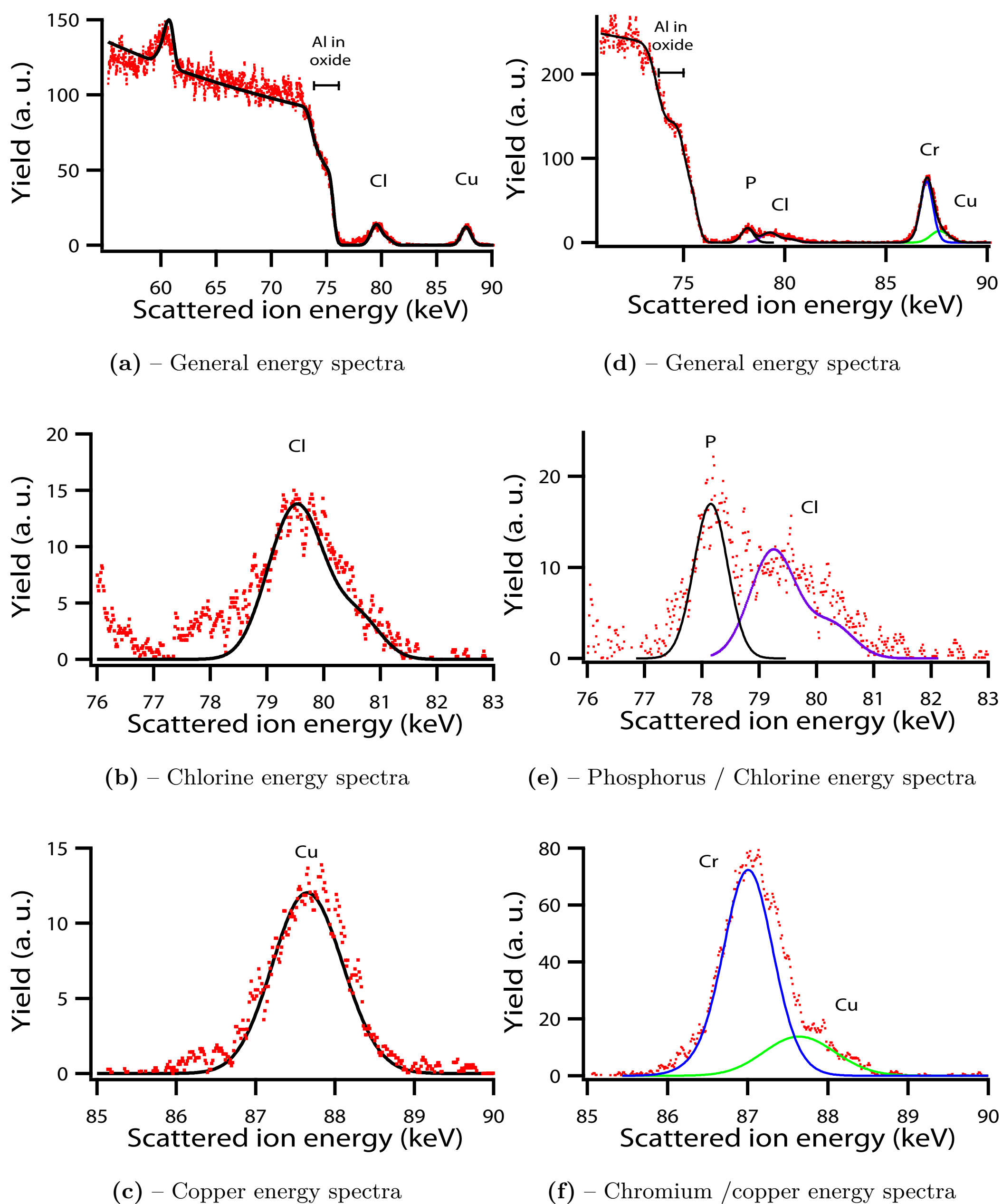

(a) – General energy spectra

(d) – General energy spectra

(b) – Chlorine energy spectra

(e) – Phosphorus / Chlorine energy spectra

(c) – Copper energy spectra

(f) – Chromium /copper energy spectra

Figure 1.10 – Measured (dots) and simulated (solid line) MEIS spectra of a superpure aluminium specimen after electropolishing, a. general energy spectra, and magnification of the energy spectra of the impurities present b. chlorine, c. copper and after successive electropolishing and stripping in a chromic / phosphoric acid solution, d. general spectra, and magnification of the the energy spectra of the impurities present e. phosphorus / chlorine, f. chromium / copper.

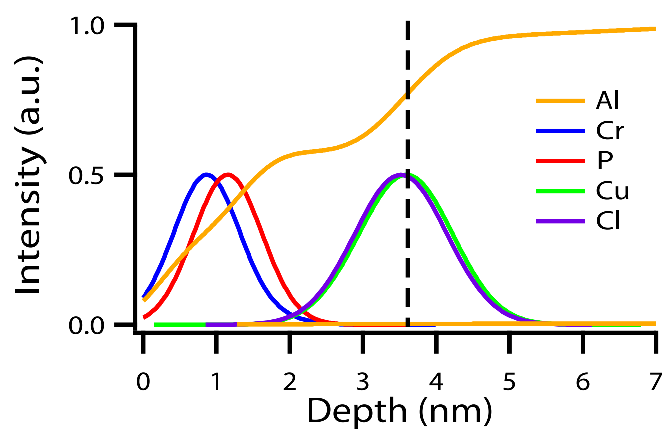

Figure 1.11 – Elemental depth profile calculated from the MEIS spectra of a superpure aluminium specimen electropolished and immersed in a chromic / phosphoric acid solution. The dashed line indicates the metal / oxide interface.

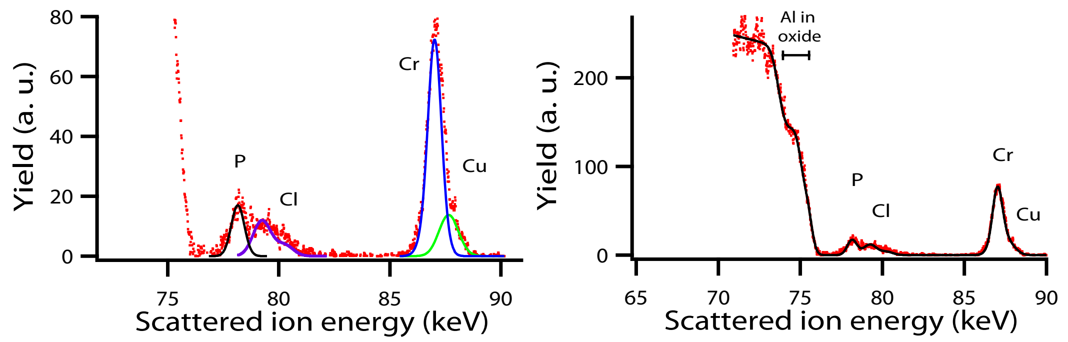

(a) – Patterning by electropolishing

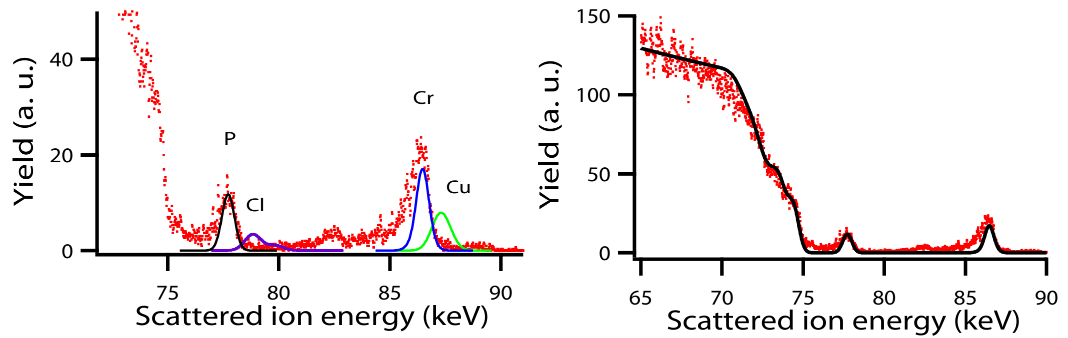

(b) – Patterning in sulphuric acid

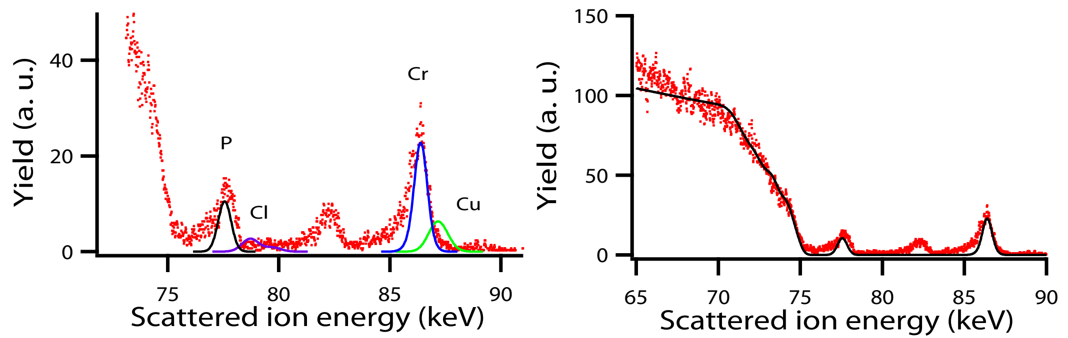

(c) – Patterning in oxalic acid

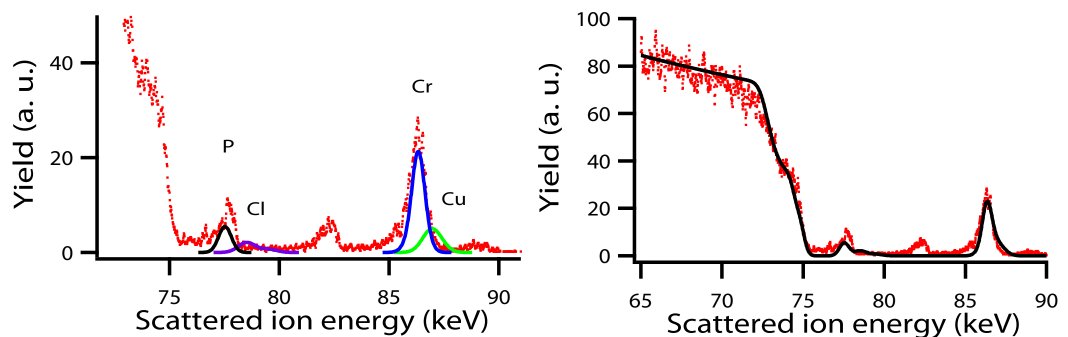

(d) – Patterning in phosphoric acid

Figure 1.12 – Superimposition of elemental spectra (solid line), simulated for P, Cl, Cr and Cl species, on MEIS spectra of a superpure aluminium specimen patterned by a. electropolishing, b. sulphuric acid, c. oxalic acid and d. phosphoric acid.

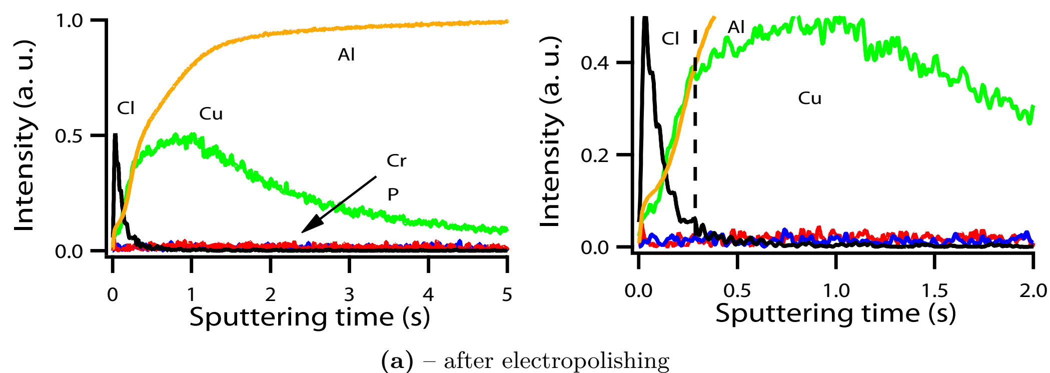

(a) – after electropolishing

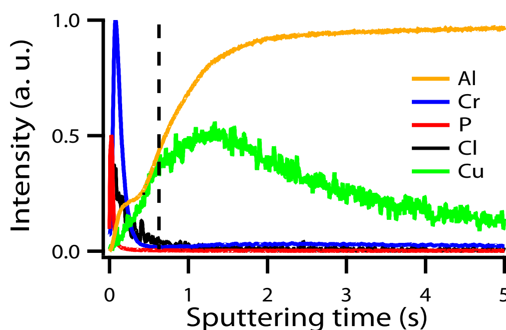

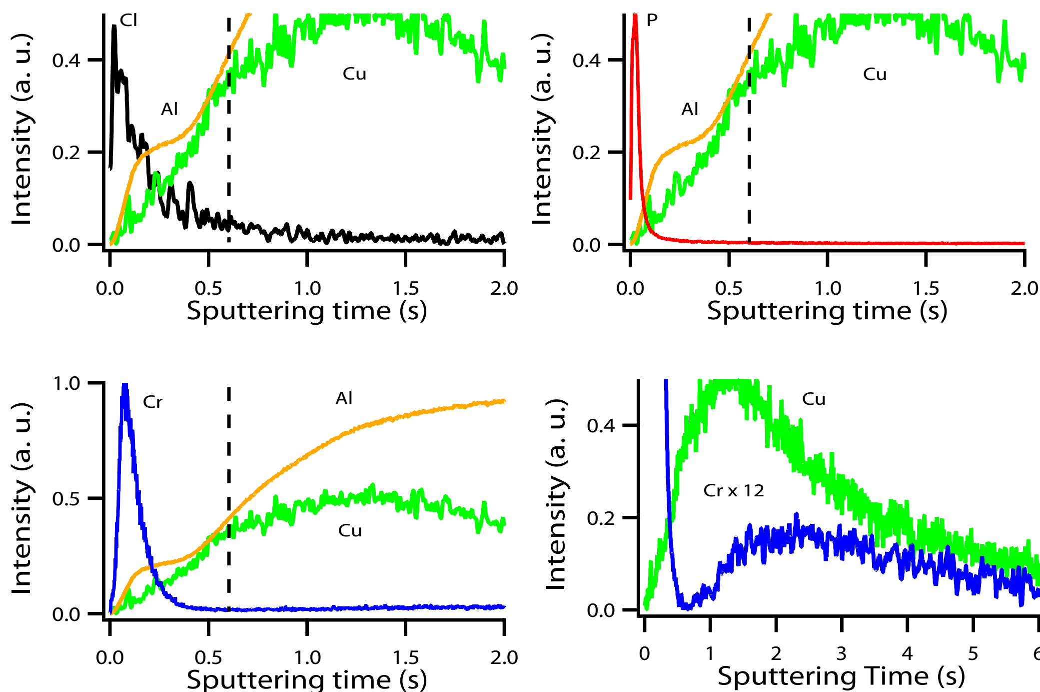

(b) – after electropolishing and stripping

Figure 1.13 – Comparison of GD-OES elemental depth profiles, measured in the pulsed mode, of air-formed films formed on superpure aluminium substrate a. electropolished in a perchloric acid / ethanol solution and b. successively electropolished and stripped in a chromium / phosphoric acid solution. General profiles are presented as well as magnifications of chlorine, phosphorus and chromium depth profiles.

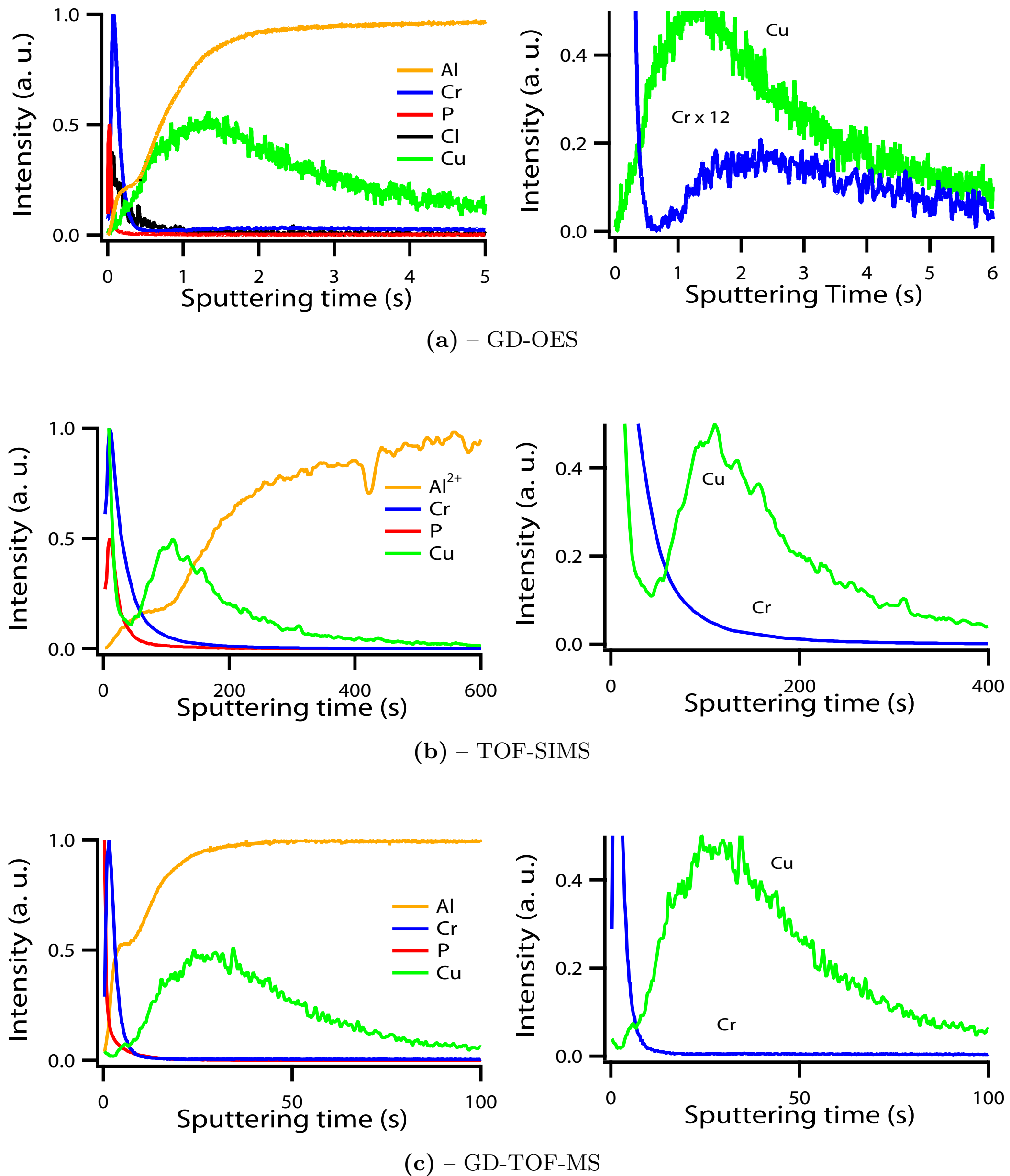

(a) – GD-OES

(b) – TOF-SIMS

(c) – GD-TOF-MS

Figure 1.14 – Comparison of elemental depth profiles of air-formed films formed on a superpure aluminium substrates successively electropolished and stripped in a chromium / phosphoric acid solution, using a. GD-OES, b. TOF-SIMS and c. GD-TOF-MS.

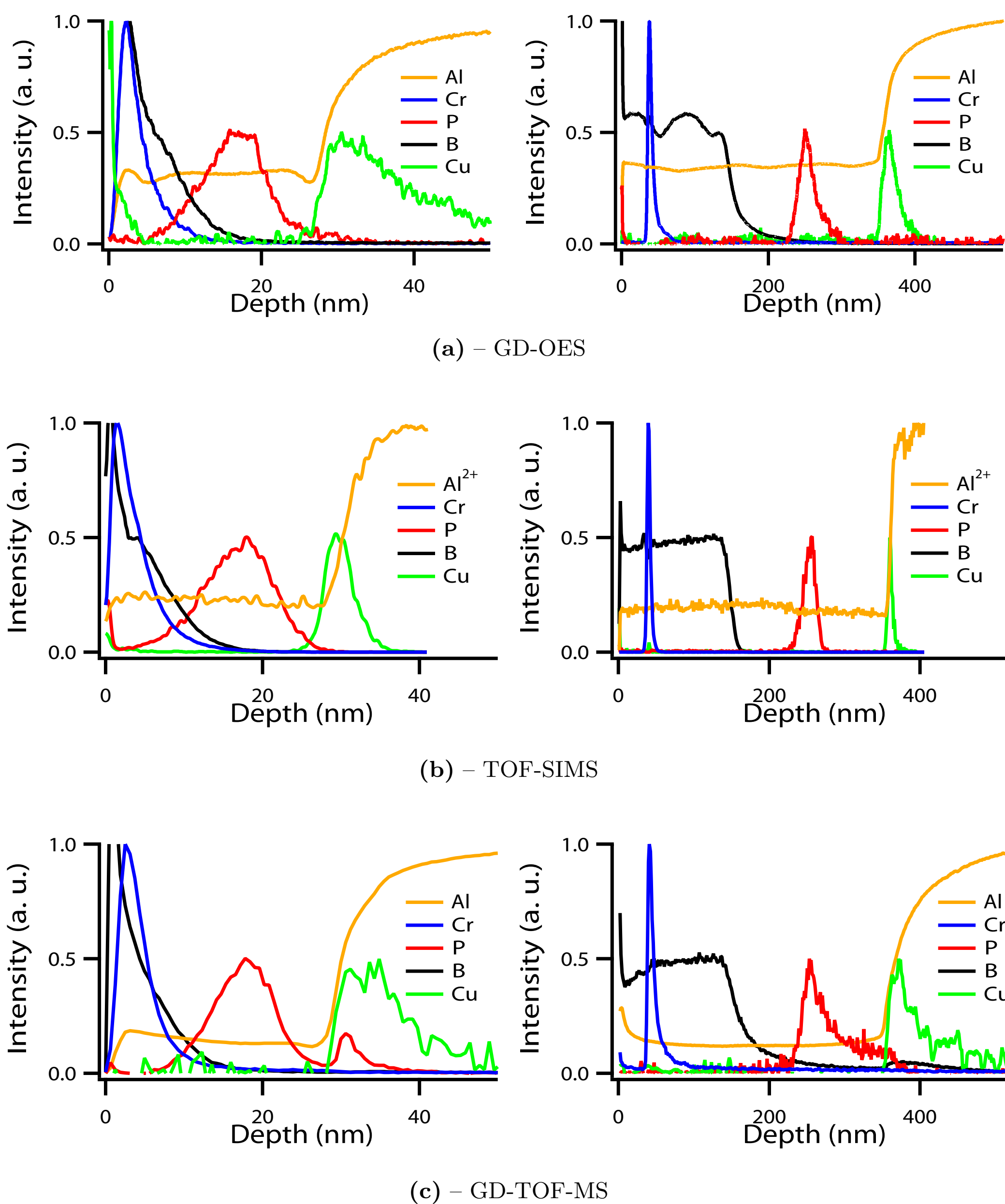

(a) – GD-OES

(b) – TOF-SIMS

(c) – GD-TOF-MS

Figure 1.15 – Elemental depth profile analysis of anodic alumina films, formed by anodizing electropolished superpure aluminium substrates in ammonium pentaborate to 30 and 360 nm, using a. GD-OES, b. TOF-SIMS and c. GD-TOF-MS.

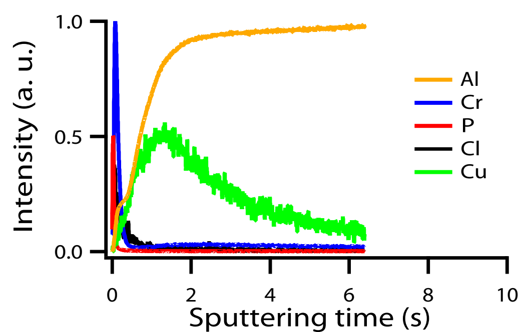

(a) – Patterning by electropolishing

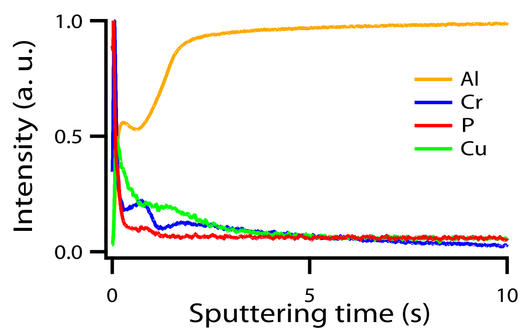

(b) – Patterning in sulphuric acid

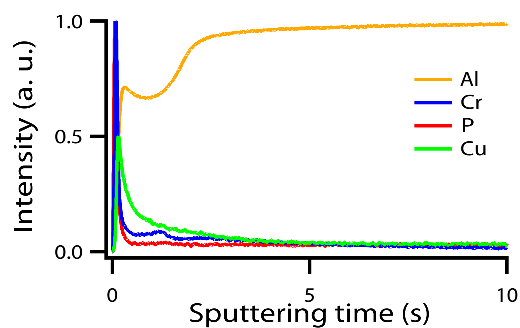

(c) – Patterning in oxalic acid

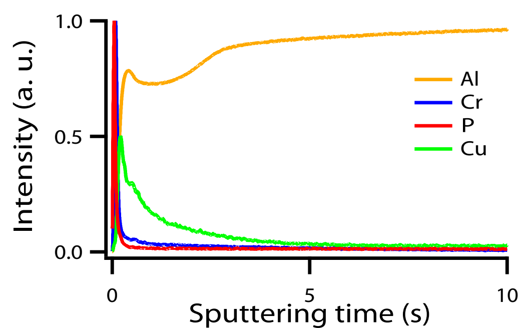

(d) – Patterning in phosphoric acid

Figure 1.16 – GD-OES elemental depth profile analysis of native oxide films present on superpure aluminium substrates patterned by a. electropolishing, b. sulphuric acid, c. oxalic acid and d. phosphoric acid.

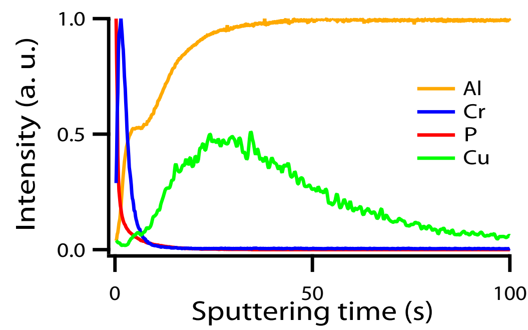

(a) – Patterning by electropolishing

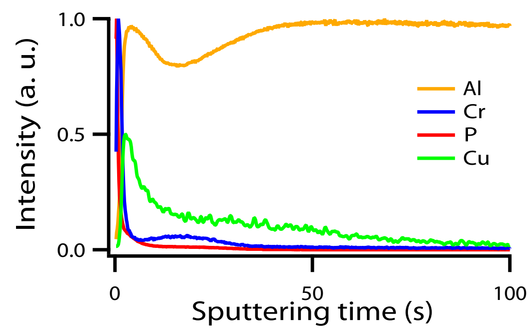

(b) – Patterning in sulphuric acid

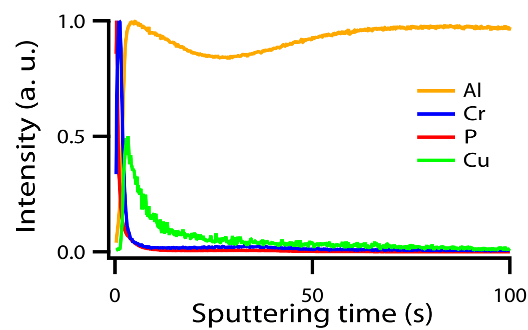

(c) – Patterning in oxalic acid

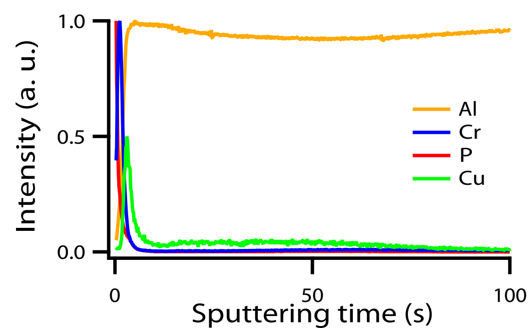

(d) – Patterning in phosphoric acid

Figure 1.17 – GD-TOF-MS elemental depth profile analysis of native oxide films present on superpure aluminium substrates patterned by a. electropolishing, b. sulphuric acid, c. oxalic acid and d. phosphoric acid.

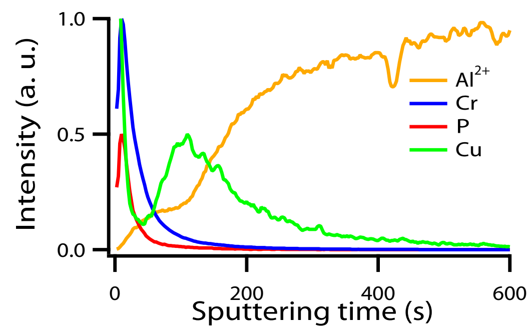

(a) – Patterning by electropolishing

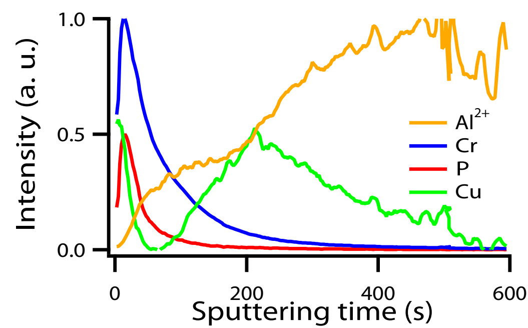

(b) – Patterning in sulphuric acid

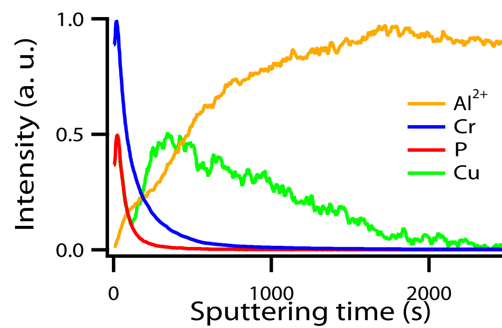

(c) – Patterning in oxalic acid

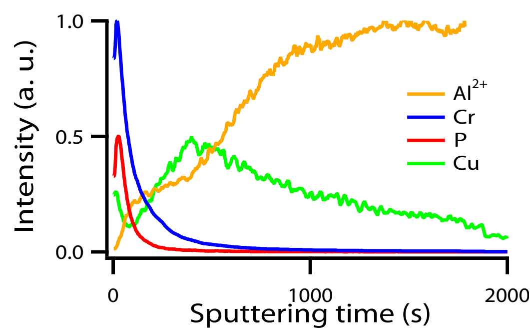

(d) – Patterning in phosphoric acid

Figure 1.18 – TOF-SIMS elemental depth profile analysis of native oxide films present on superpure aluminium substrates patterned by a. electropolishing, b. sulphuric acid, c. oxalic acid and d. phosphoric acid.

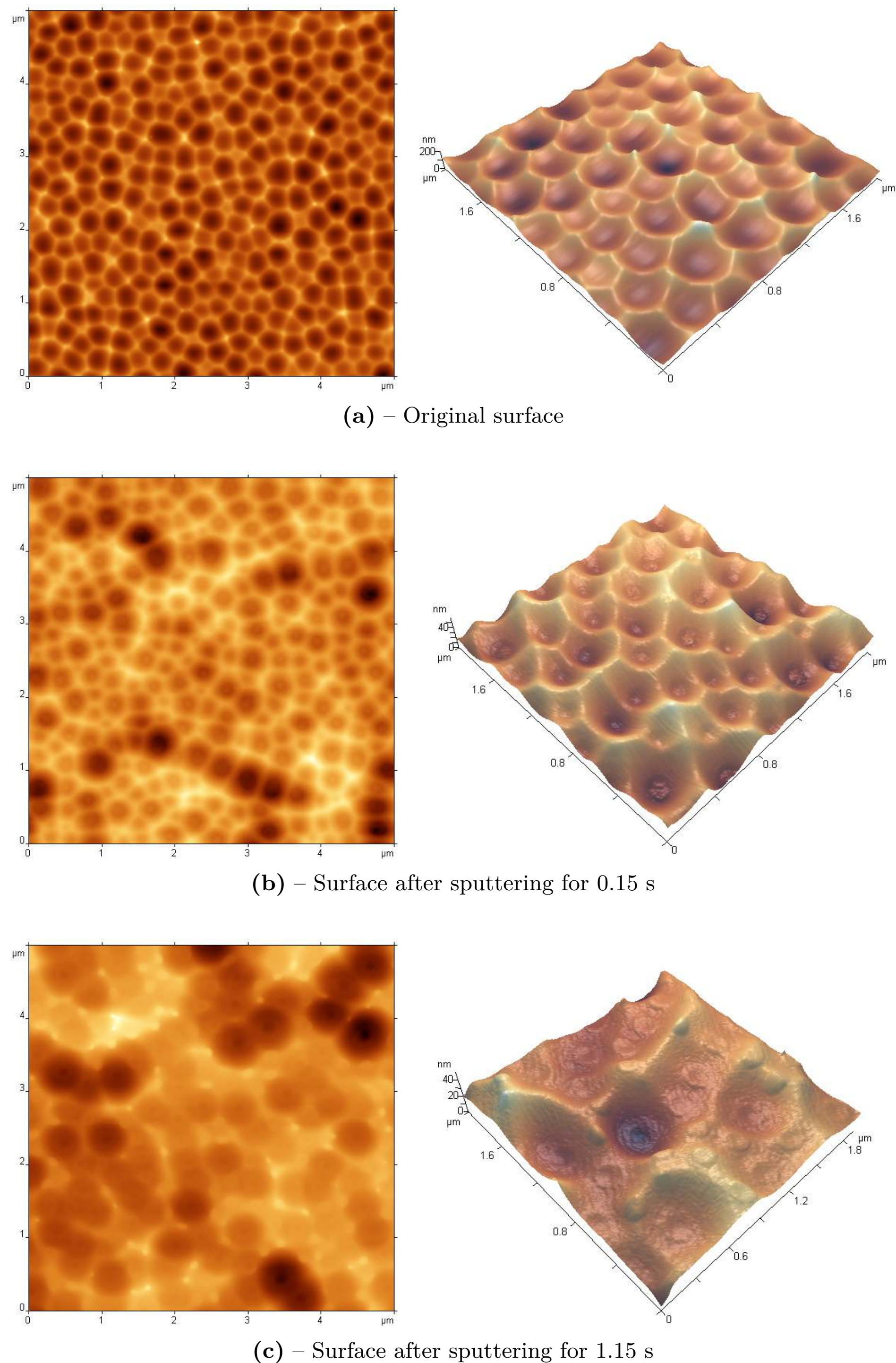

(a) – Original surface

(b) – Surface after sputtering for 0.15 s

(c) – Surface after sputtering for 1.15 s

Figure 1.19 – Atomic force microscopy images of native oxide films, formed on superpure aluminium specimens patterned by anodizing in phosphoric acid and subsequently stripped, a. original oxide film surface; and b., c. surface after sputtering, using GD-OES, of the oxide for b. 0.15 s and c. 1.15 s. The scanning area of the top view image is 5 µm^2, whereas the 3 D view area is reduced to 2 µm^2 and the z-scales represent about 200 nm for a. and 40 nm for b. and c.

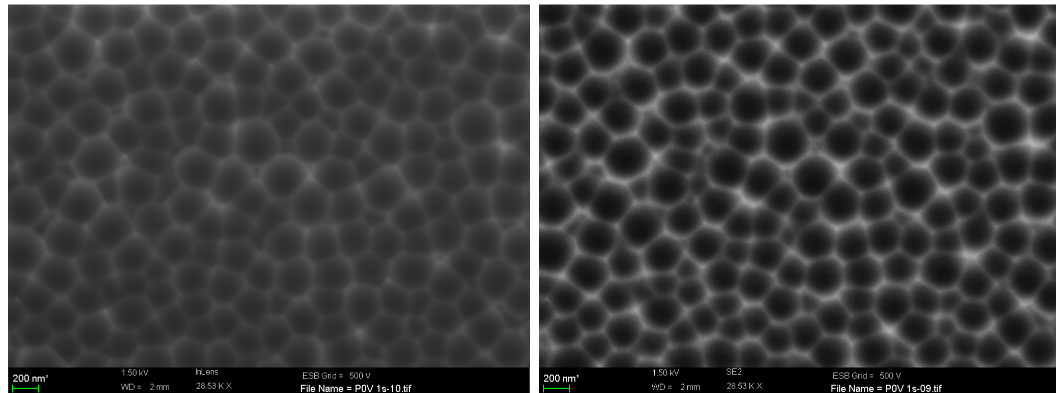

(a) – Original surface - Inlens mode **(b)** – Original surface - SE2 mode

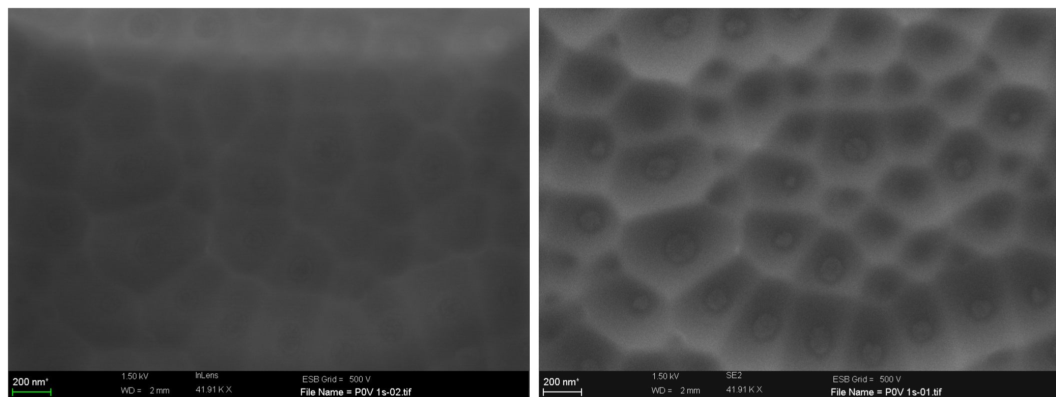

(c) – Surface after sputtering for 0.15 s - Inlens mode **(d)** – After sputtering for 0.15 s - SE2 mode

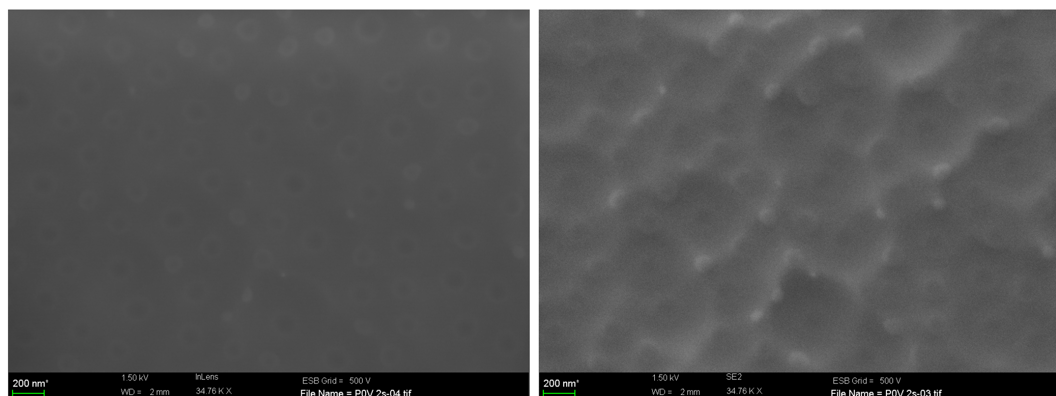

(e) – Surface after sputtering for 1.15 s - Inlens mode **(f)** – Surface after sputtering for 1.15 s - SE2 mode

Figure 1.20 – Scanning electron micrographs of native oxide films, formed on superpure aluminium specimens patterned by anodizing in phosphoric acid and subsequent stripping of the porous film, a. original oxide film surface; and b., c. surface after sputtering, using GD-OES, of the oxide for b. 0.15 s and c. 1.15 s.

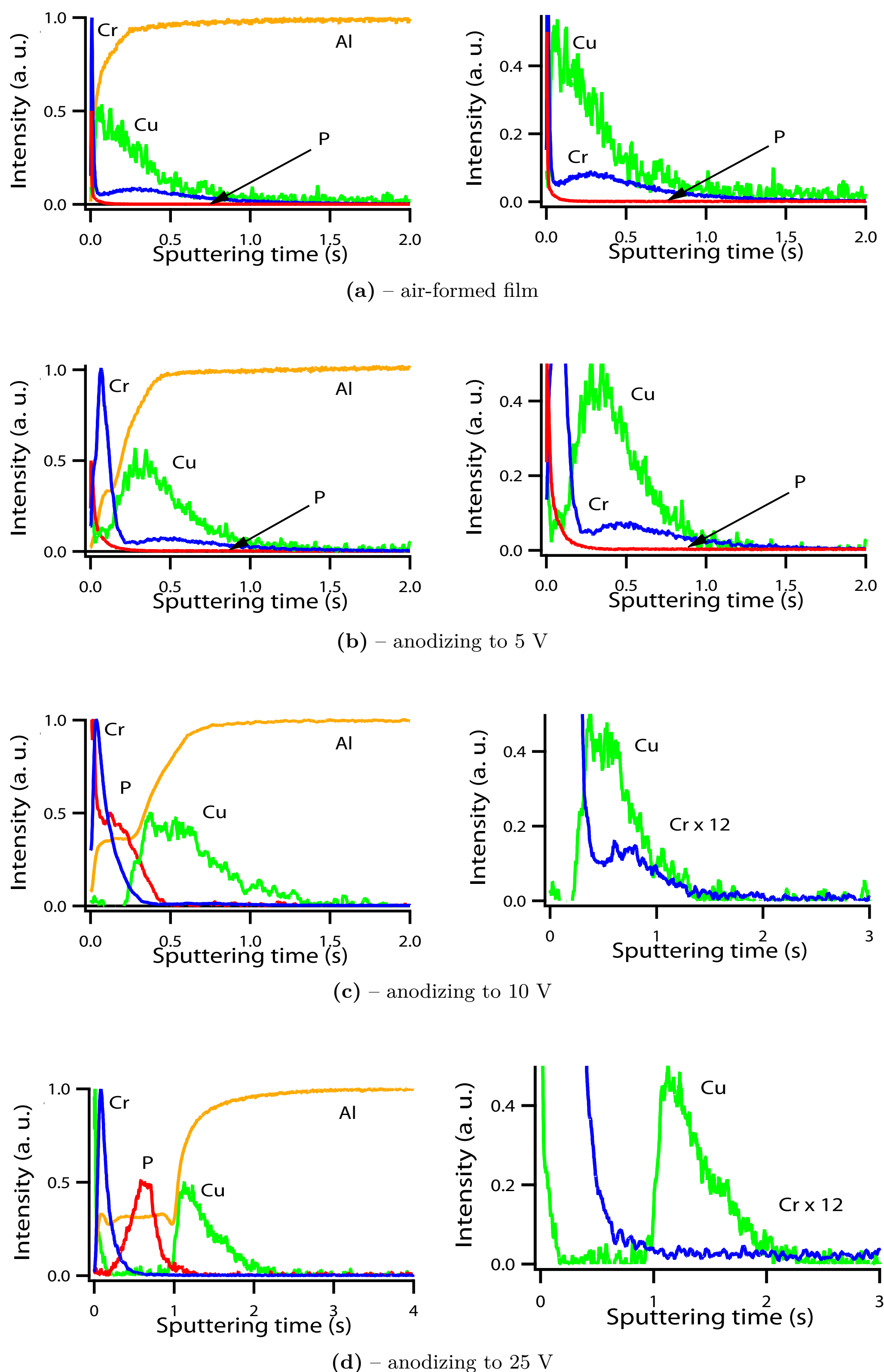

(a) – air-formed film

(b) – anodizing to 5 V

(c) – anodizing to 10 V

(d) – anodizing to 25 V

Figure 1.21 – Comparison of GD-OES elemental depth profiles measured in the continuous mode of a. an air-formed film formed on a superpure aluminium substrate successively electropolished and stripped in a chromium / phosphoric acid solution and of anodic oxide films formed by anodizing of similarly prepared substrates in ammonium pentaborate at 50 mA cm^{-2} to b. 5 V, c. 10 V and d. 25 V.

2 Anodizing of Patterned Substrates

Barrier-type anodic alumina films have been formed to different thicknesses, between 12 and 360 nm, by anodizing differently patterned superpure aluminium substrates in 0.1 M ammonium pentaborate solution. The surface topography of the anodic oxide films has been studied by atomic force microscopy and transmission electron microscopy. The distributions of electrolyte-derived species, incorporated into the various anodic oxide films, have been examined by scanning transmission electron microscopy (STEM) and elemental depth profile analyses, using GD-OES, GD-TOF-MS and TOF-SIMS.

2.1 Anodizing Process

2.1.1 Voltage-time responses

Barrier aluminium oxide films were grown anodically on superpure aluminium substrates at a constant current density of 5 mA cm^{-2} in 0.1 M ammonium pentaborate solution at 293 K. The resultant voltage-time responses reveal quasi-linear rises of the voltage with time, Fig. 2.1.a. Thus, barrier-type oxide films grow at a rate of 2.3 $\pm$ 0.1 V s^{-1} up to 300 V, at approximately 100 % current efficiency. The efficiency corresponds to the ratio of the charge associated with the aluminium ions in each film to the charge passed during anodizing of each specimen. The charge due to the aluminium ions in the films is determined from the film composition established by Rutherford backscattering spectrometry, assuming that all aluminium is oxidized during the anodizing process. Further, initial increases in voltage of 2.0 - 2.5 V indicate the presence of oxide films, of about 2.5 - 3.0 nm thicknesses, on the differently patterned superpure aluminium substrates, Fig. 2.1.b. The chromium and phosphorus species, arising from the stripping solution, are present within the oxide film in a relatively low amounts, 0.88 x 10^{15} and 0.45 x 10^{15} at cm^{-2} respectively, and, therefore, is not expected to influence the voltage-

time response during anodizing of the specimens.

Figures 2.1.b and 2.1.c compare the voltage-time responses during anodizing of differently patterned superpure aluminium substrates to 25 and 200 V in 0.1 M ammonium pentaborate solution. The different voltage-time responses, associated with the anodizing of superpure aluminium substrates of tailored roughnesses, show similar slopes of about 2.3 V s^{-1} and therefore do not disclose any influence on the anodizing process of the specimen surface roughnesses, with Sq in the range 2 - 39 nm.

The anodic oxide films, formed at a constant current density of 5 mA cm^{-2}, develop at constant electric field strength of the order 10^6 - 10^7 V cm^{-1}. Considering the range of field strength, the ionic charge transport and thereby the anodic oxide film growth are assumed to take place under high field ionic conduction. Thus, the driving force for anodic oxide film growth can be expressed as (Diggle et al., 1969):

$$i = A\,exp\,(BE) \tag{2.1}$$

where:

- i is the anodic current density.
- E is the electric field strength.
- A and B are temperature-dependent constants.

Thus, as the film thickens, the voltage increases in order to maintain the constant current density. Additionally, the electric field strength being necessarily constant across the film thickness, induces oxide growth of highly uniform thickness.

2.1.2 Thickness measurements

Anodic oxide films, formed on the differently patterned superpure aluminium substrates, were analysed using Rutherford backscattering spectroscopy. Figure 2.2 displays the energy spectra of α particles elastically scattered at 165° from anodic oxide films formed on electropolished superpure aluminium substrates to voltages of 300 V in 0.1 M ammonium pentaborate solution. The different spectra reveal a peak associated with chromium species and the oxygen yield superimposed on the aluminium yield; however, phosphorus, boron and copper species could not be detected due to

insufficient sensitivity. The amount of chromium is about 0.9 x 10^{15} at cm^{-2}, in agreement with the value previously measured by MEIS on the film resulting from the stripping. Comparison of the values reveals that no losses of chromium species occur during anodizing in 0.1 ammonium pentaborate solution of superpure aluminium substrates successively electropolished and immersed in a chromium / phosphoric acid solution.

For anodic oxide films formed on superpure aluminium substrates patterned by anodizing in sulphuric acid, oxalic acid, phosphoric acid and subsequent stripping of the porous films, little difference can be observed on the respective energy spectra. The resultant energy spectra are presented for the anodic oxide film formed on superpure aluminium substrates anodized in phosphoric acid, with subsequent stripping of the porous film to provide the patterned substrates. Thus, the energy spectra of the particles scattered from the specimen patterned in phosphoric acid present a slight decrease of the sharpness of the metal / oxide interface due to the substrate roughness, Fig. 2.3.

The energy spectra measured, for the anodic oxide films formed on patterned substrates and electropolished substrates were simulated with layers identical in thicknesses and compositions. The oxide film thicknesses have been determined from the simulation of the different RBS spectra, considering a density of 3.1 g cm^{-3} for anodic alumina. A summary of the different anodic oxide thicknesses is presented in Table 2.1.

Thus, the thickness values are homogeneous, independent of the surface roughnesses of the substrates. Figure 2.4 shows the variation of the oxide film thicknesses with the anodizing voltage. Linear fitting of the data set indicates a formation ratio of anodic alumina of about 1.2 $\pm$ 0.1 nm V^{-1} in 0.1 M ammonium pentaborate solution at a current density of 5 mA cm^{-2}.

2.1.3 Development of surface topography

Superpure aluminium substrates of controlled roughnesses were generated by anodizing electropolished aluminium specimen in sulphuric acid, oxalic acid or phosphoric acid in order to pattern the aluminium surface through growth of porous alumina layers with different cell dimensions, and then, stripping of the porous oxide layer in a chromic /

phosphoric acid solution.

The development of surface topography during anodizing of superpure aluminium substrates of controlled roughnesses has been examined by atomic force microscopy and transmission electron microscopy.

Atomic force microscopy images of differently patterned superpure aluminium specimens, reveal progressive smoothing of the initial surface roughnesses, as a result of the thickening of the barrier-type anodic alumina film during anodizing in 0.1 M ammonium pentaborate. Figure 2.5 illustrates the surface smoothing arising during anodic formation of barrier-type aluminium oxide films on superpure aluminium substrates patterned by phosphoric acid and subsequent stripping of the porous films. Smoothing of the surface results from the thickening of the oxide film that gradually fills the cells of the surface pattern. The surface roughness, Sq, decreases progressively from about 31 to 2 nm after anodizing to 200 V.

Development of surface topography during anodic formation of barrier-type aluminium oxide films has been further characterized using transmission electron microscopy. Figures 2.6 - 2.9 show transmission electron micrographs of ultramicrotomed sections of aluminium oxide films, formed on differently patterned superpure aluminium substrates, by anodizing in 0.1 ammonium pentaborate solution up to 300 V. For the substrates patterned in sulphuric, oxalic and phosphoric acid, ultramicrotomed sections are displayed until flattening of the specimen topographies is complete, achieved after anodizing to 50, 100 and 200 V respectively.

The ultramicrotomed sections disclose barrier-type oxide films attached to the superpure aluminium substrates. The anodic oxide films measured from the different transmission electron micrographs are of uniform thicknesses. The anodic alumina films, formed by anodizing aluminium specimens in 0.1 ammonium pentaborate solution between 10 and 300 V, present thicknesses of 12 to 360 nm respectively. The anodic oxide film thicknesses measured from the transmission electron micrographs are in good agreement with the values determined from simulation of the RBS spectra, Tab. 2.1.

Additionally, the surfaces of the anodic oxide films follow the changing topography of

the metal / oxide interfaces, as a result of a uniform film formation normal to any point of the aluminium substrates. Thereby, continuous smoothing of the specimen surface roughnesses arises during the formation of barrier-type anodic alumina.

The development of surface roughness has been simulated by the evolution of the aluminium ridge heights, measured from peak-to-valley from the transmission electron micrographs presented Figs 2.7 - 2.9.

Figure 2.10 displays the variation of the aluminium ridge heights with increasing anodizing voltage. The substrates patterned by anodizing in sulphuric acid, oxalic acid, phosphoric acid and subsequent stripping of the porous films present aluminium ridge heights of about 20, 35 and 70 nm respectively. The aluminium ridge heights decrease progressively, until complete smoothing of the aluminium substrate roughnesses is achieved after anodizing in 0.1 M ammonium pentaborate solution to about 50, 100 and 200 V respectively; the resulting smoothing ratio is about 0.35 - 0.40 nm V^{-1}.

Finally, examination of the development of surface topography during anodizing of patterned specimens indicates smoothing of the initial surface roughness of the superpure aluminium substrates. However, the different factors contributing to the mechanism of oxide formation and thereby to the smoothing process could not be identified by investigation of the specimens by atomic force microscopy and transmission electron microscopy. In order to understand the mechanism of surface smoothing during barrier-type anodic oxide formation, the distributions of the boron marker and the chromium- and phosphorus-tracers incorporated within the oxide films have been investigated by elemental depth profiling techniques and scanning transmission electron microscopy. The transmission detection of a field-emission gun scanning electron microscope (FEGSEM) consists of analysis of the electrons passing through the ultramicrotomed section of a specimen by an electron detector (STEM detector) positioned under the cross-section examined.

2.2 Mobilities of Incorporated Species

2.2.1 Cross-sectional analysis

Distributions of incorporated species have been investigated using scanning transmission electron microscopy. Transmission electron micrographs of ultramicrotomed sections of aluminium oxide films, as presented previously, do not disclose directly the impurity distributions within the anodic alumina layers. Indeed, transmission electron microscopy observations were carried out using an acceleration voltage of 120 kV, which is the optimal setting of the instrument. Thus, the important kinetic energy gained by electrons accelerated under such potential limits the sensitivity to elements present in low amounts. In contrast, the scanning transmission electron microscope was operated at an acceleration voltage of 20 kV, involving greater sensitivity to the dopants, namely boron, chromium and phosphorus species, present within the oxide films. Indeed, compared with transmission electron micrographs, images obtained by the STEM detection system show improved signal to noise ratio and contrast, with comparable resolution. Such enhancements are due to the significantly lower electron beam energies used in the FEGSEM, which result in the reduction of the volume excited and the increase of electron scattered from cross-sections at lower accelerating voltages (Vermeulen and Jaksch, 2005).

Figure 2.11 compares micrographs obtained by scanning electron microscopy used in the transmission mode and conventional transmission electron microscopy, of ultramicrotomed sections of electropolished superpure aluminium specimens anodized in a 0.1 M ammonium pentaborate solution to 100 V. The scanning transmission electron micrograph reveals clearly the distributions of the chromium-, phosphorus- and boron-enriched layers within the anodic alumina films. Conversely, locations of the different species are not evident in the conventional transmission electron micrograph. The nature of the different enriched-layers has been confirmed using elemental depth profiling analyses, with the results presented in the next section.

Despite the reasonable sensitivity of the scanning transmission electron microscope, examination of the distributions of the electrolyte-derived species is limited to anodic oxide films thicker than 100 nm due to insufficient lateral resolution. The scanning transmission electron micrographs of the examined specimens are presented

in Figures 2.12 - 2.15.

The scanning transmission electron micrographs disclose the distributions of chromium, boron and phosphorus species within the oxide films formed on differently patterned superpure aluminium substrates, Figs. 2.12 - 2.15. The chromium-enriched layer appears with a darker contrast than the rest of the oxide layer; conversely, the boron- and phosphorus-doped layers show brighter contrast in comparison with the pure alumina oxide.

Thus, the chromium- and phosphorus-enriched layers are respectively located in the outer and inner parts of the anodic alumina layers. Additionally, the outer part of the anodic alumina layers, about 40 % of the oxide thicknesses, present an enrichment in boron associated with the incorporation of boron species within the anodic alumina film formed at the film / solution interface.

In near-neutral electrolyte, i.e. 0.1 ammonium pentaborate solution, growth of the barrier-type anodic alumina layers proceeds by Al^{3+} egress and OH^{-} and / or O^{2-} ingress through the pre-existing air-formed film present over aluminium substrates (Skeldon et al., 1985). Hence, barrier-type anodic alumina layers develop simultaneously at the film / solution and metal / oxide interfaces. In addition, growth of anodic alumina at the film / solution interface results in the incorporation of electrolyte-derived species within the oxide film, while pure aluminium oxide develops at the metal / oxide interface.

The incorporation of boron species within the anodic alumina film developed by Al^{3+} egress occurs during anodizing in ammonium pentaborate electrolyte. The boron species are immobile; thereby, the boron-rich / boron-free oxide interface indicates the initial surface of the aluminium specimens. The boron-rich / boron-free oxide interface is located at a depth of 0.4 relative to the total film thickness, measured from the anodic oxide film formed on an electropolished aluminium substrate, Fig. 2.12.

The chromium and phosphorus species, incorporated initially into the 4-nm thick oxide films present over the differently patterned aluminium substrates, migrate in opposite directions to give two well-separated distributions (Shimizu et al., 1999b).

The chromium ions, generated by high field-assisted dissociation of the chromium oxide species incorporated into the initial air-formed films, migrate outward at a constant rate of 0.73 relative to that of aluminium ions. Conversely, the incorporated phosphorus species migrate inward at a constant rate of 0.52 relative to that of oxygen ions, as measured from Fig. 2.12.

Interestingly, from observations of Figures 2.16 - 2.18, anodic alumina layers formed on differently patterned superpure aluminium substrates, present boron-rich / boron-free oxide interfaces and phosphorus-enriched layers with wave-like patterns similar in amplitude to the differently patterned substrates, i.e. after stripping but prior to anodizing. Thus, the phosphorus-enriched layer and the boron interface amplitudes, measured from peak-to-valley, vary as a function of the initial roughnesses of the differently patterned substrates, between 15 and 60 nm. In contrast, the amplitude of the waviness of the chromium-enriched layers are progressively narrowed during the oxide growth.

The difference of distributions between the chromium- and the phosphorus-enriched layer is noticeable even for the layer formed on electropolished aluminium substrates. The chromium-enriched layer incorporated into the oxide film grown anodically on an electropolished substrate to 200 V in 0.1 ammonium pentaborate electrolyte does not display any waviness; the thickness of the chromium-enriched layer is about 2 nm, Fig. 2.16. Conversely, the distributions of chromium species, incorporated within the oxide films formed on aluminium substrates patterned by anodizing in sulphuric acid, oxalic acid and phosphoric acid and subsequent stripping of the porous films, are not completely flattened during the oxide growth; the amplitudes of the chromium species distributions, measured from peak-to-valley, are about 9, 9 and 19 nm respectively.

Thus, continuous reduction of the amplitude of the chromium distribution is concomitant with the smoothing of the specimen roughness. However, the flattening of the chromium-enriched layer proceeds less rapidly than the flattening of the oxide surface, Fig. 2.19. Once complete smoothing of the aluminium substrate roughness is achieved, the chromium-enriched layer migrates outward as a result of the uniform distribution of the electric field, associated with a relatively flat specimen surface. Therefore, depending on the initial substrate roughnesses, the chromium-enriched

layers incorporated within oxide films may present a residual waviness even for further anodizing, Fig. 2.20.

In addition, the relative depths of the boron marker and chromium and phosphorus tracers, as well as the migration rates of the tracers, have been measured from the scanning transmission electron micrographs of anodic alumina grown on differently patterned superpure aluminium substrates. Two approaches may be considered to determine the locations of the different enriched-layers that show wave-like patterns. The first approach consists in using a reference plane normal to the anodic oxide film surface in order to measure the positions of the different species. Considering the regression of the initially patterned superpure aluminium substrates during the anodic oxide growth, the oxide growth which takes place normal to the aluminium surface and the wave-like patterns of the distributions of the electrolyte-derived species, such a reference is not appropriate to describe the locations of each point of the impurity distributions. However, the definition of a reference normal to the anodic alumina film surface allows to use the mean distributions of the considered species. The second approach takes into consideration any point of the distributions of the boron marker and the chromium and phosphorus tracers; it consists in the definition of reference locations normal to the wave-like patterns of the different distributions. Local variation of the migration rates can be estimated following this approach. Global rates of migration for the chromium and phosphorus species are considered here. Thus, for the different enriched-layers that show wave-like patterns, their depths have been estimated from the mean of the patterns, Figs. 2.16 - 2.18. The migration rates of the chromium and phosphorus species are listed in Table 2.3.

The distributions of the chromium- and phosphorus-enriched layers present similar migration rates, in term of mean value, independent of the initial surface roughnesses of the substrates. However, migration rates may change locally; such variations of the migration rates are studied later in the Section entitled “Growth Mechanism of Barrier-Type Anodic Alumina”.

Finally, the distributions of electrolyte-derived species incorporated within 240-nm thick anodic alumina films have been examined using scanning transmission electron microscopy. However, due to limitation of the lateral resolution, dopant distributions

could not be studied accurately for thinner oxide films. Consequently, investigation of the impurity distributions has been undertaken by elemental depth profiling analysis techniques.

2.2.2 Elemental depth profiling analysis

The variously formed specimens were examined by sputtering-induced depth profiling analyses, using GD-OES, GD-TOF-MS and TOF-SIMS. Non-uniform sputtering arises during depth profiling analysis of specimens presenting rough surfaces. Consequently, the elemental depth profiles associated with rough specimens can not be interpreted according to a model relating the elemental intensities to the sputtering time. The elemental depth profiles should be reconstructed considering a function that describes the sputtering process associated with the rough surfaces. Thus, sputtering-induced depth profiling analyses of rough specimens are discussed later in the Section entitled "Depth Profiling Analyses of Patterned Specimens".

Depth profiling analyses of flat anodic oxide films are discussed in this section. The distributions and migration rates of the impurities are determined from the elemental depth profiles and compared with the values measured by scanning transmission electron microscopy.

The elemental depth profiles of 360 nm thick anodic oxide films, formed on electropolished aluminium substrates, acquired using the different sputtering-induced depth profiling techniques, are presented to describe the distributions of species within the anodic oxide films, Fig. 2.21.

Considering aluminium, the profile is steady throughout the anodic oxide film, and rises dramatically once the metal / oxide interface is reached and the aluminium substrate is exposed. Thus, depth calibration of the profiles has been performed using the metal / oxide interface position determined by an increase of 50 % in the aluminium profile and considering a constant sputtering rate for the anodic alumina layer; the oxide film thicknesses have been previously determined by simulation of Rutherford backscattering spectra.

The elemental depth profile related to copper species reveals copper-enrichment in the metal directly below the metal / oxide interface. Development of a copper-enriched layers have been shown to arise due to preferential oxidation of aluminium during electropolishing and anodizing.

The elemental depth profiles disclose the distributions of boron, chromium and phosphorus species incorporated into the anodic alumina film. Further, the elemental depth profile of the boron species reveals boron-enrichment in the outermost part of the anodic oxide film; the interface between the boron-enriched and boron-free oxide indicates the location of the original surface of the substrate. The elemental depth profiles associated with the chromium and phosphorus species show local chromium- and phosphorus-enrichments in the outer and inner parts of the anodic oxide film respectively.

Locations of the different enriched-layers, relative to the total thickness of oxide layers, have been determined from the elemental depth profiles obtained using GD-OES, GD-TOF-MS and TOF-SIMS. Figures 2.22 - 2.25 display the positions of the chromium and phosphorus tracers as well as the interface for the boron marker as a function of the anodic oxide film thickness for anodic oxide layers formed by anodizing in 0.1 M ammonium pentaborate of differently patterned superpure aluminium substrates up to 300 V. Thus, the data sets have been fitted by linear functions; the slopes of the different fitting plots represent the mean locations of the various impurity distributions relative to the oxide thicknesses.

The relative locations of the dopants are presented in Table 2.2. The distributions of the chromium and phosphorus-enriched layers are determined at depths of 0.10 - 0.11 and 0.66 - 0.74 relative to the thickness of the oxide layer respectively. The boron interface was measured in a range 0.40 - 0.44 relative to the oxide layer thickness.

The standard deviation calculated on the whole range of data is about 0.5 % for the measurements associated with the chromium distributions and increases to 1.3 and 2.0 % for the data sets relative to the boron and phosphorus species. The data are uniformly dispersed, independent of the techniques used. Thus, the data associated with the boron and phosphorus species present a slightly higher dispersion than the data related to the

chromium distribution. Such dispersion is probably due to the uncertainty of the curve fitting for the boron and phosphorus profiles, as well as the degradation of the depth resolution associated with sputtering depth. Further, the chromium profiles can be best fitted by an exponential-modified Gaussian function. However, the boron profiles present specific features that may affect the fitting using the Sigmoid function, namely the optical interferences at the commencement of the depth profile (GD-OES), and the extensive decay after the boron-rich / boron-free oxide interface (GD-TOF-MS). In addition, the phosphorus profiles, associated with the phosphorus-enriched layers incorporated within anodic oxide layers formed on substrates patterned by anodizing in sulphuric acid, oxalic acid and phosphoric acid and subsequent stripping of the porous films, are best fitted by the convolution of two Gaussian peaks. The depth of the phosphorus-enriched layer has been established as the mean of the depth of the two peaks obtained after deconvolution of the elemental depth profiles, thereby introducing an additional uncertainty on the measure.

Migration rates of the chromium and phosphorus tracers have been calculated from the locations of the impurity distributions determined previously, the results are shown in Table 2.3. For the oxide layers formed anodically on electropolished aluminium substrates, the migration rates of chromium and phosphorus species are 0.74 ± 0.01 and 0.50 ± 0.02 relative to that of aluminium and oxygen ions respectively. The data measured by sputtering-induced depth profiling techniques are in agreement with the values obtained from RBS and STEM; further they are consistent with the Literature (Shimizu et al., 1999b).

For the anodic oxide layers grown on superpure aluminium substrates patterned by anodizing in sulphuric acid, oxalic acid and phosphoric acid and subsequent stripping of the porous films, i.e. relatively rough substrates, the migration rates of chromium and phosphorus species are 0.76 ± 0.01 and 0.45 ± 0.03 relative to that of aluminium and oxygen ions respectively. The migration rates of chromium and phosphorus tracers are consistent, independent of the initial roughnesses of the aluminium substrates.

The migration rates measured for the chromium and phosphorus distributions incorporated into anodic oxide layers grown on relatively rough superpure aluminium substrates, are slightly lower and higher in comparison with the respective migrations

rates established for the impurities incorporated within anodic oxide layers grown on electropolished aluminium substrates. However, the difference is probably due to the uncertainty with which the locations of the different impurities are determined. Thus, as the mean of the distribution has been considered here, the difference in the migration rates is not considered to represent any influence of the substrate roughness on the migration of the chromium and phosphorus tracers.

Finally, the chromium-, phosphorus- and boron-enriched layers have been shown to present certain wave-like patterns associated with the initial surface roughnesses of the aluminium specimen substrates, as observed by scanning transmission electron microscopy. The influence of the initial substrate roughnesses is also evident on the chromium, phosphorus and boron elemental depth profiles.

Figures 2.26 - 2.28 show a comparison of the elemental depth profiles measured respectively by GD-OES, GD-TOF-MS and TOF-SIMS, for anodic alumina films formed by anodizing differently patterned superpure aluminium substrates in ammonium pentaborate to 360 nm. Significant broadening of the boron and phosphorus profiles arises with the increase of the initial substrate roughnesses. Conversely, the width of the chromium profiles is slightly influenced by the initial aluminium roughnesses.

The chromium and phosphorus depth profiles have been modelled by an exponential-modified Gaussian and a Gaussian function respectively. The amplitude of the wave-like patterns of the chromium- and phosphorus-enriched layers have been evaluated, as defined by convention, by measurement of the Full Width at Half Maximum (FWHM) of their associated depth profiles. Figure 2.29 displays the FWHM of the chromium and phosphorus tracers as a function of the depths of the enriched-layers, measured from depth profiles obtained using TOF-SIMS, GD-OES and GD-TOF-MS on anodic oxide films grown, on electropolished aluminium substrates, to thicknesses of 12, 30, 60, 120, 240, 270, 300, 330 and 360 nm.

By experimentally varying the positions of the chromium and phosphorus tracers, the width of the layers has been measured over a range of depths of 2 - 40 nm and 25 - 250 nm respectively. The different data sets have been fitted using linear functions. The trend of the fitting functions indicates the depth profile broadening associated with

the sputtering process relative to the depth profiling technique employed, whereas, the y-intercept represents the thickness or the amplitude of the wave-like pattern of the layer studied.

For the GD-TOF-MS and GD-OES techniques, broadening of the profiles takes place at a ratio of about 9 %, representing about two times the broadening occurring during depth profiling using TOF-SIMS (5 %). The characteristic crater shape developed during glow discharge depth profiling analysis, as well as the difference in the area of measurement ($\sim$13 mm^2 for the GD techniques compared with $\sim$225 µm^2 for TOF-SIMS) may explain the larger ratio of broadening arising during glow discharge depth profile analysis. During depth profiling of the chromium and phosphorus tracers, the FWHM values of the layers have been determined by GD-TOF-MS, GD-OES and TOF-SIMS to be about 3.4 $\pm$ 0.4 nm and 7.2 $\pm$ 0.4 nm respectively.

Thus, the FWHM values of the phosphorus profiles indicates the amplitude of the patterns of the phosphorus distributions. In contrast, scanning transmission electron microscopy observations of the chromium-enriched layers incorporated into oxide films grown anodically on electropolished substrates, disclosed uniformly flat distributions of the chromium species. Therefore, the FWHM values of the chromium profiles represents the thicknesses of the chromium-enriched layers.

A similar approach has been used to evaluate the residual pattern amplitudes of the chromium- and phosphorus-enriched layers incorporated within alumina layers grown anodically on superpure aluminium substrates patterned by anodizing in sulphuric acid, oxalic acid, phosphoric acid and subsequent stripping of the porous films. The amplitudes of the patterns of chromium- and phosphorus-enriched layers are considered here after flattening of the surface roughnesses of the various specimens, after anodizing to sufficient voltages.

The data are relatively spread and thereby can not be fitted without constraint of the fitting parameters. Consequently, the FWHM values of the chromium and phosphorus profiles have been fitted using the mean values of the data sets, Figs. 2.30 - 2.32. A summary of the FWHM values of the chromium and phosphorus distributions is presented in Tables 2.4 and 2.5 respectively.

Thus, after flattening of the specimen roughnesses, the residual amplitudes of the patterns of the chromium-enriched layers incorporated within alumina layers, grown anodically on superpure aluminium substrates patterned by electropolishing and by anodizing in sulphuric acid, oxalic acid, phosphoric acid and subsequent stripping of the porous films, are 3 ± 1 nm, 8 ± 1 nm, 8 ± 1 nm and 15 ± 3 nm respectively. Hence, significant narrowing of the chromium distributions arises during growth of anodic oxide on rough substrates.

The amplitudes of the distributions of the phosphorus species incorporated into alumina layers grown anodically on superpure aluminium substrates, patterned by electropolishing and by anodizing in sulphuric acid, oxalic acid, phosphoric acid and subsequent stripping of the porous films, are 8 ± 2 nm, 28 ± 9 nm, 40 ± 7 nm and 66 ± 6 nm respectively. Thus, the initial distributions of the phosphorus species within the oxide films resulting from stripping, present over the differently patterned superpure aluminium substrates, remain during the formation of anodic oxide films on the respective aluminium substrates.

2.3 Conclusions

Barrier aluminium oxide films have been formed anodically on differently patterned superpure aluminium substrates at a constant current density of 5 mA cm^{-2} in 0.1 M ammonium pentaborate solution at 293 K. In such conditions, the anodic oxide growth proceeds uniformly at a formation ratio of about 1.2 nm V^{-1}, independent of the initial substrate roughnesses.

In addition, progressive smoothing of the initial surface roughness of the superpure aluminium substrates have been determined by examination of the surface topography development during anodizing of patterned aluminium substrates. A smoothing ratio of about 0.35 - 0.40 nm V^{-1} has been estimated by transmission electron microscopy.

Finally, the distributions of impurities, namely boron, chromium and phosphorus, incorporated within anodic alumina films, have been examined using scanning transmission electron microscopy and elemental depth profiling analysis techniques. The

boron electrolyte-derived species are immobile while the chromium and phosphorus species, incorporated initially into the 4-nm thick oxide films present over the differently patterned aluminium substrates, migrate in opposite directions to give two well-separated distributions.

For anodic oxide layers formed on electropolished substrates, the migration rates of chromium and phosphorus species have been determined to be 0.74 ± 0.01 and 0.50 ± 0.02 relative to that of aluminium and oxygen ions respectively.

Further, the initial distributions of the phosphorus species within the oxide films resulting from stripping, present over the differently patterned superpure aluminium substrates, remain during the formation of anodic oxide films on the respective aluminium substrates; conversely, significant narrowing of the chromium distributions arises. The differences in the migration process for the chromium and the phosphorus tracers are discussed further in the Section entitled “Growth Mechanism of Barrier-Type Anodic Alumina”.

Tables

Table 2.1 – Thicknesses of anodic oxide layers formed by anodizing differently patterned aluminium substrates in 0.1 M ammonium pentaborate.

Anodizing potential (V)	Substrate patterned by electro-polishing		sulphuric acid		oxalic acid		phosphoric acid	
	Film thickness (nm), measured by							
	RBS	TEM	RBS	TEM	RBS	TEM	RBS	TEM
10	-	-	-	11	-	13	-	11
25	30	-	30	30	30	30	30	32
50	61	58	61	58	61	55	61	57
100	123	121	123	117	123	120	123	125
200	239	-	239	-	239	-	239	231
300	363	374	363	-	363	-	363	-

For the rough specimens, thicknesses are measured normal to the aluminium substrates

Table 2.2 – Depths of the chromium and phosphorus tracers as well as the boron marker relative to the total anodic oxide film thicknesses.

Texturing treatment	Tracers / Marker	Relative depth of the tracers / marker, measured using GD-OES	GD-TOF-MS	TOF-SIMS	STEM	RBS
Electro-polishing	Cr	0.11	0.11	0.11	0.11	0.11
	P	0.70	0.70	0.72	0.71	0.7†
	B	0.42	0.43	0.43	0.40	0.4†
Anodizing in sulphuric acid	Cr	0.10	0.10	0.11	0.11	0.11
	P	0.68	0.66	0.68	-	-
	B	0.42	0.43	0.41	0.40	-
Anodizing in oxalic acid	Cr	0.10	0.10	0.11	0.11	0.11
	P	0.70	0.67	0.68	0.71	-
	B	0.41	0.42	0.44	0.41	-
Anodizing in phosphoric acid	Cr	0.10	0.10	0.11	0.11	0.11
	P	0.69	0.71	0.68	0.74	-
	B	0.42	0.44	0.42	0.44	-

† (Skeldon et al., 1985)

Table 2.3 – Migration rates of the chromium and phosphorus tracers relative to aluminium and oxygen species respectively.

Texturing treatment	Tracers	Migration rates of the tracers, measured using				
		GD-OES	GD-MS	TOF-SIMS	STEM	RBS
Electro-polishing	Cr	0.74	0.74	0.74	0.73	0.73
	P	0.48	0.47	0.51	0.52	0.50
Anodizing in sulphuric acid	Cr	0.76	0.77	0.73	0.73	-
	P	0.45	0.40	0.46	-	-
Anodizing in oxalic acid	Cr	0.76	0.76	0.75	0.73	-
	P	0.49	0.43	0.43	0.51	-
Anodizing in phosphoric acid	Cr	0.76	0.77	0.73	0.75	-
	P	0.47	0.48	0.46	0.54	-

Table 2.4 – Comparison of the amplitude (thickness) of the pattern (layer) of the distributions of chromium species measured by sputtering-induced, depth profiling techniques and by scanning transmission electron microscopy.

Technique	Amplitude of the chromium-enriched layer (nm)			
	Superpure aluminium substrates patterned by			
	phosphoric acid	oxalic acid	sulphuric acid	electropolishing
TEM (substrates)	65 ± 6	36 ± 4	18 ± 2	10 ± 2
STEM	19 ± 1	9 ± 1	9 ± 1	4 ± 1
TOF-SIMS	13 ± 1	7 ± 1	7 ± 1	3.8 ± 0.1
GD-OES	15 ± 1	8 ± 1	8 ± 1	3.0 ± 0.1
GD-TOF-MS	18 ± 1	8 ± 1	8 ± 1	3.3 ± 0.1

Table 2.5 – Comparison of the amplitude of the distribution of the phosphorus-enriched layers measured by sputtering-induced depth profiling techniques scanning transmission electron microscopy and transmission electron microscopy.

Technique	Amplitude of the phosphorus-enriched layer (nm)			
	Superpure aluminium substrates patterned by			
	phosphoric acid	oxalic acid	sulphuric acid	electropolishing
TEM (substrates)	65 ± 6	36 ± 4	18 ± 2	10 ± 2
STEM	59 ± 6	35 ± 4	20 ± 2	12 ± 2
TOF-SIMS	72 ± 5	48 ± 2	38 ± 1	7 ± 1
GD-OES	48 ± 2	34 ± 2	26 ± 1	8 ± 1
GD-TOF-MS	101 ± 3	56 ± 3	38 ± 3	7 ± 1

Figures

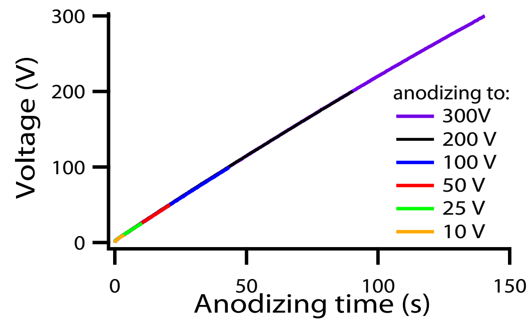

(a)

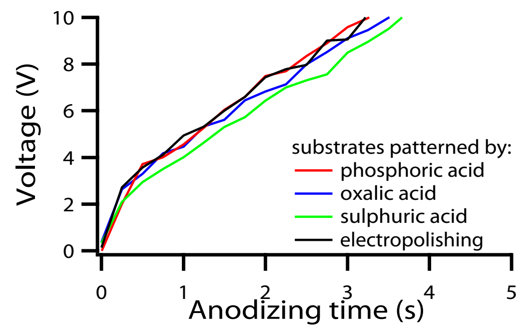

(b) – Anodizing to 25 V

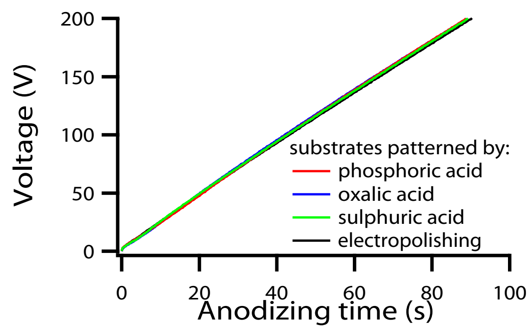

(c) – Anodizing to 200 V

Figure 2.1 – Voltage-time responses of superpure aluminium specimens anodized at 5 mA cm^{-2} in 0.1 M ammonium pentaborate electrolyte at 293 K; a. comparison of the voltage-time responses during anodizing of electropolished substrates from 10 to 300 V, b. and c. influence of the substrate roughnesses during anodizing of differently patterned substrates to 25 V and 200 V respectively.

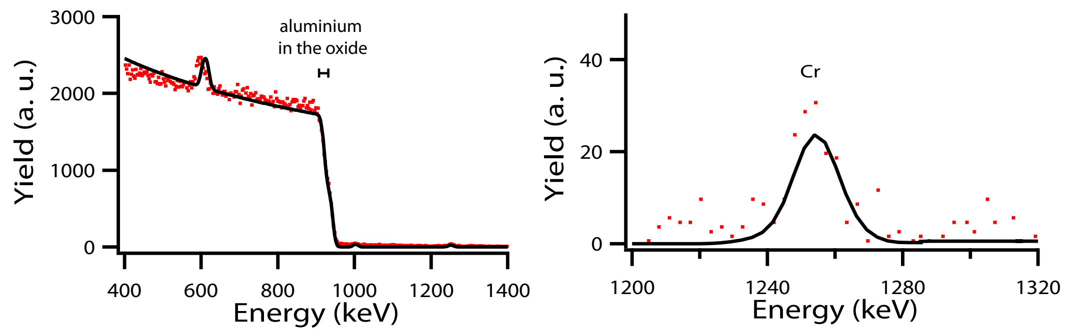

(a) – Anodizing to 25 V

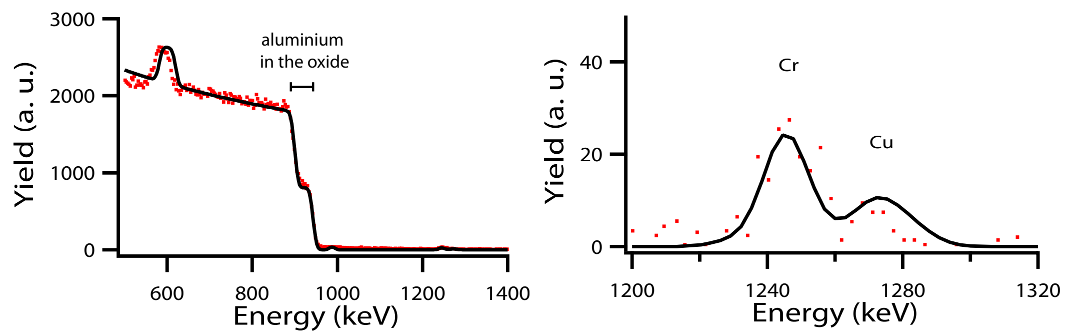

(b) – Anodizing to 50 V

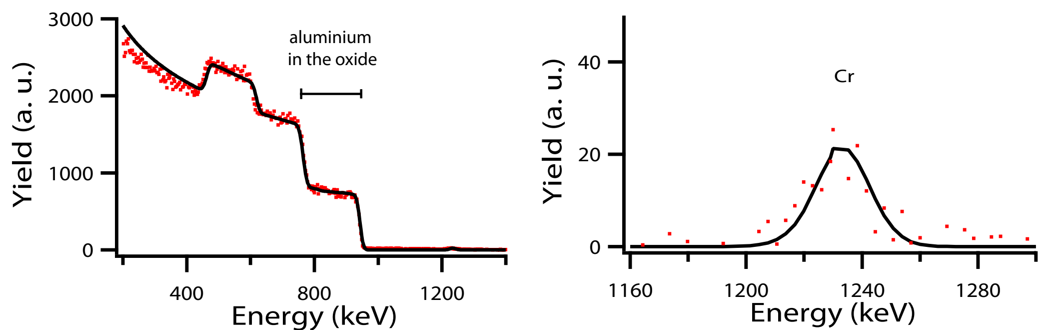

(c) – Anodizing to 200 V

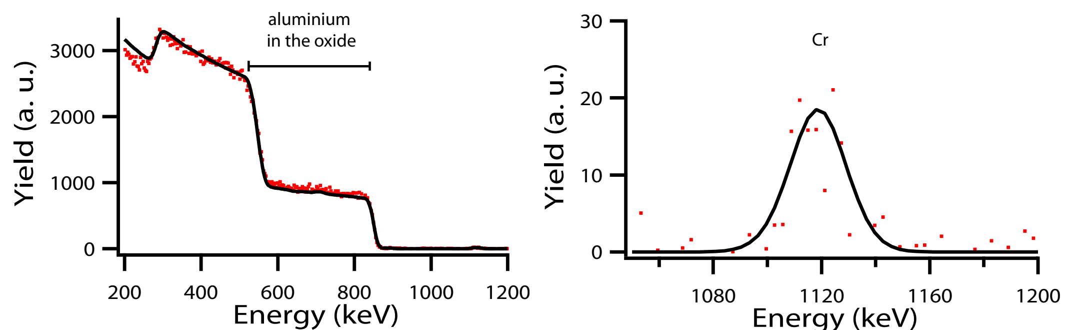

(d) – Anodizing to 300 V

Figure 2.2 – Measured (dots) and simulated (solid line) RBS spectra of superpure aluminium specimens successively electropolished, immersed in a chromic / phosphoric acid stripping solution and anodized in 0.1 M ammonium pentaborate solution to a. 25, b. 50, c. 200 and d. 300 V.

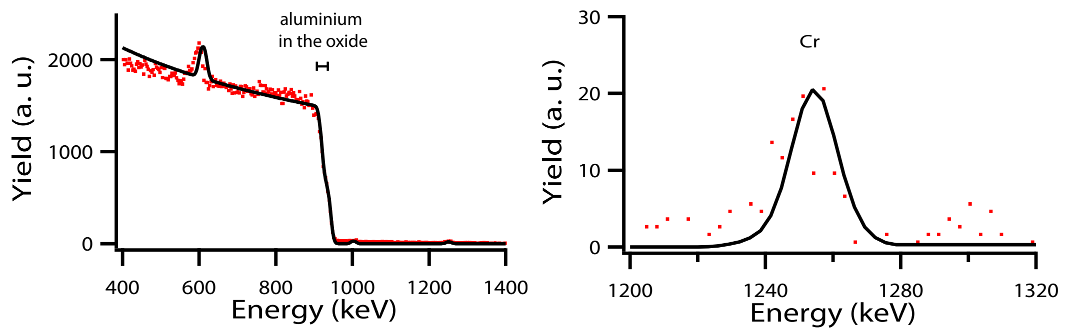

(a) – Anodizing to 25 V

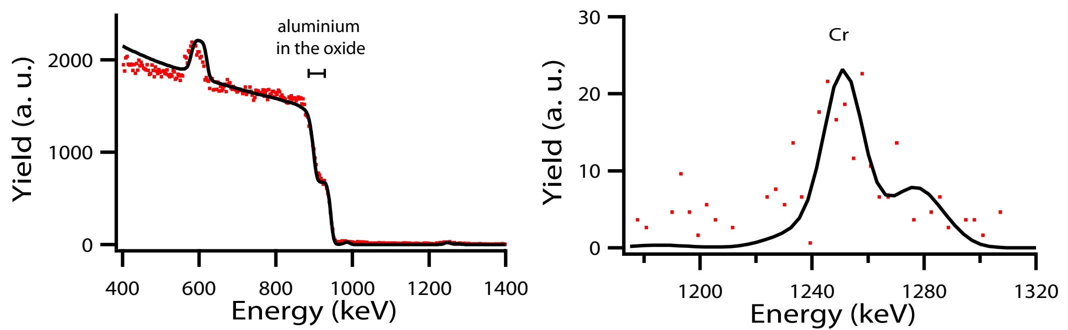

(b) – Anodizing to 50 V

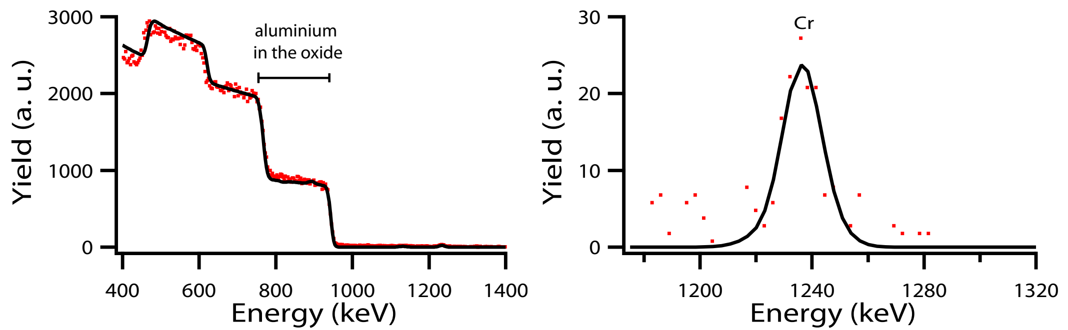

(c) – Anodizing to 200 V

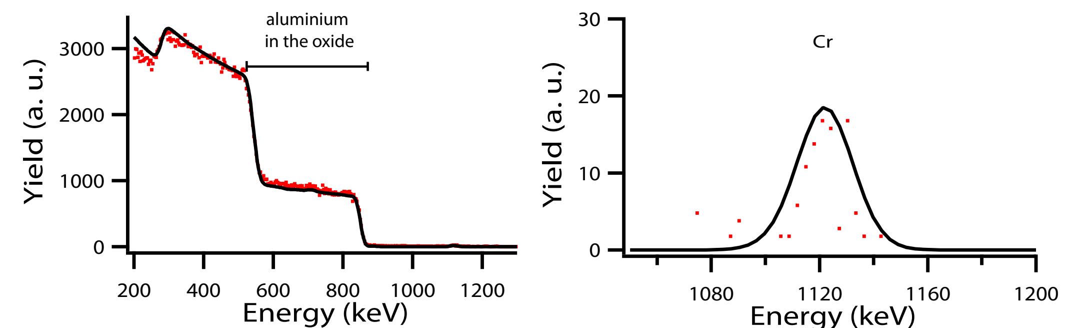

(d) – Anodizing to 300 V

Figure 2.3 – Measured (dots) and simulated (solid line) RBS spectra of superpure aluminium specimens successively patterned in phosphoric acid, immersed in a chromic / phosphoric acid stripping solution and anodized in 0.1 M ammonium pentaborate solution to a. 25, b. 50, c. 200 and d. 300 V.

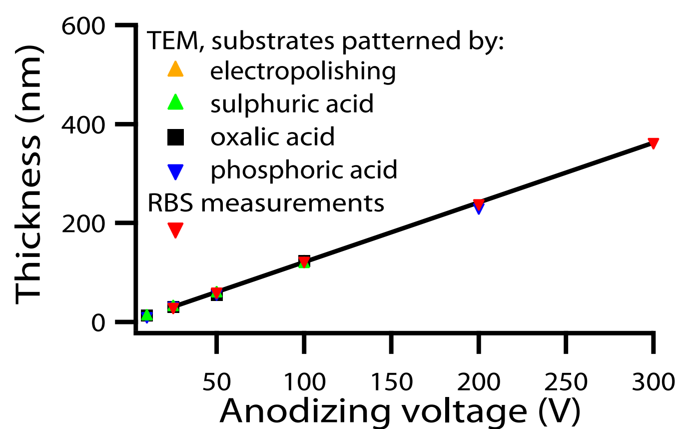

Figure 2.4 – Measured and fitted (solid line) thicknesses of anodic oxide films formed on differently patterned superpure aluminium specimens, by anodizing in 0.1 M ammonium pentaborate solution up to 300 V.

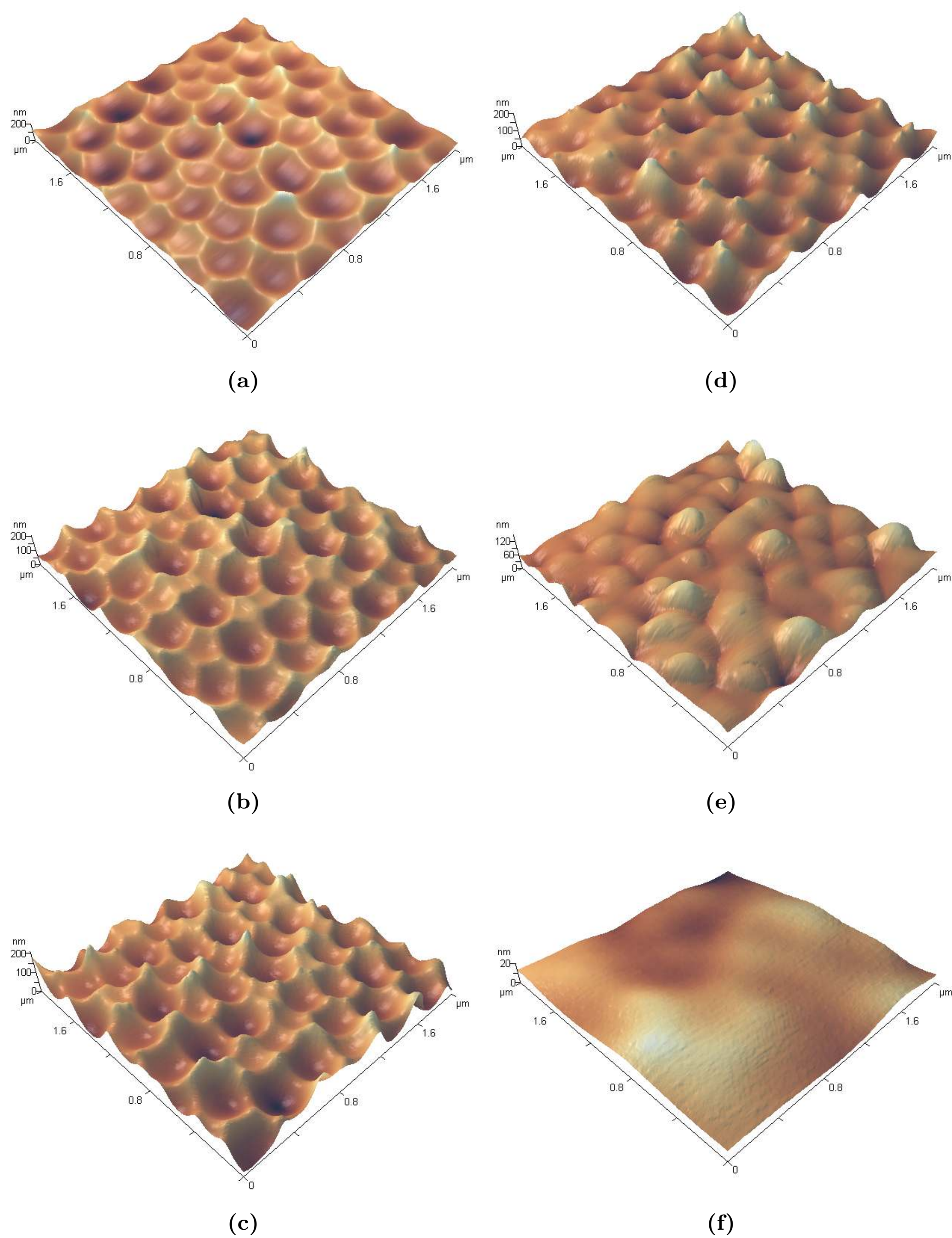

Figure 2.5 – Atomic force microscopy images of superpure aluminium specimens patterned in phosphoric acid, and subsequently stripped of the porous film, a. air-formed film, then, anodized in 0.1 M ammonium pentaborate solution to b. 10 V, c. 25 V, d. 50 V, e. 100 V and f. 200 V.

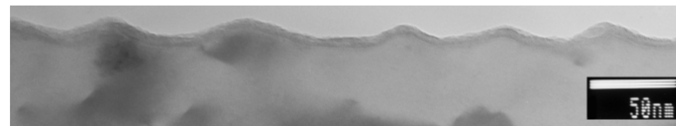

(a)

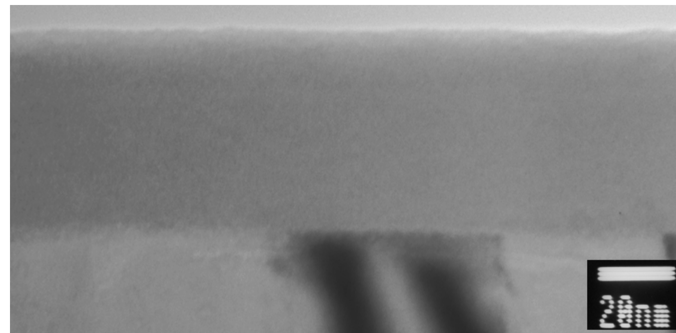

(b)

(c)

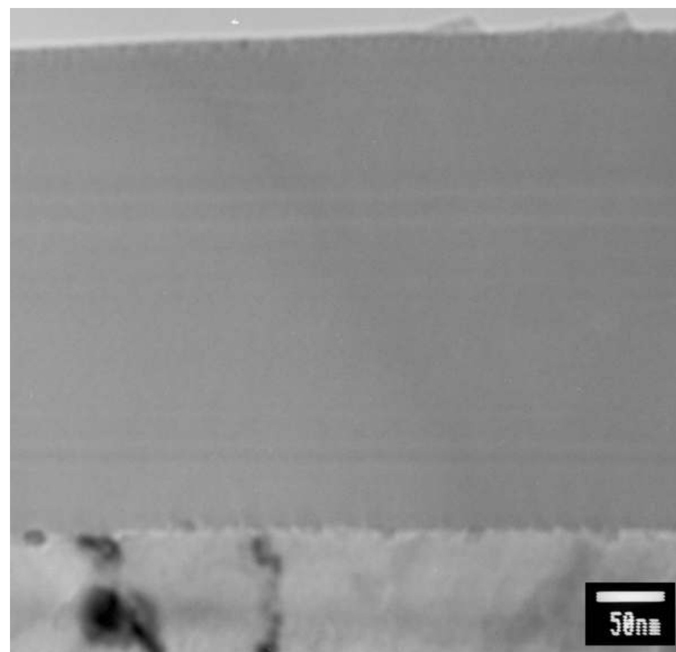

(d)

Figure 2.6 – Transmission electron micrographs of ultramicrotomed sections of superpure aluminium specimens patterned by electropolishing a. air-formed film, and anodized in a 0.1 M ammonium pentaborate solution to b. 50 V, c. 100 V, d. 300 V.

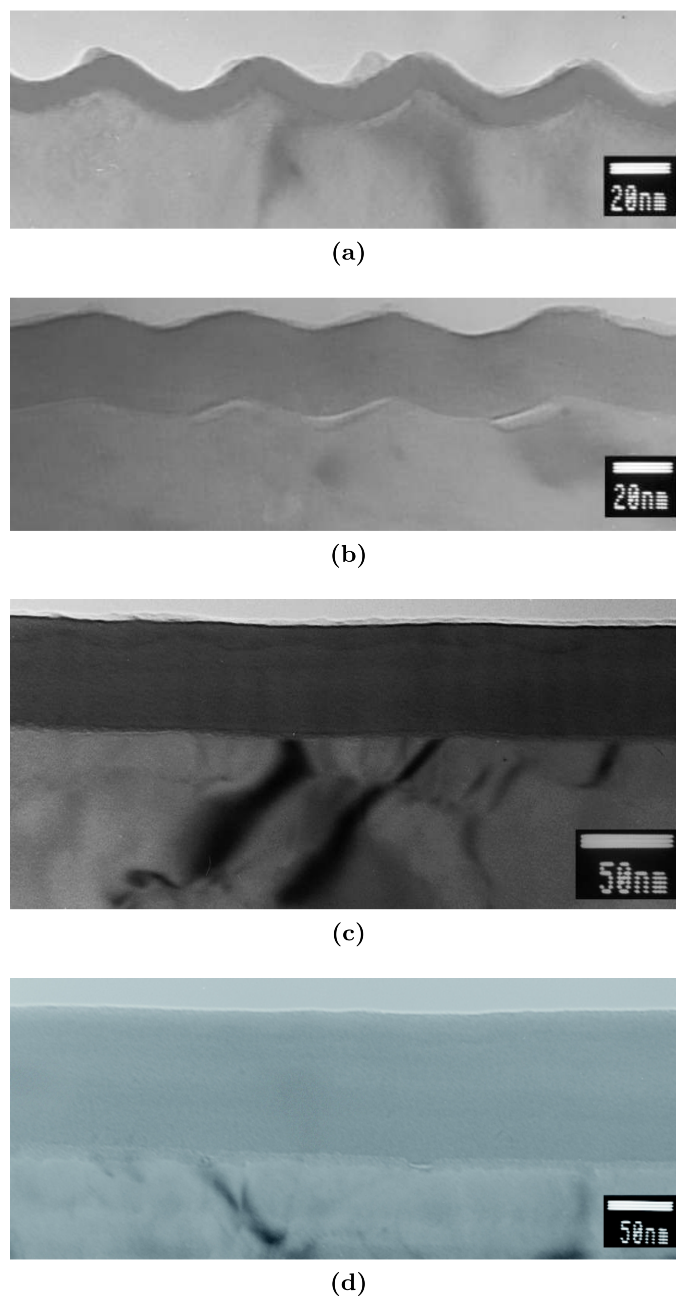

Figure 2.7 – Transmission electron micrographs of ultramicrotomed sections of superpure aluminium specimens patterned by anodizing in sulphuric acid and subsequent stripping of the porous film, and anodized in 0.1 M ammonium pentaborate solution to a. 10 V, b. 25 V, c. 50 V and d. 100 V.

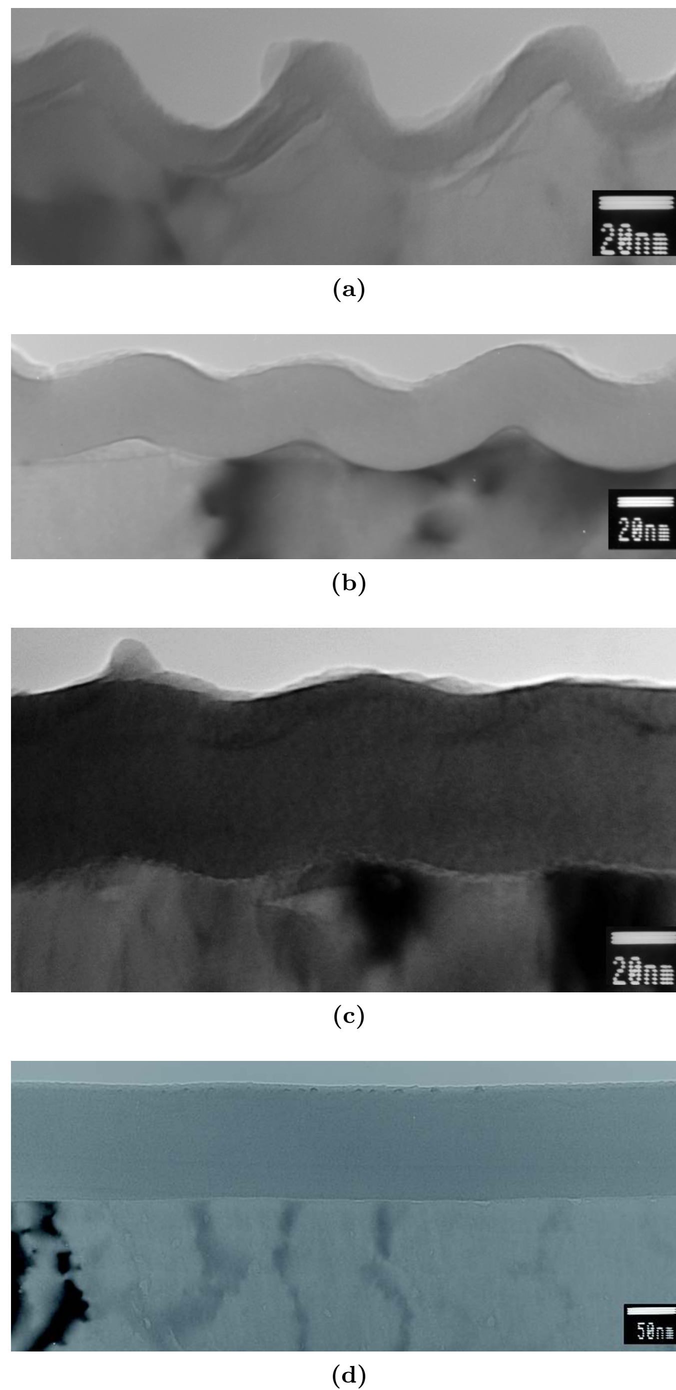

Figure 2.8 – Transmission electron micrographs of ultramicrotomed sections of superpure aluminium specimens patterned by anodizing in oxalic acid and subsequent stripping of the porous film, and anodized in a 0.1 M ammonium pentaborate solution to a. 10 V, b. 25 V, c. 50 V and d. 100 V.

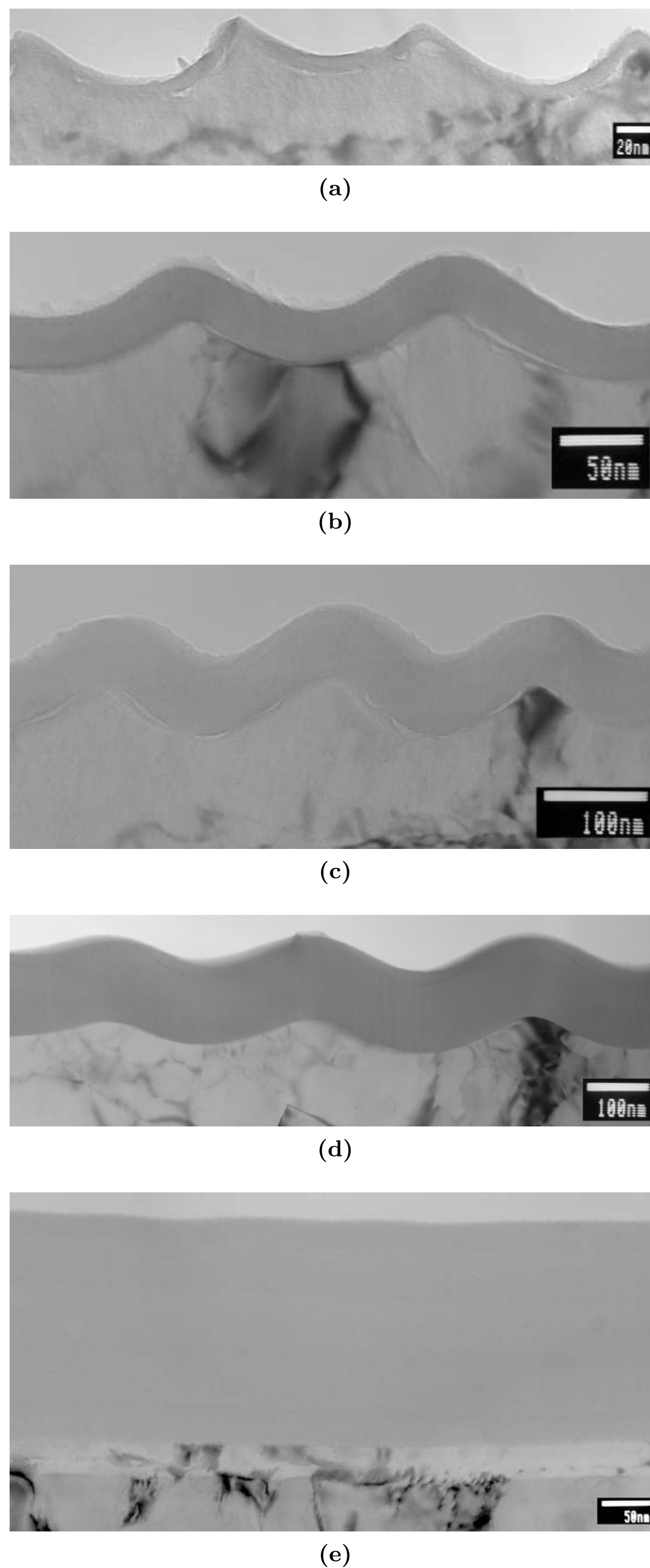

Figure 2.9 – Transmission electron micrographs of ultramicrotomed sections of superpure aluminium specimens patterned in phosphoric acid and subsequent stripping of the porous film, and anodized in 0.1 M ammonium pentaborate solution to a. 10 V, b. 25 V, c. 50 V, d. 100 V and e. 200 V.

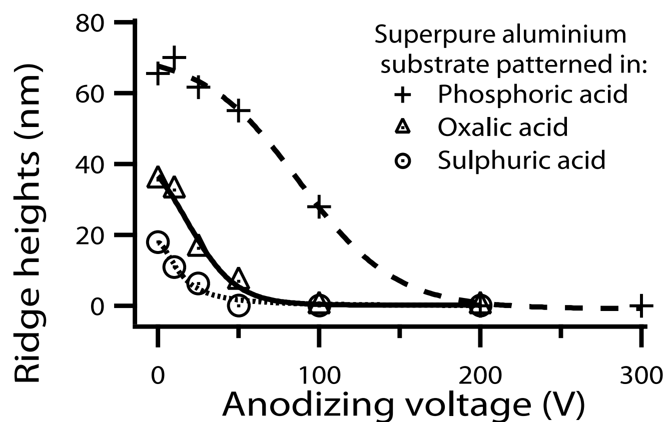

Figure 2.10 – Evolution of the substrate ridge heights as a function of increasing anodizing voltage, showing the flattening of the superpure aluminium substrates, initially textured by anodizing in sulphuric acid, oxalic acid, phosphoric acid and subsequent stripping of the porous films, during anodizing in 0.1 M ammonium pentaborate solution to various voltages. The height of the aluminium substrate ridges were measured from the transmission electron micrographs of ultramicrotomed sections of specimens anodized to 10, 25, 50, 100, 200 and 300 V.

(a) – STEM

(b) – TEM

Figure 2.11 – Comparison of a. a scanning transmission electron micrograph and b. a transmission electron micrograph of ultramicrotomed sections of electropolished superpure aluminium specimens immersed in a chromic / phosphoric acid stripping solution and anodized in 0.1 M ammonium pentaborate solution to 100 V.

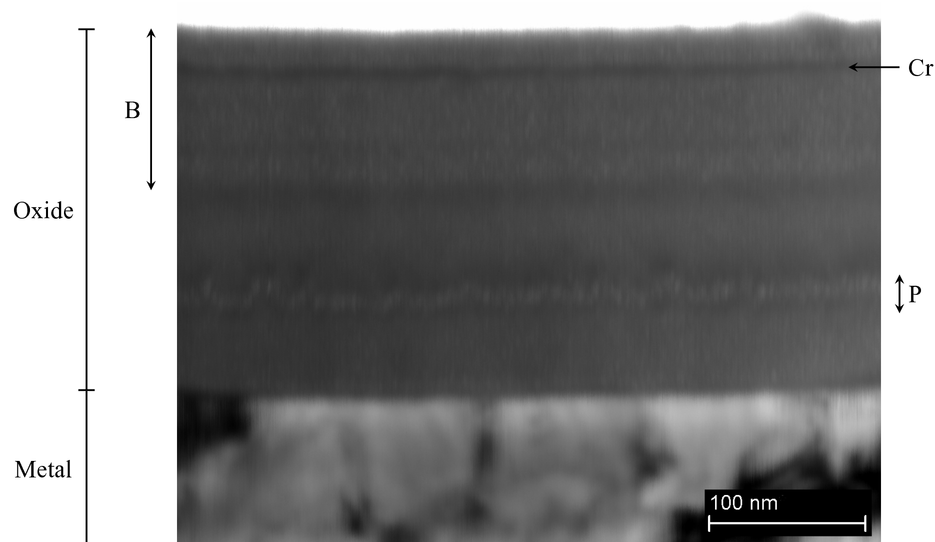

Figure 2.12 – Scanning transmission electron micrograph of an ultramicrotomed section of an electropolished superpure aluminium specimen, immersed in a chromic / phosphoric acid stripping solution and anodized in 0.1 M ammonium pentaborate solution to 200 V.

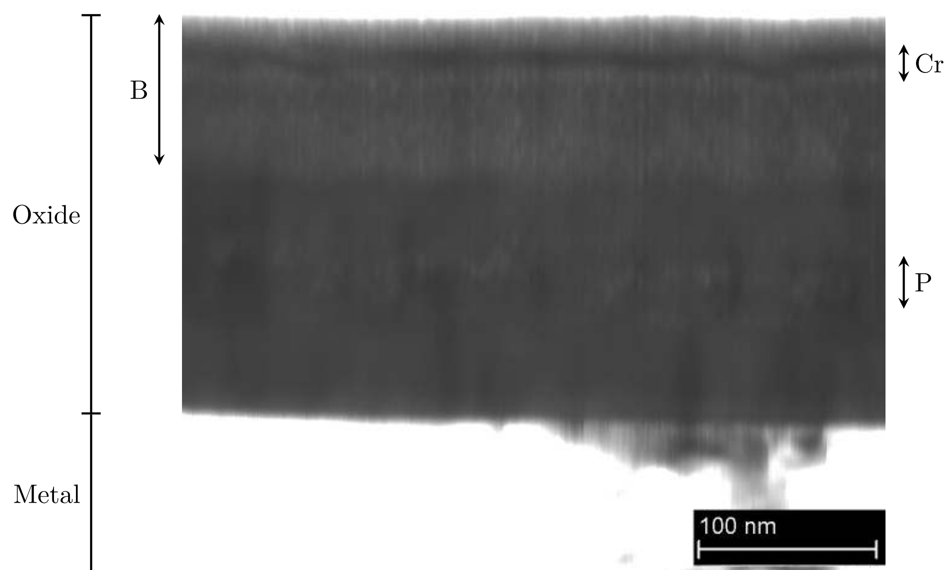

Figure 2.13 – Scanning transmission electron micrograph of an ultramicrotomed section of a superpure aluminium specimen patterned by anodizing in sulphuric acid and subsequent stripping of the porous film, and anodized in 0.1 M ammonium pentaborate solution to 200 V.

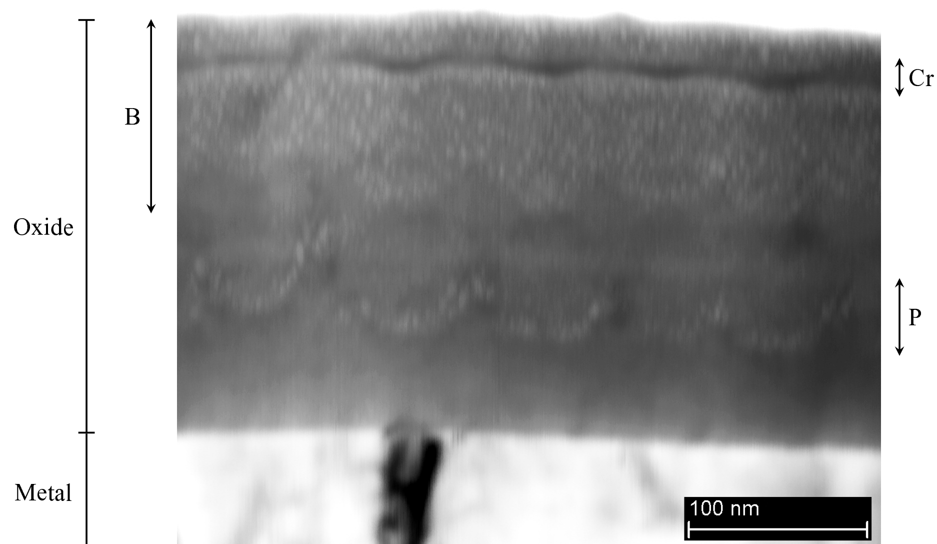

Figure 2.14 – Scanning transmission electron micrograph of an ultramicrotomed section of a superpure aluminium specimen patterned by anodizing in oxalic acid and subsequent stripping of the porous film, and anodized in 0.1 M ammonium pentaborate solution to 200 V.

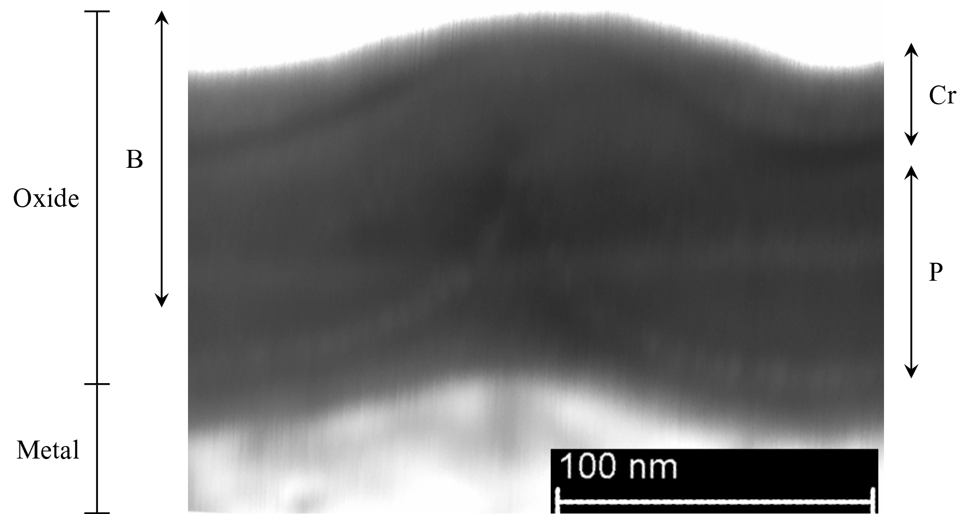

(a) – Anodizing to 100 V

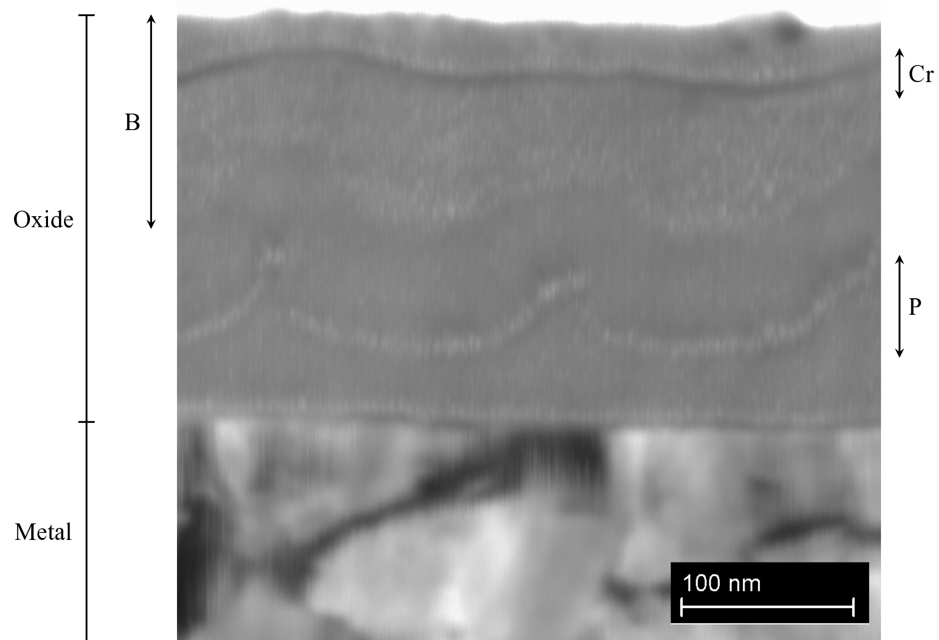

(b) – Anodizing to 200 V

Figure 2.15 – Scanning transmission electron micrographs of ultramicrotomed section of superpure aluminium specimens patterned by anodizing in phosphoric acid and subsequent stripping of the porous film, and anodized in 0.1 M ammonium pentaborate solution to a. 100 V and b. 200 V.

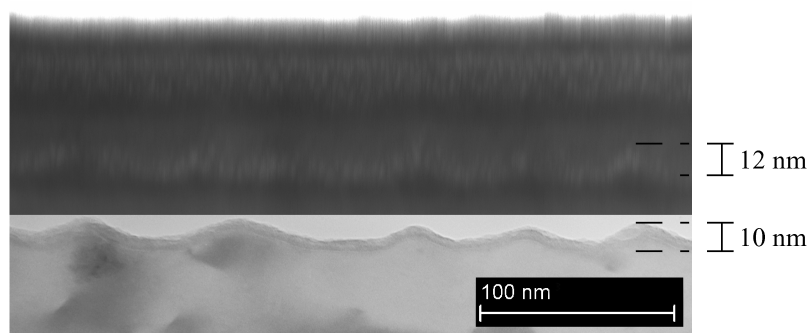

Figure 2.16 – Scanning transmission electron micrograph of an ultramicrotomed section of an electropolished superpure aluminium specimen, immersed in a chromic / phosphoric acid solution and anodized in 0.1 M ammonium pentaborate solution to 100 V. A transmission electron micrograph of an ultramicrotomed section of the initial superpure aluminium substrate, i.e. before anodizing in 0.1 M ammonium pentaborate solution, is superimposed on the STEM image. The amplitude of the distribution of the phosphorus species within the anodic oxide film is 12 nm, while the amplitude of the pattern of the electropolished superpure aluminium substrate immersed in a chromic / phosphoric acid solution, is measured at 10 nm.

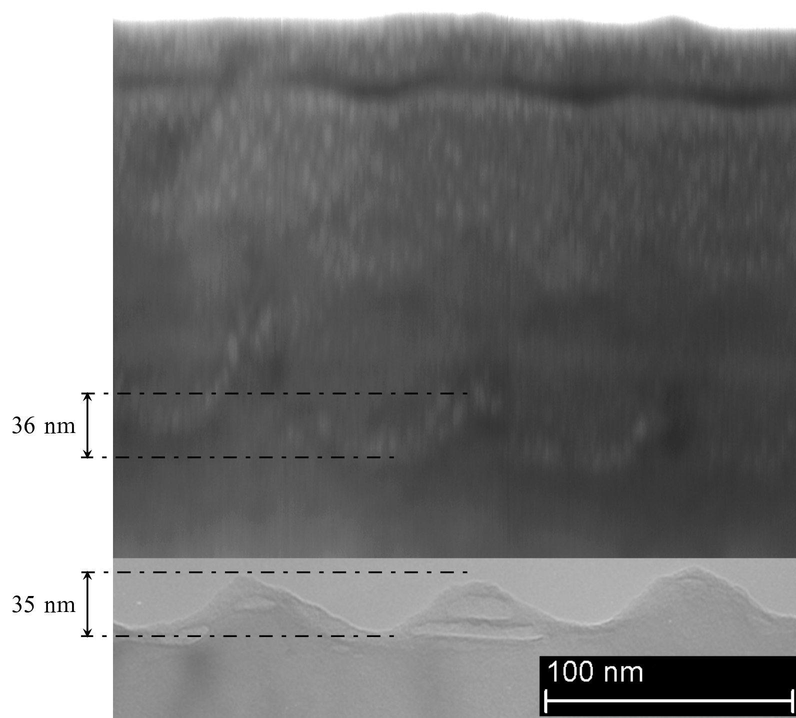

Figure 2.17 – Scanning transmission electron micrograph of an ultramicrotomed section of a superpure aluminium specimen patterned by anodizing in oxalic acid and subsequent stripping of the porous film, and anodized in 0.1 M ammonium pentaborate solution to 200 V. A transmission electron micrograph of an ultramicrotomed section of the patterned superpure aluminium substrate, i.e. before anodizing in 0.1 M ammonium pentaborate solution, is superimposed to the STEM image. The amplitude of the distribution of the phosphorus species within the anodic oxide film is 36 nm, while the amplitude of the initial pattern of the superpure aluminium substrate is measured at 35 nm.

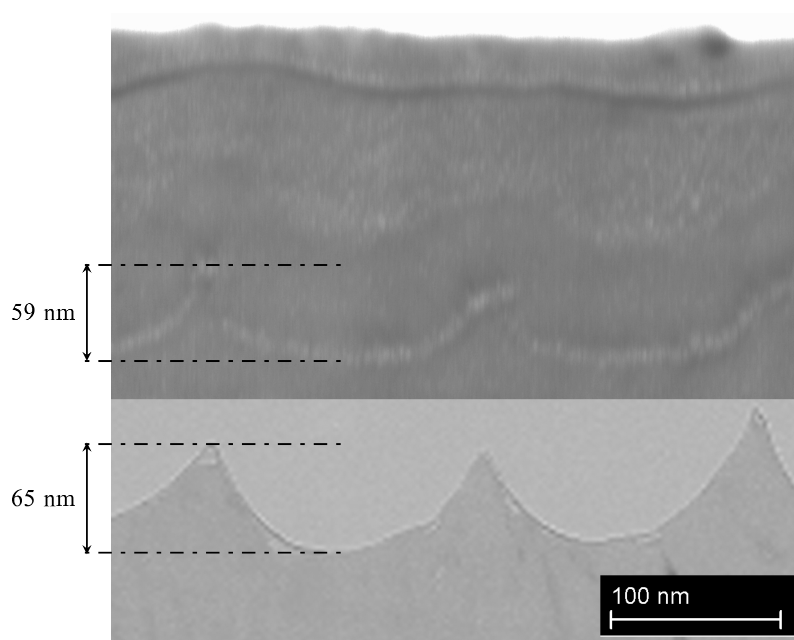

Figure 2.18 – Scanning transmission electron micrograph of an ultramicrotomed section of a superpure aluminium specimen patterned by anodizing in phosphoric acid and subsequent stripping of the porous film, and anodized in 0.1 M ammonium pentaborate solution to 200 V. A transmission electron micrograph of an ultramicrotomed section of the initial superpure aluminium substrate, i.e. before anodizing in 0.1 M ammonium pentaborate solution, is superimposed to the STEM image. The amplitude of the distribution of the phosphorus species within the anodic oxide film is 59 nm, while the amplitude of the initial pattern of the superpure aluminium substrate is measured at 65 nm.

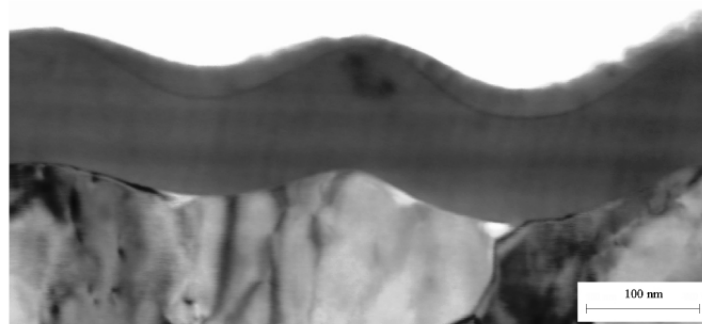

(a) – Anodizing to 100 V

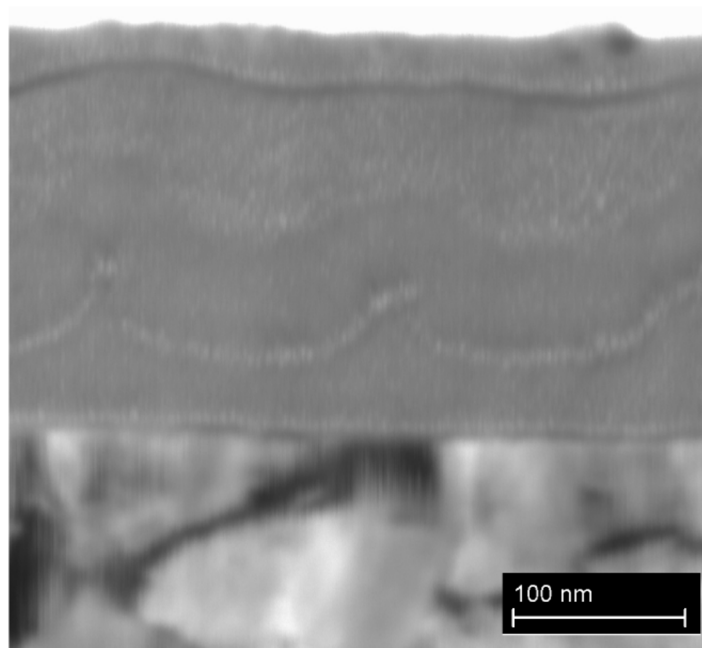

(b) – Anodizing to 200 V

Figure 2.19 – Scanning transmission electron micrograph of an ultramicrotomed section of a superpure aluminium specimen patterned in phosphoric acid and anodized in 0.1 M ammonium pentaborate solution to a. 100 V and b. 200 V. The comparison of the amplitude of the distributions of the chromium-enriched layers from the micrographs presented in a. and b. shows significant flattening of the chromium-enriched layers during anodic alumina growth.

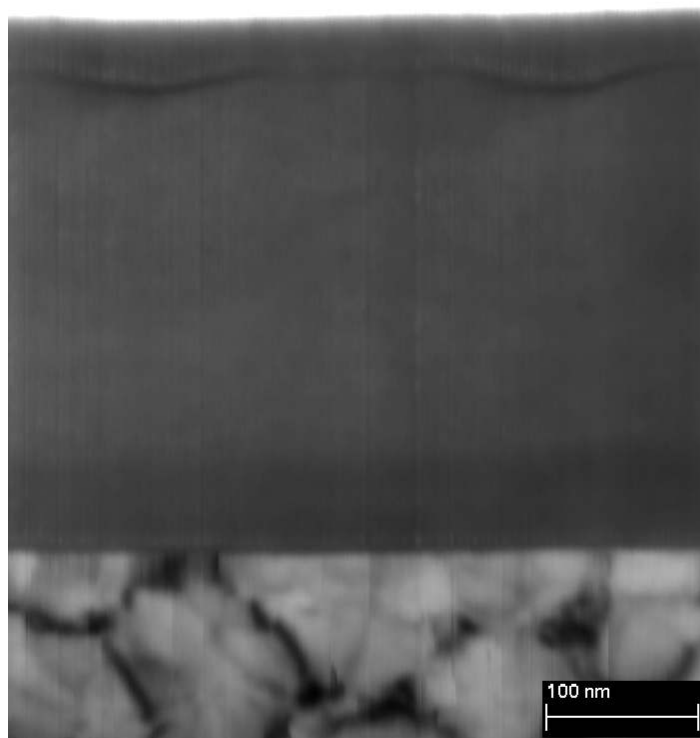

Figure 2.20 – Scanning transmission electron micrograph of an ultramicrotomed section of a superpure aluminium specimen patterned by anodizing in phosphoric acid and subsequent stripping of the porous film, and anodized in 0.1 M ammonium pentaborate solution to 300 V.

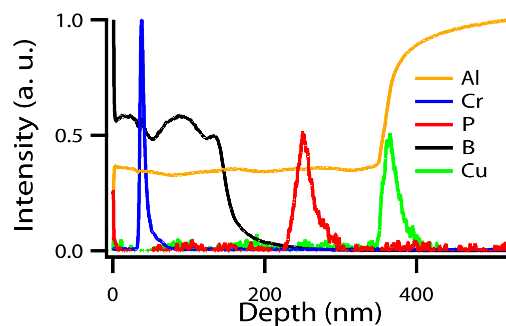

(a) – GD-OES

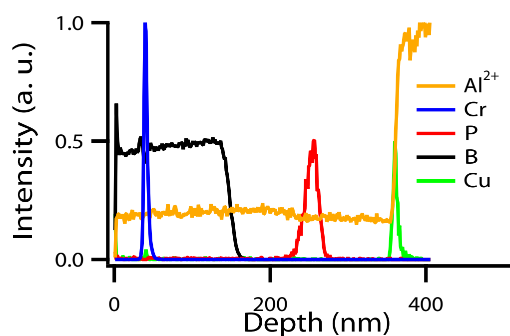

(b) – TOF-SIMS

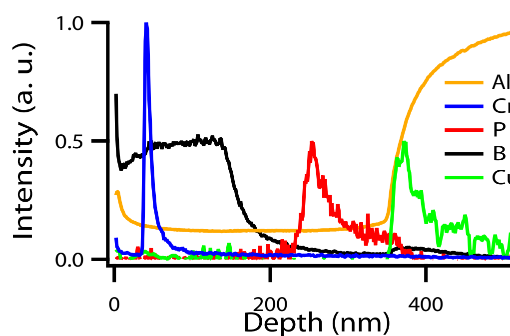

(c) – GD-TOF-MS

Figure 2.21 – Elemental depth profile analysis of anodic alumina films, formed by anodizing electropolished superpure aluminium substrates in ammonium pentaborate to 360 nm, using a. GD-OES, b. TOF-SIMS and c. GD-TOF-MS.

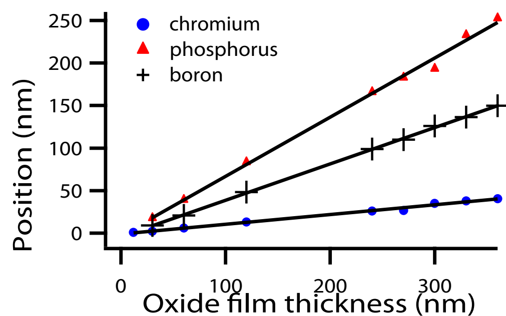

(a) – GD-OES

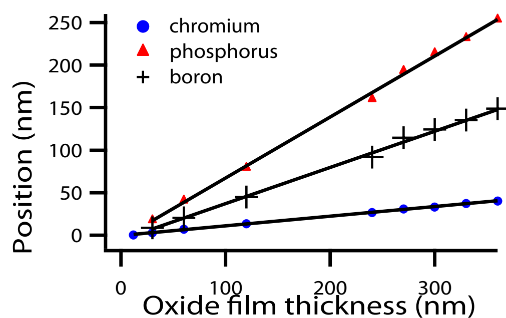

(b) – TOF-SIMS

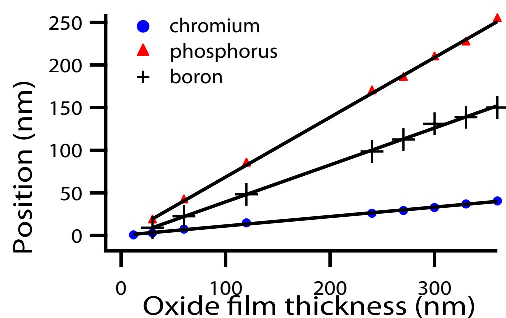

(c) – GD-TOF-MS

Figure 2.22 – Positions of the chromium and phosphorus tracers as well as the boron marker as a function of the anodic oxide film thickness, measured from elemental depth profiles, acquired using a. GD-OES, b. TOF-SIMS and c. GD-TOF-MS, of anodic oxide layers formed by anodizing electropolished superpure aluminium substrates in 0.1 M ammonium pentaborate to 10, 25, 50, 100, 200, 225, 250, 275 and 300 V.

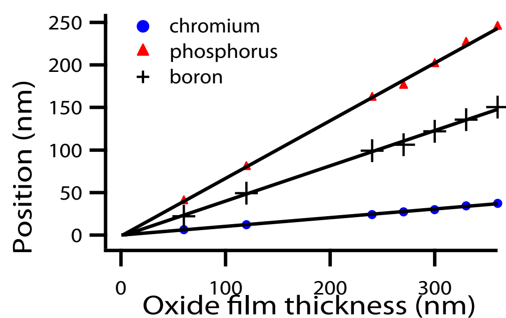

(a) – GD-OES

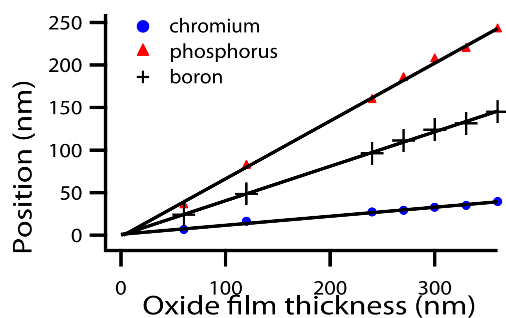

(b) – TOF-SIMS

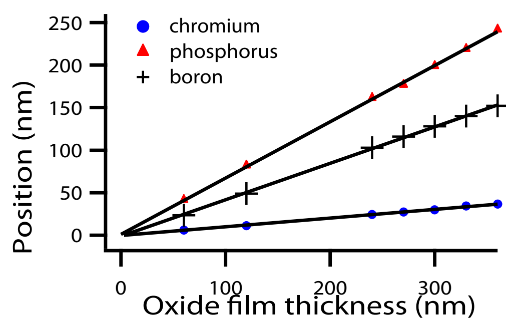

(c) – GD-TOF-MS

Figure 2.23 – Positions of the chromium and phosphorus tracers as well as the boron marker as a function of the anodic oxide film thickness, measured from elemental depth profiles, acquired using a. GD-OES, b. TOF-SIMS and c. GD-TOF-MS, of anodic oxide layers formed by anodizing superpure aluminium substrates, patterned by anodizing in sulphuric acid and subsequent stripping of the porous film, in 0.1 M ammonium pentaborate to 50, 100, 200, 225, 250, 275 and 300 V.

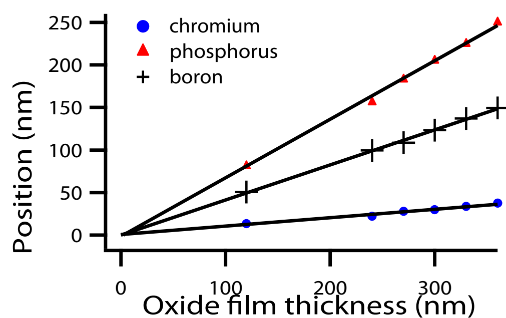

(a) – GD-OES

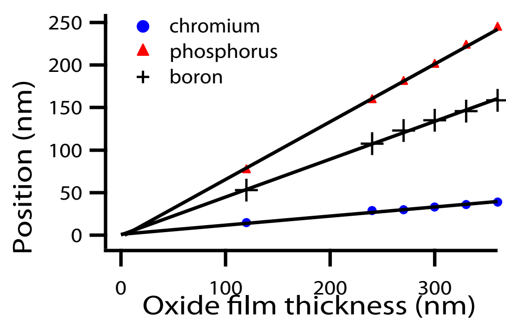

(b) – TOF-SIMS

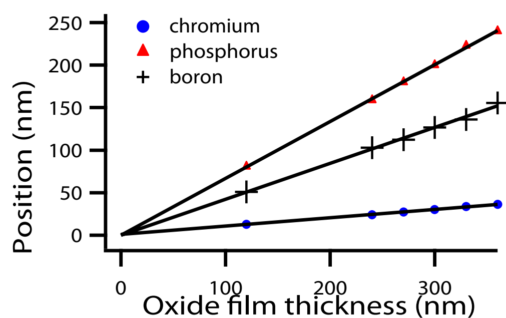

(c) – GD-TOF-MS

Figure 2.24 – Positions of the chromium and phosphorus tracers as well as the boron marker as a function of the anodic oxide film thickness, measured from elemental depth profiles, acquired using a. GD-OES, b. TOF-SIMS and c. GD-TOF-MS, of anodic oxide layers formed by anodizing superpure aluminium substrates, patterned by anodizing in oxalic acid and subsequent stripping of the porous film, in 0.1 M ammonium pentaborate to 100, 200, 225, 250, 275 and 300 V.

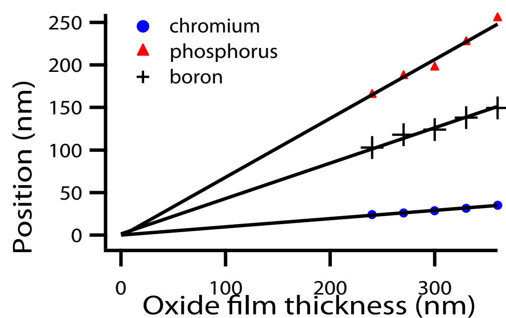

(a) – GD-OES

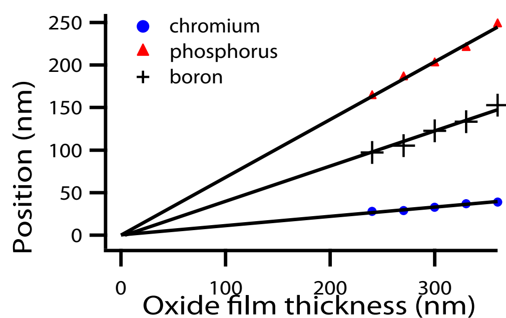

(b) – TOF-SIMS

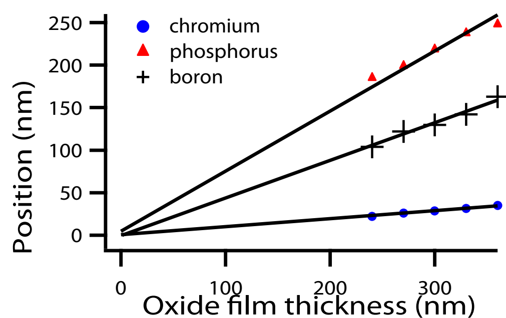

(c) – GD-TOF-MS

Figure 2.25 – Positions of the chromium and phosphorus tracers as well as the boron marker as a function of the anodic oxide film thickness, measured from elemental depth profiles, acquired using a. GD-OES, b. TOF-SIMS and c. GD-TOF-MS, of anodic oxide layers formed by anodizing superpure aluminium substrates, patterned by anodizing in phosphoric acid and subsequent stripping of the porous film, in 0.1 M ammonium pentaborate to 200, 225, 250, 275 and 300 V.

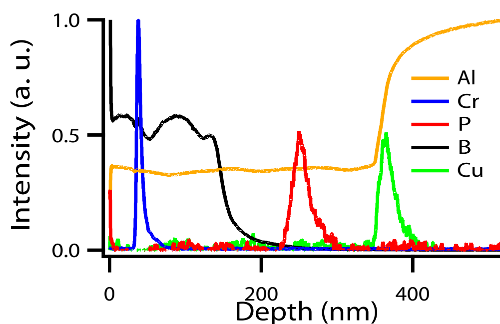

(a) – patterning by electropolishing

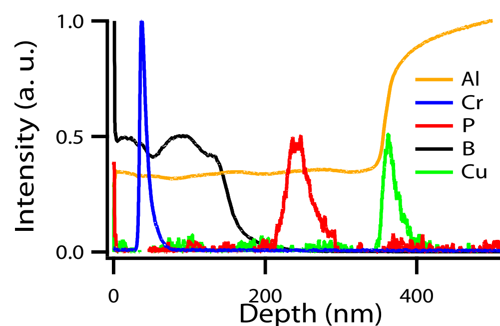

(b) – patterning by sulphuric acid

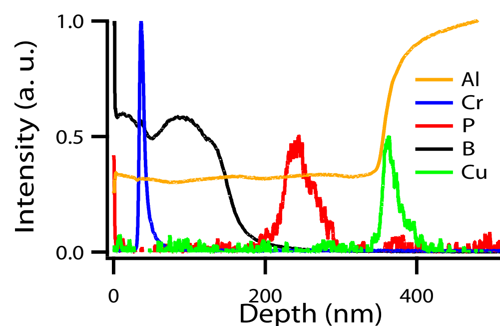

(c) – patterning by oxalic acid

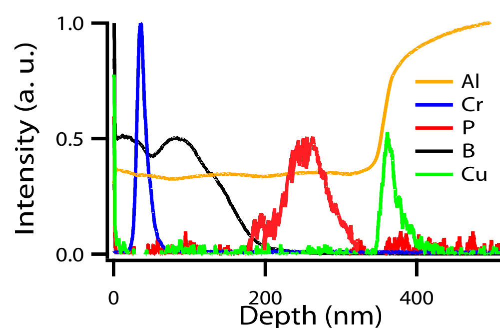

(d) – patterning by phosphoric acid

Figure 2.26 – GD-OES elemental depth profile analysis of anodic alumina films, formed by anodizing in ammonium pentaborate to 360 nm of superpure aluminium substrates patterned by a. electropolishing and by anodizing in b. sulphuric acid, c. oxalic acid, d. phosphoric acid, and subsequent stripping of the porous films.

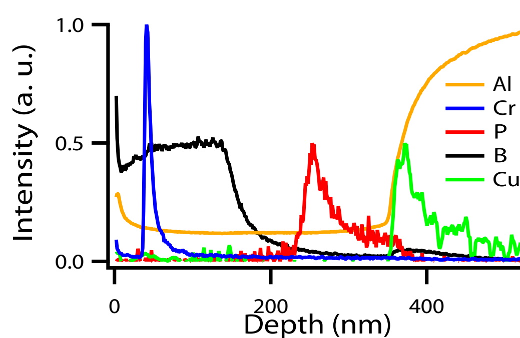

(a) – patterning by electropolishing

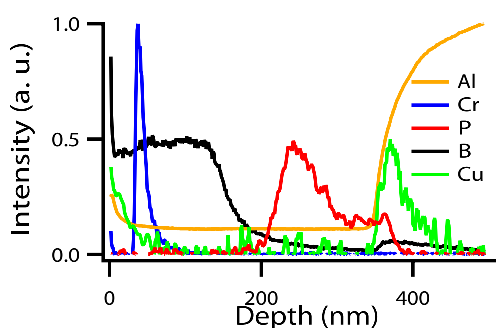

(b) – patterning by sulphuric acid

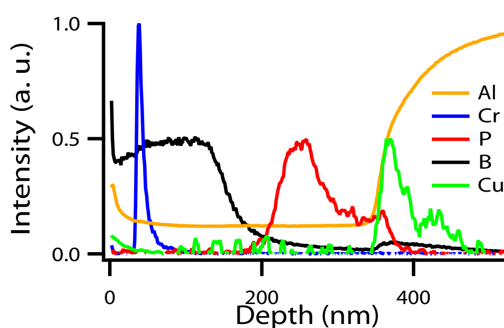

(c) – patterning by oxalic acid

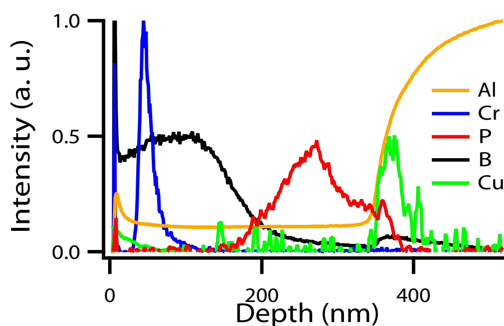

(d) – patterning by phosphoric acid

Figure 2.27 – GD-TOF-MS elemental depth profile analysis of anodic alumina films, formed by anodizing in ammonium pentaborate to 360 nm of superpure aluminium substrates patterned by a. electropolishing and by anodizing in b. sulphuric acid, c. oxalic acid, d. phosphoric acid, and subsequent stripping of the porous films.

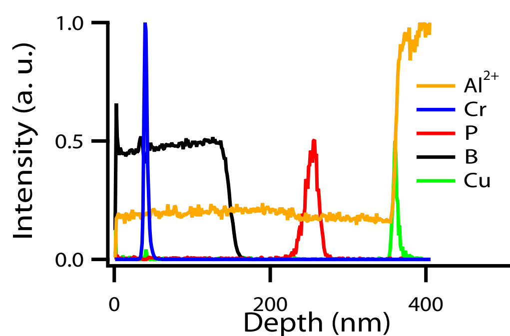

(a) – patterning by electropolishing

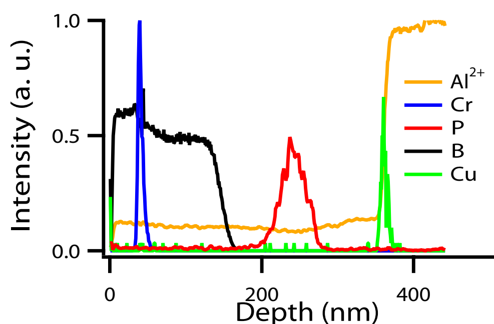

(b) – patterning by sulphuric acid

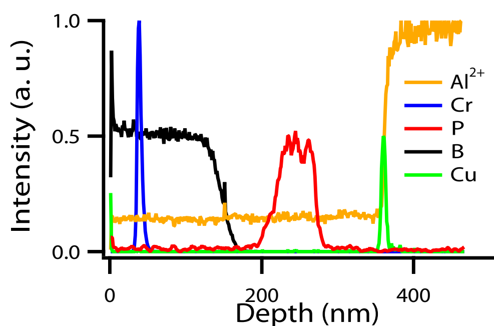

(c) – patterning by oxalic acid

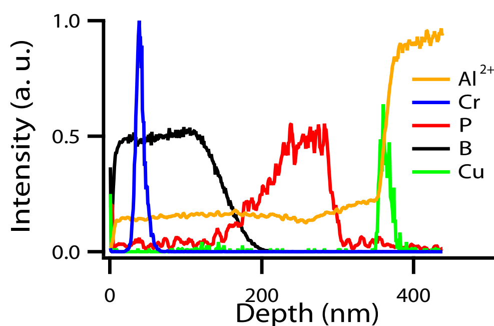

(d) – patterning by phosphoric acid

Figure 2.28 – TOF-SIMS elemental depth profile analysis of anodic alumina films, formed by anodizing in ammonium pentaborate to 360 nm of superpure aluminium substrates patterned by a. electropolishing and by anodizing in b. sulphuric acid, c. oxalic acid, d. phosphoric acid, and subsequent stripping of the porous films.

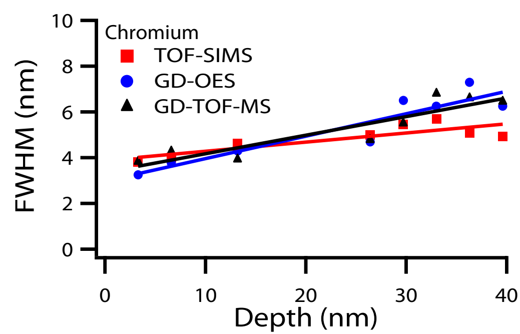

(a) – Chromium tracer

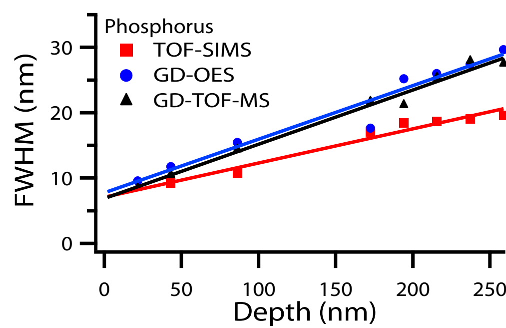

(b) – Phosphorus tracer

Figure 2.29 – Depth profiling using TOF-SIMS, GD-OES and GD-TOF-MS of anodic oxide films formed on substrates patterned by electropolishing; depth resolution as a function of depth measured for a. the chromium tracer and b. the phosphorus tracer.

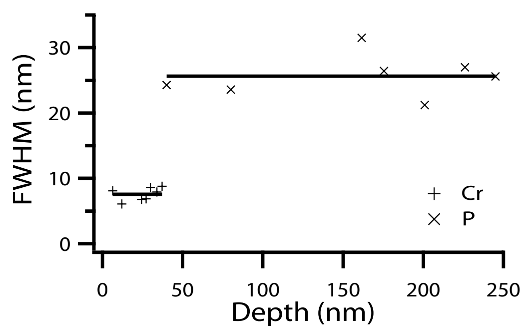

(a) – anodizing in sulphuric acid

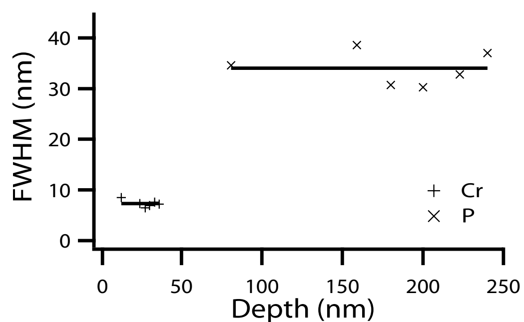

(b) – anodizing in oxalic acid

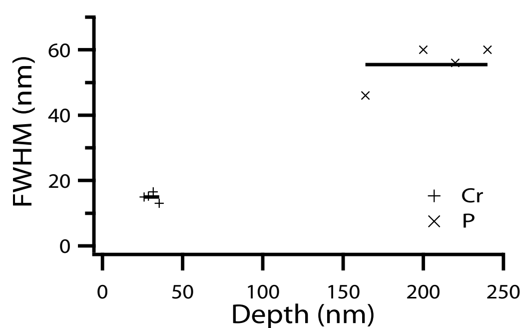

(c) – anodizing in phosphoric acid

Figure 2.30 – GD-OES elemental depth profile analysis of anodic alumina films, formed by anodizing in ammonium pentaborate to 360 nm of superpure aluminium substrates patterned by anodizing in a. sulphuric acid, b. oxalic acid, c. phosphoric acid and subsequent stripping of the porous films.

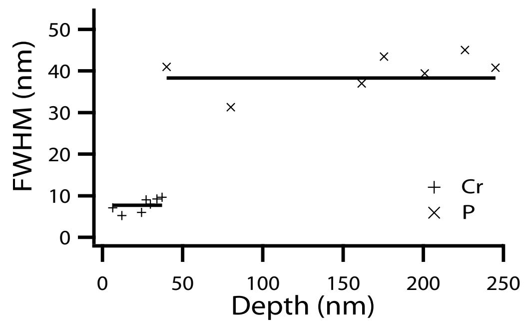

(a) – anodizing in sulphuric acid

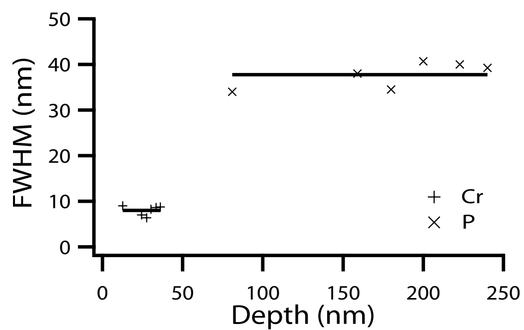

(b) – anodizing in oxalic acid

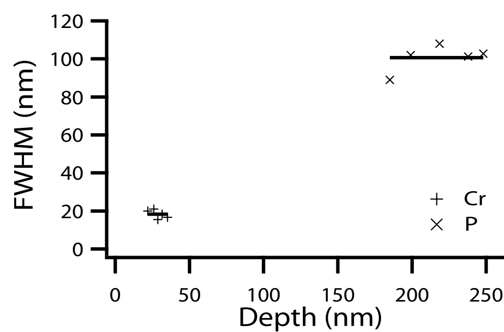

(c) – anodizing in phosphoric acid

Figure 2.31 – GD-TOF-MS elemental depth profile analysis of anodic alumina films, formed by anodizing in ammonium pentaborate to 360 nm of superpure aluminium substrates patterned by anodizing in a. sulphuric acid, b. oxalic acid, c. phosphoric acid and subsequent stripping of the porous films.

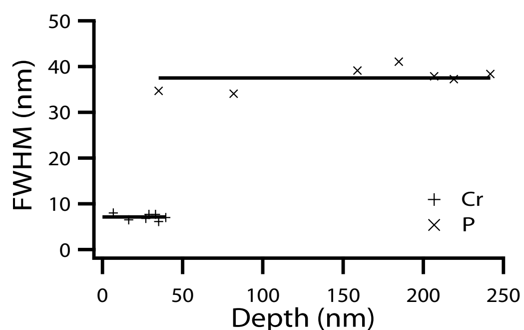

(a) – anodizing in sulphuric acid

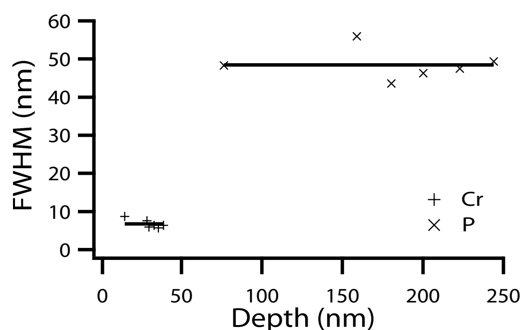

(b) – anodizing in oxalic acid

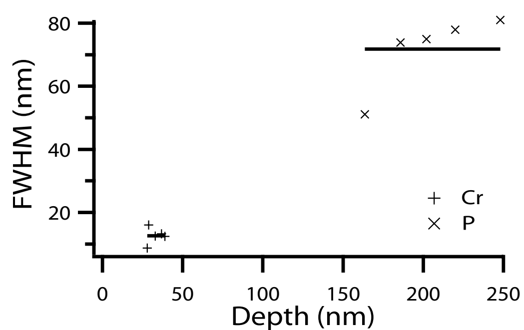

(c) – anodizing in phosphoric acid

Figure 2.32 – TOF-SIMS elemental depth profile analysis of anodic alumina films, formed by anodizing in ammonium pentaborate to 360 nm of superpure aluminium substrates patterned by anodizing in a. sulphuric acid, b. oxalic acid, c. phosphoric acid and subsequent stripping of the porous films.

3 Depth Profiling Analyses of Patterned Specimens

Elemental depth profiling analyses of specimens showing relatively flat surfaces, Sq = 1 - 2 nm, were achieved with high depth resolutions using GD-OES, GD-TOF-MS and TOF-SIMS. Thus, the distributions of the boron marker, and the chromium and phosphorus tracers within the oxide films were probed precisely, thereby allowing determination of the transport numbers for the chromium and phosphorus species. The accuracy of sputtering-induced depth profiling techniques relies dramatically on the erosion process, which may involve atomic mixing, re-deposition of sputtered material and sputtering-induced surface topography development. Depth profiling analyses of patterned specimens using GD-OES, GD-TOF-MS and TOF-SIMS are examined in this section. The sputtering processes associated with initial topography of the various specimens are discussed in detail relative to the different depth profiling techniques.

3.1 Sputtering Sources

GD-OES, GD-TOF-MS and TOF-SIMS rely on different techniques for material removal, with the former employing a glow discharge plasma and the last using a primary ion-beam. However, despite using different sputtering techniques, GD-OES, GD-TOF-MS and TOF-SIMS perform elemental depth profiling analysis with high depth resolution, as shown in the previous section.

In term of depth resolution, the performances achieved by the different sputtering-induced depth profiling techniques depend on the erosion process. A brief summary of the methods used to ensure the material removal during GD-OES, GD-TOF-MS and TOF-SIMS depth profiling analyses follows.

During depth profile analyses performed by GD-OES and GD-TOF-MS, the erosion process is carried out by energetic particles (charged species and neutral atoms) present in the sheath of the glow discharge plasma (Bogaerts, 2007). The glow discharge plasma ensures a high sputtering rate due to the high flux of energetic species. Additionally, the species contributing to sputtering are of low energy (< 50 eV), resulting in a low penetration depth and limiting the surface damage to a very shallow layer of about 2 nm thick (Laude and Chapon, 2005).

The glow discharge plasma is thus highly appropriate for reliable depth profile analysis (Berneron and Charbonnier, 1981; Bings et al., 2008; Escobar-Galindo et al., 2009; Pisonero et al., 2006; Shimizu et al., 2003; Teo and Hirokawa, 1988). However, the variations in sputtering rate across the crater and the resulting crater geometry (Payling, 1997), the re-deposition of sputtered material (Hoffmann et al., 2003) and the sputtering-induced surface topography development (Shimizu et al., 1999a) can affect dramatically the depth resolution achieved. The three effects are dependent on the specimen characteristics and the subsequent surface-plasma interaction, the first two being possibly minimized by adjusting the operating parameters.

In contrast, TOF-SIMS analyses are performed in the dual beam mode by employing sputter- and analysis-ion beams, with energies in the range 1 - 25 keV. The transfer of momentum from primary ions to target atoms through atomic collisions generates a collision cascade, which results in the ejection of neutral or charged species (atoms and molecular compounds) from the surface. Thus, etching of the specimen surface is undertaken by a mono-atomic (Ga^+, Cs^+, $O_2{}^+$, Ar^+...) or cluster ($Au_3{}^+$, $C_{60}{}^+$...) primary ion beam over a defined area, typically about 200 x 200 μm^2, while analysis is performed using a beam over a concentric area, e.g. 10 x 10 μm^2. Thereby, loss of depth resolution associated with the crater geometry is avoided with such a configuration of primary-ion beams. Further, the sputtering process, and consequently the depth resolution, may be optimized by selection of:

- The nature of the primary-ions, i.e. cluster-ion beams have been shown to induce less damage than mono-atomic ion beam (Vickerman, 2009).
- The energy of the primary-ions.
- The incident angle of the primary-ion beams.

Finally, for the different depth profiling techniques, considering specimens of uniform composition, the development of surface topography under bombardment with energetic particles results from various effects (Hofmann, 1998), as indicated below:

- The statistical nature of the ejection of surface atoms during sputtering leading to a certain induced roughness, which is however limited to the atomic scale.
- The thermally induced surface relaxation through atomic diffusion.
- The dependence of the sputtering yield on crystal orientation.
- The local perturbations in the sputtering yield resulting from variation in the surface topography.

The predominant sputtering-induced surface modifications arise from local variations of the sputtering yield due to crystallographic orientation or surface topography.

In the previous section, depth profiling analyses of flat anodic alumina layers have been performed by GD-OES, GD-TOF-MS and TOF-SIMS. For those specific specimens, the different sputtering-induced techniques demonstrated similar depth resolution; however the GD techniques showed more significant broadening of the depth profile than TOF-SIMS.

Elemental depth profiling analyses of patterned anodic alumina layers, undertaken by GD-OES, GD-TOF-MS and TOF-SIMS are discussed in the following section, with particular emphasis on the sputtering process associated with the different techniques.

3.2 Surface Roughnesses

In order to determine the influence of the specimen surface roughnesses on the sputtering process, different roughnesses have been achieved by texturing the aluminium surface by electropolishing or through growth of porous alumina layers of different cell dimensions. The electropolished superpure aluminium substrates present a surface roughness, Sq, of about 2 nm; substrates patterned by anodizing in sulphuric acid, oxalic acid, phosphoric acid and striping of the porous films initially display surface roughnesses of about 7, 12 and 32 nm respectively. Subsequently, barrier-type anodic oxide layers of 30-nm thickness, with incorporation of electrolyte-derived species, namely boron as a marker, and chromium and phosphorus species as tracers, have been produced and the distributions of the different species studied using GD-TOF-MS, GD-OES and TOF-SIMS, Figs. 3.1 - 3.3 respectively.

The comparison of GD-OES and GD-TOF-MS elemental depth profiles of 30-nm thick oxide layers formed on differently patterned superpure aluminium substrates, reveals an increase of the sputtering rate with the surface roughnesses. The metal / oxide interface is revealed in the aluminium profile or can be located using the profile associated with the copper-enriched layer close to the interface. Figures 3.1.a and 3.1.b show that during depth profiling using GD-OES, the metal substrate is exposed after about 0.25 and 1 s for the specimens patterned by phosphoric acid and by electropolishing respectively. Similarly, during elemental depth profile analysis performed by GD-TOF-MS of 30-nm thick anodic alumina layers formed on specimens patterned by phosphoric acid and by electropolishing, the substrate is reached after about 3 and 13 s respectively, Figs. 3.2.a and 3.2.b.

Thus, the sputtering rates achieved by the glow discharge techniques for the oxide layers formed anodically on substrates patterned by anodizing in phosphoric acid and stripping of the porous film are about 4 times faster than for the oxide film grown on electropolished superpure aluminium substrates.

Conversely, Figures 3.3.a and 3.3.b reveal that during depth profiling analysis performed using TOF-SIMS the sputtering rate is apparently independent of the roughnesses, with the metal substrates being exposed after about 350 s for the different specimens.

As a result of the variation of the sputtering rates, the chromium and phosphorus elemental depth profiles obtained by GD-OES and GD-TOF-MS depth profiling analyses of anodic oxide layers, formed on superpure aluminium substrates patterned by anodizing in sulphuric acid, oxalic acid, phosphoric acid and stripping of the porous films, display significant modifications of shape, in comparison with the respective profiles measured by TOF-SIMS, Figs. 3.1.c, 3.1.d, 3.2.c, 3.2.d, and 3.3.c, 3.3.d respectively.

The generation of primary ions, using an ion beam, is independent of the specimen for TOF-SIMS. Conversely, during depth profile analyses using glow discharge techniques, the production of primary ions relies on a glow discharge plasma, whose sustainability is dependent on the emission of secondary electrons from the surface. Additionally, during glow-discharge depth profile analyses, the sputtering process results from the bombardment of the specimen surface by primary ions accelerated under the electric field reigning within the cathode dark space. The distribution of the electric field is influenced by the surface roughness of the specimen analysed.

Thus, enhancement of the sputtering yield by the surface roughness involves variations of the sputtering rate throughout the layers analysed. In order to obtain further information on the erosion process, sputtering induced surface topography has been examined during depth profiling of patterned specimens using GD-TOF-MS, GD-OES and TOF-SIMS.

3.3 Elemental Depth Profiles

The anodic oxide layers formed on variously patterned substrates were examined by sputtering-induced depth profiling analyses, using GD-OES, GD-TOF-MS and TOF-SIMS. Figures 3.4 - 3.6 compare the elemental depth profiles obtained by the different sputtering techniques of anodic oxide films of different thicknesses, namely 30, 120, 240 and 360 nm, formed on superpure aluminium substrates patterned either by electropolishing or by anodizing in phosphoric acid and subsequent stripping of the porous film.

For the anodic oxide films formed on electropolished superpure aluminium substrates, the elemental depth profiles reveal the distributions of the aluminium as well as the electrolyte-derived species incorporated within the anodic oxide, namely boron, chromium and phosphorus species. The steep rise in the aluminium signal indicates the metal / oxide interface. Boron species are incorporated into the outer part of the anodic oxide. The interface between the boron-enriched and the boron-free layers locates the position of the original surface of the substrate prior to anodizing. The elemental depth profiles associated with the chromium, phosphorus, copper species display narrow peaks, while the aluminium and boron elemental present sharp interfaces. The aluminium and boron depth profiles can be modelled by Sigmoid functions, while copper, phosphorus, chromium, depth profiles are best fitted by Gaussian and exponential-modified Gaussian functions.

In contrast, for the alumina layers grown anodically on superpure aluminium substrates patterned by anodizing in phosphoric acid and stripping of the porous film, the elemental depth profiles relative to the different species present mostly broad features; in addition, narrowing of the chromium, aluminium and copper depth profiles arises for the 240- and 360-nm thick oxide layers.

The growth of anodic alumina on superpure aluminium substrates patterned by anodizing in phosphoric acid and stripping of the porous films, has been previously shown by transmission electron microscopy, to result in the flattening of the anodic oxide surface and of the aluminium substrates after the formation of 240-nm thick oxide layers.

Additionally, the distributions of the boron marker and the chromium and phosphorus tracers within the anodic oxide films have been shown to be related to the initial roughness of the differently patterned substrates. Further, the formation of anodic oxide films on patterned superpure aluminium substrates result in the narrowing of the distribution of the chromium species, whereas the distribution of the phosphorus species remain intact, Figures 3.7 - 3.9.

The distributions of the different enriched-layers are directly influenced by the initial surface roughnesses of the substrates. In addition, the surface roughnesses of the specimens and the associated sputtering processes have to be taken into account for the interpretation of the elemental depth profiles measured for the alumina layers grown anodically on patterned superpure aluminium substrates.

The variation of the elemental depth profiles associated with the different species, as a result of the specimen surface pattern are discussed for each technique.

3.3.1 Glow discharge analyses

Figures 3.4.a and 3.4.b disclose the GD-OES depth profiles of 30-and 120-nm thick oxide layers formed on electropolished substrates; the GD-TOF-MS depth profiles measured for identical specimens are presented in Figures. 3.5.a and 3.5.b. The elemental depth profiles measured by both glow discharge techniques reveal the distributions of the aluminium as well as the electrolyte-derived species incorporated within the anodic oxide, namely boron, phosphorus and chromium species. The boron, phosphorus and chromium depth profiles can be modelled by a sigmoid, a Gaussian and an exponential-modified Gaussian function respectively.

The GD-OES and GD-TOF-MS depth profiles of 30- and 120-nm thick oxide layers, formed on substrates textured by anodizing in phosphoric acid and stripping of the porous films, are shown in Figures 3.4.e and 3.4.f, and Figures 3.5.e and 3.5.f respectively. For both techniques, broadening of the different elemental depth profiles is evident.

Thus, the Gaussian and the exponential-modified Gaussian functions are no longer suitable to fit the phosphorus and chromium profiles. The elemental depth profiles obtained by GD-OES and GD-TOF-MS are similar in shape; however, the sputtering rate achieved by GD-TOF-MS is about 4 times slower than for GD-OES. The following discussion concerns the elemental depth profiles measured by GD-OES but is relevant for the depth profiles obtained by GD-TOF-MS taking into consideration the sputtering rates respective to each technique.

For the 120-nm thick oxide, the chromium and phosphorus distributions show the convolution of different peaks respectively. For GD-OES the sputtering rate is about 30 nm s^{-1}, which is similar to the sputtering rate of alumina layers formed on electropolished substrates.

For the 30-nm thick oxide, the boron, chromium and phosphorus depth profiles show a peak in the first 0.25 s of sputtering, and then a slow decay through the analysis of the oxide; this time is assumed to correspond to the sputtering of the 30 nm thick oxide layer present over the ridges. Thus, the sputtering rate is 120 nm s^{-1} for about 0.25 s then, due to the anisotropic erosion and the subsequent development of a peak-like texture, the aluminium signal increases gradually with sputtering time. By comparison, the sputtering rate of alumina layers formed on substrates textured by electropolishing is about 26 nm s^{-1}.

3.3.2 Secondary ion mass analysis

Figures 3.6.a and 3.6.b present the TOF-SIMS depth profile of 30- and 120-nm thick oxide layers formed on electropolished superpure aluminium substrates. The elemental depth profiles of aluminium are shown, with the steep rise in the aluminium signals indicating the location of the metal / oxide interfaces. Additionally, the boron, chromium and phosphorus electrolyte-derived species, incorporated within the anodic oxides, are revealed as narrow peaks within the thickness of the barrier-type anodic.

For such specimens, the elemental depth profiles performed by TOF-SIMS and GD-OES and GD-TOF-MS, show good agreement on the distributions of the different species. The depth resolutions achieved by TOF-SIMS, GD-OES and GD-TOF-MS have been assessed by examination of the distributions of incorporated species within

barrier anodic oxide films. Evaluation of the depth resolution of the chromium and phosphorus profiles has been carried out by measurement of the Full Width at Half Maximum (FWHM), as defined by convention for a Gaussian-like profile. Thus, elemental depth profiles of 30 nm thick oxide layers formed on substrates patterned by electropolishing, performed by TOF-SIMS, GD-OES and GD-TOF-MS, present comparable depth resolutions. Indeed, during depth profiling of the chromium-enriched layer, the depth resolutions achieved by TOF-SIMS, GD-OES and GD-TOF-MS have been estimated at 4.2 ± 0.5 nm, 3.2 ± 0.4 nm and 3.8 ± 0.4 nm respectively. Similarly, the depth resolutions evaluated from the phosphorus profiles obtained by TOF-SIMS, GD-OES and GD-TOF-MS are 9 ± 1 nm, 12 ± 1 nm and 11 ± 1 respectively.

The elemental depth profiles, performed by TOF-SIMS on 30- and 120-nm thick oxide films formed on substrates, patterned by anodizing in phosphorus acid and subsequent stripping of the porous films are presented in Figures 3.6.e and 3.6.f respectively. In comparison with the elemental depth profiles measured for anodic oxide layers formed on electropolished substrates, a slight broadening of profiles associated with the different species arises, thereby the influence of the surface roughness on the depth resolution appears to be relatively limited. Further, the sputtering rates for the 30- and 120-nm thick oxide layers are independent of the roughness of the specimens, with the metal substrates being exposed after about 35 and 180 s of sputtering, for both oxide layers formed anodically on electropolished superpure aluminium substrates and patterned by anodizing in phosphoric acid and stripping of the porous films.

Thus, elemental depth profiling measured using TOF-SIMS and glow discharge techniques of 30- and 120-nm thick oxide layers formed on substrates patterned by anodizing in phosphoric acid, are significantly different. For the 30-nm thick anodic oxide films, the GD-OES and GD-TOF-MS elemental depth profiles of the chromium and phosphorus distributions display decay-like features, comprised of sharp peaks over the first 0.25 and 1 s of sputtering, and subsequent slow decays with further sputtering of the anodic oxide. In contrast, the elemental depth profiles, determined by TOF-SIMS, present Gaussian-like peaks for the chromium and phosphorus enriched-layers. Finally, during depth profiling of patterned specimens, TOF-SIMS analysis allow the determination of the location of the different species within the oxide films, whereas glow discharge analyses present limitations for this purpose.

In order to explain the difference of performances associated with the analyses of patterned specimens using TOF-SIMS, GD-OES and GD-TOF-MS. Models of the sputtering processes associated with the different specimens and the different depth profiling techniques have been ascertained by examination of partially depth profiled specimens using atomic force microscopy, transmission electron microscopy and scanning electron microscopy.

3.4 Sputtering-Induced Surface Modifications

3.4.1 Glow-discharge induced surface modifications

Figures 3.10 and 3.11 show the surface topography development, under GD-OES sputtering, of 30- and 120-nm thick oxide films respectively, formed on substrates patterned by anodizing in phosphoric acid and subsequent stripping of the porous films. The sputtering occurs non-uniformly, resulting in surface pattern modification leading to the development of peak-like features over the specimen surfaces. For such specimens, identical sputtering processes arise during GD-TOF-MS depth profile analysis.

Transmission electron micrographs of ultramicrotomed sections of 30- and 120-nm thick oxide layers after sputtering for 1s and for 2, 3, 4 and 5 s respectively are presented in Figures 3.14 and 3.15. For the 30-nm thick anodic oxide layer, preferential erosion of the surface ridges is evident; thus, the transmission electron micrograph discloses that while the initial peaks of the surface have been removed after sputtering for 1 s, the thickness of the oxide layer is unchanged at the valleys. For the 120-nm thick film preferential sputtering under particle bombardment, lead to the flattening of the specimen surface. The erosion continues uniformly until the aluminium substrate is reached as displayed in Figures 3.15.c and 3.15.d. Finally, the substrate is exposed locally; consequently, the aluminium is removed faster due to an increased sputtering yield in comparison with the aluminium oxide, leading to the roughening of the surface.

The sputtering process taking place during GD-OES depth profiling analysis of 30-nm thick anodic oxide layer, formed on superpure aluminium substrates patterned by anodizing in phosphoric acid and stripping of the porous film, was examined by scanning electron microscopy using the InLens (detection of secondary electrons generated by

primary electrons at the near surface (SE1)), SE2 (contribution of secondary electrons created by backscattered electrons as they escape the specimen) and EsB (detection of back-scattered electrons) detectors.

Figure 3.16.a displays a scanning electron micrograph, in the InLens mode, of the anodic oxide surface. The peaks of the surface, i.e. the walls between the cells of the array, appear brighter than the cells of the pattern. In the SE2 mode, the surface features are revealed in an identical manner, Fig. 3.16.b.

After GD-OES depth profiling for 0.15 s, the sputtering process commences at the peaks of the surface, Figs. 3.17.a and 3.17.b. The scanning electron micrograph using the EsB detector, Fig. 3.17.c, shows an important contrast between the peaks and the valleys of the surface, disclosing the areas of the surface preferentially sputtered. The brighter areas may correspond to the aluminium substrate or to oxide from which surface contaminants have been removed under glow discharge sputtering.

For further erosion, the sputtering process results in the separation of the individual cells of the surface array pattern, Figs. 3.18 and 3.19. Interestingly, Figures 3.18.a and 3.18.b, and, 3.19.a and 3.19.b, reveal that the areas of low secondary electron emission, i.e. dark areas in the InLens image, correspond to the parts protruding from the surface in the micrograph using the SE2 mode. Despite the possible differences involved in the secondary electron emission processes induced by 1-keV primary electrons and 50-eV primary ions, the scanning electron images using the InLens detector may indicates the influence of the secondary electrons on the glow discharge sputtering process.

Thus, examination of barrier anodic oxide layers, formed on substrates textured by anodizing in phosphoric acid and subsequent stripping of the porous films, exposed to glow discharge bombardment, reveals sputtering induced surface topography development leading to the roughening or smoothing of the original specimen texture.

The 30-nm thick oxide layers, formed on substrates patterned by anodizing in phosphoric acid and stripping of the porous film, present a ratio of the film thickness to the amplitude of the substrate texture less than 1; consequently, the peaks of the aluminium substrate are located above the valleys of the oxide layer. Glow discharge

sputtering of such specimens has been shown to lead to roughening of the surface texture. The roughening of oxide surface results from the combination of topography- and composition-enhanced sputtering yields. Thus, at the commencement of sputtering, the surface ridges are sputtered more rapidly than the valleys; in addition, the oxide material at the peaks of the surface is sputtered 5 times faster than on a flat surface. Consequently, the aluminium substrate is rapidly exposed at the surface ridges. The aluminium is then removed markedly faster at the peaks of the surface than the surrounding oxide present over the surface valleys, due to the difference of sputtering yield between aluminium and alumina, therefore contributing to selective material removal. Finally, glow discharge sputtering leads to the roughening of the surface pattern as a result of the development of a peak-like texture.

For the 120-nm thick oxide layers, formed on substrates patterned by anodizing in phosphoric acid and stripping of the porous film, the oxide film thickness is about twice the amplitude of the original substrate texture. Surface topography modifications consist of smoothing of the surface roughness and the development of a peak-like texture at the oxide / metal interface. Due to a ratio of film thickness to the amplitude of the substrate texture greater than 1, erosion of the surface ridges does not expose directly the aluminium substrate tips. Thus, unlike the previous case, no roughening of the surface topography takes place. Consequently, the peaks are eroded faster than the valleys of the surface as a result of an increased yield of sputtering.

The local increase in sputtering yield has been considered by Shimizu et al (Shimizu et al., 1999e) to be a result of the local enhancement of the electric field at ridges of the originally rough substrate, leading to a sputtering rate over the peaks about 5 times greater than over the adjacent valleys.

However, the transmission electron micrographs of ultramicrotomed sections of the 120-nm thick anodic oxide layers, formed on substrates patterned by anodizing in phosphoric acid and stripping of the porous film, Figs. 3.15.c and 3.15.d, reveal that once the surface roughness is flattened, the erosion proceeds uniformly until the aluminium substrate is exposed. The local enhancement of the sputtering rate no longer exists as the oxide / metal interface is approached. Thus, the sputtering yield appears to be surface curvature dependent and leads to preferential sputtering of the surface peaks.

The surface-site dependence of the sputtering yield could possibly be correlated with the variation of the electric field induced by the surface roughness of the specimen or by the secondary electron emission coefficient of the surface. Finally, development of a peak-like texture at the oxide / metal interface occurs as a result of the increased yield of sputtering for aluminium compared with alumina.

3.4.2 Ion-beam induced surface modifications

Examination of topographical modifications resulting from TOF-SIMS elemental depth profiling have been carried out by atomic force microscopy on 30- and 120-nm thick anodic oxide films formed on aluminium substrates patterned by anodizing in phosphoric acid and subsequent stripping of the porous film.

Figures 3.20 and 3.21 display the evolution under ion beam of the surface topography of 30- and 120-nm thick oxide films formed on patterned aluminium substrates. In contrast to the development of peak-like features over the specimen surface under glow discharge sputtering, the original hexagonal cell array pattern of the surface largely remains during ion-beam depth profiling of the anodic oxide layer.

Argon-ion beam sputtering of 30-nm thick anodic oxide layers, formed on rough substrates patterned by anodizing in phosphoric acid, proceeds relatively uniformly throughout the analysis of the film. The original texture of the tailored specimens mostly persists until the metal / oxide interface is reached after sputtering for 500 s. An angle of about 30° is defined between the tangent to the centre of a cell and the line rising from the cell centre to the top of a ridge. The dimensions of the cell diameter and of a surface ridge, defined from the bottom of a cell to the top of a ridge, have been measured from transmission electron micrographs of ultramicrotomed sections of specimens anodized to 30 V. Thus, shadowing of the valleys by the ridges is limited, as a result of the combination of the ratio of the characteristic dimensions of the surface and the configuration of the primary-ion beams set at 45° relative to the normal to the specimen surface. Thereby, employing low-energy primary ion beams at an angle of incidence of 45° relative to the normal of the specimen surface restrains topographical modifications.

3.5 Conclusions

The degradation of the depth resolution during glow discharge depth profile analyses of oxide films formed on initially rough surfaces has been assessed by examination of the distributions of incorporated species within barrier anodic oxide films. Deviation between the original elemental depth distribution and the measured profile results from anisotropic sputtering and the subsequent induced surface modifications as well as the variation of sputtering rate through the film removal. The specimen surface topography has been shown to influence the uniformity of the erosion process by local enhancement of the sputtering yield. Thus, as a result of the extent of the surface roughening, the degradation of the depth distribution is mainly dependent on the non-uniform ion bombardment and the development of peak-like texture. Consequently, deformation of the Gaussian-like shape of the elemental depth profiles of the corresponding chromium and phosphorus distributions takes place through the non-unique information depth. Finally, variation in sputtering rate during elemental depth profiling does not allow an accurate conversion of sputtering time into sputtered depth, resulting in an increase of the uncertainty associated with the determination of the location of the different elemental depth profiles.

In contrast to the sputtering processes induced by glow discharge techniques, no preferential sputtering occurs over the surface pattern of the different specimens during TOF-SIMS depth profiling analysis. The original surface pattern remains during depth profiling of the oxide layers, thus the material is potentially removed uniformly. Finally, during TOF-SIMS analysis, in dual beam mode by employing primary ion beams at an angle of incidence of 45° (relative to the normal to the specimen surface), the influence of the surface roughness on the erosion process appears relatively limited, allowing depth profiling of thin films formed on patterned substrates. However, the selection of a reference for the depth calibration of the elemental depth profiles is not straightforward. As a result, the distributions of the different electrolyte-derived species can not directly be determined. The evolution of the distributions of species is discussed and estimated in the next Section entitled "Growth Mechanism of Barrier-Type Anodic Alumina".

Figures

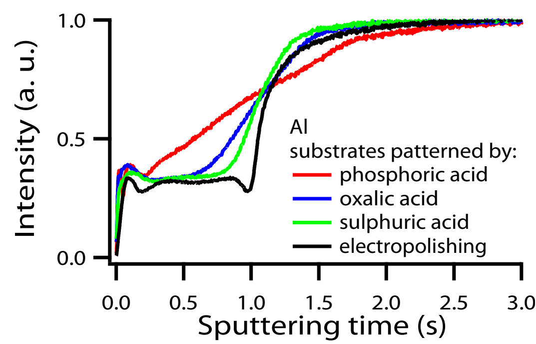

(a) – Al (30 nm)

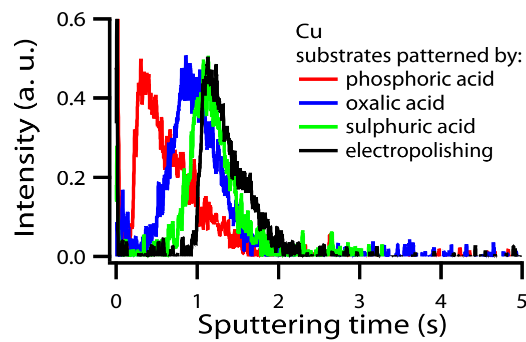

(b) – Cu (30 nm)

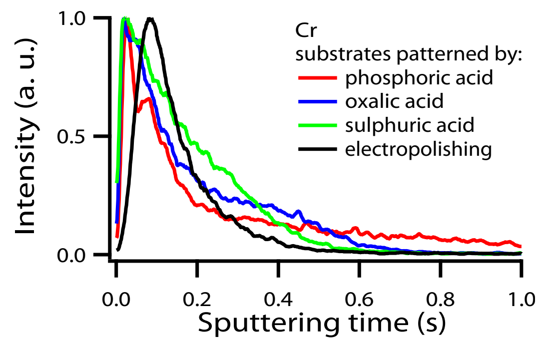

(c) – Cr (30 nm)

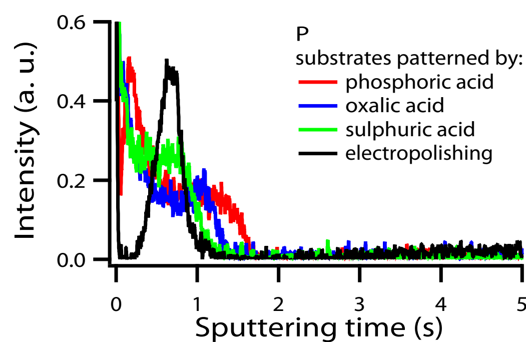

(d) – P (30 nm)

Figure 3.1 – Comparison of the elemental depth profiles performed by GD-OES on anodic oxide layers, formed by anodizing in ammonium pentaborate of superpure aluminium substrates differently patterned to 30 nm.

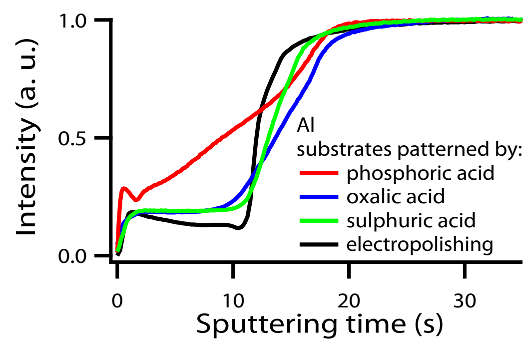

(a) – Al (30 nm)

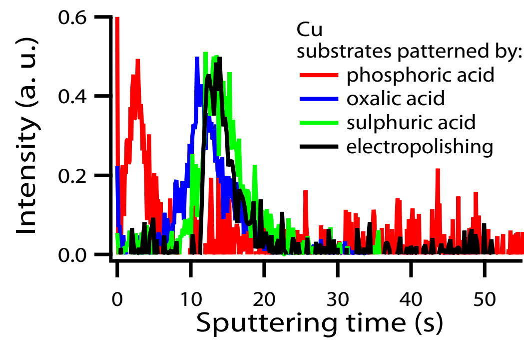

(b) – Cu (30 nm)

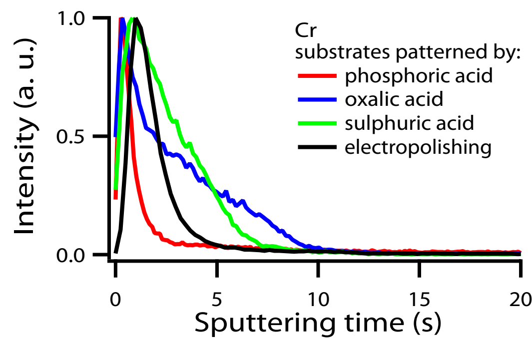

(c) – Cr (30 nm)

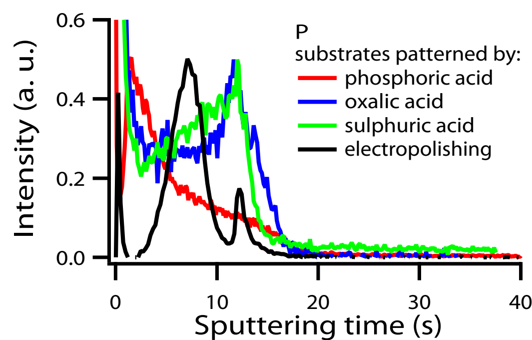

(d) – P (30 nm)

Figure 3.2 – Comparison of the elemental depth profiles performed by GD-TOF-MS on anodic oxide layers, formed by anodizing in ammonium pentaborate of superpure aluminium substrates differently patterned to 30 nm.

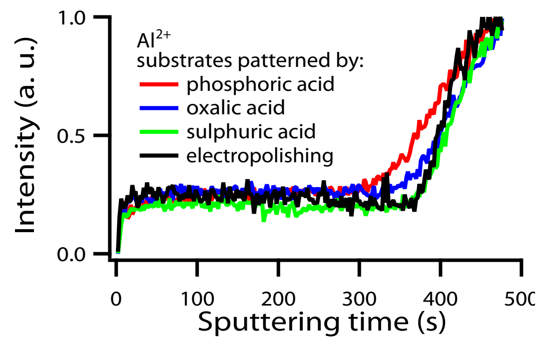

(a) – Al (30 nm)

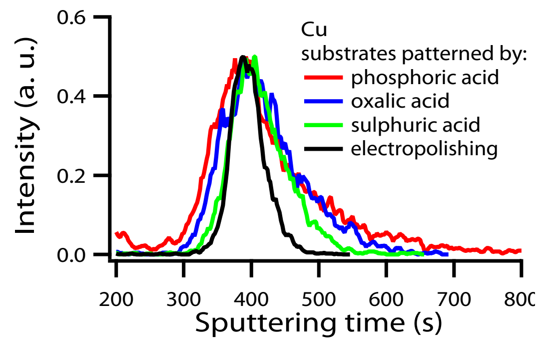

(b) – Cu (30 nm)

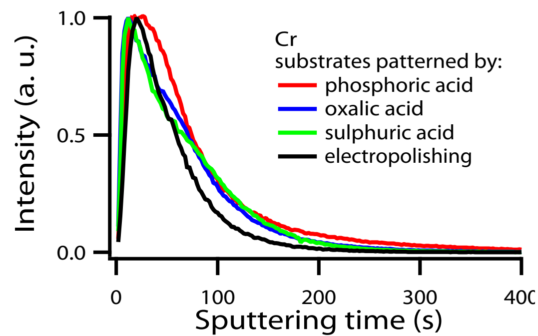

(c) – Cr (30 nm)

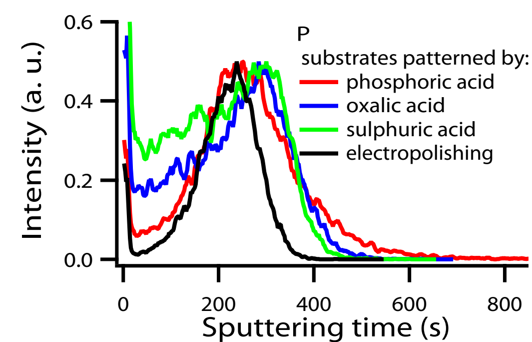

(d) – P (30 nm)

Figure 3.3 – Comparison of the elemental depth profiles performed by TOF-SIMS on anodic oxide layers, formed by anodizing in ammonium pentaborate of superpure aluminium substrates differently patterned to 30 nm.

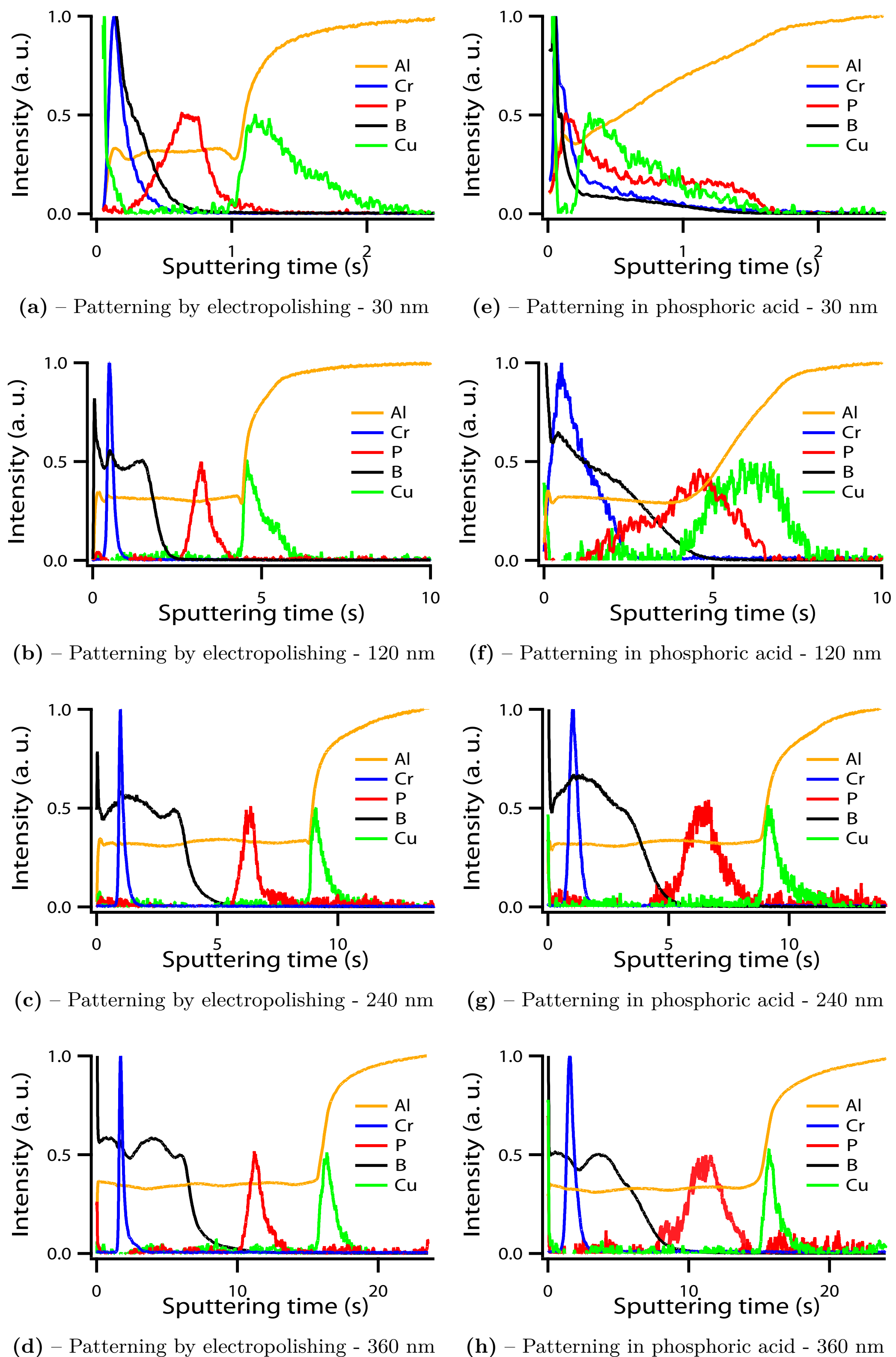

(a) – Patterning by electropolishing - 30 nm
(e) – Patterning in phosphoric acid - 30 nm
(b) – Patterning by electropolishing - 120 nm
(f) – Patterning in phosphoric acid - 120 nm
(c) – Patterning by electropolishing - 240 nm
(g) – Patterning in phosphoric acid - 240 nm
(d) – Patterning by electropolishing - 360 nm
(h) – Patterning in phosphoric acid - 360 nm

Figure 3.4 – GD-OES elemental depth profile analysis of anodic alumina films, formed by anodizing in ammonium pentaborate to 30, 60, 240 and 360 nm of aluminium substrates patterned by electropolishing (a - d) and of aluminium substrates successively electropolished, patterned in phosphoric acid and stripped in a chromic / phosphoric acid solution (e - h).

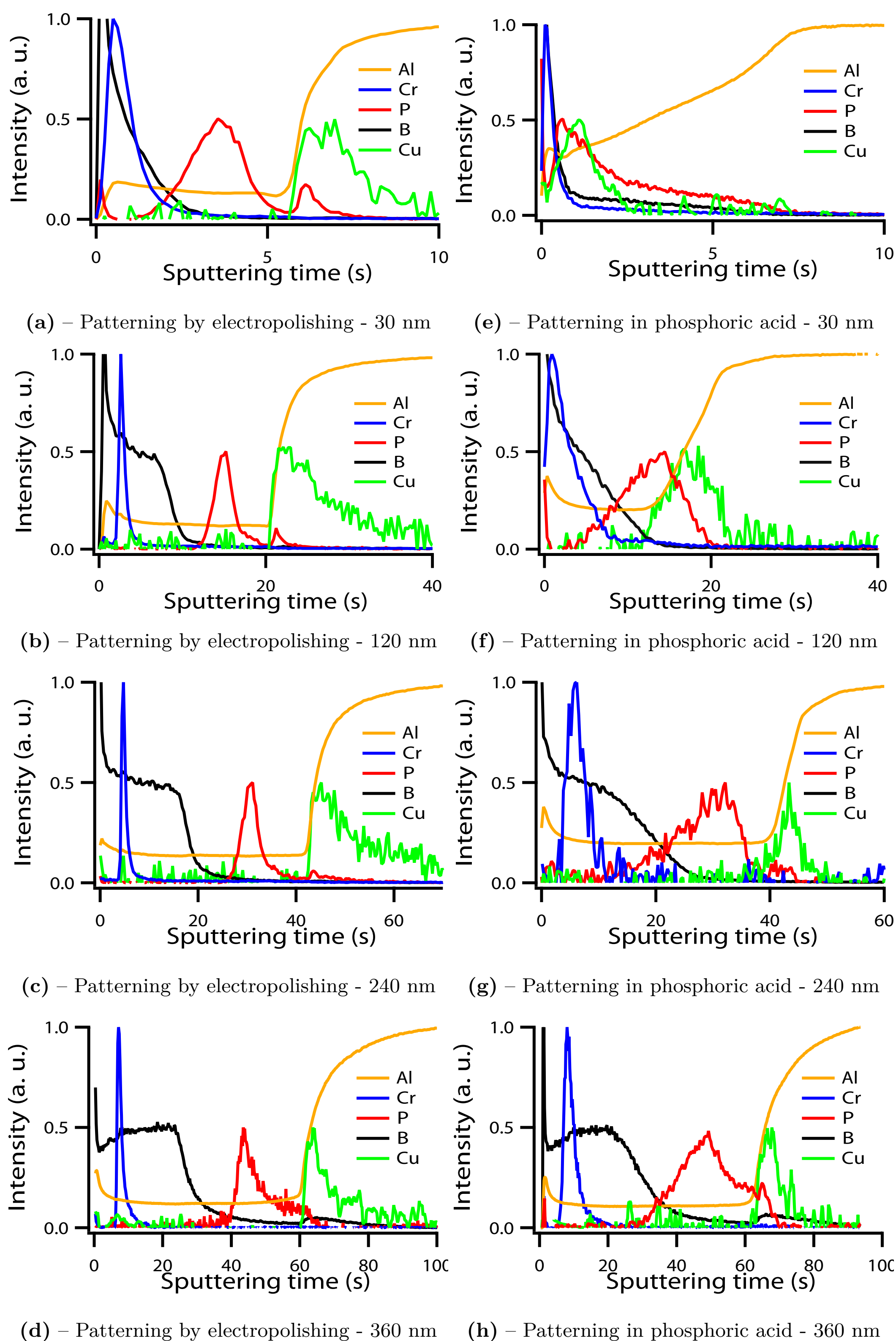

(a) – Patterning by electropolishing - 30 nm

(e) – Patterning in phosphoric acid - 30 nm

(b) – Patterning by electropolishing - 120 nm

(f) – Patterning in phosphoric acid - 120 nm

(c) – Patterning by electropolishing - 240 nm

(g) – Patterning in phosphoric acid - 240 nm

(d) – Patterning by electropolishing - 360 nm

(h) – Patterning in phosphoric acid - 360 nm

Figure 3.5 – GD-TOF-MS elemental depth profile analysis of anodic alumina films, formed by anodizing in ammonium pentaborate to 30, 60, 240 and 360 nm of aluminium substrates patterned by electropolishing (a - d) and of aluminium substrates successively electropolished, patterned in phosphoric acid and stripped in a chromic / phosphoric acid solution (e - h). The sputtering times have been normalized as a function of the sputtering rate of the 360-nm thick specimen.

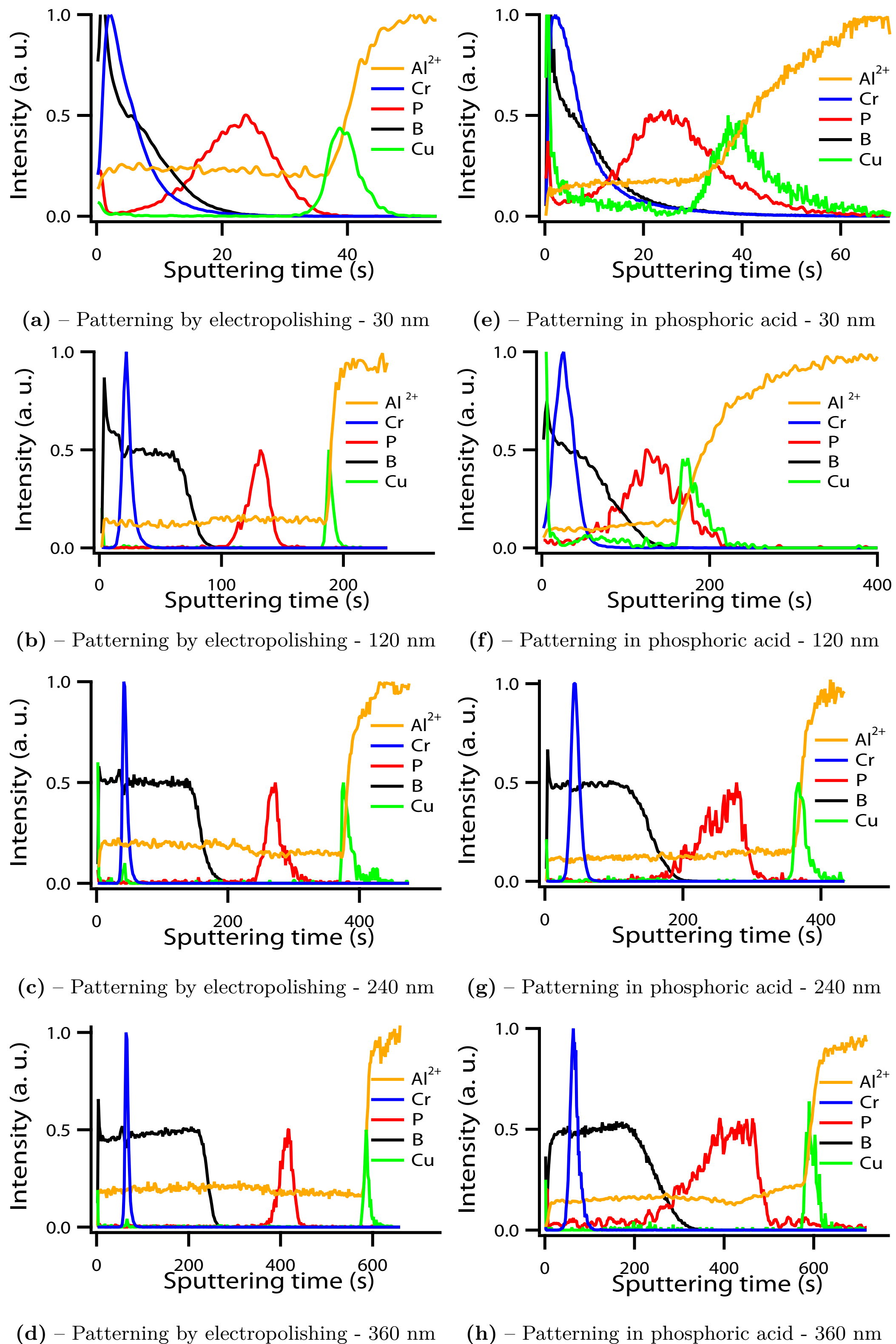

(a) – Patterning by electropolishing - 30 nm

(e) – Patterning in phosphoric acid - 30 nm

(b) – Patterning by electropolishing - 120 nm

(f) – Patterning in phosphoric acid - 120 nm

(c) – Patterning by electropolishing - 240 nm

(g) – Patterning in phosphoric acid - 240 nm

(d) – Patterning by electropolishing - 360 nm

(h) – Patterning in phosphoric acid - 360 nm

Figure 3.6 – TOF-SIMS elemental depth profile analysis of anodic alumina films, formed by anodizing in ammonium pentaborate to 30, 60, 240 and 360 nm of aluminium substrates patterned by electropolishing (a - d) and of aluminium substrates successively electropolished, patterned in phosphoric acid and stripped in a chromic / phosphoric acid solution (e - h). The sputtering times have been normalized as a function of the sputtering rate of the 360-nm thick specimen.

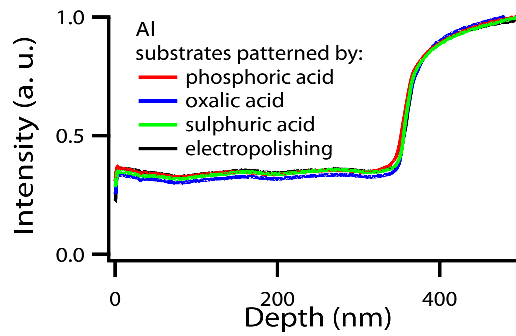

(a) – Al (360 nm)

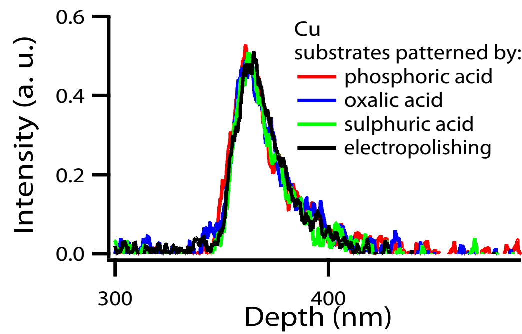

(b) – Cu (360 nm)

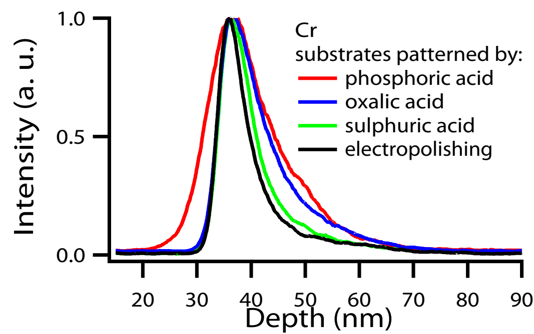

(c) – Cr (360 nm)

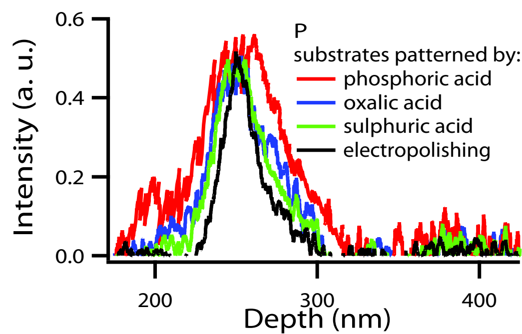

(d) – P (360 nm)

Figure 3.7 – Comparison of the elemental depth profiles performed by GD-OES on anodic oxide layers, formed by anodizing in ammonium pentaborate of superpure aluminium substrates differently patterned to 360 nm.

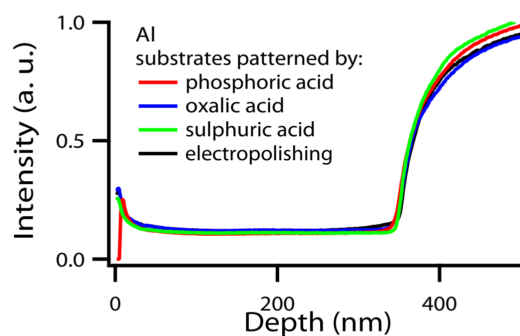

(a) – Al (360 nm)

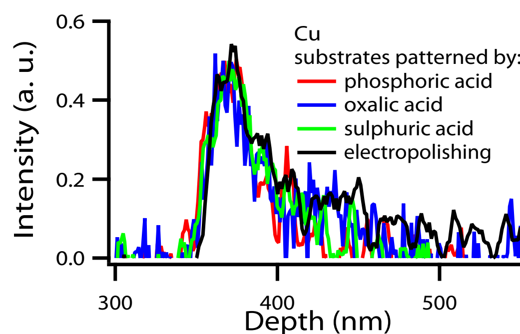

(b) – Cu (360 nm)

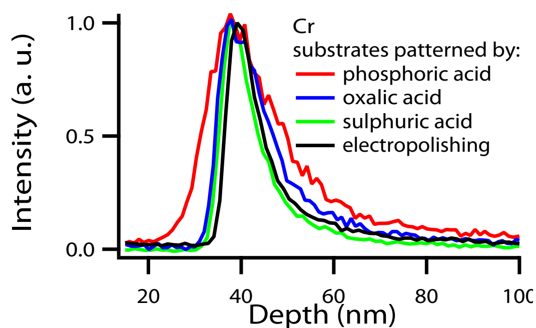

(c) – Cr (360 nm)

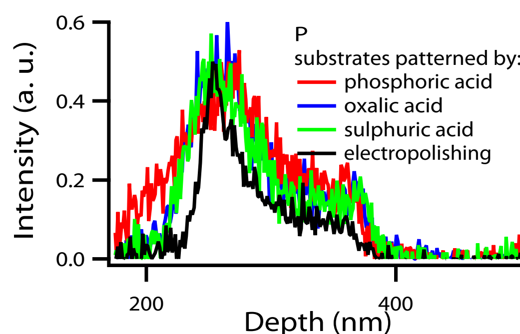

(d) – P (360 nm)

Figure 3.8 – Comparison of the elemental depth profiles performed by GD-TOF-MS on anodic oxide layers, formed, by anodizing in ammonium pentaborate of superpure aluminium substrates differently patterned to 360 nm.

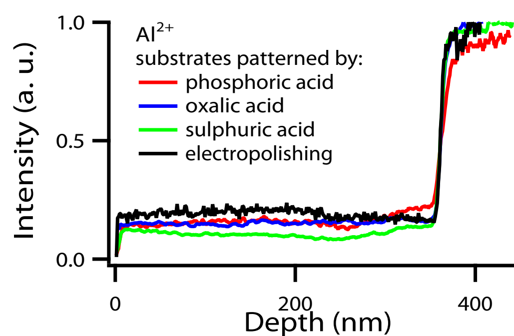

(a) – Al (360 nm)

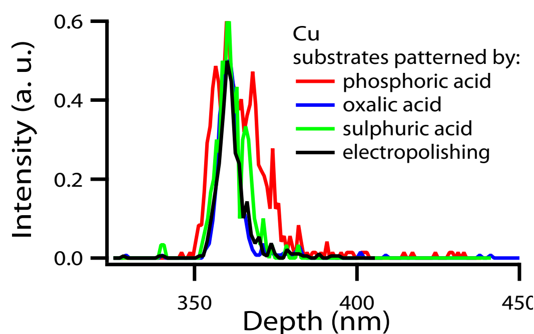

(b) – Cu (360 nm)

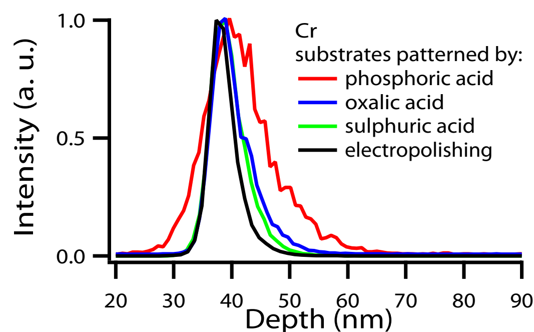

(c) – Cr (360 nm)

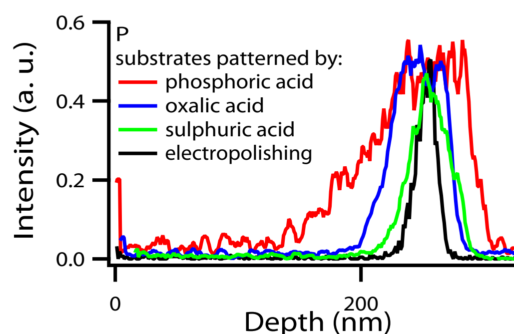

(d) – P (360 nm)

Figure 3.9 – Comparison of the elemental depth profiles performed by TOF-SIMS on anodic oxide layers, formed, by anodizing in ammonium pentaborate of superpure aluminium substrates differently patterned to 360 nm.

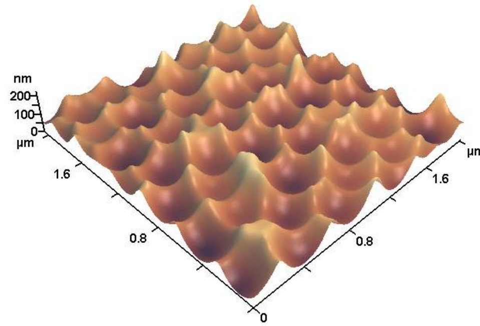

(a) – Original surface

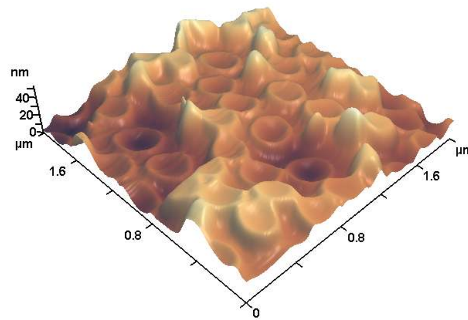

(b) – After sputtering for 0.5 s

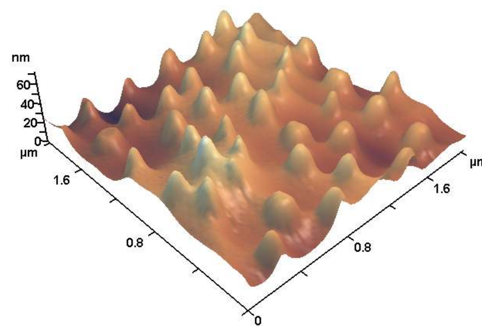

(c) – After sputtering for 1 s

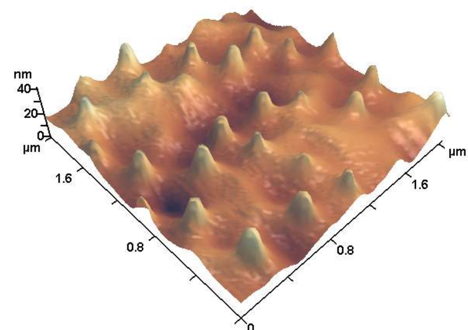

(d) – After sputtering for 2 s

Figure 3.10 – Atomic force microscopy images of 30 nm thick oxide films, formed on substrates patterned by anodizing in phosphoric acid and subsequent stripping of the porous film: a. original oxide film surface; after GD-OES elemental depth profiling for b. 0.5 s, c. 1 s, d. 2 s.

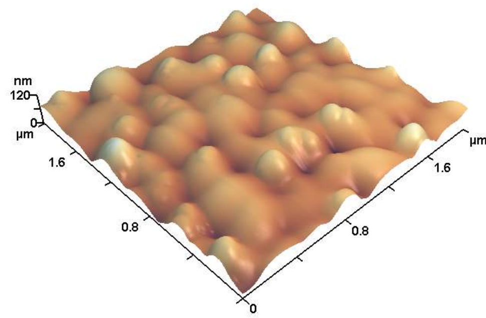

(a) – Original surface

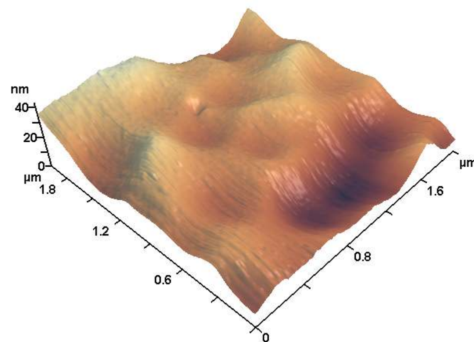

(b) – After sputtering for 2 s

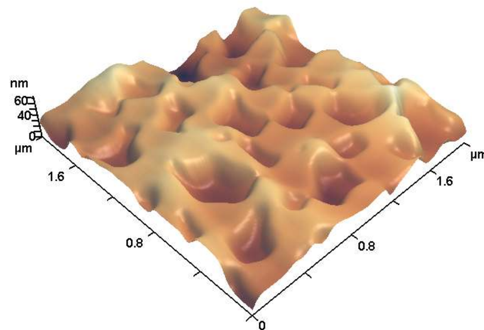

(c) – After sputtering for 5 s

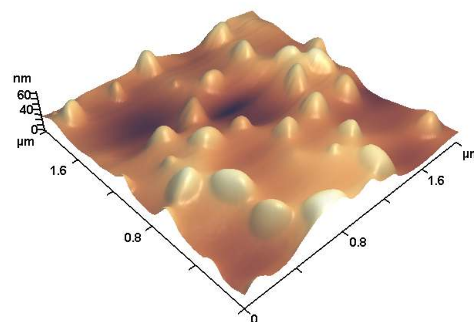

(d) – After sputtering for 7 s

Figure 3.11 – Atomic force microscopy images of 120 nm thick oxide films, formed on substrates patterned by anodizing in phosphoric acid and subsequent stripping of the porous film: a. original oxide film surface; after GD-OES elemental depth profiling for b. 2 s, c. 5 s, d. 7 s.

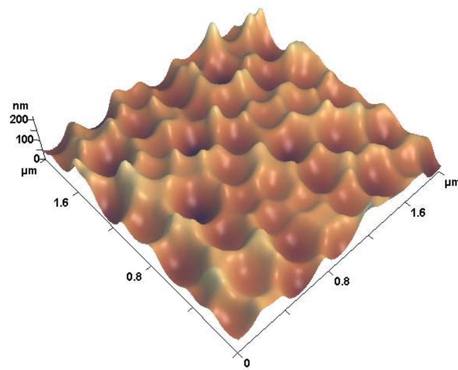

(a) – Original surface

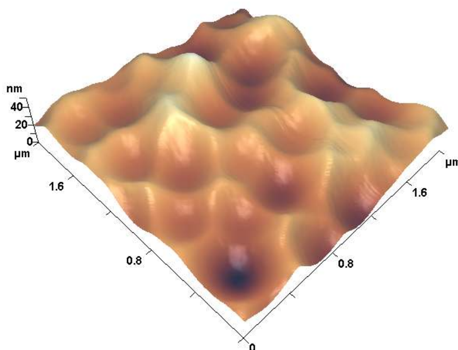

(b) – After sputtering for 1 s

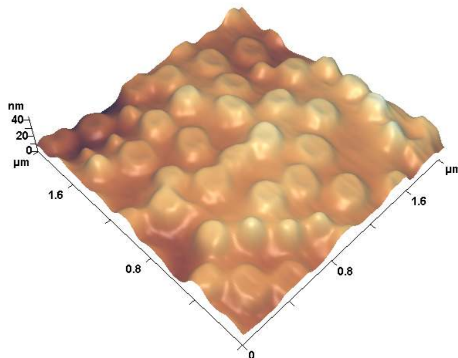

(c) – After sputtering for 4 s

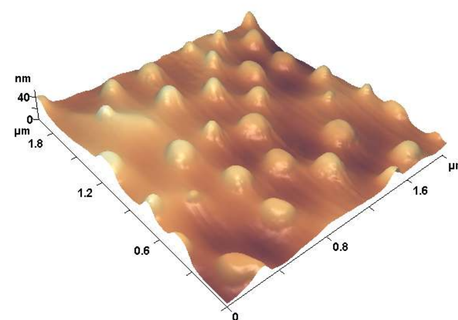

(d) – After sputtering for 6 s

Figure 3.12 – Atomic force microscopy images of 30 nm thick oxide films, formed on substrates patterned by anodizing in phosphoric acid and subsequent stripping of the porous film: a. original oxide film surface; after GD-TOF-MS elemental depth profiling for b. 1 s, c. 4 s, d. 6 s.

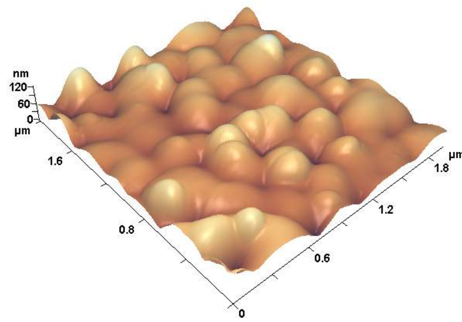

(a) – Original surface

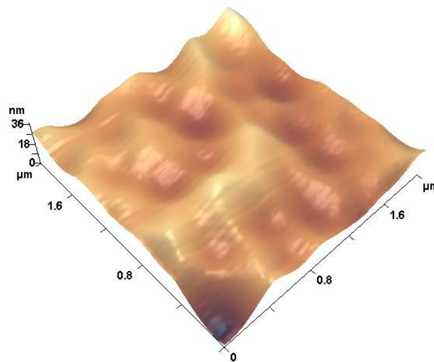

(b) – After sputtering for 5 s

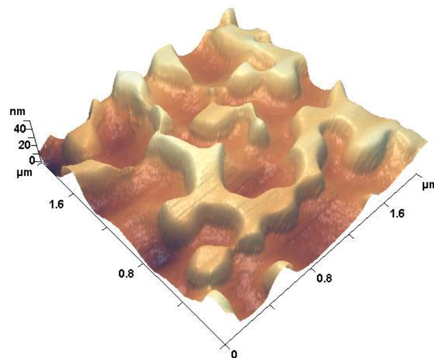

(c) – After sputtering for 15 s

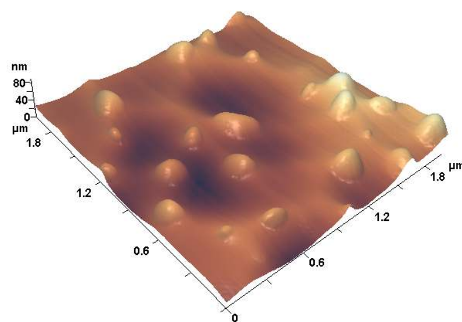

(d) – After sputtering for 18 s

Figure 3.13 – Atomic force microscopy images of 120 nm thick oxide films, formed on substrates patterned by anodizing in phosphoric acid and subsequent stripping of the porous film: a. original oxide film surface; after GD-TOF-MS elemental depth profiling for b. 5 s, c. 15 s, d. 18 s.

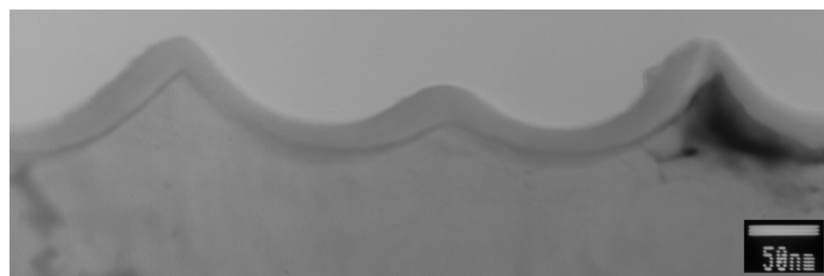

(a) – Original specimen

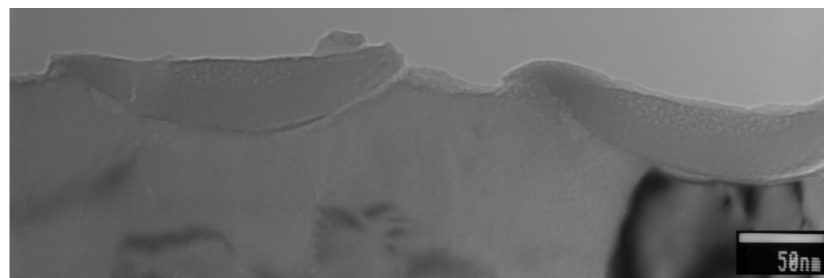

(b) – Sputtering for 1 s

Figure 3.14 – Transmission electron micrographs of ultramicrotomed sections of superpure aluminium specimens patterned in phosphoric acid and stripping of the porous film, and anodized in ammonium pentaborate to 100 V, a. initially patterned oxide film; after GD-OES depth profile analysis for b. 1 s.

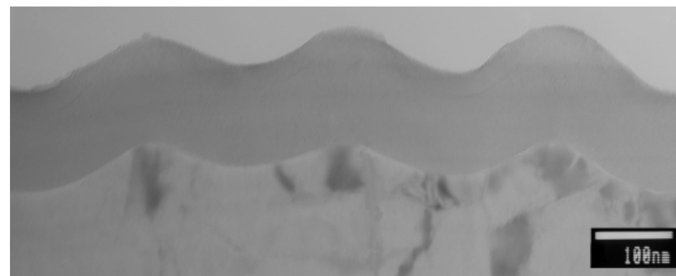

(a) – Original specimen

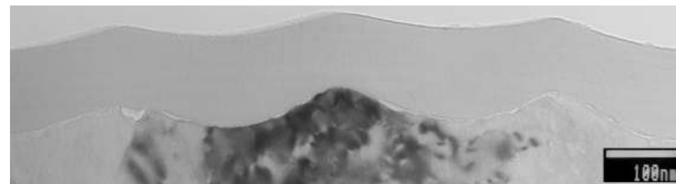

(b) – Sputtering for 2 s

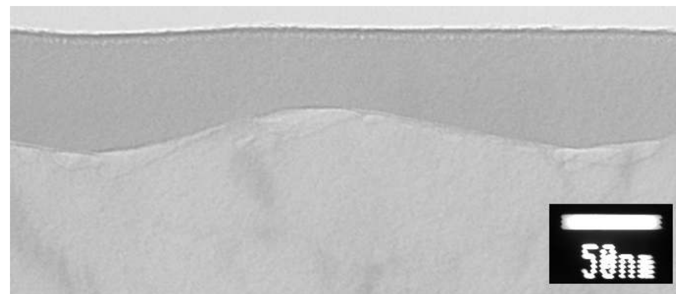

(c) – Sputtering for 3 s

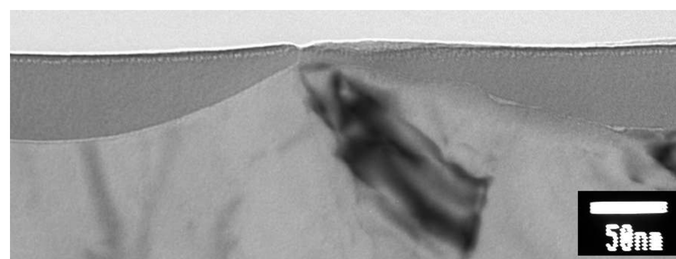

(d) – Sputtering for 4 s

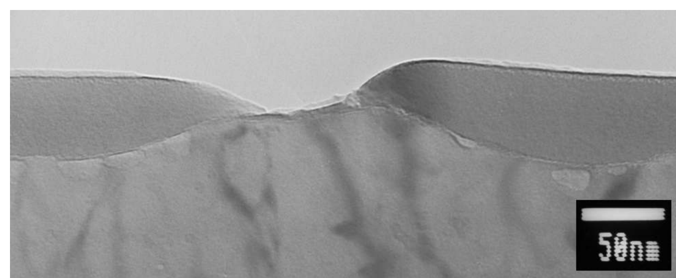

(e) – Sputtering for 5 s

Figure 3.15 – Transmission electron micrographs of ultramicrotomed sections of superpure aluminium specimens patterned in phosphoric acid and stripping of the porous film, and anodized in ammonium pentaborate to 100 V, a. initially patterned oxide film; after GD-OES depth profile analysis for b. 2 s, c. 3 s, d. 4 s and e. 5 s.

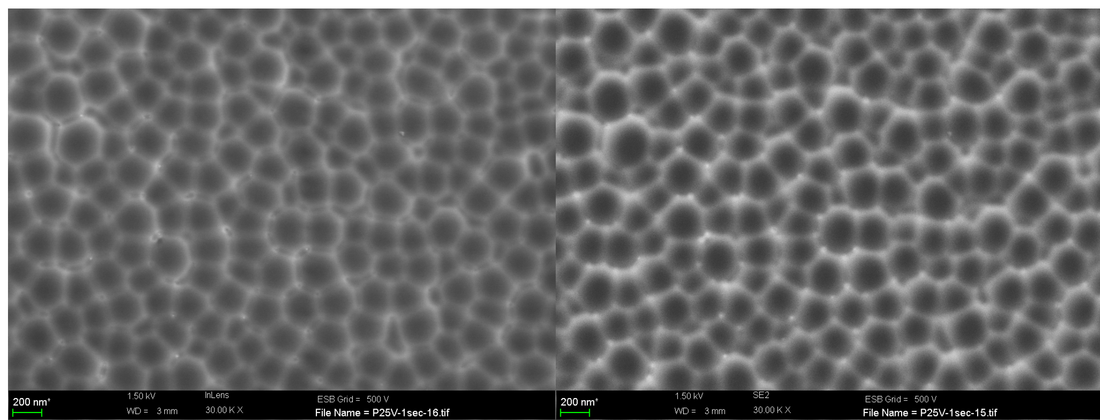

(a) – Original surface - InLens mode **(b)** – Original surface - SE2 mode

Figure 3.16 – Scanning electron micrographs of 30-nm oxide films, formed on superpure aluminium specimens patterned by anodizing in phosphoric acid and subsequent stripping of the porous film, a. and b. micrographs in the InLens mode and in the SE2 mode of the original anodic oxide surface.

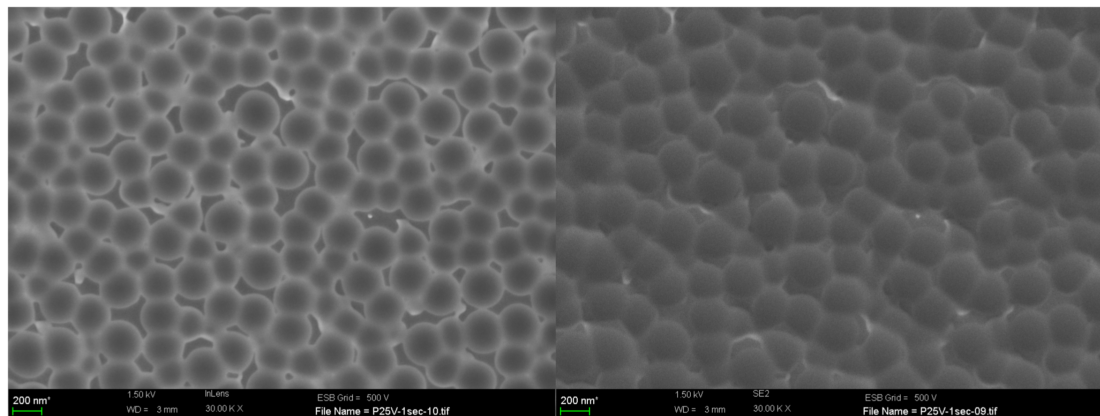

(a) – After sputtering for 0.15 s - InLens mode **(b)** – After sputtering for 0.15 s - SE2 mode

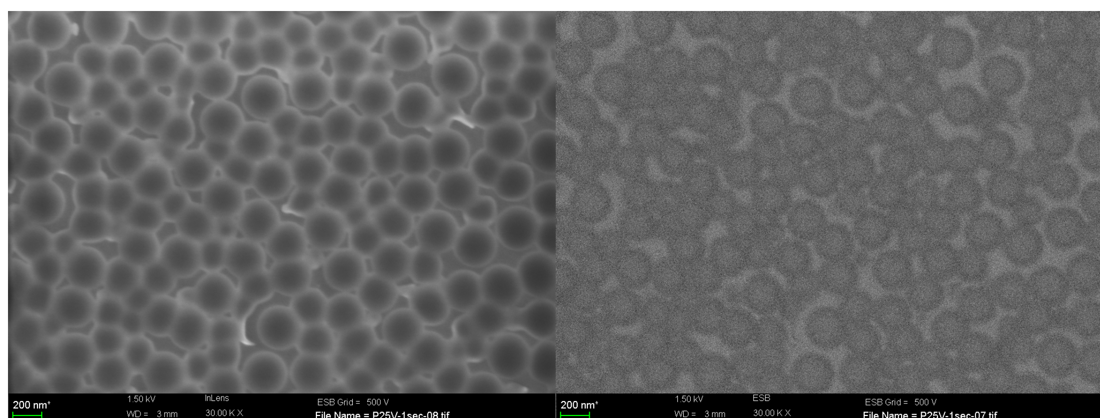

(c) – After sputtering for 0.15 s - InLens mode **(d)** – After sputtering for 0.15 s - EsB mode

Figure 3.17 – Scanning electron micrographs of 30-nm oxide films, formed on superpure aluminium specimens patterned by anodizing in phosphoric acid and subsequent stripping of the porous film, after sputtering for 0.15 s, a. and b. micrographs in the InLens mode and in the SE2 mode, c. and d. micrographs in the InLens mode and in the EsB mode.

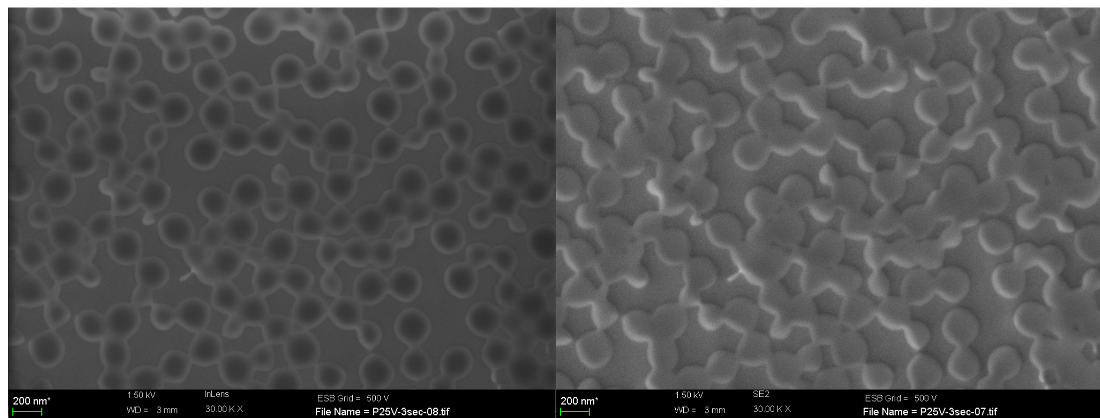

(a) – After sputtering for 2.15 s - InLens mode **(b)** – After sputtering for 2.15 s - SE2 mode

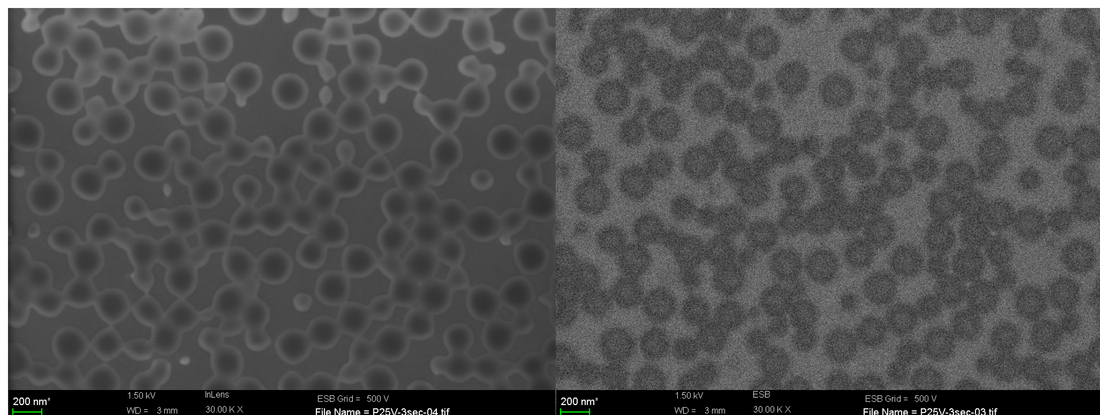

(c) – After sputtering for 2.15 s - InLens mode **(d)** – After sputtering for 2.15 s - EsB mode

Figure 3.18 – Scanning electron micrographs of 30-nm oxide films, formed on superpure aluminium specimens patterned by anodizing in phosphoric acid and subsequent stripping of the porous film, after sputtering for 2.15 s, a. and b. micrographs in the InLens mode and in the SE2 mode, c. and d. micrographs in the InLens mode and in the EsB mode.

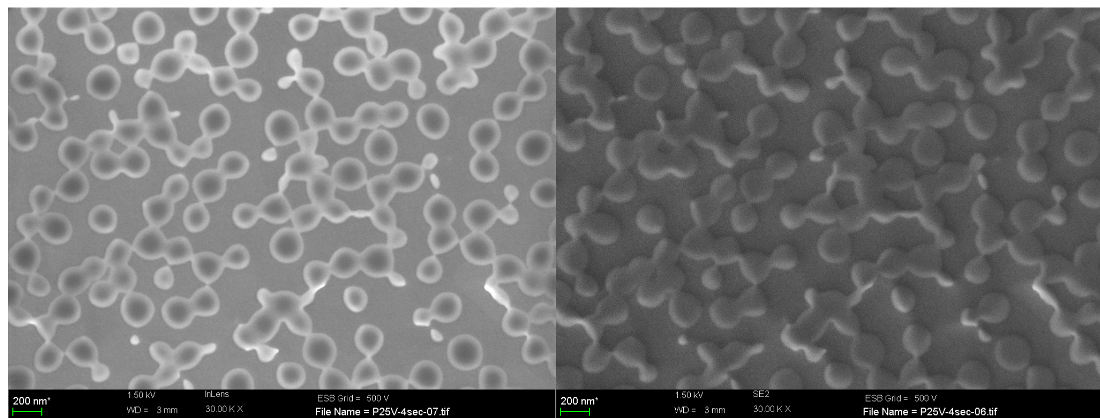

(a) – After sputtering for 3.15 s - InLens mode **(b)** – After sputtering for 3.15 s - SE2 mode

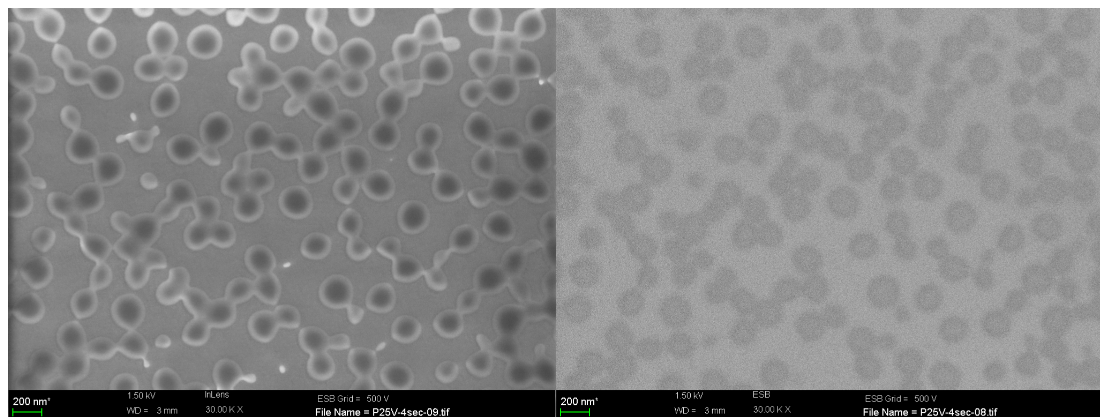

(c) – After sputtering for 3.15 s - InLens mode **(d)** – After sputtering for 3.15 s - EsB mode

Figure 3.19 – Scanning electron micrographs of 30-nm oxide films, formed on superpure aluminium specimens patterned by anodizing in phosphoric acid and subsequent stripping of the porous film, after sputtering for 3.15 s, a. and b. micrographs in the InLens mode and in the SE2 mode, c. and d. micrographs in the InLens mode and in the EsB mode.

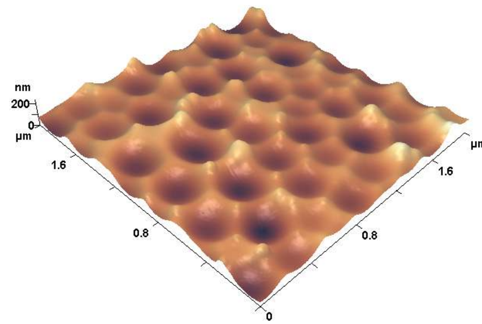

(a) – Original surface

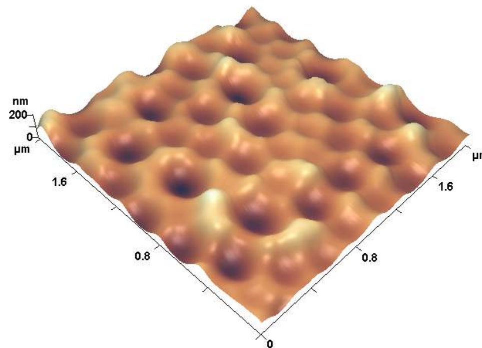

(b) – After sputtering for 150 s

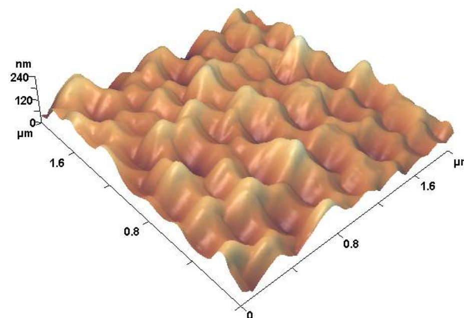

(c) – After sputtering for 300 s, thus reaching the metal /oxide interface

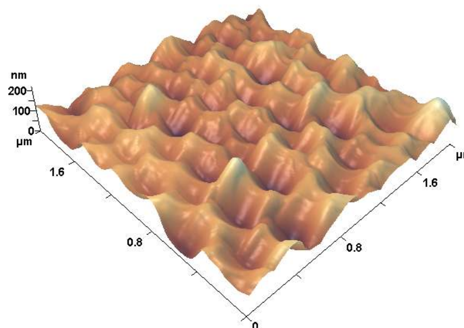

(d) – After sputtering for 500 s

Figure 3.20 – Atomic force microscopy images of material removal during TOF-SIMS depth profiling of 30 nm thick oxide films, formed on substrates patterned by anodizing in phosphoric acid and stripping of the porous film, and sputtered to different times a. original oxide film surface; b. 150 s, c. 300 s, d. 500 s.

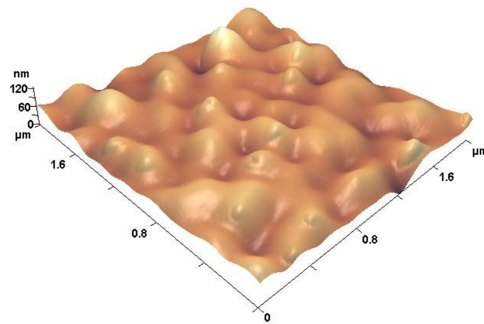

(a) – Original surface

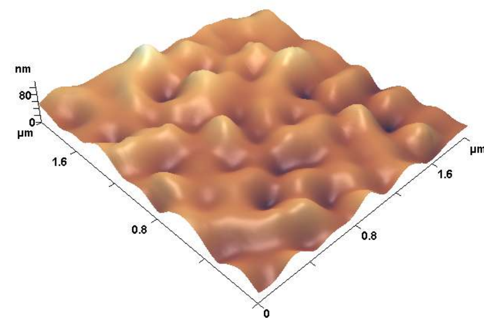

(b) – After sputtering for 430 s

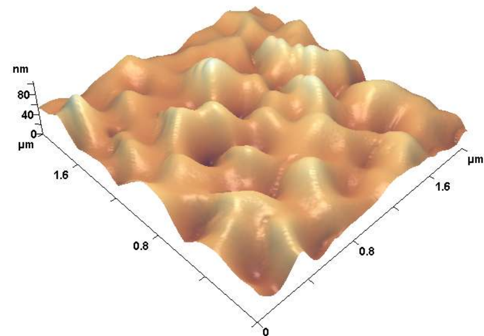

(c) – After sputtering for 875 s, thus reaching the metal /oxide interface

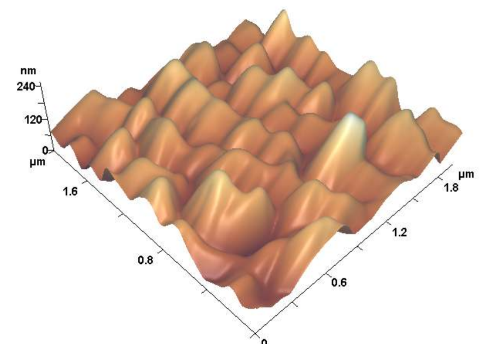

(d) – After sputtering for 950 s

Figure 3.21 – Atomic force microscopy images of material removal during TOF-SIMS depth profiling of 30 nm thick oxide films, formed on substrates patterned by anodizing in phosphoric acid and stripping of the porous film, and sputtered to different times a. original oxide film surface; b. 150 s, c. 300 s, d. 950 s.

4 Growth Mechanism of Barrier-Type Anodic Alumina

The transport mechanisms taking place during barrier-type anodic alumina growth on patterned superpure aluminium substrates are examined in this section, with considerations of high field ionic conduction and electrostrictive stress. A boron marker and chromium and phosphorus tracers were employed in order to investigate the transport mechanisms. The incorporation of the boron marker and the migration of the chromium and phosphorus tracers were probed using scanning transmission electron microscopy in a scanning electron microscope.

4.1 Potential and Stress Distributions

4.1.1 Potential distribution

The potential distribution at the surface of the substrate and within the anodic oxide film, is of fundamental importance since it controls ionic conduction and, consequently, the motion of the interfaces. The electric potential, U, and the electric field, $E = -\nabla U$ are related to the ionic space-charge density, ρ_e, by the Poisson equation (Houser and Hebert, 2006):

$$\nabla^2 U = \nabla E = -\frac{\rho_e}{\varepsilon\, \varepsilon_0} \tag{4.1}$$

where ε_0 is the permittivity of free space and ε is the dielectric constant of the material.

Simulation of the potential distribution was performed using the software application Quickfield (Tera Analysis). The potential distributions were calculated for a specimen presenting a flat surface and for a patterned substrate of amplitude and period of 65 and 200 nm respectively; the previous approximate to the pattern dimensions achieved

by anodizing aluminium substrates in phosphoric acid with subsequent stripping of the porous film to reveal the scalloped metal surface. For the simulation, a potential of 1 V was applied between the anode and the cathode. The relative electric permittivity of the electrolyte was selected as 80, which is the value measured for water at 20°C.

Figure 4.1 compares the modifications in the potential distributions induced by the pattern of the anode surface. For the flat specimen, the simulation displays a uniform distribution of the electric field; conversely, for the patterned specimen, the potential distribution is concentrated at the peaks at the surface. Thus, the electric field is enhanced at the convexities in the surface; as a result, the field strength is about 5 times greater at the peaks than at the adjacent valleys in the surface.

The simulations deal with the very commencement of the anodizing of the aluminium specimen; in order to simplify the modelling, the presence of an oxide layer at the surface of the aluminium substrate has not been introduced. The presence of the oxide layer at the metal surface is not expected to influence the direction of the electric field, since it depends exclusively on the curvature of the metal surface. For the patterned specimen, the geometry of an aluminium substrate supporting an oxide layer is difficult to reproduce due to the requirement of a constant oxide thickness in the direction of the electric field, i.e. normal to the metal substrate. Indeed, coupling the specific dimensions of the patterned substrates with a constant oxide thickness in the direction of the electric field is particularly demanding geometrically.

4.1.2 Stress distribution

Anodic oxide films formed on aluminium are associated with intrinsic stress at open-circuit (Bradhurst and Leach, 1966; Vermilyea, 1963). Indeed, anodic oxide films formed at 100 % efficiency present compressive stress at open-circuit, due to a Pilling-Bedworth ratio of 1.6 - 1.7 (Thompson, 1997). Further, growing anodic oxide films are subject to additional stress as a result of the electric field applied. Thus, the electrostrictive stress, σ_{ES}, resulting from the applied electric field, E, along a dielectric film attached to a substrate can be expressed as (Vanhumbeeck and Proost, 2008):

$$\sigma_{ES} = -\frac{\nu}{1-\nu}\,\frac{\varepsilon_0}{2}\left[\varepsilon - (\alpha_1 + \alpha_2)\right] E^2 \tag{4.2}$$

where:

- ν and ε are the Poisson coefficient and the relative dielectric constant of the oxide film respectively.
- ε_0 is the vacuum permittivity.
- α_1 and α_2 are 2 electrostriction parameters.

Thus, the electrostrictive stress varies with the square of the electric field; its presence has been considered to lead to plastic deformation and material flow (Sato, 1971; Skeldon et al., 2006), particularly during porous anodic film formation on aluminium in suitable electrolytes.

At the beginning of the oxide formation on the patterned specimen, the compressive stress induced within the oxide film at the peaks is 25 times greater than at the valleys in the surface. The electrostrictive stress ratio at the peaks and the valleys in the surface probably decreases during oxide growth as a result of the smoothing of the aluminium ridges at the metal / oxide interface. The value calculated can be considered as a maximum; consequently, electrostrictive stress driven transport, if applicable, should be more significant at the beginning of anodizing of the patterned specimens.

The electrostriction-induced material displacement has been examined during the formation of barrier-type oxide films by anodizing differently patterned superpure aluminium substrates in 0.1 ammonium pentaborate solution. This enables the locations of a boron marker and of the chromium and phosphorus tracers to be followed.

The growth mechanism of barrier-type alumina film, including the incorporation of the boron marker and the migration of the chromium and phosphorus tracers, during anodizing of relatively flat aluminium substrates is considered below.

During anodizing of aluminium substrate in 0.1 ammonium pentaborate solution, at approximately 100 % efficiency, growth of the barrier-type anodic alumina layer proceeds by aluminium ion egress and oxygen ion ingress through the pre-existing air-formed film present over the aluminium surface (Skeldon et al., 1985). Hence, barrier-type anodic alumina layers develop simultaneously at the film / solution and metal / oxide interfaces. The chromium and phosphorus species are initially

incorporated within a 4-nm thick oxide film present over the aluminium substrates after stripping of the previously formed porous films. During anodizing of the chromium- and phosphorus-containing aluminium substrates, the chromium ions, generated by high field-assisted dissociation of the incorporated units of Cr_2O_3, migrate outward at a constant rate of 0.74 relative to that of aluminium ions, and the incorporated phosphorus ions migrate inward at a constant rate of 0.50 relative to that of oxygen ions (Shimizu et al., 1999a). Additionally, the boron species are introduced within the anodic alumina film developed by aluminium ion egress during anodizing of the superpure aluminium substrate in 0.1 M ammonium pentaborate solution. The boron species are immobile; thus, the boron-rich / boron-free oxide interface is located at the initial surface of the aluminium specimens. During anodizing of electropolished specimens, i.e. a relatively flat substrate, the boron-rich / boron-free oxide interface is located at a depth of 0.40 relative to the total film thickness (Skeldon et al., 1985).

During anodizing of differently patterned superpure aluminium specimens, the development of the distributions of the boron marker and of the phosphorus and chromium tracers has been studied by scanning transmission electron microscopy, Figs. 4.2 - 4.5. The following consideration of the anodic oxide growth mechanism results from examination of the scanning transmission electron micrograph of the superpure aluminium substrate patterned by anodizing in phosphoric acid and subsequent stripping of the porous film, and anodized in 0.1 M ammonium pentaborate solution, Fig. 4.5. This micrograph has been selected since the amplitudes of the distributions of the different incorporated species are significantly larger than for the anodic oxide films formed by anodizing electropolished substrates or superpure aluminium substrates patterned by anodizing in sulphuric acid or oxalic acid and subsequent stripping of the porous films.

Figure 4.5 presents the scanning transmission electron micrograph of a 240-nm thick anodic oxide formed on a superpure aluminium substrate patterned by anodizing in phosphoric acid and subsequent stripping of the porous film. The micrograph reveals the locations and distributions of the boron marker and of the chromium and phosphorus tracers within the anodic oxide film. The locations of the boron-rich / boron-free oxide interface and of the chromium and phosphorus tracers have been considered at two positions across the oxide thickness, namely at a concavity

(toward the metal / oxide interface) and at a convexity (toward the oxide surface) in the distributions; the positions are labelled 1 and 2 respectively in Figure 4.6.

4.2 Distributions of the Incorporated Species

4.2.1 Boron marker

The boron species are located in the outer region of the anodic oxide film. The boron-rich / boron-free oxide interface reveals the initial location of the aluminium substrate. The interface shows a waviness with amplitude and period close to that of the pattern of the original aluminium substrate. The contrast due to the presence of boron is relatively uniform within the boron-containing alumina film material. The location of the boron-rich / boron-free oxide interface has been determined for two positions along the interface, namely at a concavity toward the metal / oxide interface and at a convexity toward the oxide surface. The locations are considered to match an original peak and valley in the surface of the substrate.

For the two positions previously defined, the interface of the boron marker and the underlying boron-free alumina is located at depths of 0.53 and 0.34 relative to the total film thickness. Thus, at concavities in the boron-rich / boron-free oxide interface, the interface is located further from the surface in comparison with that determined for a boron-rich / boron-free oxide interface within an anodic oxide film formed on a relatively flat aluminium substrate. Such a configuration results in part from the changes in surface area that the growing oxide has to accommodate. Thus, the oxide growing outward has to accommodate a reduction in surface area, whereas the oxide growing inward has to rearrange over an increasing surface area, Fig. 4.7.a. Additionally, at concavities in the surface, the oxide grows by aluminium egress in directions converging towards the centre of the curvature defined by the metal / oxide interface, thereby increasing the amount of oxide to be rearranged within the volume available, Fig. 4.7.b.

Consequently, at concavities in the surface, the apparent transport numbers of the aluminium and oxygen species are considered to be greater than 0.40 and less than 0.60 respectively; the previous values represent the transport numbers associated with aluminium and oxygen species during anodizing of a flat specimen. As a result, the boron-rich / boron-free oxide interface at concavities in the surface appears further

from the surface than for a flat specimen, i.e. more than 0.40 relative to the total film thickness.

At convexities in the boron-rich / boron-free oxide interface, the interface is located at a shallower depth from the surface than that determined for a boron-rich / boron-free oxide interface within an anodic oxide film formed on a relatively flat aluminium substrate, i.e 0.40 relative to the total film thickness. Thus, with consideration of the increasing surface area that the growing oxide has to cover during anodizing of convexities in the surface, the aluminium species are assumed to present a transport number less that 0.40. In contrast, the transport number of the oxygen species is considered to be greater than 0.60 due to the reduction in surface area accommodated by the oxide that grows inward, Fig. 4.8.a. Additionally, at convexities in the surface, oxide grows by oxygen ingress in directions converging towards the centre of the curvature defined by the metal / oxide interface, thereby increasing the amount of oxide to be accommodated within the limited volume available and, consequently, inducing a change in the shape of the metal / oxide interface, Fig. 4.8.b.

As a result, at convexities, the boron-rich / boron-free oxide interface is expected to be located at a shallower distance than 0.40 relative to the total film thickness.

Considering the features of the boron-rich / boron-free oxide interface, namely its location, amplitude, period, the interface does not present significant distortions and appears relatively similar to the original pattern of the aluminium substrate. In order to complete the investigations into electrostrictive stress induced oxide flow during anodizing of patterned aluminium specimens in 0.1 M ammonium pentaborate solution, the distributions of the phosphorus and chromium tracers have also been examined.

4.2.2 Phosphorus tracer

The phosphorus species are initially located in the 4-nm thick oxide present over the superpure aluminium substrate after stripping of the porous film. During anodizing of the patterned aluminium specimen in 0.1 M ammonium pentaborate, the phosphorus species migrate inward under the influence of the high electric field. The resulting distribution of the phosphorus species presents a significant waviness. The amplitude and the period of the distribution of the phosphorus species are similar with that of

the original aluminium surface, Fig. 4.9.

However, in spite of the similar waviness dimensions, the distributions of the phosphorus species and of the boron-rich / boron-free oxide interface slightly differ in terms of shape, with the phosphorus distribution showing widening of the concavities and narrowing of the convexities. Such modifications of the phosphorus distribution results probably from the changes in direction of the electric field associated with the recession of the aluminium peaks in the substrate surface. Indeed, during anodizing of a patterned specimen, due to a varying potential distribution along the specimen surface, the aluminium peaks are not oxidized uniformly. Consequently, the aluminium surface does not regress following a homothetic transformation (a transformation of space that allows conservation of the initial shape of the features, which differ only in their relative scaling), but shows preferential oxidation of the tips of the peaks, Fig. 4.10.

Consequently, the direction of the electric field is not uniform during the anodizing of patterned specimens, but varies with the change of the aluminium surface topography, Fig. 4.11. Thus, such changes in the electric field direction induce variations in the direction of the transport and migration of the different species. Further, at the commencement of the anodizing, due to the sharpness of the peaks in the surface, the direction of the electric field allows narrowing of the width of the convexities in the phosphorus distribution.

The migration rates of the phosphorus species have been calculated at the positions of a concavity and a convexity in the phosphorus distribution, noted 1 and 2 in Figure 4.6. The migration rates are 0.57 and 0.41 relative to that of the oxygen species, which are respectively greater and less than the migration rate, i.e. 0.50, of the phosphorus species during anodizing of a relatively flat specimen in 0.1 M ammonium pentaborate.

At concavities in the phosphorus-enriched layer, which correspond initially to valleys in the aluminium substrate surface topography, the increase in the migration rate of the phosphorus species is associated with the apparent reduction in the transport number of the oxygen species as a result of the increase of the surface area, Fig. 4.12. In other words, the phosphorus species migrate under the high electric field at a standard rate of 0.50 relative to that of the oxygen species, as if the oxygen species were presenting

a transport number of 0.60. However, at concavities in the surface, the oxide formed as a result of oxygen ingress occupies a narrower thickness in comparison with the same volume of oxide formed on a flat surface; consequently, this results in an apparent increase in the migration rate of the phosphorus species.

Similarly, at convexities in the phosphorus distribution, which correspond initially to peaks in the aluminium topography, the reduction in the migration rate of the phosphorus species is induced by the apparent increase in the transport number of the oxygen species associated with the decrease of the surface area, Fig. 4.13. Therefore, the oxide formed by oxygen ingress fills a volume of larger thickness than if grown on a flat surface. Consequently, the phosphorus species appears to migrate at a lower rate than within an oxide film formed on a flat surface.

4.2.3 Chromium tracer

Chromium species are incorporated in the 4-nm oxide film covering the patterned aluminium substrate subsequently to the stripping of the porous film. During anodizing of the patterned aluminium specimen in 0.1 M ammonium pentaborate, the chromium species migrate outward; as a result, the chromium-enriched layer is located in the outer region of the anodic oxide layer.

A significant distortion of the original chromium distribution is evident, considering that the chromium and phosphorus species are initially located within the 4-nm thick oxide covering the aluminium substrate and, hence, present similar original distributions.

Thus, narrowing of the distribution of the chromium species, i.e. reduction of the distance from peak-to-valley in the chromium-enriched layer, arises during anodizing of patterned aluminium substrate in 0.1 M ammonium pentaborate solution.

The migration rates of chromium species have been calculated respectively as 0.72 and 0.62 relative to that of aluminium species at a concavity and a convexity in the chromium-enriched layer. The migration rate at convexities in the chromium distribution is less than the value calculated for the migration rate of chromium ions during anodizing of a relatively flat specimen in 0.1 M ammonium pentaborate, i.e. 0.74. In contrast, the migration rate at concavities in the chromium distribution is

close to the value measured for the migration rate of chromium ions during anodizing of a relatively flat specimen in 0.1 M ammonium pentaborate. The difference in the migration rates at the peaks and valleys in the surface reveals the greater displacement of the chromium species in the valleys.

The increase in the migration rate of the chromium species at concavities in the chromium distribution may result from the rearrangement of the volume of oxide formed by aluminium egress. Indeed, at the specimen surface, oxide grows by aluminium egress in directions converging towards the centre of the curvature defined by the metal / oxide interface, thereby increasing the volume of oxide formed at the surface of concavities, Fig. 4.14. The volume of the growing oxide is therefore larger than the volume available for the surface to expand without changing shape. Consequently, this leads to the smoothing of the concavities.

The reduction in the migration rate of the chromium species at convexities in the chromium-enriched layer is unexpected. Indeed, as established previously, at convexities in the boron-rich / boron-free oxide interface, due to the increasing surface area covered by the oxide that formed by aluminium egress, the aluminium species are assumed to present a transport number less than 0.40, Fig. 4.15.

4.3 Oxide Surface and Metal / Oxide Interface Smoothing

The mechanisms of smoothing for the oxide surface and the metal / oxide interface are based on the observations of the distributions and locations of the boron marker and chromium and phosphorus tracers by scanning transmission electron microscopy.

Despite the non-uniformity of the electric-field associated with the topography of the specimens, the current-electric field dependence requires uniformity of the oxide thickness following the direction of the field. Thus, anodizing of patterned substrates results in the formation of barrier-type anodic alumina films of constant thicknesses in the direction normal to the metal / oxide interface.

Thus, the growth of barrier-type anodic oxide layers of constant thicknesses involves either flow of oxide formed at the peaks in the surface, i.e. the location where the

strength of the electric field is initially greater than at the valleys in the surface, Figs. 4.16 and 4.17, or redistribution of the electric field over the pattern of the specimens, i.e. the strength of the electric field becomes greater at the valleys, Fig. 4.18, as a result of the faster thickening of the oxide at the peaks in the surface at the commencement of the anodizing, Fig. 4.16. As a result of the redistribution of the electric field, electrostrictive stress may not be maintained at the same strength or at the same location during the oxide growth and, hence, film thickening.

The main consequence of oxide flow may be the associated displacement of the chromium and phosphorus tracers from the tips of the peaks to the valleys, Fig. 4.17. In contrast, thickening of the oxide layer over the valleys as a result of the redistribution of the electric field may not induce any displacement of the chromium and phosphorus tracers from the peaks to the valleys, therefore presenting a better agreement with the observations performed by the scanning transmission electron microscopy of anodizing of differently patterned specimens in 0.1 M ammonium pentaborate up to complete flattening of the specimens, Figs. 4.2 - 4.5.

Thus, the growth of barrier-type alumina films formed anodically on patterned aluminium substrate takes place by aluminium ion egress and oxygen ion ingress. During anodizing of patterned specimens in 0.1 M ammonium pentaborate, the smoothing of the oxide surface and of the metal / oxide interface is a continuous process that arises due to the simultaneous migration in opposite directions of aluminium and oxygen species respectively. Thus, flattening of the oxide surface takes place as a result of aluminium egress; smoothing of the metal / oxide interface arises due to oxide growth associated with ingress of oxygen species.

The smoothing of the valleys in the surface results from the growth of anodic alumina, by aluminium ion egress, in directions that converge toward the centre of the valleys. Flattening of the chromium-enriched layer indicates that such a rearrangement of the growing oxide takes place at the valleys in the surface. The plasticity of the oxide ensures the rearrangement of the oxide material in order to accommodate the volume expansion inherent to the conversion of aluminium into alumina and the decrease in surface area associated with the geometry of the valleys.

The smoothing of the aluminium peaks in the surface is considered to proceed in a similar manner to that described for the valleys; however, the oxide growth is induced by oxygen ion ingress. The phosphorus tracer does not reveal directly anodic alumina rearrangement at the peaks in the surface; however, the apparent augmentation in the transport number of the oxygen species and reduction in the migration rate of the phosphorus species at the convexities in the phosphorus-enriched layer suggest that the smoothing of the peaks in the surface proceeds in such a manner.

4.4 Conclusions

The transport mechanisms during growth of barrier-type anodic alumina formed anodically on patterned superpure aluminium substrates that lead to the smoothing of the oxide surface and of the metal / oxide interface were examined, with consideration of high field ionic conduction and electrostrictive stress. The development of the distributions of a boron marker and of chromium and phosphorus tracers, during anodizing of differently patterned specimens in 0.1 ammonium pentaborate solution, were observed by scanning transmission electron microscopy.

For patterned aluminium substrates, the surface curvature has been shown to induce apparent augmentation and reduction in the transport number of the aluminium and oxygen species in comparison with that of a flat substrate; i.e. at the peaks in the surface the transport numbers of the aluminium and the oxygen species are less than 0.40 and greater than 0.60 respectively. Conversely, at the valleys in the surface, the transport numbers of the aluminium and the oxygen species are greater than 0.40 and less than 0.60 respectively.

In addition, the smoothing mechanism of the specimen is considered to arise by aluminium ion egress at the valleys in the surface and oxygen ion ingress at the aluminium peaks in the metal / oxide interface. Thus, the flattening of the specimen is associated with both the augmentation in volume due to the conversion of aluminium into alumina and the reduction in the surface area that the oxide film has to accommodate.

Finally, with consideration of the relatively uniform distributions of the chromium and

phosphorus-enriched layers along the anodic alumina film, thickening of the oxide film over the surface topography is not considered to proceed by oxide flow from the peaks to the valleys, which may result in the absence of the tracers at the peaks in the surface, but by redistributions of the electric field over the surface topography.

Figures

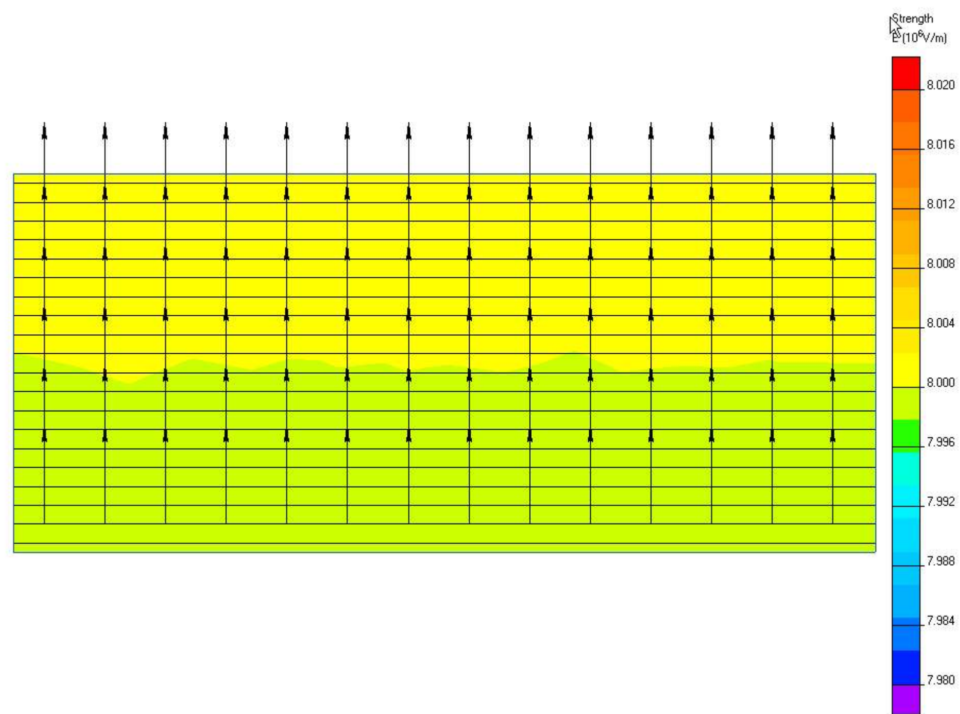

(a)

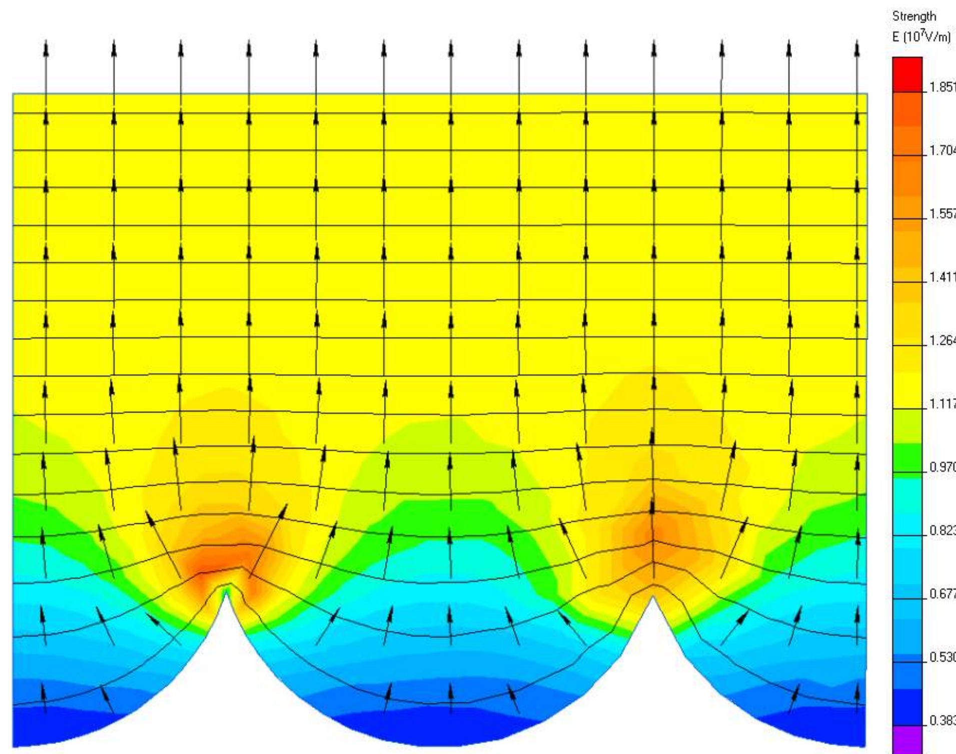

(b)

Figure 4.1 – Simulation of the potential distribution on a. a flat surface and b. a rough surface, showing the pattern dimension of a specimen patterned by anodizing in phosphoric acid and stripping of the porous film. The potential gradient is given by the equilines. Arrows indicate the direction of the electric field. The colour scale represents the field strength a. 7.98 x 10^6 - 8.02 x 10^6 V m^{-1} and b. 0.38 x 10^7 - 1.85 x 10^7 V m^{-1}.

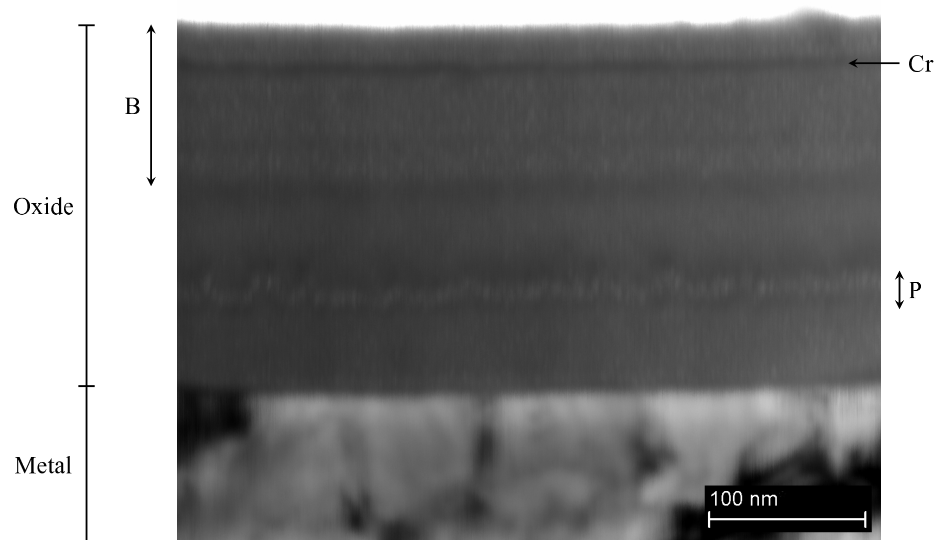

Figure 4.2 – Scanning transmission electron micrograph of an ultramicrotomed section of an electropolished superpure aluminium specimen, after immersion in a chromic / phosphoric acid stripping solution and anodizing at a current density of 5 mA cm^{-2} in 0.1 M ammonium pentaborate solution to 200 V.

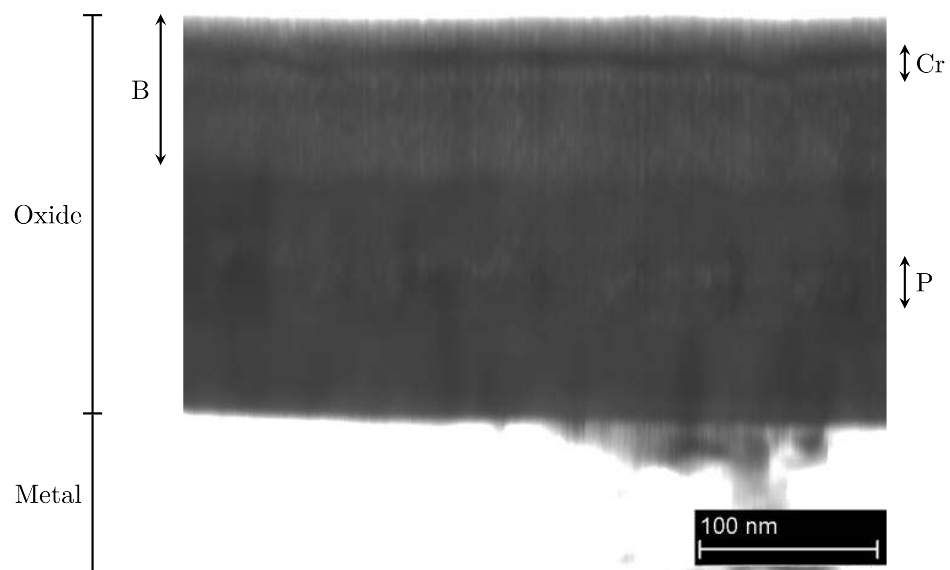

Figure 4.3 – Scanning transmission electron micrograph of an ultramicrotomed section of a superpure aluminium specimen patterned by anodizing in sulphuric acid and subsequent stripping of the porous film, with final anodizing at a current density of 5 mA cm^{-2} in 0.1 M ammonium pentaborate solution to 200 V.

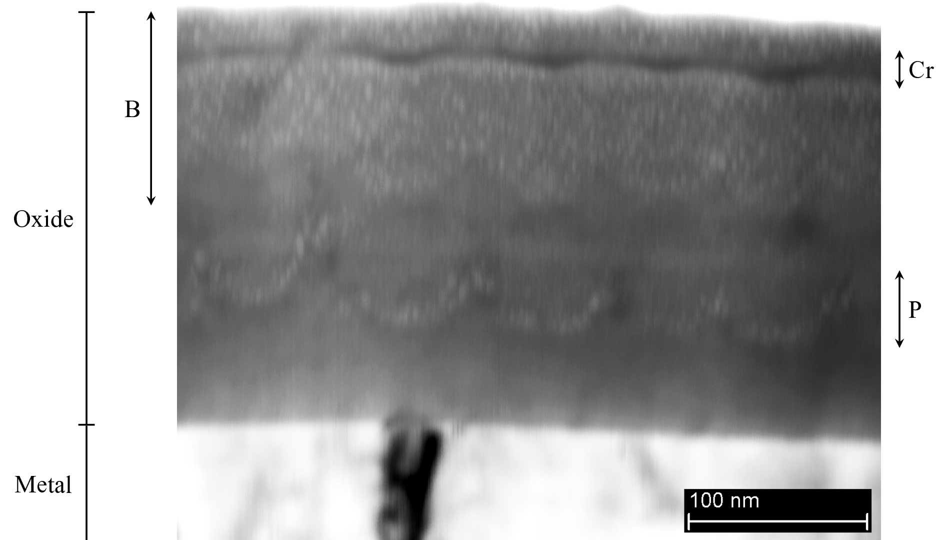

Figure 4.4 – Scanning transmission electron micrograph of an ultramicrotomed section of a superpure aluminium specimen patterned by anodizing in oxalic acid and subsequent stripping of the porous film, with final anodizing at a current density of 5 mA cm^{-2} in 0.1 M ammonium pentaborate solution to 200 V.

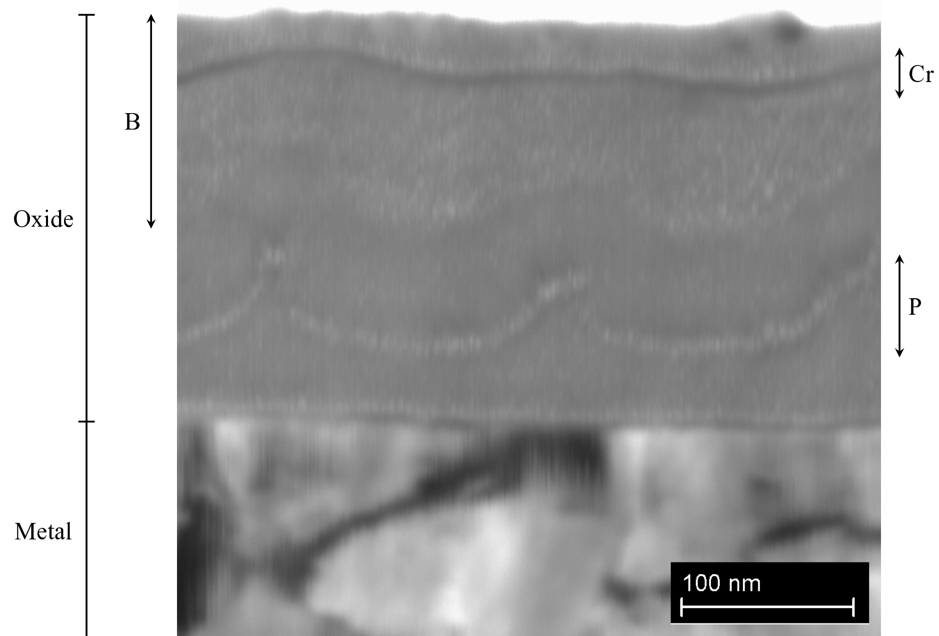

Figure 4.5 – Scanning transmission electron micrograph of an ultramicrotomed section of a superpure aluminium specimen patterned by anodizing in phosphoric acid and subsequent stripping of the porous film, with final anodizing at a current density of 5 mA cm^{-2} in 0.1 M ammonium pentaborate solution to 200 V.

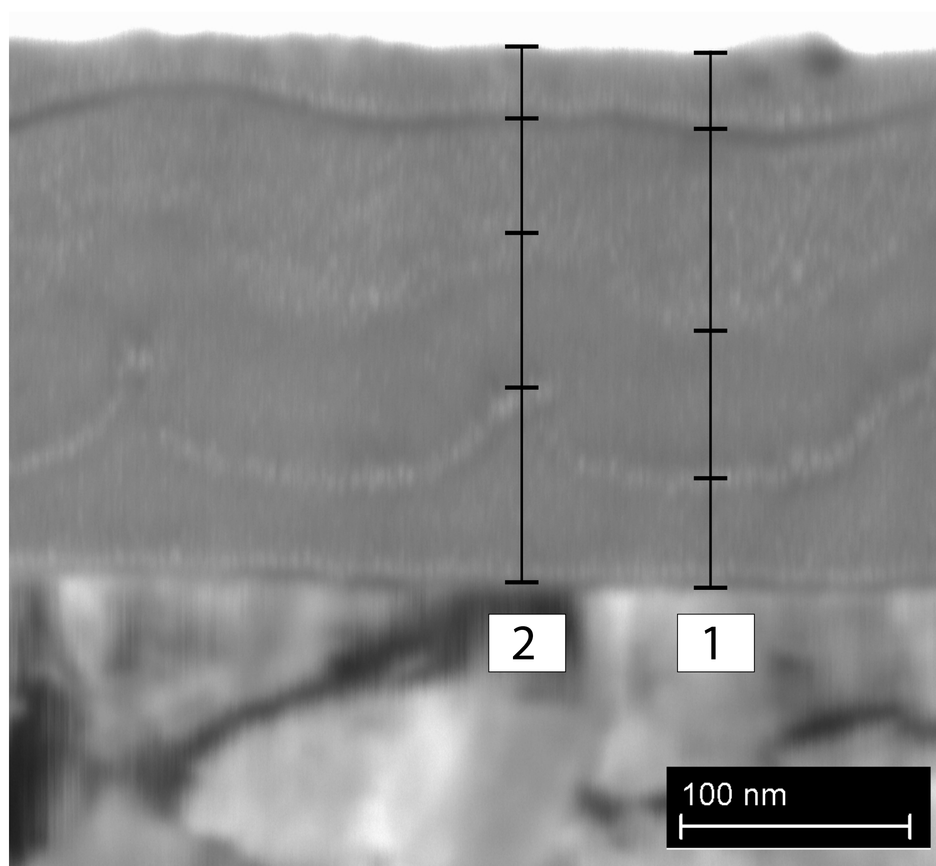

Figure 4.6 – Scanning transmission electron micrograph of an ultramicrotomed section of a superpure aluminium specimen patterned by anodizing in phosphoric acid and subsequent stripping of the porous film, with final anodizing at a current density of 5 mA cm^{-2} in 0.1 M ammonium pentaborate solution to 200 V.

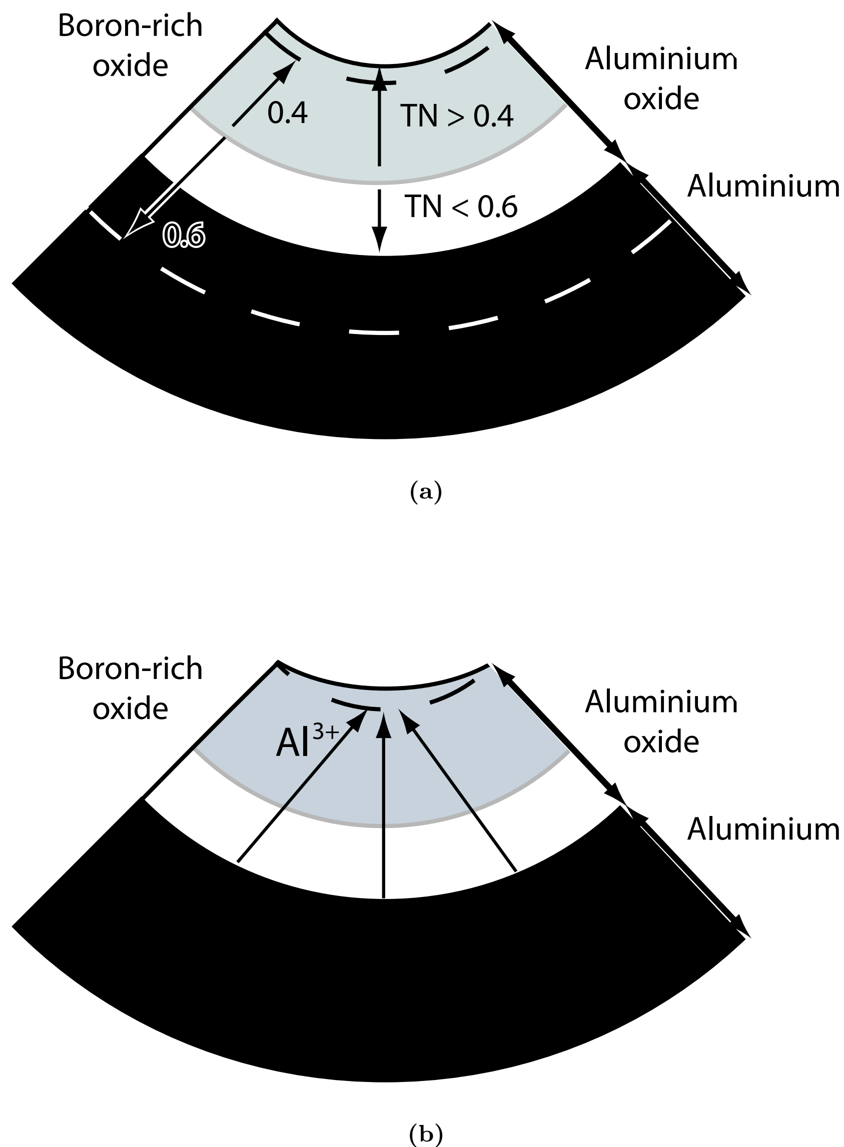

(a)

(b)

Figure 4.7 – Schematic diagrams of a concavity in a patterned specimen surface, showing the aluminium oxide (white) and the boron-containing oxide (grey) supported by the aluminium substrate (black). a. The schematic diagram describes the augmentation and reduction in the transport number (TN) of aluminium and oxygen respectively as a result of the curvature of the substrate and the associated decrease and increase in surface area respectively, the boron-rich / boron-free oxide interface is used as a reference for the determination of the transport number of aluminium and oxygen species. The dashed lines represent the location of the oxide surface and metal / oxide interface for aluminium and oxygen transport numbers of 0.4 and 0.6 (flat surface). b. The schematic diagram illustrates the flattening of the oxide surface in a valley as a result of growth of anodic oxide associated with aluminium egress in directions converging toward the centre of the curvature defined by the metal / oxide interface.

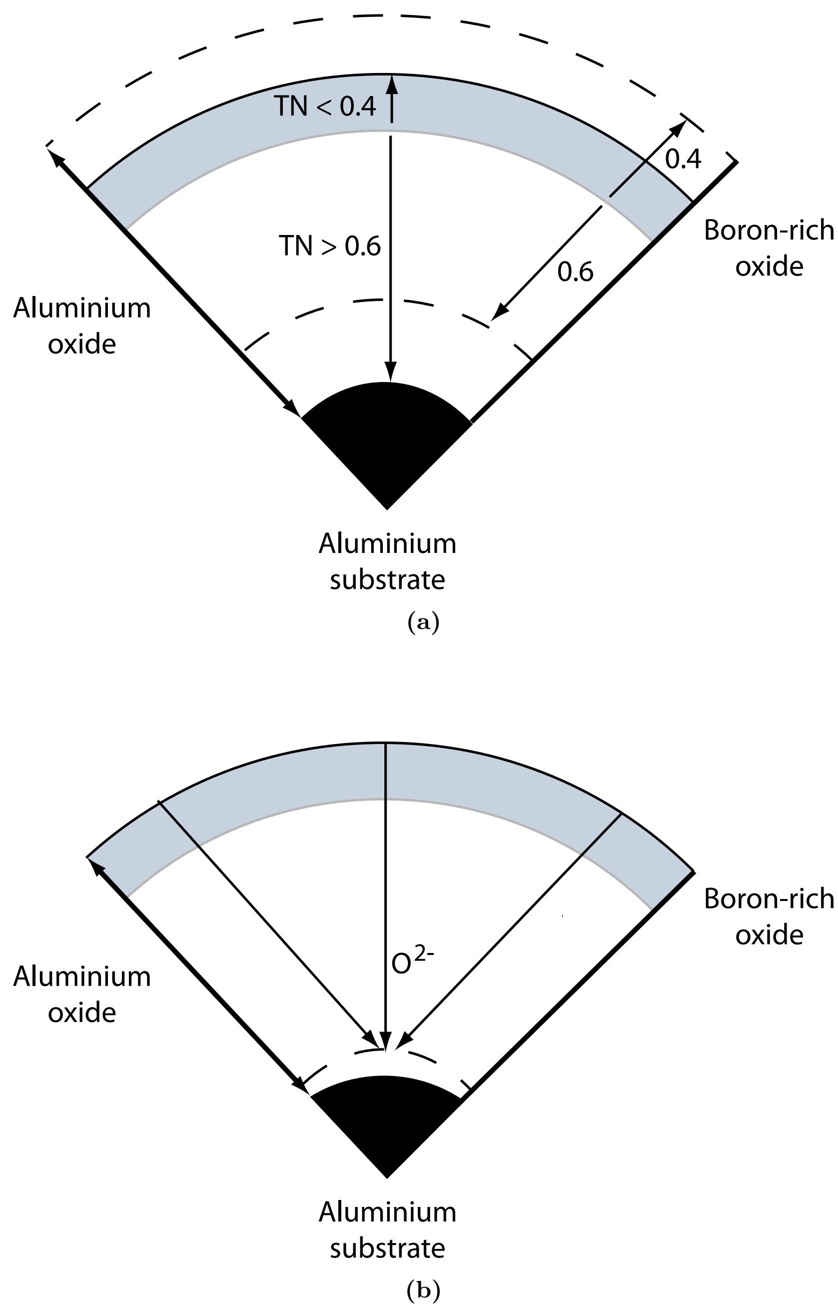

Figure 4.8 – Schematic diagrams of a convexity in a patterned specimen surface, showing the aluminium oxide (white) and the boron-containing oxide (grey) supported by the aluminium substrate (black). a. The schematic diagram describes the reduction and augmentation of the transport number (TN) in aluminium and oxygen respectively as a result of the curvature of the substrate and the associated decrease and increase in surface area respectively, the boron-rich / boron-free oxide interface is used as a reference for the determination of the transport number of aluminium and oxygen species. The dashed lines represent the location of the oxide surface and metal / oxide interface for aluminium and oxygen transport numbers of 0.4 and 0.6 (flat surface). b. The schematic diagram illustrates the flattening of the metal / oxide interface in a valley as a result of growth of anodic oxide associated with ingress of oxygen species in directions converging toward the centre of the curvature defined by the metal / oxide interface.

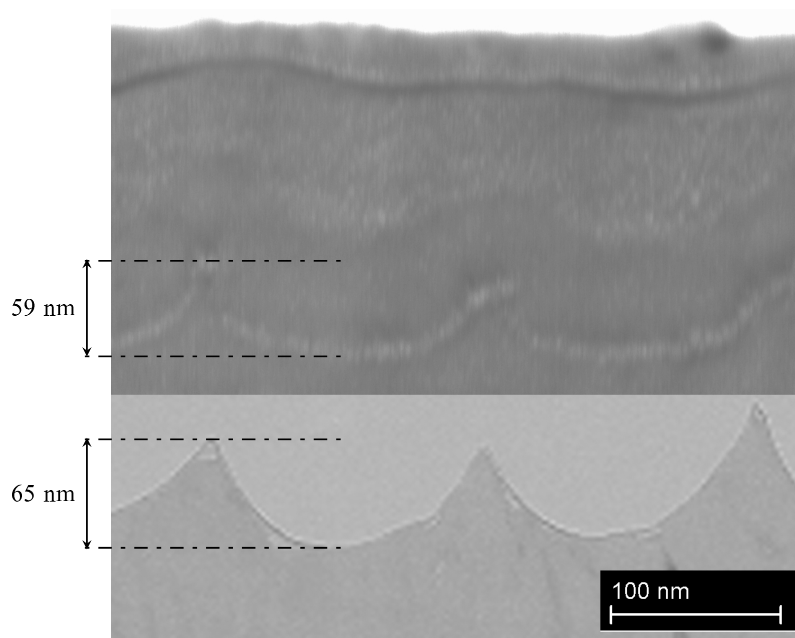

Figure 4.9 – Scanning transmission electron micrograph of an ultramicrotomed section of a superpure aluminium specimen patterned by anodizing in phosphoric acid and subsequent stripping of the porous film, and anodized in 0.1 M ammonium pentaborate solution to 200 V. A transmission electron micrograph of an ultramicrotomed section of the initial superpure aluminium substrate, i.e. before anodizing in 0.1 M ammonium pentaborate solution, is superimposed to the STEM image. The amplitude of the distribution of the phosphorus species within the anodic oxide film is 59 nm, while the amplitude of the initial pattern of the superpure aluminium substrate is measured at 65 nm.

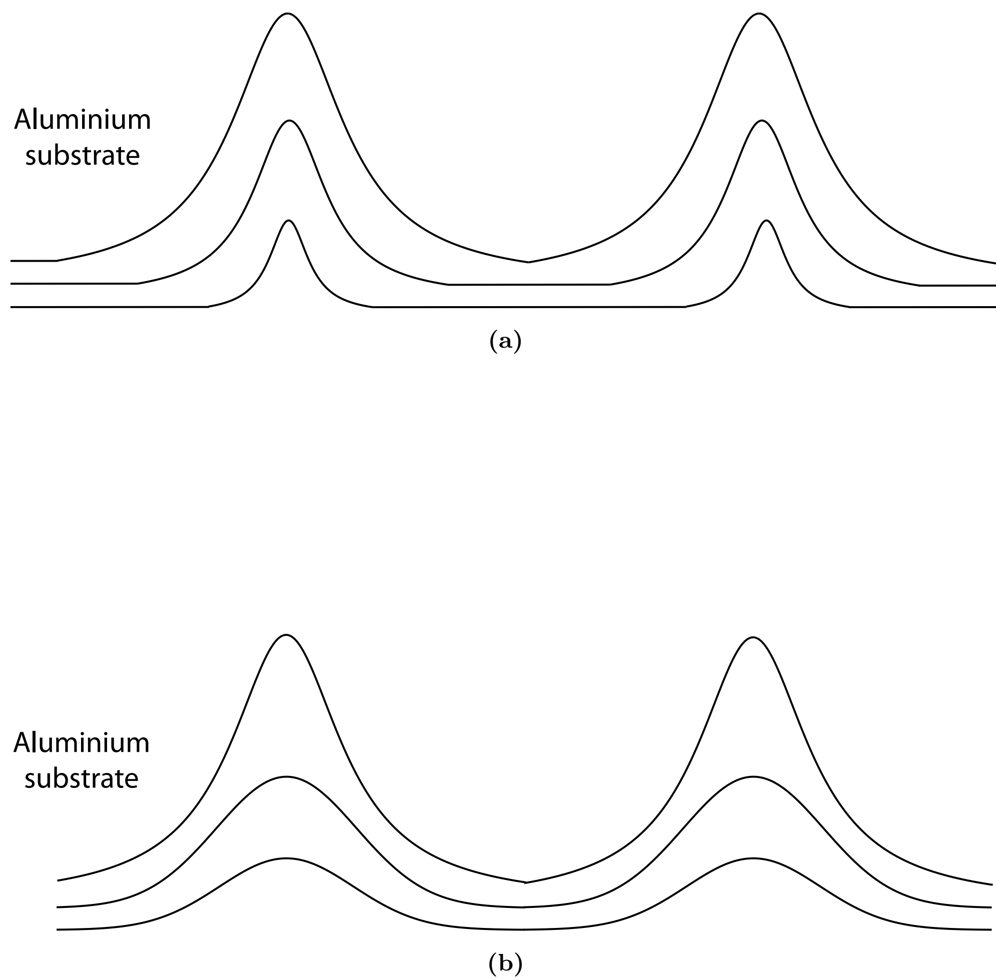

Figure 4.10 – Schematic diagram of the evolution of the substrate pattern during anodizing in 0.1 M ammonium pentaborate, the aluminium oxide surface is not represented; showing a. an homothetic transformation of the substrate pattern, the substrate presents patterns of similar shapes, but with reduction of the tip dimensions, and b. changes in the shape of the patterns, with preferential oxidation of the tips in the substrate.

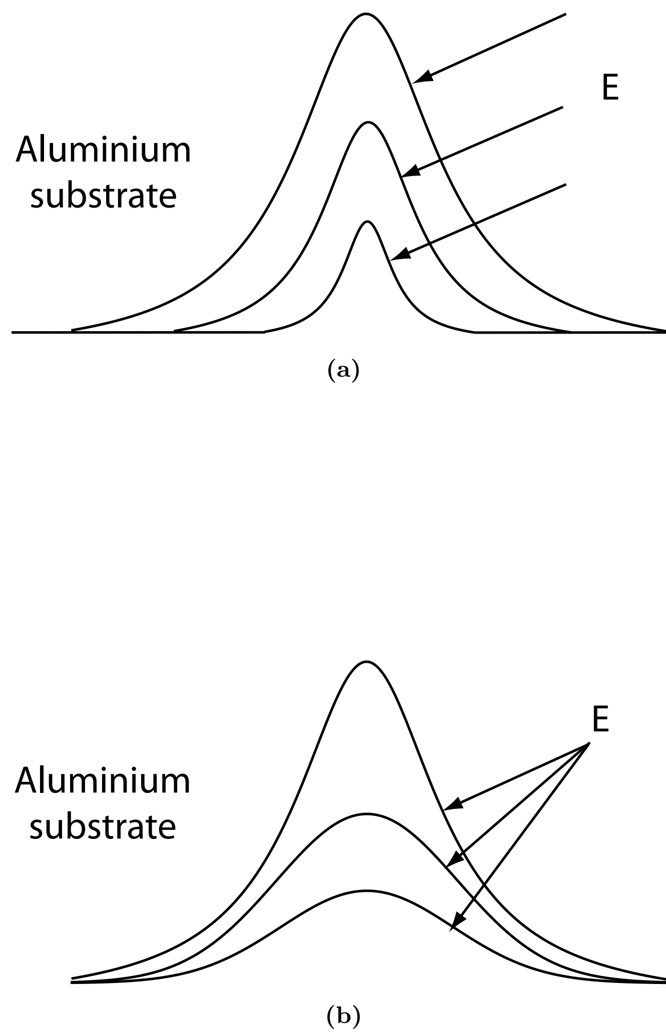

Figure 4.11 – Schematic diagram of the evolution of the direction of the electric field as a function of the aluminium substrate topography, showing a. a constant direction of the electric field associated with an homothetic transformation of the substrate pattern during anodizing and b. a variation of the direction of the electric field induced by the preferential oxidation of the tips in the substrate pattern.

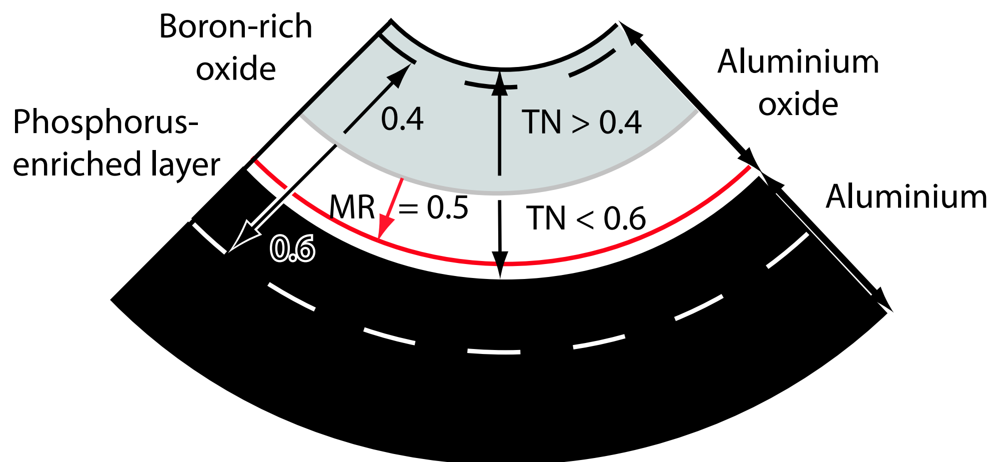

Figure 4.12 – Schematic diagram of a concavity in a patterned specimen surface, showing the aluminium oxide (white) and the boron-containing oxide (grey) supported by the aluminium substrate (black). The schematic diagram illustrates the apparent increase of migration rate (MR) in the phosphorus species (red) relative to that of the oxygen species. The increase in the migration rate of the phosphorus species is associated with the reduction in the transport number (TN) of the oxygen species as a result of the curvature of the substrate and the associated increase of surface area. The phosphorus species migrate under the high electric field at a rate of 0.50 relative to that of the oxygen species, as if the oxygen species were presenting a transport number of 0.60. The boron-rich / boron-free oxide interface is used as a reference for the determination of the transport number of aluminium and oxygen species. The dashed lines represent the location of the oxide surface and metal / oxide interface for aluminium and oxygen transport numbers of 0.4 and 0.6 (flat surface).

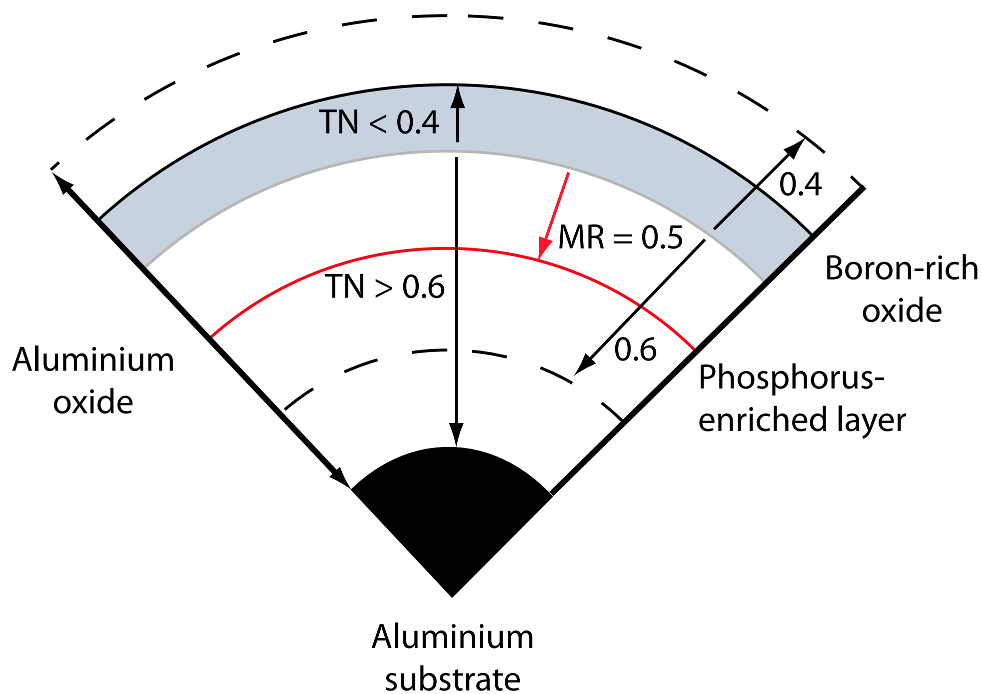

Figure 4.13 – Schematic diagram of a convexity in a patterned specimen surface, showing the aluminium oxide (white) and the boron-containing oxide (grey) supported by the aluminium substrate (black). The schematic diagram describes the decrease in the migration rate (MR) of the phosphorus species (red) relative to that of the oxygen species. The reduction in the migration rate of the phosphorus species is associated with the increase in the transport number (TN) of the oxygen species as a result of the curvature of the substrate and the associated decrease of surface area. The phosphorus species migrate under the high electric field at a rate of 0.50 relative to that of the oxygen species, as if the oxygen species were presenting a transport number of 0.60. The boron-rich / boron-free oxide interface is used as a reference for the determination of the transport number of aluminium and oxygen species. The dashed lines represent the location of the oxide surface and metal / oxide interface for aluminium and oxygen transport numbers of 0.4 and 0.6 (flat surface).

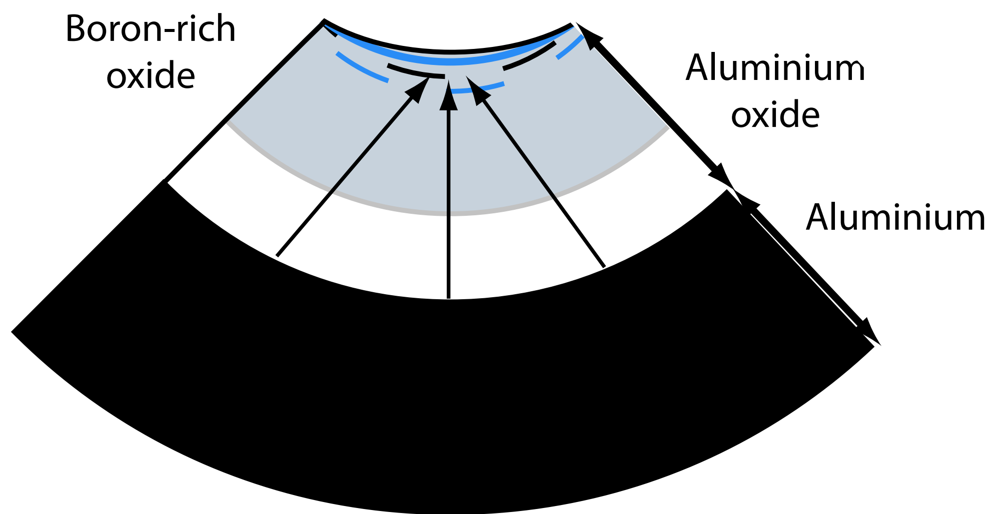

Figure 4.14 – Schematic diagram of a concavity in a patterned specimen surface, showing the aluminium oxide (white) and the boron-containing oxide (grey) supported by the aluminium substrate (black). The schematic diagram illustrates the flattening of the chromium-enriched layer in a valley simultaneously to the flattening of the oxide surface as a result of growth of anodic oxide associated with aluminium egress in directions converging toward the centre of the curvature defined by the metal / oxide interface.

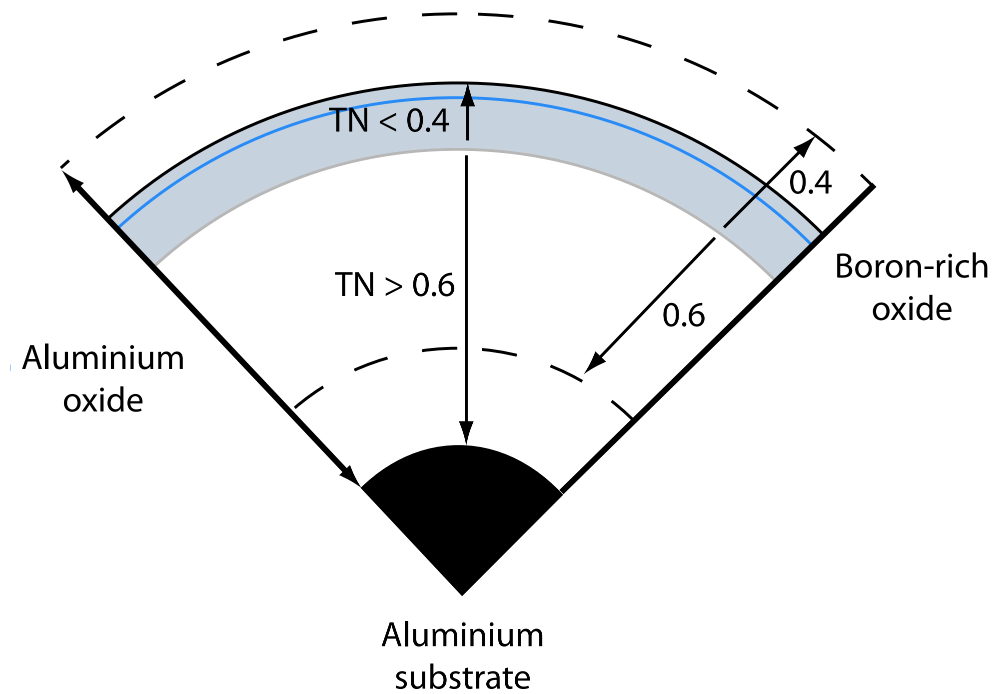

Figure 4.15 – Schematic diagram of a convexity in a patterned specimen surface, showing the aluminium oxide (white) and the boron-containing oxide (grey) supported by the aluminium substrate (black). The schematic diagram describes the increase in the migration rate (MR) of the chromium species associated with the reduction in the transport number (TN) of the aluminium species as a result of the curvature of the substrate and the associated increase of surface area. The boron-rich / boron-free oxide interface is used as a reference for the determination of the transport number of aluminium and oxygen species. The dashed lines represent the location of the oxide surface and metal / oxide interface for aluminium and oxygen transport numbers of 0.4 and 0.6 (flat surface).

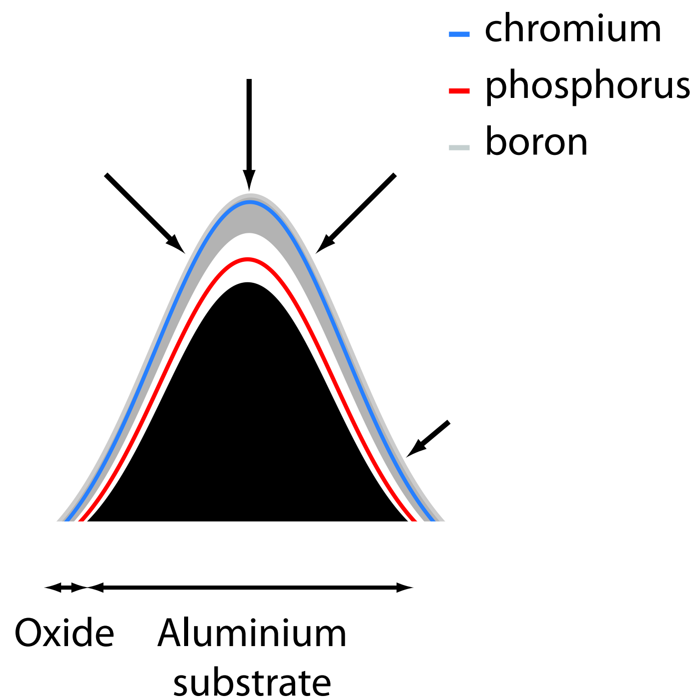

Figure 4.16 – Schematic diagram of a peak in the surface topography showing a local enhancement of the electric field at the tip (long arrows) in comparison with the valley (short arrow), which results in a faster thickening of the oxide layer over the tip than at the valley in the surface.

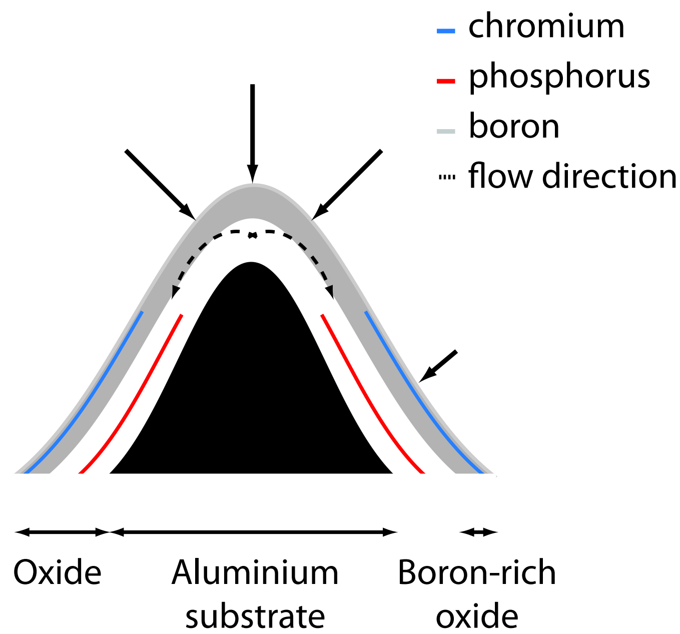

Figure 4.17 – Schematic diagram of a peak in the surface topography showing a local enhancement of the electric field at the tip (long arrows) in comparison with the valley (short arrow), resulting in oxide flow from the tip to the valley in order to equalise the oxide thickness over the surface topography. Consequently, the chromium and phosphorus tracers are absent from the tip of the peak as a result of the oxide flow.

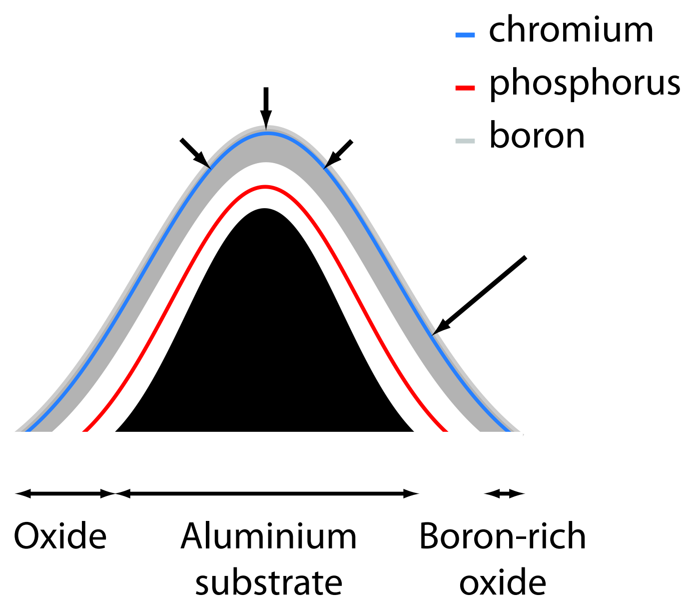

Figure 4.18 – Schematic diagram of a peak in the surface topography showing a redistribution of the electric field from the tip to the valley (long arrow) resulting in a faster thickening of oxide film over the valley, thereby equalising the thickness of the oxide layer over the surface topography. In this case, the chromium and phosphorus tracers are present uniformly along the oxide layer.

General Summary and Conclusions

Over the years, a considerable interest has been focused on elucidating the growth mechanisms of barrier-type anodic films, in order to control their compositions and properties for fundamental interest or for specific applications in various fields, namely electrical engineering, microelectronics, corrosion resistance and tribology.

The influence of the surface roughness of the substrate on the growth of barrier-type anodic alumina films has been examined in order to gain insight into their mechanisms of formation and precise knowledge of the material transport leading to the smoothing of the oxide surface and metal / oxide interface. The investigations were undertaken by (i) generation of superpure aluminium substrates of controlled roughnesses, (ii) incorporation of a boron marker, and chromium and phosphorus tracers and (iii) probing the distributions of the incorporated species during the formation of alumina films by anodizing the differently patterned superpure aluminium substrates in 0.1 M ammonium pentaborate solution. Hence, studying the distributions of incorporated species, used as markers and tracers, revealed variations of the anodic oxide film composition associated with surface topography modifications during anodizing of patterned aluminium substrates; and consequently, led to the understanding of the nature of the processes taking place during growth of barrier-type anodic aluminium oxide layers.

Superpure aluminium substrates of tailored patterns have been generated by electropolishing and anodizing in different acids, namely sulphuric acid, oxalic acid, phosphoric acid. A chromic / phosphoric acid solution was used in order to dissolve the porous anodic oxide layers, thereby revealing the pattern of aluminium surface through development of the hexagonal alumina cells that penetrate the substrate in a hemispherical manner. As a result, the surface roughnesses of the superpure aluminium specimens have been tailored in the range 1 - 32 nm.

The electropolishing and stripping processes have been found to result in the incorporation of chlorine, chromium and phosphorus species into the 4-nm thick oxide layer formed over the patterned substrates. The surface film composition has been described using XPS and MEIS techniques. The oxide film formed on specimen successively electropolished and immersed in a chromic / phosphoric acid solution consists of an aluminium oxide layer variously doped with chlorine, chromium and

phosphorus impurities in amounts of about 0.43 x 10^{15}, 0.88 x 10^{15} and 0.45 x 10^{15} at cm^{-2} respectively. In addition, a copper-enriched layer containing about 0.15 x 10^{15} at cm^{-2} is located at the metal / oxide interface. The enrichment of copper results from preferential oxidation, during electropolishing, of aluminium in comparison with copper impurities present in the metal. For the specimens patterned by anodizing in sulphuric acid, oxalic acid, phosphoric acid and stripping of the porous films, the different enriched layers could not be quantified due to the degradation of the depth resolution of the MEIS technique associated with the surface roughness of the specimens.

Subsequently, barrier-type alumina films have been formed anodically on differently patterned superpure aluminium substrates at a constant current density of 5 mA cm^{-2} in 0.1 M ammonium pentaborate solution at 293 K. In such conditions, the anodic oxide growth proceeds uniformly at a formation ratio of about 1.2 nm V^{-1}, independent of the initial substrate roughnesses.

The TEM and AFM examinations of the surface topography development during anodizing of patterned aluminium substrates revealed progressive smoothing of the initial surface roughness of the superpure aluminium substrates. In addition, the distributions of dopants, namely boron, chromium and phosphorus, incorporated within anodic alumina films, have been examined during the growth of the alumina films using STEM and elemental depth profiling analysis techniques, namely GD-OES, GD-TOF-MS and TOF-SIMS. The boron electrolyte-derived species are immobile while the chromium and phosphorus species, incorporated initially into the 4-nm thick oxide films present over the differently patterned aluminium substrates, migrate in opposite directions to give two well-separated distributions.

For anodic oxide layers, formed on the differently patterned substrates, the mean migration rates of chromium and phosphorus species have been determined to be 0.74 $\pm$ 0.01 and 0.50 $\pm$ 0.02 relative to that of aluminium and oxygen ions respectively. Further, the initial distributions of the phosphorus species, incorporated within the oxide films present over the differently patterned superpure aluminium substrates, remain during the formation of alumina films by anodizing the differently patterned superpure aluminium substrates; conversely, significant narrowing of the amplitude of

the chromium distributions arises.

In addition, the depth resolutions associated with the different elemental depth profiling techniques have been evaluated using the $\sim$ 4-nm thick chromium-enriched layer incorporated in the anodic alumina films formed by anodizing of electropolished specimens. During depth profiling of the chromium tracers, the FWHM values of the depth profiles associated with the chromium-enriched layers have been determined by GD-TOF-MS, GD-OES and TOF-SIMS to be about 3.4 ± 0.4 nm respectively. Thus, the depth resolutions achieved by the different elemental depth profiling techniques are similar; however, degradation of the depth resolution arises faster for the GDS techniques than for TOF-SIMS. Indeed, for the GD-TOF-MS and GD-OES techniques, broadening of the profiles takes place at a ratio of about 9 %, representing about two times the broadening occurring during depth profiling using TOF-SIMS (5 %). The characteristic crater shape developed during glow discharge depth profiling analysis, as well as the difference in the area of measurement ($\sim$13 mm^2 for the GD techniques compared with $\sim$225 μm^2 for TOF-SIMS) may explain the larger ratio of broadening arising during glow discharge depth profile analysis.

Probing distributions of the boron marker and the chromium and phosphorus tracers within alumina layers on relatively rough aluminium substrates has been challenging both using scanning transmission electron microscopy due to lateral resolution limitation and by elemental depth profiling analyses as a result of sputtering-induced surface topography modifications.

For GDS techniques, the surface topography of the differently patterned specimens has been shown to influence the uniformity of the erosion process by local enhancement of the sputtering yield. Thus, deviation between the original elemental depth distributions and the measured profiles results from anisotropic sputtering and the subsequent development of peak-like textures as well as the variation of sputtering rate through the film removal. Consequently, deformation of the Gaussian-like shape of the elemental depth profiles of the corresponding chromium and phosphorus distributions takes place through the non-unique depth of information. In contrast, no preferential sputtering occurs over the surface pattern of the different specimens during TOF-SIMS depth profiling analysis, using a dual beam mode configuration and by employing primary

ion beams at an angle of incidence of 45° relative to the normal to the specimen surface. The original surface pattern remains largely during depth profiling of the oxide layers, with the material being potentially removed uniformly. TOF-SIMS analysis allowed depth profiling of thin films formed on patterned substrates; however, the selection of a reference for the depth calibration of the elemental depth profiles was not straightforward. As a result, the distributions of the different incorporated species could not be determined directly.

The growth mechanism of anodic alumina films formed by anodizing differently patterned aluminium substrates has been examined using scanning transmission electron micrographs of cross-section of the oxide layers showing the distributions of the boron marker and the chromium and phosphorus tracers. The transport mechanisms taking place during the growth of barrier-type anodic alumina formed anodically on patterned superpure aluminium substrates that lead to the smoothing of the oxide surface and of the metal / oxide interface were examined considering high field ionic conduction and electrostrictive stress. The development of the distributions of a boron marker and of chromium and phosphorus tracers, during anodizing of differently patterned specimens in 0.1 ammonium pentaborate solution, were probed by scanning transmission electron microscopy.

For patterned aluminium substrates, the surface curvatures have been shown to induce augmentation and reduction in the transport number of the aluminium and oxygen species in comparison with that of a flat substrate; i.e. at the peaks in the surface the transport numbers of the aluminium and the oxygen species are less than 0.4 and greater than 0.6 respectively; conversely, at the valleys in the surface the transport numbers of the aluminium and the oxygen species are greater than 0.4 and less than 0.6 respectively. In addition, the smoothing mechanism of the specimen is considered to arise by aluminium ion egress at the valleys in the surface and oxygen ion ingress at the aluminium peaks in the metal / oxide interface; it is also associated with both the augmentation in volume due to the conversion of aluminium into alumina and the reduction in the surface area that the oxide film has to accommodate. Thus, the expanding volume of the growing oxide adapts the recessing aluminium surface. The rearrangement of the volume of the growing oxide is revealed by the narrowing of the chromium-enriched layer during anodizing. Smoothing of the chromium distribution is

evident during anodizing of each of the patterned substrates. Thus, independent of the amplitude of the initial aluminium substrate topographies, achieved by electropolishing or by anodizing in sulphuric acid, oxalic acid, phosphoric acid and stripping of the porous films, the smoothing process of the differently patterned superpure aluminium substrate is identical. Finally, with consideration of the relatively uniform distributions of the chromium and phosphorus-enriched layers along the anodic alumina film, thickening of the oxide film over the surface topography is not considered to proceed by oxide flow from the peaks to the valleys, which may result in the absence of the tracers at the peaks in the surface, but by redistributions of the electric field over the surface topography.

Considering the growth mechanism proceeding during anodizing of patterned aluminium substrates, the influence of the substrate roughnesses on the distributions of incorporated species and the composition of the anodic alumina films is of primary importance. A careful control of the initial substrate roughness is therefore required in order to control the composition of the generated anodic oxide layers.

Finally, the use of boron marker, and chromium and phosphorus tracers have been of immense value for the investigation of the growth mechanism of barrier-type anodic alumina on patterned substrates. In contrast to elemental depth profiling analysis, the examination of the different enriched-layers by scanning transmission electron microscopy provided insight on the material transport within the oxide layers with a lateral resolution matching the dimensions of the specimen surface roughnesses. However, in order to achieve such a resolution, the thickness of the anodic alumina layer has to be larger than 200 nm, thereby limiting the observations of thinner specimens.

For the different elemental depth profiling techniques, the chromium tracer incorporated within anodic alumina formed by anodizing electropolished substrates has been an excellent delta layer, allowing the determination of the depth resolution achieved by the different techniques. The depth resolutions achieved by GD-TOF-MS, GD-OES and TOF-SIMS have been found to be similar for layers thinner than about 20 nm; while for thicker specimens the GDS techniques present a more significant broadening than TOF-SIMS. In contrast to the chromium tracer, the distribution of the phosphorus tracer has been shown to be influenced by the surface roughness of electropolished

substrates; and thereby, resulting in a significant broadening of the phosphorus depth profile in comparison with the chromium depth profile.

GD-TOF-MS and GD-OES elemental depth profiling analyses of patterned specimens have been shown to lead to the development of peak-like textures at the surface of the different specimens; thereby limiting the depth resolution achieved by the glow-discharge sputtering techniques. Conversely, for TOF-SIMS, the use of primary-ion beams at an angle of 45° relative to the normal to the specimen surface allowed relatively uniform material removal, with a limited influence of the specimen surface roughnesses.

Suggestions for Future Work

Following the investigations described in this thesis, several lines of research arise.

Scanning transmission electron microscopy examinations have been of primary importance for this work; however, they have been limited by the lateral resolution achieved by the microscope. Elaboration of substrates with a larger pattern period, for instance by anodizing in phosphoric acid at 195 V, would allow growth of thicker oxide layer before complete smoothing of the oxide surface and metal / oxide interface, than in the present work. As a result, STEM investigations could be facilitated and more precise information would be gained.

The formation of anodic alumina films have been investigated using a boron marker, and a chromium and phosphorus tracers. Complementary investigations could be undertaken using a different set of markers or tracers, for instance a multi-layer system of tungsten alloy tracers deposited by magnetron sputtering, tungsten alloy tracers offering an excellent Z-contrast for transmission electron microscopy.

The growth mechanism of barrier-type anodic alumina layer formed on patterned specimens relies mainly on the electric field distribution across the surface of the specimen. Therefore, further understanding of the alumina layer formation requires a complete modelling of the potential distribution coupled with the field-induced ion transport during anodizing of patterned aluminium substrates.

Further, modelling of the growth mechanism of barrier-type anodic oxide may be of interests for other metals, namely tantalum, niobium, titanium. In addition, such a model could provide significant insight into the growth of porous films, with information on the transition from barrier-type to porous-type layers.

Finally, barrier-type anodic alumina containing markers and tracers have been shown to be excellent specimens for the characterisation of the sputtering process taking place during sputtering-induced elemental depth profiling analysis, due to the controlled and reproducible thickness of the layers and precise locations of the markers and tracers. Further investigations could be carried on the reconstruction of the elemental depth profiles using a similar approach to the MRI model (Mixing, Roughness, Information depth).

Bibliography

Alexander, M. R., Thompson, G. E. and Beamson, G., *Surf. Interface Anal.*, **2000**, 29, 7, 468.

Alford, T., Feldman, L. and Mayer, J., Fundamentals of Nanoscale Film Analysis, chapter 10: X-ray Photoelectron Spectroscopy, 199–213, Springer US, **2007**.

Allen, P. N. and Dowsett, M. G., *Surf. Interface Anal.*, **1994**, 21, 3, 206.

Angeli, J., Bengtson, A., Bogaerts, A., Hoffmann, V., Hodoroaba, V.-D. and Steers, E., *J. Anal. At. Spectrom.*, **2003**, 18, 670.

Benninghoven, A., *Surf. Sci.*, **1971**, 28, 541.

Berneron, R. and Charbonnier, J. C., *Surf. Interface Anal.*, **1981**, 3, 134.

Biesinger, M. C., Brown, C., Mycroft, J. R., Davidson, R. D. and McIntyre, N. S., *Surf. Interface Anal.*, **2004**, 36, 12, 1550.

Bings, N., Bogaerts, A. and Broekaert, J., *Anal. Chem.*, **2008**, 80, 4317.

Bogaerts, A., *J. Anal. At. Spectrom.*, **2007**, 22, 13.

Bogaerts, A. and Gijbels, R., **1998**, 1–42.

Bogaerts, A., van Straaten, M. and Gijbels, R., **1995**, 179–196.

Bradhurst, D. H. and Leach, J. S. L., *J. Electrochem. Soc.*, **1966**, 113, 12, 1245.

Broekaert, J. A. C., Glow Discharge Plasmas in Analytical Spectroscopy, chapter 2.2, Glow Discharges, Wiley, **2003**.

Cabrera, N. and Mott, N. F., *Rep. Prog. Phys.*, **1948**, 12, 163.

Caicedo-Martinez, C. E., Koroleva, E. V., Thompson, G. E., Skeldon, P., Shimizu, K., Habazaki, H. and Hoellrigl, G., *Surf. Interface Anal.*, **2002**, 34, 405.

Carter, G., *Vacuum*, **1996**, 47, 409.

Carter, G. and Nobes, M., *Vacuum*, **1994**, 45, 539.

Carter, G., Gras-Marti, A. and Nobes, M. J., *Radiat. Eff. Defects Solids*, **1982**a, 62, 119.

Carter, G., Nobes, M. and Armour, D., *Vacuum*, **1982**b, 32, 509.

Cayless, R. B. C., ASM Handbook, volume 2: Properties and Selection: Nonferrous Alloys and Special-Purpose Materials, chapter Alloy and Temper Designation Systems for Aluminium and Aluminium Alloys, **2002**.

Chalk, D. B., ASM Handbook, volume 5: Surface Engineering, chapter Classification and Selection of Cleaning Processes, **2002**.

Cordier, F. and Ollivier, E., *Surf. Interface Anal.*, **1995**, 23, 601.

Dapor, M. and Marchetti, F., *Surf. Interface Anal.*, **1989**, 14, 524.

Davies, J. A., Domeij, B., Pringle, J. P. S. and Brown, F., *J. Electrochem. Soc.*, **1965**, 112, 675.

Diggle, J. W., Downie, T. C. and Goulding, C. W., *Chem. Rev.*, **1969**, 69, 365 .

Egerton, R. F., Physical Principles of Electron Microscopy, chapter 5: The Scanning Electron Microscope, 125–153, Springer, **2005**.

Escobar-Galindo, R., Fornies, E. and Albella, J. M., *J. Anal. At. Spectrom.*, **2005**a, 20, 10, 1108.

Escobar-Galindo, R., Fornies, E. and Albella, J. M., *J. Anal. At. Spectrom.*, **2005**b, 20, 10, 1116.

Escobar-Galindo, R., Gago, R., Albella, J., Galindo, R. E., Gago, R. and Lousa, A., *TrAC, Trends Anal. Chem.*, **2009**, 28, 4, 494.

Frost, F., Ziberi, B., Schindler, A. and Rauschenbach, B., *Appl. Phys. A: Mater. Sci. Process.*, **2008**, 91, 4, 551.

Garcia-Vergara, S. J., Skeldon, P., Thompson, G. E. and Habazaki, H., *Electrochim. Acta*, **2006**, 52, 681.

Godard, H. P., Jepson, W. B., Bothwell, M. R. and Kane, R. L., The Corrosion of Light Metals, John Wiley & Sons, **1967**.

Godehardt, R., Lebek, W., Adhikari, R., Rosenthal, M., Martin, C., Frangov, S. and Michler, G. H., *Eur. Polym. J.*, **2004**, 40, 917 .

Habazaki, H., Shimizu, K., Skeldon, P., Thompson, G. E., Wood, G. C. and Zhou, X., *Corros. Sci.*, **1997**, 39, 731.

Hatch, J. E., ASM Handbook, volume 2: Properties and Selection: Nonferrous Alloys and Special-Purpose Materials, chapter Aluminium: Properties and Physical Metallurgy, **1984**.

Hebert, K. R. and Houser, J. E., *J. Electrochem. Soc.*, **2009**, 156, 8, C275.

Hideki Masuda, K. Y. and Osaka, A., *Jpn. J. Appl. Phys.*, **1998**, 37, L1340.

Hoffmann, V., Dorka, R., Wilken, L., Hodoroaba, V.-D. and Wetzig, K., *Surf. Interface Anal.*, **2003**, 35, 575.

Hofmann, S., *Surf. Interface Anal.*, **1980**, 2, 148.

Hofmann, S., *Surf. Interface Anal.*, **1986**, 8, 87.

Hofmann, S., *Rep. Prog. Phys.*, **1998**, 61, 827.

Hofmann, S. and Mader, W., *Surf. Interface Anal.*, **1990**, 15, 794.

Hofmann, S. and Zalar, A., *Thin Solid Films*, **1979**, 60, 201.

Hofmann, S. and Zalar, A., *Surf. Interface Anal.*, **1987**, 10, 7.

Hollingsworth, E. and Hunsicker, H., ASM Handbook, volume 13: Corrosion, chapter Corrosion of Aluminium and Aluminium Alloys, **2002**.

Houser, J. E. and Hebert, K. R., *J. Electrochem. Soc.*, **2006**, 153, 12, B566.

Houser, J. E. and Hebert, K. R., *phys. status solidi a*, **2008**, 205, 10, 2396.

Houser, J. E. and Hebert, K. R., *Nat. Mater.*, **2009**, 8, 5, 415.

Hsiung, P. and Trocellier, P., *J. Radioanal. Nucl. Chem.*, **1987**, 109, 459.

Hunsicker, H. J., ASM Handbook, volume 2: Properties and Selection: Nonferrous Alloys and Special-Purpose Materials, chapter Properties of Pure Metals, **2002**.

Hunter, M. S. and Fowle, P., *J. Electrochem. Soc.*, **1956**, 103, 482.

Jaksch, H., in Materials World, **1996** .

Jessensky, O., Muller, F. and Gosele, U., *Appl. Phys. Lett.*, **1998**, 72, 1173.

Jones, D. A., Principles and Prevention of Corrosion, 2nd edition edition, **1995**.

Jones, D. G., Glow Discharge Optical Emission Spectroscopy, chapter 3, Instrumentation and Operation, John Wiley & Sons, **1997**.

Karolewski, M. A., *Appl. Surf. Sci.*, **2009**, 255, 7226.

King, B. V., Glow Discharge Optical Emission Spectroscopy, chapter 6, Sputtering, John Wiley & Sons, **1997**.

King, B. V. and Tsong, I. S. T., *J. Vac. Sci. Technol., A*, **1984**, 2, 4, 1443.

Laude, J. P. and Chapon, P., Tech. Ing., volume P 2, chapter 715v2, Spectrometrie de decharge luminescente (GDOS et GDMS), **2005**.

Lewis, J. E. and Plumb, R. C., *Appl. Radiat. Isot.*, **1956**, 1, 33.

Li, A. P., Muller, F., Birner, A., Nielsch, K. and Gosele, U., *J. Appl. Phys.*, **1998**, 84, 6023.

Masuda, H. and Fukuda, K., *Science*, **1995**, 268, 1466.

Masuda, H., Hasegwa, F. and Ono, S., *J. Electrochem. Soc.*, **1997**, 144, L127.

Nelis, T. and Pallosi, J., *Appl. Spectrosc. Rev.*, **2006**, 41, 227.

Nelis, T., Aeberhard, M. and Hohl, M., *J. Anal. At. Spectrom*, **2006**, 2, 112.

O'Sullivan, J. P. and Wood, G. C., *Proceedings R. Soc. Lond. Philos. Trans. Ser. A Math. Phys. Eng. Sci.*, **1970**, 317, 511.

Parkhutik, V. P. and Shershulsky, V. I., *J. Phys. D: Appl. Phys.*, **1992**, 25, 1258.

Payling, R., Glow Discharge Optical Emission Spectroscopy, John Wiley & Sons, **1997**.

Pernick, J., ASM Handbook, volume 13: Corrosion, chapter Aluminium Anodizing, Stripping of Anodized Coatings, **2002**.

Pisonero, J., Fernandez, B., Pereiro, R., Bordel, N. and Sanz-Medel, A., *TrAC, Trends Anal. Chem.*, **2006**, 25, 1, 11.

Postawa, Z., Czerwinski, B., Szewczyk, M., Smiley, E. J., Winograd, N. and Garrison, B. J., *J. Phys. Chem. B*, **2004**, 108, 7831.

Pourbaix, M., Atlas of Electrochemical Equilibria in Aqueous Solutions, Pergamon Press, **1966**.

Pringle, J. P. S., *J. Electrochem. Soc.*, **1972**, 119, 4, 482.

Pringle, J. P. S., *J. Electrochem. Soc.*, **1973**a, 120, 10, 1391.

Pringle, J. P. S., *J. Electrochem. Soc.*, **1973**b, 120, 398.

Pringle, J. P. S., *Electrochim. Acta*, **1980**, 25, 1403.

Quentmeier, A., *J. Anal. At. Spectrom.*, **1994**, 9, 355.

Richards, S., **http://www.dl.ac.uk/MEIS/, 2010**.

Rooy, E. L., ASM Handbook, volume 2: Properties and Selection: Nonferrous Alloys and Special-Purpose Materials, chapter Introduction to Aluminium and Aluminium Alloys, **2002**.

Safrany, J. S., Tech. Ing., chapter M 1630, Anodisation de l'Aluminium et des ses Alliages, **2007**.

Sato, N., *Electrochim. Acta*, **1971**, 16, 10, 1683.

Seah, M. P., Sanz, J. M. and Hofmann, S., *Thin Solid Films*, **1981**, 81, 239.

Shah, S. I., Handbook of thin film process technology, chapter A3.0, Sputtering: Introduction and General Discussion, IOP, **1995**.

Shimizu, K., Kobayashi, K., Thompson, G. E. and Wood, G. C., **1991**, 42, 645.

Shimizu, K., Brown, G. M., Habazaki, H., Kobayashi, K., Skeldon, P., Thompson, G. E. and Wood, G. C., *Surf. Interface Anal.*, **1999**a, 27, 24.

Shimizu, K., Brown, G. M., Habazaki, H., Kobayashi, K., Skeldon, P., Thompson, G. E. and Wood, G. C., *Electrochim. Acta*, **1999**b, 44, 2297.

Shimizu, K., Brown, G. M., Habazaki, H., Kobayashi, K., Skeldon, P., Thompson, G. E. and Wood, G. C., *Surf. Interface Anal.*, **1999**c, 27, 153.

Shimizu, K., Habazaki, H., Skeldon, P., Thompson, G. E. and Wood, G. C., *Surf. Interface Anal.*, **1999**d, 27, 11, 998.

Shimizu, K., Habazaki, H., Skeldon, P., Thompson, G. E. and Wood, G. C., *Surf. Interface Anal.*, **1999**e, 27, 950.

Shimizu, K., Habazaki, H., Skeldon, P. and Thompson, G. E., *Surf. Interface Anal.*, **2003**, 35, 564.

Shirley, D. A., *Phys. Rev. B*, **1972**, 5, 4709.

Sigmund, P., *Phys. Rev.*, **1969**, 184, 383.

Sigmund, P., *Nucl. Instrum. Methods Phys. Res., Sect. B*, **1987**, 27, 1, 1.

Skeldon, P., Shimizu, K., Thompson, G. E. and Wood, G. C., *Thin Solid Films*, **1985**, 123, 127.

Skeldon, P., Thompson, G. E., Garcia-Vergara, S. J., Iglesias-Rubianes, L. and Blanco-Pinzon, C. E., *Electrochem. Solid-State Lett.*, **2006**, 9, B47.

Starke, U., **http://www.fkf.mpg.de/ga/Optical Profiler, 2003**.

Strohmeier, B. R., *Surf. Interface Anal.*, **1990**, 15, 1, 51.

Taglauer, E., Surface Analysis: The Principal Techniques, chapter 6: Low-Energy Ion Scattering and Rutherford Backscattering, 269–331, John Wiley and Sons, **2009**.

Takahashi, H. and Nagayama, M., *Electrochem. Acta*, **1978**, 23, 279.

Takashima, F., Miwa, K., Sakairi, M. and Takahashi, H., *J. Surf. Finish. Soc. Jpn.*, **2000**, 51, 6, 625.

Tanuma, S., Powell, C. J. and Penn, D. R., *Surf. Interface Anal.*, **1994**, 21, 3, 165.

Tempez, A., Canulescu, S., Molchan, I. S., Dobeli, M., Whitby, J. A., Lobo, L., Michler, J., Thompson, G. E., Bordel, N., Chapon, P., Skeldon, P., Delfanti, I., Tuccitto, N. and Licciardello, N., *Surf. Interface Anal.*, **2009**, 41, 966.

Teo, W. B. and Hirokawa, K., *Surf. Interface Anal.*, **1988**, 11, 533.

Thompson, G. E., *Thin Solid Films*, **1997**, 297, 192.

Tougaard, S., *Surf. Interface Anal.*, **1997**, 25, 137.

Unveren, E., Kemnitz, E., Hutton, S., Lippitz, A. and Unger, W. E. S., *Surf. Interface Anal.*, **2004**, 36, 1, 92.

Urbassek, H. M., Sputtering by Particle Bombardment: Experiments and Computer Calculations from Threshold to MeV Energies, chapter Results of Molecular Dynamics Calculations, 189–230, Springer, **2007**.

Vanhumbeeck, J. and Proost, J., *Electrochim. Acta*, **2008**, 53, 21, 6165.

Vermeulen, J. P. and Jaksch, H., in Imaging & Microscopy, **2005** .

Vermilyea, D. A., *J. Electrochem. Soc.*, **1963**, 110, 4, 345.

Vickerman, J. C., Surface Analysis: The Principal Techniques, chapter 4: Molecular Surface Mass Spectrometry by SIMS, 113–205, John Wiley and Sons, **2009**.

Williams, D. B. and Carter, C. B., Transmission Electron Microscopy: A Textbook for Materials Science, Springer, **2009**.

Winchester, M. R. and Payling, R., *Spectrochim. Acta, Part B*, **2004**, 59, 607.

Wuthrich, N., *Electrochim. Acta*, **1980**, 25, 6, 819.

Wuthrich, N., *Electrochim. Acta*, **1981**, 26, 11, 1617.

Yamamura, Y. and Shindo, S., *Radiat. Eff. Defects Solids*, **1984**, 80, 57.

Yuzhakov, V. V., Chang, H. C. and Miller, A. E., *Phys. Rev. B: Condens. Matter Mater. Phys.*, **1997**, 56, 12608 .

Zalm, P. C., *Rep. Prog. Phys.*, **1995**, 58, 10, 1321.

Zhou, X., Habazaki, H., Shimizu, K., Thompson, P. S. G. E. and Wood, G. C., *Thin Solid Films*, **1997**, 293, 327.

Ziegler, J. F., **http://www.srim.org/, 2010**.